Investigating the Interactions of Nanoscale Calcium Phosphates with Polymer Additives

Laura Mary Shallcross

A Thesis submitted for the Degree of Doctor of Philosophy

Department of Chemistry, University of Sheffield

January 2017

Acknowledgements

This research was funded by the EPSRC Doctoral Training Centre in Tissue Engineering and Regenerative Medicine, a collaboration between the Universities of Leeds, Sheffield and York. Grant number EP/500513/1.

The present work could not have been finished without the help of a large number of people. I would firstly like to thank my supervisors Dr Seb Spain and Professor Paul Hatton for all their help and advice. I would also like to thank Professor Steve Armes for his advice; Professor Ken Stanton for allowing me to undertake my placement with him at UCD and Dr Kevin Roche for all his help and advice during the placement which went on to shape the rest of my PhD project.

Thank you to the many technicians within the Chemistry department and Dental school, in particular: Rob Hanson for his assistance with TGA; Harry Adams for his assistance with running XRD samples; Keith Owens for his help with the Grubbs system; Dr Svet Tsokov for patiently teaching me to use the TEM and analyse the results, and Kirsty Franklin for her assistance with tissue culture. Thanks also go to Pete and Nick, the wonderful store masters for everything from troubleshooting orders to playing football to being around for a friendly chat; Denise and Louise in accounts for being so helpful and finally to Pauline Boulding for all the cups of tea and smiles that got me through many years of this project.

Thanks go to Dr Elliot Carrington and Tom Roseveare in the Brammer group for their assistance with running and analysing XRD and also for the many climbing trips.

Dr Caroline Wilcock, Dr Martin Santocildes Romero and Dr Sarah Lindsay, thank you so much for your time and patience with teaching me cell culture and assay protocols.

I would not have finished this PhD without the help and support of the Spain Group particularly Kat Murray and Dom Gray, we went through some tough times but made it through. Thank you to Tom Neal for running the SAXS measurements on the polymers, you were a life saver! Rheanna Perry, Jasmine Lord, Emma Owens, Laila Alhaidari, Kathy Clitherow, Nat Parsons and Charlie Pearce, I have had a fantastic time working with you all and wish you all luck for the future and also thank you to Ziska Stahl for being a fantastic Erasmus student. Thanks also to Dr Sarah Canning, Dr Simon Finnegan, Pavintorn

Teratanatorn (Mew), Dave Pownall, Dr Luke Cartwright, Nathan Rutland and the Armes group, specifically Dr Joe Lovett, Dr Matt Derry, Dr Lizzy Jones and Dr Vicki Cunningham for their help and friendship throughout this project. Steven Spall and Kate Cash, thank you for being great housemates.

I have to thank my wonderful family for supporting me throughout my whole life. Mum, Dad, Eleanor, Sarah, Jean, Chris, Grandma and Grandad, Ste, Sue, Chris, Lucy, Jodie, Leo, Lynne, Kev, Julie and Manuel – thank you all for your all you love and encouragement.

Finally, I have to thank my wonderful David Smith. Without you I would have crumbled from stress a long time ago. Thank you for putting up with me, I love you and can't wait to start the next chapter of my life with you and Ninja Dog (Luna) ☺

Abstract

Highly branched and linear polymers and block copolymers were used to create nanocomposites with hydroxyapatite (HA) and fluorhydroxyapatite (FHA) to demonstrate an enabling technology with the possibility of opening new opportunities in medicine, dentistry and other non-health sectors. To test this highly branched polymers of poly(acrylic acid) (PAA), poly(methacrylic acid) (PMAA) and poly(2-acrylamido-2-methylpropane sulfonic acid) (PAMPS) were synthesised by reversible addition-fragmentation chain transfer self-condensing vinyl polymerisation (RAFT-SCVP) while low and high molecular weight linear poly(acrylic acid)s were commercially sourced. The highly-branched polymers were difficult to characterise due to being insoluble in many solvents while the PAMPS only achieve very low conversions and were found to destroy the RAFT agent during the polymerisation. The highly branched and linear polymers were added to the synthesis of fluorhydroxyapatite (FHA) and hydroxyapatite (HA) nanoparticles. Analysis via FTIR, XRD, TGA and TEM demonstrated that the inclusion of the polymer in the (F)HA samples had an effect on the morphology and size of the particles, with the FHA composites being much smaller and more needle-like than the HA samples. These nano composites were then introduced into cell culture of a human fibroblast cell line (MG63) to determine their effect on metabolic activity and cell membranes. It was found that 10 mg ml^{-1} of the nanocomposites when added to the cells produced a greater cytotoxic effect than the lower concentration of 1 mg ml^{-1}; this was also found to be the case when looking at cell membrane activity. Linear block copolymers of poly(ethylene glycol-co-hydroxyethyl acrylamide) (PEG-co-HEA) with varying degrees of polymerisation (DP) of the HEA block ratios and two different molecular weights of the PEG block (1900 Da or 5000 Da) were donated by Erasmus student Sarahfranziska Stahl. The copolymers were synthesised by single electron transfer living radical polymerisation (SET-LRP) using a PEGisobutryl bromide initiator in a one pot synthesis. These polymers were included in the synthesis of (F)HA. Again, analysis via FTIR, XRD, TGA and TEM determined the inclusion of the polymer in the (F)HA samples had an effect on the morphology and size of the particles, with the FHA composites becoming much smaller and more needle-like than the HA samples. It was found that while the PEG block had no effect on the particle size of the composite formed, increasing the DP of the HEA block caused the particles to become smaller.

List of common abbreviations

AA	Acrylic acid
AIBN	Azobisisobutyronitrile
ACVA	4,4’-azobis(4-cyanovaleric acid)
ATR-FTIR	Attenuated total reflectance fourier transform infrared spectroscopy
ATRP	Atom transfer radical polymerisation
$CDCl_3$	Deuterated chloroform
CEA	2-carboxyethyl acrylate
CTA	Chain transfer agent
Đ	Dispersity
DB	Degree of Branching
DLS	Dynamic light scattering
DMSO	Dimethyl sulfoxide
D_2O	Deuterated water
DI Water	Deionised water
E5	Low molecular weight poly(acrylic acid) 9000 Da
E11	High molecular weight poly(acrylic acid) 210000 Da
EDTA	Ethylenediaminetetraacetic acid
FHA	Fluorhydroxyapatite
FTIR	Fourier transform infrared spectroscopy
FA	Fluorapatite
GPC	Gel permeation chromatography
HA	Hydroxyapatite
HEA	N-(2-hydroxyethyl) acrylamide
IPA	Isopropyl alcohol
KBr	Potassium bromide disc
LDH	Lactate dehydrogenase
L-Glu	L-glutamine
LRP	Living radical polymerisation
MAA	Methacrylic acid
MG63	Human fibroblast cell line (osteosarcoma)

M_n	Number average molecular weight
M_W	Weight average molecular weight
NEAA	Non-essential amino acids
NMR	Nuclear magnetic resonance spectroscopy
PAA	Poly(acrylic acid)
PAMPS	Poly(2-acrylamido-2-methylpropane sulfonic acid)
PB	PrestoBlue
PBS	Phosphate buffered saline
PEG	Poly(ethylene glycol)
PEG-co-HEA	Poly(ethylene glycol-co-[N-(2-hydroxyethyl) acrylamide])
PMAA	Poly(methacrylic acid)
P/S	Penicillin / streptomycin
RAFT	Reversible addition-fragmentation chain transfer polymerisation
RPM	Revolutions per minute
SAXS	Small angle x-ray scattering
SCVP	Self-condensing vinyl polymerisation
SD	Standard deviation
SE	Standard Error
SET-LRP	Single electron transfer living radical polymerisation
TEM	Transmission electron microscopy
TGA	Thermogravimetric analysis
UCD	University college Dublin
UoS	University of Sheffield
VBC	4-vinylbenzyl chloride
VBD	4-vinylbenzyl dithiobenzoate
VPC	4-vinylbenzyl N-pyrrolecarbodithioate
XRD	X-ray diffraction

Contents

Chapter 1 – Introduction

Nanotechnology has been recognised as having significant potential for use in medicine and dentistry. However, there are currently relatively few medical and dental products which are based on nanoscience; products which presently use nanoparticles are relatively unsophisticated and little evidence exists to suggest that they have improved previous clinical technologies.[1] As a result, the full potential of nanoparticles for clinical applications remains untapped. If the current challenges surrounding the design and preparation of functional nanoparticles can be resolved, then this could allow the development of nanoscale technologies for medical and dental applications.[2, 3]

Nanoscale apatites are being developed for applications in an increasing number of medical and related healthcare technologies where their size and morphology is known to have a significant impact on their properties and behaviour. The addition of other materials such as polymers during the synthesis of apatites, or the modification of nanoparticle precipitation using a polymer environment, provides opportunities to both control particle morphology and develop novel functional materials for biomedical and wider applications. Despite the potential value of these systems, very little work on the fabrication of nanoscale calcium phosphates in the presence of functional polymers has been reported to date.

1.1 Nanotechnology and Nanoparticles

Nanotechnology is attractive for medical applications as the size of cells and the extracellular matrix is on the microscale, hence nanoparticles could potentially have the ability to enter cells to deliver therapies.[4] Current research is aiming to improve the interactions between tissues and the surfaces of implanted materials by utilising nanotechnology.

1.1.1 Natural nanoparticles vs synthetic analogues

Nanoscale structures are found throughout nature, from malleable materials including silk to solid structural materials such as bone.[5] The nanoscale constructs provide large surface areas per unit mass for enhanced functionality while their structures maximise the strength of the material. Crosslinking in silk[6-8] and the composite arrangement of calcium phosphate and collagen in bone[9-11] form arrangements which provide strength to the bulk material. This demonstrates the potential of synthetic nanostructures for use in medicine and dentistry to provide strength to damaged areas of the body, for example: broken bones and tooth cavities.[9, 12]

Other instances of nanoparticles in nature show the potential of synthetic nanotechnology as anticancer agents. The flesh-eating fungus *Arthrobotrys oligospora* was recently discovered to produce nanoparticles which form a trap and digest parasites; it was then discovered that the nanoparticles also act as anticancer agents and prevent the growth of tumours on the fungus.[13] If new synthetic analogues of these nanoparticles could be created this would open up new avenues for cancer treatments. Nanoparticles have been found to selectively accumulate in cancer tissue due to the phenomenon of enhanced permeability and retention.[14] This could lead to the targeted delivery of anticancer agents directly to tumours and improved cancer therapies.[14, 15]

Current challenges in the progression of nanotechnology include the design and preparation of nanoparticles, along with subsequent processing and surface functionalisation. A current lack of reproducibility could lead to problems of unknown toxicity if implanted into tissue.[16] If a solution could be found to these problems this could allow the improved development of nanoscale technologies for numerous medical and dental applications and potentially non-clinical uses as well. The main challenge faced is the lack of nanoscale functionality due to the aggregation of nanoparticles.[17] If a solution could be found which would enable the dispersion of nanoparticles and prevent aggregation, then this could lead to the creation of particles with nano-functionality as opposed to current particles with macro-functionality due to the preferred formation of aggregates.

1.1.2 Applications of Nanoparticles

The unique nature of nanoparticles with their high surface area to volume ratios means they can be tailor-made to suit specific applications in a wide range of fields including medical, cosmetic, ecological and even food technologies.[18] Studies into nanoparticle safety and toxicology have led to the discovery of the vast potential of nanotechnology and nanomaterials for future applications in almost every sector.[19] Medically these include diagnostic techniques,[14] drug carrier systems[5, 20, 21] and much beyond.[22] Ecological studies could lead to new soil and water purification techniques which could vastly improve the water purity in developing countries.[23]

Nanotechnology is widely used in everyday products from electronic components in mobile phones to UV absorbers in sun-cream, and cements in sensitive toothpastes.[24, 25] In these instances, the nanoparticles are usually held in a suspension. The drawback of this approach is due to the bulk use of passive nanoparticles, whereby the property of the material or product is tailored by the amount of nanoparticles rather than their size.[26] As a result, in cases such as sun cream, the overall effectiveness of the product is reduced when nanoparticle dimensions are reduced. This bulk application does not fully utilise the functionality of discrete nanoparticles; aggregates of nanoparticles, as found in the examples mentioned above, have reduced functionality compared to dispersed particles.[24]

1.1.3 Nanoparticle functionality

The size and shape of nanoparticles are the main determinant of their functionality. The reactivity of the particles generally correlates with their size: the smaller the particle, the greater its reactivity. This is due to the high surface area to volume ratio of nanoparticles as illustrated in figure 1.1; however, this relationship does not always hold true.[27]

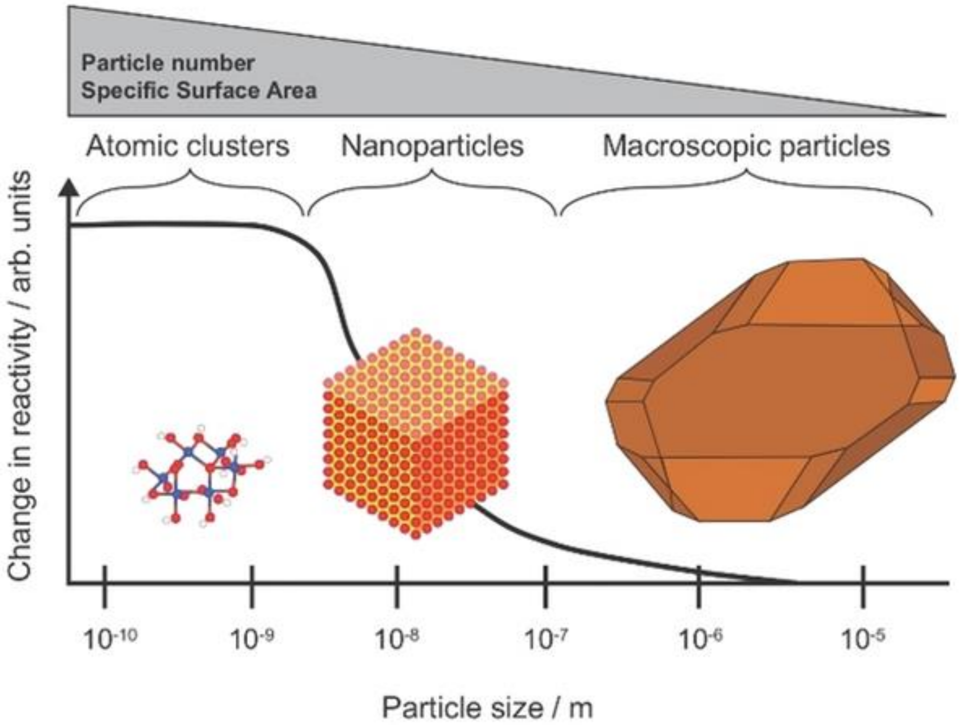

Figure 1.1. Generalisation of the trend for the reduction in reactivity of a material with increasing size.[27]

The nanoscale, 10^{-9} m, represents a transition region between atomic and bulk macroscopic reactivity. Chemical structure, electronic and optical properties undergo great changes on going from the atomic to the bulk region; this results in a significant difference in the reactivity of particles. This change in reactivity over the transition region between atomic clusters and macroscopic molecules can be attributed to four main reasons:

1. As the size of a particle is reduced, the quantity and distribution of atoms at the surface rapidly increases which causes the surface reactivity to change. Reactivity is dependent on the topography of the particle.[27]
2. The surface free energy of the particle is directly proportional to particle size; this can affect the thermodynamic stability of the particle changing the reactivity.[27, 28]
3. Differences in bond angles and bond lengths in the molecules making up the particle become more pronounced. Structural variations and defects in the surface occur changing the chemical make-up of regions on the particle surface. This can also differ from particle to particle depending on the chemical make-up.[27, 29]
4. As the particle size is reduced the electronic band structure becomes more similar to the discrete energy levels of atoms and molecules rather than the conduction and valence bands of bulk materials.[27, 30, 31]

One or more of these factors can contribute to the functionality of nanoparticles; particle composition will determine which factors are relevant.[27] The difference in the reactivity of a nanoparticle or bulk material made from the same chemical can be extremely pronounced. For example, bulk gold is unreactive yet gold nanoparticles are extremely reactive with properties that can be tailored by varying their size.[32-34]

As a result of the link between particle size and functionality, the processing of nanoparticles is extremely important. This can be challenging due to the tendency for nanoparticles to form large aggregates in order to maintain thermodynamic stability.[35]

1.1.4 Nanoparticle toxicity

There are rising concerns regarding the safety of nanoparticle production and use. At present little is understood about the long-term effects of the use of nanoparticles for medical applications involving the ingestion or intravenous uptake of products utilising nanotechnology.[19, 25, 36] Currently the possible toxicity related to long-term exposure to nanoparticles is unknown.[37] Studies into the toxicity associated with the inhalation of nanoparticles are the most widespread at present due to concerns over possible respiratory problems.[16, 38, 39] The inhalation of nanoparticles is known to cause deposition throughout the respiratory system. The size of the nanoparticles inhaled will determine their point of deposition with smaller particles traveling further than larger particles as the former can cross the gas exchange barrier and deposit in the lungs.[25] The deposition of inhaled nanoparticles is known to induce inflammation in the pulmonary region. For example, inhalation of nanoparticles of asbestos is well known to cause breathing difficulties;[40, 41] this is especially prevalent in people with respiratory problems such as asthma.[16]

Other health concerns over the possibility of nanoparticles penetrating the skin from sources such as sun cream are being widely investigated.[16] Early investigations into the photocatalytic activity of TiO_2 and ZnO nanoparticles used in sun creams in 2001 uncovered evidence to suggest that the use of these nanoparticles would cause skin damage.[42] Later studies showed that these nanoparticles do penetrate the dermis of the skin. However, the extent of penetration was low and the particles were not determined to be detrimental to skin health.[43] This is consistent with the accepted opinion that TiO_2 nanoparticles with diameters greater than 100 nm are biologically inert.[25]

The main concern with nanoparticles entering the body is the possibility that the deposition of particles on or in vital organs may occur, which could potentially cause severe illness.[37] The deposition of non-biodegradable or slowly degradable nanoparticles in organs could lead to the saturation of phagocytes, which are cells that consume and destroy foreign matter. This could then initiate a stress response, causing inflammation and compromising the body's defence against other pathogens. Alternatively, if particles were to adsorb to the surface of macromolecules such as proteins within the body, this could lead to a change in the regulatory mechanisms of enzymes and affect vital bioprocesses which could theoretically lead to autoimmune diseases.[23] The use of biodegradable, biocompatible nanoparticles could potentially negate these effects. One possible approach could to be to incorporate well-tested biomaterials into or onto these nanoparticles as composites or coatings respectively. Many biocompatible materials exist including ceramics and composites, yet the most easily processed and researched biomaterials so far are polymers.

1.2 Polymers

Polymers are extremely useful materials found in everyday objects. Various monomers can be used to create functional polymers with particular architectures. These polymers can be manipulated to form large scale products such as plastic carrier bags or micro or nanoscale constructs such as scaffolds or coatings. The functionality a polymer can have is directly dependant on polymer architecture and side group functionality. Both polymer architecture and functionality can be tailored for specific applications.

1.2.1 Polymer architecture

Architecture has a pronounced effect on the properties of a polymer. Many polymer architectures are possible but, some polymer formations are more useful than others depending on their intended application.

Linear homopolymers have the simplest architecture. These are formed by vinyl monomers with a functional side chain (R), into simple chains. In general, the vinyl end of the monomer will be activated by the initiator which will then go on to react with the vinyl group of another monomer and so on to build up a chain as shown in Figure 1.2. The R group on the vinyl monomer will determine the properties of the polymer.

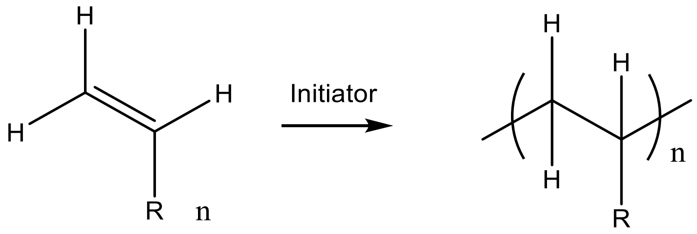

Figure 1.2. Schematic diagram of the formation of a homopolymers from a vinyl monomer.

Branched polymers are also possible. These occur either by using a bifunctional monomer or by the addition of a branching agent; this is shown in figure 1.3.

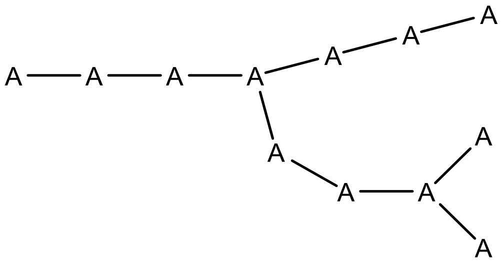

Figure 1.3. Schematic diagram of the formation of a branched polymer.

Branching agents (BA) can be used to control the level of branching within the polymer. By changing the ratio of monomer to BA highly or hyperbranched polymers can be formed.[44] These polymers are not true homopolymers due to the incorporation of the BA. Branching agents can also be other monomers; the incorporation of 2 or more monomers together is known as a copolymer.[45, 46]

Copolymers can have various architectures; they can be linear, branched, highly branched or they can be used to create other more complex formations. The simplest conformations of a copolymer are shown in figure 1.4.

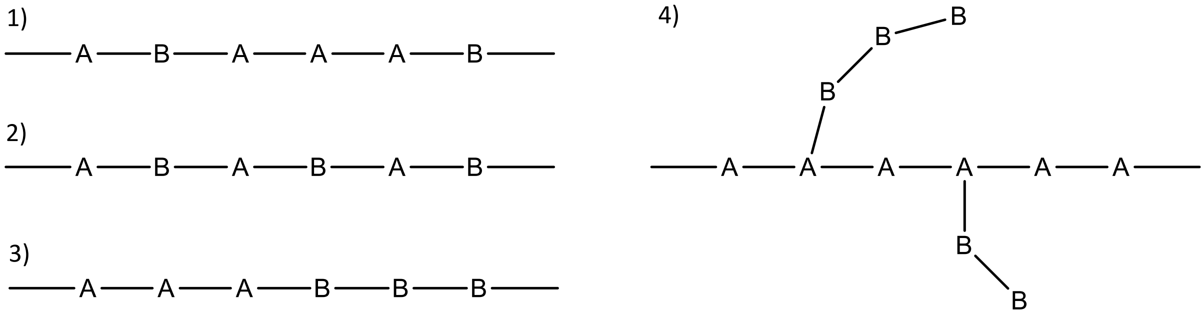

Figure 1.4. Schematic diagram of copolymer architectures: 1) Statistical, 2) Alternating, 3) Block, 4) Graft.

These are based on linear backbones and can be statistical, alternating, block or grafted. The use of BAs and polyfunctional monomers can also lead to crosslinking of polymer chains or complex architectural formations such as dendrimers,[47] stars,[48] pom-poms,[49] and combs.[50] These formations can be created to alter the properties of the polymer in order to create useful materials for specific applications. In order to tailor specific properties, the synthesis of the polymer must be controlled.[51]

1.2.2 Methods of synthesis

There are many differing polymerisation techniques which can be used to create specific polymer architectures including: polycondensation,[52, 53] ionic polymerisation,[54] and free radical polymerisation.[55]

Polycondensation is the formation of a polymer with the loss of a small molecule, e.g. H_2O or HCl. This is the main polymerisation technique used to form polyesters, polyamides and polyacetals.[52] Polycondensation is a step polymerisation technique using bifunctional monomers such as diols or diacids to form linear polymers. Other architectures are also possible via polycondensation reactions; these are dependent on the functionality of the monomer i.e. if the monomer contains a side chain which can react, this will cause further reactions leading to branching or crosslinking.[56]

Ionic polymerisation uses cationic or anionic initiators and is kinetically controlled through a chain mechanism with an ionic active centre. The active centre is a carbocation or carbanion for cationic and anionic polymerisations respectively. The formation and stabilisation of the active centre is dependent on the side chain (R) of the vinyl monomer $CH_2=CHR$.[57] As a result of this, the range of monomers that can undergo ionic polymerisations is limited due to electronic requirements. Electron-donating side groups are required to stabilise the π-orbitals in cationic polymerisations due to the delocalised positive charge on the chain end; electron-withdrawing side groups are required for anionic polymerisation to stabilise the delocalised negative charge. Ionic polymerisations also require tightly-controlled reaction conditions and can require high concentrations of catalysts such as organic peroxides or strong Lewis acids or bases,[58] low temperatures and thoroughly dry solvents.[59] Additionally, there are issues with rapid reaction rates due to the labile nature of the ionic centres which lead to poor reproducibility. Therefore, apart from very few exceptions,[56] ionic polymerisations are ill-suited to large-scale polymer production in industry due to the necessity for rigorous reaction conditions.[54]

Free radical polymerisation is a more adaptable chain growth technique that can be performed under mild conditions and as a result is widely used. A far wider range of functional monomers can be used in free radical polymerisations, making this technique highly versatile and hence useful on an industrial scale.[57] However, the poor selectivity associated with free radical polymerisation means the technique offers poor control over dispersity and molecular weight. Living radical polymerisations or controlled radical polymerisations have been developed over recent years. These methods provide greater control over dispersity and molecular weight by suppressing side reactions which could cause termination of the polymer chain growth.[60, 61]

Living polymerisation is restricted to anionic polymerisation as no current controlled radical polymerisation is truly a living system. In these techniques termination of the polymerisation is prevented by maintaining active chains in the reaction mixture hence the system is kept ‘alive’ by the concentration of reactants available.[57] Assuming there are no protic impurities in the system, the polymerisation will still be 'alive' once the monomer is consumed, hence for a system to be living there must be no termination reaction available.[62] In living radical polymerisation (LRP) the polymerisation reaction still undergoes bimolecular termination. However, the rate of propagation of radical chains far exceeds the rate of termination. This leads to the rapid formation of a dynamic equilibrium between radical growing chains and dormant species caused by the rapid reversible capping of the radical. This diminishes the overall concentration of the propagating radical chain-ends, hence minimising termination via combination and disproportionation. As a result, chain growth occurs in a highly controlled manner, producing polymers with well-defined architectures, molecular weights and polydispersities.[63] Living polymerisations are characterised as having controlled molecular weights and constant chain growth rates which result in narrow polydispersities of around 1.1 - 1.2.

Some of the most widely used living radical polymerisation techniques include reversible addition-fragmentation chain transfer (RAFT)[64] polymerisation, single electron transfer living radical polymerisation (SET-LRP)[65] and atom transfer radical-polymerisation (ATRP).[66]

1.2.2.1 Reversible Addition Fragmentation Chain Transfer Polymerisation

The RAFT process was developed in 1998 by Rizzardo and co-workers.[52] Chain growth in RAFT polymerisation is controlled by reversible chain transfer rather than chain capping, differing from other common LRP techniques. Chain transfer is possible due to the use of a thiocarbonylthio chain transfer agent (CTA), the general structure of which is shown in figure 1.6.

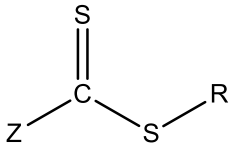

Figure 1.6. General structure of a dithioester chain transfer agent with Z and R side groups.

The mechanism for RAFT polymerisation differs from the other polymerisation methods due to the inclusion of a reinitiation step caused by the chain transfer agent. The polymerisation is carried out using a free radical initiator, normally a peroxide such as benzyl peroxide (BPO) or an azo compound for example 4,4'-azobis(4-cyanovaleric acid) (ACVA). The initiator undergoes thermal decomposition (as in a typical free radical polymerisation) producing two radical species $I^\bullet$. These radicals then react with the monomer to form propagating polymer radicals, $P_n^\bullet$. The polymer radicals react with the CTA to form a radical adduct; this then fragments producing a radical species $R^\bullet$ and an inactive chain, which is capped by the dithioester group. The radical species, $R^\bullet$, can then initiate further polymerisation in the reinitiation step to produce another propagating radical polymer chain, $P_m^\bullet$. This leads to the establishment of a chain-end transfer equilibrium between the propagating radicals and dormant polymer chains. The equilibrium provides the living character of the polymerisation. The low concentration of propagating species at any one time means that the probability of bimolecular termination is significantly reduced. The chain length of the polymer is also controlled by the equilibrium. Every chain exists in the inactive and propagating states for a comparable amount of time; therefore, the chains have similar lengths. This results in the formation of a near-monodisperse polymer; dispersities of 1.1 – 1.2 have been reported.[55] Scheme 1.1 illustrates the steps of a RAFT polymerisation.

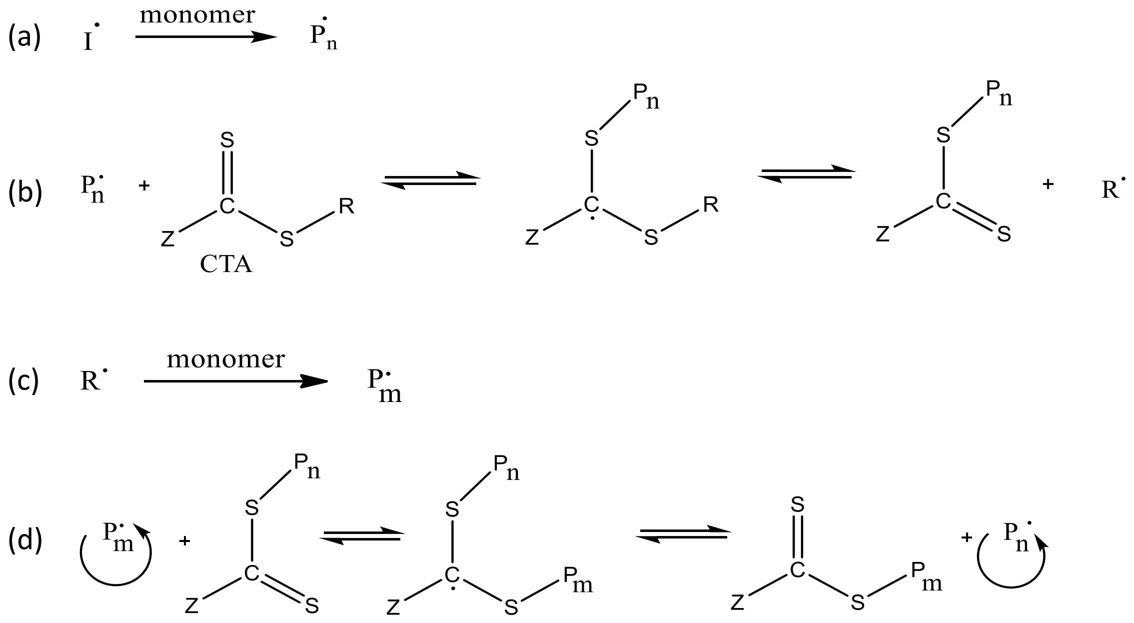

Scheme 1.1. RAFT polymerisation mechanism: (a) initiation (b) addition-fragmentation (c) reinitiation (d) chain-end transfer equilibrium.

The number of polymer molecules with dithioester-capped ends is well in excess of the number of chains terminated by normal bimolecular termination. This is achieved by maximising the extent of chain transfer, requiring the use of CTAs with large chain transfer constants. Using high concentrations relative to the amount of initiator causes chain transfer to dominate. These conditions allow RAFT polymerisation to proceed with very narrow molecular weight distributions. Experiments to model the polymerisation kinetics have shown that the effective transfer constant must be greater than 100 at low conversion to achieve polydispersity of 1.1 or lower.[67] To obtain higher molecular weight polymers or block copolymers further monomer can be added to the reaction mixture.

The substituents, Z and R, of the CTA are important for a successful RAFT polymerisation. To ensure the CTA has a sufficiently high transfer constant, the Z substituent must activate the C=S bond towards radical addition whilst stabilising the intermediate radical adduct produced by the addition of the propagating radical. Common Z substituents are ester or aryl groups for example, benzene.[68] The Z group modifies the rate of addition of $P_m^\bullet$ to the thiocarbonyl and the rate of fragmentation of the intermediate radical.[69] The R substituent must be a good leaving group and simultaneously form a stable radical to reinitiate the polymerisation, otherwise the reaction will be retarded.[69] The optimum choice of CTA is dependent on the class of monomer which is to be polymerised. The incorporation of the RAFT agent into the final polymer can be used to change its functionality.[70] It is also possible to remove the RAFT ends after the polymerisation; alternatively, the RAFT ends can be cleaved to give saturated or unsaturated chain ends through aminolysis or thermolysis.[59, 69]

RAFT is an exceptionally versatile polymerisation technique and can be adapted to be used in a wide range of reaction conditions, including organic and aqueous solutions, suspension, emulsion and bulk polymerisations.[71-75] RAFT is compatible with a wide range of monomers, including functional monomers, and is also tolerant of functionality in the CTA compound, solvent and initiator. This allows the synthesis of functional polymers with reactive side chain and/or end-groups without the need for deprotection after synthesis.[76] The main disadvantage of RAFT polymerisation is the cost of the commercially available RAFT agents. The high cost means that it is often necessary to synthesise RAFT agents 'in house' which can require expensive reagents and complicated synthetic and purification procedures.[52] Other disadvantages of RAFT agent synthesis include odour due to the presence of sulfur atoms in the molecule and hence reagents used to produce the agents. RAFT agents are also often highly coloured; this causes the polymers themselves to become coloured which is often undesirable. A particular subset of RAFT polymerisations known as self-condensing vinyl polymerisation (SCVP) involves a bifunctional RAFT agent with a vinyl group on the R or Z group.

1.2.2.2 RAFT-mediated Self-Condensing Vinyl Polymerisation (RAFT-SCVP)

Self-condensing vinyl polymerisation (SCVP) was discovered in 1995, a few years before RAFT, by Fréchet et al.[77] Fréchet and co-workers reported on the synthesis of dendrimers of 3-(1-chloroethyl)-ethenylbenzene using a combination of polycondensation and vinyl chain-growth polymerisations. The vinyl chain growth portion of the reaction forms oligomers which then react together by the initiation of functional sidechains in a step-growth polymerisation to give highly branched polymers.

RAFT-SCVP is known to work well as RAFT is a versatile technique which operates under mild conditions and is compatible with highly functional monomers. Wang et al. published the first report of RAFT-SCVP using the technique to synthesise highly branched polystyrenes with various chain transfer agents (CTA).[78] Wang et al. used a Z-group mediated approach which creates highly branched polymers with thiocarbonylthio moieties at the branch points of the polymer using a CTA with a vinyl group on the Z group. This causes the branch points to be fairly unstable and susceptible to hydrolysis which causes the polymer to disintegrate. A more useful method of RAFT-SCVP is to use the R-group mediated approach which uses a CTA with the vinyl group on the R group, hence forming highly branched polymers with thiocarbonylthio end groups. This increases the stability of the polymers and allows further functionalisation after synthesis as the thiocarbonylthio end groups can be easily removed or used to derivatise the polymer further.

The R-group mediated approach has been explored more thoroughly than the Z-group mediated method due to the improved scope for post-polymerisation functionalisation and the lack of weak thiocarbonylthio linkages within the polymer that could easily lead to degradation. Common monomers used in R-group meditated RAFT-SCVP are acrylates and methacrylates as well as acrylamides. Choosing the correct Z and R groups is essential for successful RAFT-SCVP reactions to ensure useful polymer properties along with the maximum monomer conversion during polymerisation. For example, the polymerisation of Methyl methacrylate (MMA) requires a RAFT agent where Z = benzyl or pyrrole and R = $C(CH_3)_2CN$ or $C(CH_3)COOEt$ as the MMA is a highly active monomer and hence requires a highly active RAFT agent.[68, 78] The average length of the polymer branches along with the degree of branching is highly dependent on the monomer conversion and can be tuned by varying the ratio of monomer to CTA. Polymer properties can vary if the monomer used is significantly more hydrophobic / hydrophilic than the CTA as this can cause the chain ends to aggregate causing anomalies during polymer characterisation.[79]

It is also possible to synthesise biologically-active hyperbranched polymers by RAFT-SCVP. Hyperbranched polymers based on amino acids were prepared by De et al. by reacting tert-butyl carbamate (Boc)-L-valine acryloyloxyethyl ester with S-(4-vinyl)benzyl S'-butyltrithiocarbonate which acted as both a CTA and monomer. The hyperbranched copolymers were then chain extended by RAFT to form star polymers with the hyperbranched polymers at the core and poly(ethylene glycol) methacrylate arms.[80] Deprotection to remove the Boc groups lead to self-assembly of the polymers due to the pH responsive core and thermoresponsive arms of the star polymers. The self-assembly of these polymers makes them attractive as drug delivery or carrier systems. This shows that RAFT-SCVP is useful technique to form highly branched polymers; however, it is not possible to polymerise all monomers in this manner due to the relative reactivities of the monomer and vinyl group on the CTA which influence branch formation and segment distribution along the polymer chains. Hence other controlled living radical polymerisations may be necessary to polymerise monomers with functionalities that differ from (meth)acrylates and acrylamides[77, 81]

1.2.2.3 Atom Transfer Radical Polymerisation (ATRP)

ATRP was developed separately in 1995 by Wang and Matyjaszewski[82] and also by Sawamoto and co-workers.[71] ATRP uses a transition metal catalyst and an alkyl halide initiator; the transfer of terminal halogen atoms from the polymer chain ends to the metal complex controls the polymer chain growth. This causes rapid reversible chain capping, which suppresses the concentration of instantaneous propagating radicals hence minimising termination and allowing tight control over the molecular weight distribution.[83] Normally a copper (I) halide is used along with a nitrogen-based complexing ligand such as N,N,N',N',N''-pentamethyldiethylenetriamine.[84] ATRP can be carried out in bulk and also in various solvents, making it adaptable and scalable. Unlike other ionic polymerisation techniques ATRP is tolerant of protic solvents, which allows polymerisations in alcohols and even water making it an attractive technique due to the mild reaction conditions.[85] ATRP has a high tolerance for functionality such as allyl, amino, epoxy, hydroxy and vinyl groups on both the monomer and initiator.[57] ATRP allows synthesis in very high yield with a short reaction time for polymers such as low dispersity linear poly(2-hydroxypropyl methacrylate).[86] The kinetics of the reaction can be controlled by modifying the concentration of monomer in the starting mixture and via the addition of further monomer during the reaction.[87] The main disadvantage of ATRP is the relatively large amount of metal catalyst (0.1-1% of the reaction mixture) which must be removed from the final polymer product. This can be time-consuming and difficult to achieve for high molecular weight polymers.[17] Other controlled LRP techniques such as reversible addition-fragmentation chain transfer polymerisation, do not suffer from this problem.

The compatibility with functional monomers makes controlled living polymerisation techniques useful for the production of well-defined polyelectrolytes. This particular class of polymers can be difficult to synthesise by other methods due to their functionality causing side reactions, leading to high dispersity and a broad molecular weight distribution.

1.2.3 Polyelectrolytes

Polyelectrolytes are functional polymers with ionic repeat units; these include both polycations and polyanions. The main feature of all polyelectrolytes is that they dissolve in water in the form of charged chains. The charge density is dependent on the level of ionisation; full ionisation is characteristic of a strong polyelectrolyte, while partial ionisation is representative of a weak polyelectrolyte.[88] Polyelectrolytes have features of both polymers and electrolytes; solutions of these polymers are both viscous and conduct electricity.[86] The molecular weight of the polyelectrolyte along with the charge density of the ionic repeat unit determines both the viscosity and conductivity of the solution.[89] While this adds to the functionality of the polymer, it can make characterisation of these polymers extremely difficult. For weak polyelectrolytes, characterisation by gel permeation chromatography (GPC) can be achieved by the addition of a salt to the eluent. This screens the charges of the polymer and breaks up polar interactions between the polymer and eluent allowing the polymer to flow through the aqueous GPC column.[90] Strong polyelectrolytes are more difficult to characterise as the concentration of salt that needs to be added to the eluent to shield the charges is much higher than that needed for weak polyelectrolytes. This can have an effect on the chromatogram produced. The inclusion of other analytical techniques such as multi angle light scattering or low angle laser light scattering can be used to improve confidence in the results.[91-93]

Aside from the difficulties of characterisation, polyelectrolytes are extremely useful materials utilised in both technological and industrial areas. They are particularly attractive for uses as biomaterials as many natural biological macromolecules, such as polypeptides, are polyelectrolytes.[94] Biocompatible polyelectrolytes are undergoing significant investigation for applications such as implant coatings and controllable drug release systems. Drug release systems in particular could utilise biocompatible weak polyelectrolytes, as these are sensitive to changes in pH and counter-ion concentration. Polyelectrolytes are also useful as models of the electrochemical behaviour of biological macromolecules such as proteins in blood due to their solution properties.[94] Synthetic analogues of proteins can be created and used as models to determine the effects of biomaterials which could be used as implants or other medical devices. One disadvantage is that the synthesis of certain polymers can be arduous and time-consuming, especially if the polydispersity or molecular weight must be tightly controlled.[38] This has seen recent advancement due to the development of the polymeric synthesis procedures mentioned earlier; as a result, current research is getting closer to creating synthetic biopolymer analogues.[95-97]

1.3 Specific Background

1.3.1 Polyelectrolytes as coatings

Polyelectrolytes have been used as coatings for many years for various applications including a layer-by-layer approach to form polyelectrolyte coatings for substrates. This has the advantage of electrostatic adhesion between oppositely charged polymer layers which make the coatings easy to deposit. Functionalisation of these polymer coatings is also possible, making them useful for bioengineering prospects. Polyelectrolyte multilayers formed by layer-by-layer deposition can be produced in aqueous solution making them useful for biological applications.[98] Currently there is a lot of interest in the use of polyelectrolytes as coatings for nanoparticles. Theoretical studies of the use of polyelectrolytes as nanoparticle coatings show they are feasible depending on the molecular weight of the polymers used.[99]

The use of polymers as tools for the encapsulation of small molecules and particles is currently undergoing significant research in the area of biomaterials.[100, 101] The effect of polyelectrolytes adsorbing directly onto the surface of particles in solution leads to their enhanced colloidal stability. The charged surfaces created when a polyelectrolyte adsorbs onto colloid particles leads to electrostatic stabilisation whereby charges repel each other, leading to particle dispersal and preventing aggregation.[102] Steric stabilisation due to the unfavourable reduction in conformation entropy occurs when particles with adsorbed polymers draw near one another; for the particles to be able to aggregate the polymer chains would be compressed which is thermodynamically unfavourable, hence particle aggregation is reduced.[100] This technique is widely used in paints. The opposite effect of adsorbing polymers with opposing charges onto particle surfaces to cause attraction and hence aggregation or flocculation is used within the water treatment industry.[103-105] Causing contaminant particles to flocculate creates larger species which can be filtered more easily; contaminant targeting can be achieved using specific anionic or cationic polymers.[106, 107]

1.3.2 Nanoparticles

Nanoparticles are frequently used to coat bulk implant materials for use in the body. These include uses as bone fillers with the potential to act as antibacterial agents and improve osteogenesis and angiogenesis in large bone defects.[108] Nanoparticles dispersed in biocompatible, biodegradable polymers have been used *in vitro* to study the effects of implants on bone reformation.[9, 109, 110] The bone extracellular matrix is formed mainly of calcium phosphate; this requires mineralisation to undergo osteogenesis. Studies to introduce bioactive nanoparticles distributed through a polymer scaffold to improve the mechanical properties of a bone defect region have been conducted and showed promising results.[9] *In vitro* testing found that material similar in structure and mechanical stability to bone could be created using a polypeptide/hydroxyapatite composite. The composite was dispersed in water and allowed to flow into the simulated extracellular matrix. When dehydrated the hydroxyapatite (HA) crystallised to form a structure which mimicked the strength and architecture of natural bone. However, these HA crystals were found to form large aggregates if dehydration of the material was not achieved rapidly.[9] The use of biocompatible ceramics is attractive due to their abilities to stimulate cell growth, especially if such ceramics are analogues of minerals found within the body such as hydroxyapatite.

1.3.3 Apatites

Apatites are a group of calcium phosphate minerals produced and used in biological micro-environments. Naturally occurring apatite minerals, an example of which is shown in figure 1.7, are primarily used for the production of fertiliser, as the subgroups fluorapatite and chlorapatite are excellent sources of phosphorous.[111] Phosphoric acid is produced by breaking down fluorapatite with fuming sulphuric acid. A by-product of this is the generation of hydrofluoric acid.[111] Other applications include green and blue pigments in paints. However, the apatite subgroups hydroxyapatite and fluorapatite are also useful for clinical applications.

Figure 1.7. Naturally occurring fluoro-chlorapatite mineral, $Ca_{10}(PO_4)_6(OH,F,Cl)_2$.[112]

1.3.3.1 Hydroxyapatite

Hydroxyapatite (HA) is a biocompatible ceramic widely used in regenerative therapies for bone defects. The mineral composition of HA ($Ca_{10}(PO_4)_6(OH)_2$) is very similar to natural bone, making it an ideal material for products to aid bone healing. The unit cell comprises two entities which gives HA its porous structure as shown in figure 1.8 a and b.

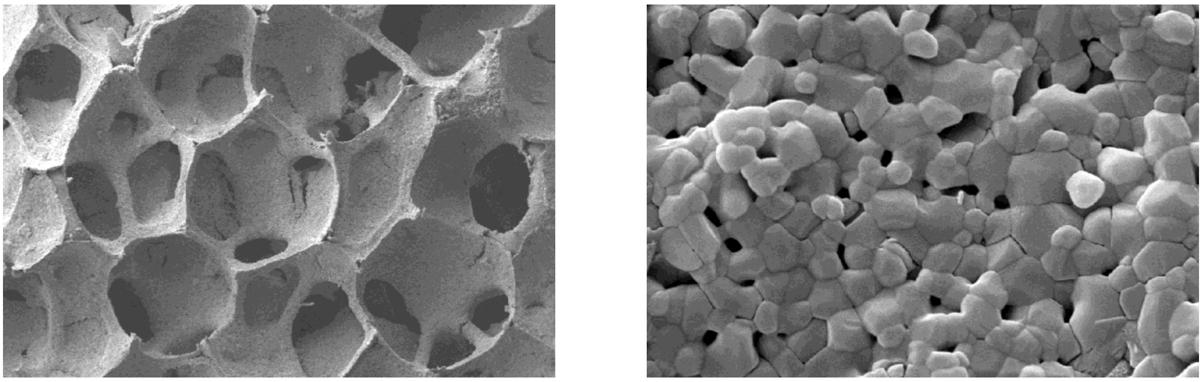

Figure 1.8 a) Optical microscope image of natural HA in bone, b) SEM micrograph of aggregated HA nanoparticles.[113]

Nanoscale hydroxyapatite (nanoHA) has been widely used in polymer scaffolds along with bone morphogenic proteins to allow bone reformation after damage or disease.[113] NanoHA is particularly useful, as it efficiently encourages cell attachment and osteogenesis through scaffolds, which would otherwise be far less prolific.[113]

The similarity of HA to natural bone mineral is very useful clinically as it is naturally biocompatible and bioactive. HA and other morphologies of calcium phosphate (CaP) have been used medically in various forms, such as powders and granules or as blocks.[114, 115] The density and porosity of these forms along with the inclusion of other ionic species to form composites determines the properties and usefulness of the material.[10, 115-118]

In naturally calcified materials such as bone, nanoscale needle-like crystals of CaP, with widths of approximately 5-20 nm and lengths of up to 60 nm, along with an apatite phase consisting of CO_3^{2-}, Na^+, F^- and other ions within a matrix of collagen fibres, form the main species in the tissue.[119] The synthesis and processing techniques used to create synthetic HA can be manipulated to tailor nanoparticles of specific size and morphology simply by changing pH, temperature, mixing rate and starting materials.[119] Many techniques exist for the production of nanoHA; all have merit and can be used to optimise the properties of the synthetic HA for a particular application.[120-122] This includes the incorporation of small molecules such as antibiotics or counter-ions such as those found in natural bone tissue. Such molecules can be used to increase the effectiveness of the HA when implanted. Previous works have incorporated antibiotics into the production of HA to prevent post-surgical infections[123] or integrated bone morphogenic proteins into scaffolds containing nanoHA to encourage the invasion and proliferation of osteoclasts to initiate new bone growth.[124]

The versatility of HA nanoparticles makes them particularly useful for applications within medicine and dentistry. However, their functionality is currently hindered by their aggregation, which reduces the surface area available for the particles to interact with external species such as cells. Coating HA nanoparticles with functional polymers could enable them to be dispersed more readily leading to increased surface area and hence nanofunctionality. This is beneficial over the macrofunctionality exhibited by aggregates as the particle aggregation reduces the surface area available for cell attachment, and hence causes the material to behave with the functionality of the bulk material. In order to prevent aggregation, the electrostatic interactions between the reactive nanoparticles must be disrupted.

This could potentially be achieved by coating the nanoparticles with an ionic polymer to induce electrostatic repulsion between the nanoparticles. However, very little literature exists on the use of polymer coatings on ceramic nanoparticles, especially in the solid state. Instead ceramic nanoparticles are used to coat implants in order to improve their biocompatibility.[115, 122-124] The literature that does exist most often utilises the polymer as a dispersant rather than a coating, such as the inclusion of nanoparticles in a polymer solution for the production of electrospun scaffolds.[108, 125] More recently, the dispersal of coated nanoparticles throughout a single crystal has been achieved.[102] A disadvantage of using HA is acid sensitivity. This causes leeching of OH^- ions to neutralise the pH of the environment and breaks down the calcium phosphate structure.[126] Fluorapatite is an acid stable analogue of hydroxyapatite.

1.3.3.2 Fluorapatite

Fluorapatite (FA), $Ca_5(PO_4)_3F$, is biocompatible and found naturally as the inorganic component of enamel. FA has greater mechanical strength and thermal stability than HA, making it preferable for dental applications.[127, 128] The use of HA/FA hybrids, fluorhydroxyapatite (FHA), are attractive as fluorine has biological benefits including the production of functionally and mechanically improved bone after trauma, while the inclusion of HA will allow bone turnover for healthy tissue production.[127] FHA allows the controlled release of fluoride ions which are required for natural tooth and bone development and sustainability.

Fluoride ions are present in blood plasma and saliva and improve the stability of HA in biological environments by exchanging with hydroxyl ions.[127] The fluoride ions prevent mineral breakdown in enamel and bone, hence the inclusion of fluoride in toothpaste and low concentrations in drinking water.[129] This is advantageous for dental applications as fluoride ions can be used to improve the strength of dental enamel. However, only low concentrations of fluoride ions are required for normal bone regeneration.[126] The introduction of a high concentration of fluoride ions in the body leads to adverse effects. This was revealed when fluorides were investigated as a possible treatment for osteoporosis by Riggs *et al.* in 1980;[130] patients underwent a sodium fluoride treatment which lead to fractural reoccurrences along with synovitis and recurrent vomiting. Fracturing was attributed to the formation of insoluble fluorapatite which prevented bone turnover and any subsequent tissue regeneration. The other adverse side effects were found to be due to the build-up of fluoride ions in the kidneys.[130] The insolubility of FA means that clinical use will not cause the release of dangerously high concentrations of fluoride ions, but will allow the testing of analogues of HA in an acidic environment.

1.3.4 Biomedical applications of apatites

Apatites have significant applications in bone and dental research. There is a growing need for improved treatments for conditions such as osteoporosis which are heavily associated with the aging population.[131, 132] Traditional methods of treating large tissue defects such as autografts are not ideal as they can lead to necrosis around the donor site and require the sacrifice of healthy tissue from another area of the body to heal the defect.[131-134] Allografts do not require the sacrifice of healthy tissue from the patient and have been used effectively to treat massive bone defects for many years. However, there are issues with allografts due to the use of foreign tissue, this requires patients to take immunosuppressant drugs to prevent rejection of the implanted tissue.[132-135] Both autografts and allografts leave patients open to the possibility of infection at the site of the defect, and donor site in the case of autografts.[136, 137] As a result of these issues there is a need for new therapies to treat bone defects that do not require the use of native tissue if possible. Tissue engineering has recently begun to develop new methods in which a patient's own cells can be grown on a scaffold which can then be implanted into the defect.[9, 10, 114, 115, 132, 134, 135, 138, 139] Two of the most important techniques for bone tissue engineering involve scaffolds for cell ingrowth and hydroxyapatite as a coating or nanostructure for enhance cell interaction within the defect site. Hydroxyapatite is a common coating for bone implants to enhance bioactivity and prevent rejection.[140] Therefore, by introducing hydroxyapatite nanoparticles with enhanced functionality due to the inclusion of novel polymers, this could allow a new avenue of bone defect therapeutics to be realised.

1.3.5 Cytotoxicity of apatites

As with any therapeutic material, there is a possibility that new therapies could have cytotoxic effects on native tissue. Apatites in general have previously been found to have no cytotoxic effects, even when doped with elements such as strontium and barium.[141, 142] Other metal-doped hydroxyapatites were found to have a distinct cytotoxic effect on cells when cultured for 24 hours.[143] The cytotoxic effects are directly related to the type of metal used to dope the HA, for example Zhao et al. reported on arginine functionalised europium doped hydroxyapatite nanoparticles with no cytotoxic effects while de Lima et al. found that doping with magnesium or cobalt had a pronounced cytotoxic effect causing high levels of apoptosis.[143, 144] This demonstrates the necessity of ensuring every aspect of a composite material is biologically safe before it can be used therapeutically. Methods to determine cell viability are therefore extremely important during the research and development of new bioactive materials.

1.4 Aims and Objectives

To summarise, nanoscale apatites are employed in an increasing number of medical and related healthcare technologies where their size and morphology is known to play a key role in their properties and behaviour. The addition of polymers, or the modification of the nanoparticle synthesis using a polymer environment, provides opportunities to both control particle morphology and develop novel functional materials for biomedical and wider applications. Despite the potential value of these approaches, very little work on the fabrication of nanoscale calcium phosphates in the presence of polymers has been reported to date. The main aim of this PhD was to therefore to synthesise nanoscale hydroxyapatite and fluorhydroxyapatite in the presence of functional polymers, and investigate the effects of this novel process on the properties of the products. The specific objectives were:

1. Synthesise hyperbranched homopolymers of acrylic acid (AA), methacrylic acid (MAA) and 2-acrylamido- 2-methylpropane sulfonic acid (AMPS) via RAFT polymerisation.
2. Characterise these polymers through nuclear magnetic resonance (NMR) spectroscopy, gel permeation chromatography (GPC) and small angle x-ray scattering (SAXS).
3. Determine the most effective method for combining the homopolymers and calcium phosphate particles.
4. Synthesise and characterise hydroxyapatite (HA) and fluorapatite (FA) composite nanoparticles via precipitation in the presence of hyperbranched and linear acid homopolymers.
5. Synthesise and characterise hydroxyapatite (HA) and fluorapatite (FA) composite nanoparticles via precipitation in the presence of poly(ethylene glycol-co-hydroxyethyl acrylamide) (PEG-co-HEA) copolymers with differing length PEG blocks and HEA block with differing degrees of polymerisation.

6. Determine the in vitro biocompatibility of novel materials using cell viability testing based on cytotoxicity evaluation using PrestoBlue (resazurin), LDH and live/dead assays.

On completion, this work has the potential to demonstrate an enabling technology for applications in medicine (e.g. drug delivery systems and bone fillers), dentistry (e.g. sensitive toothpastes and dental cements) and consumer health, ultimately influencing other non-health sectors through the controlled synthesis of functional nanoscale composites. We hypothesised that charged polymers would interact with the (F)HA nanoparticles during their formation and hence influence their final structure. Polymers were characterised and used to assess their suitability as a coating by particle sizing analysis and transmission electron microscopy (TEM). Additionally, different RAFT agents were investigated to determine which was the most suitable for the selected monomers. It was also important to ensure that the RAFT agents used did not prevent the polymer from adsorbing onto the hydroxyapatite nanoparticles when the time came for co-synthesis.

1.5 References

1. O. Health Quality, *Ontario health technology assessment series*, 2006, **6**, 1-43.
2. N. Desai, *Aaps Journal*, 2012, **14**, 282-295.
3. M. E. Davis, *Molecular Pharmaceutics*, 2009, **6**, 659-668.
4. E. Engel, A. Michiardi, M. Navarro, D. Lacroix and J. A. Planell, *Trends in Biotechnology*, 2007, **26**, 39-47.
5. P. Willi and C. P. Sharma, *Trends in Biomaterials and Artificial Organs*, 2012, **26**, 1-2.
6. N. N. Ashton, D. S. Taggart and R. J. Stewart, *Biopolymers*, 2012, **97**, 432-445.
7. G. Bratzel and M. J. Buehler, *Biopolymers*, 2012, **97**, 408-417.
8. S. Keten and M. J. Buehler, *Journal of the Royal Society Interface*, 2010, **7**, 1709-1721.
9. M. J. Olszta, X. Cheng, S. S. Jee, R. Kumar, Y.-Y. Kim, M. J. Kaufman, E. P. Douglas and L. B. Gower, *Materials Science & Engineering R-Reports*, 2007, **58**, 77-116.
10. M. R. S. Bose, A. Bandyopadhyay, *Trends in Biotechnology*, 2012, **30**, 546-554.
11. M. J. Seibel, *Clin. Biochem. Rev*, 2005, **26**, 97-122.
12. F. Rose and R. O. C. Oreffo, *Biochemical and Biophysical Research Communications*, 2002, **292**, 1-7.

13. Y. Wang, L. Sun, S. Yi, Y. S. Huang, C. Lenaghan and M. Zhang, *Advanced Functional Materials*, 2012, **23**, 2175-2184.
14. I. Brigger, C. Dubernet and P. Couvreur, *Advanced Drug Delivery Reviews*, 2012, **64**, 24-36.
15. M. Zhang, *Nanomedicine*, 2013, **8**, 313-316.
16. A. El-Ansary, S. Al-Daihan, A. B. Bacha and M. Kotb, *Methods in molecular biology (Clifton, N.J.)*, 2013, **1028**, 47-74.
17. D. Yang, J. Ma, M. Gao, M. Peng, Y. Luo, W. Hui, C. Chen, Z. Wang and Y. Cui, *Rsc Advances*, 2013, **3**, 9681-9686.
18. V. K. Khanna, *Sensor Review*, 2008, **28**, 39-45.
19. K. Donaldson, V. Stone, C. L. Tran, W. Kreyling and P. J. A. Borm, *Occupational and Environmental Medicine*, 2004, **61**, 727-728.
20. P. Galvin, D. Thompson, K. B. Ryan, A. McCarthy, A. C. Moore, C. S. Burke, M. Dyson, B. D. MacCraith, Y. K. Gun'ko, M. T. Byrne, Y. Volkov, C. Keely, E. Keehan, M. Howe, C. Duffy and R. MacLoughlin, *Cellular and Molecular Life Sciences*, 2012, **69**, 389-404.
21. Y. Wang, L. Zhang, Q. Wang and D. Zhang, *Journal of Biomedical Nanotechnology*, 2014, **10**, 543-558.
22. L. Zhang and T. J. Webster, *Nano Today*, 2009, **4**, 66-80.
23. S. P. Thomas, E. M. Al-Mutairi and S. K. De, *Arabian Journal for Science and Engineering*, 2013, **38**, 457-477.
24. G. Brumfiel, *Nature*, 2002, **424**, 246-248.
25. C. Buzea, I. I. Pacheco and K. Robbie, *Biointerphases*, 2007, **2**, MR17-MR71.
26. B. Gulson, M. McCall, M. Korsch, L. Gomez, P. Casey, Y. Oytam, A. Taylor, M. McCulloch, J. Trotter, L. Kinsley and G. Greenoak, *Toxicological Sciences*, 2010, **118**, 140-149.
27. N. S. Wigginton, K. L. Haus and M. F. J. Hochella, *Journal of Environmental Monitoring*, 2007, **9**, 1306-1316.
28. L. Vayssieres, *International Journal of Nanotechnology*, 2005, **2**, 411-439.
29. X. Z. Wang, Y. Yang, R. Li, C. McGuinnes, J. Adamson, I. L. Megson and K. Donaldson, *Nanotoxicology*, 2014, **8**, 465-476.
30. G. R. Wang, L. Wang, R. Qiang, J. Wang, J. Luo and C.-J. Zhong, *Journal of Materials Chemistry*, 2007, **17**, 457-462.

31. M. Seijo, M. Pohl, S. Ulrich and S. Stoll, *Journal of Chemical Physics*, 2009, **131**.

32. A. M. Gobin, G. Zhang, 2011, Patent number US2011064676-A1.

33. M. F. Costa De Sousa, S. Krol, A. Legname, 2010, Patent number WO2010052665-A2; WO2010052665-A3; CA2742915-A1; EP2362769-A2; KR2011089171-A; US2011262546-A1; IT1391687-B; JP2012508226-W.

34. J. A. Jamison, E. L. Bryant, S. B. Kadali, M. S. Wong, V. L. Colvin, K. S. Matthews and M. K. Calabretta, *Journal of Nanoparticle Research*, 2011, **13**, 625-636.

35. H. Zhang, J. Han and B. Yang, *Advanced Functional Materials*, 2010, **20**, 1533-1550.

36. A. M. Schrand, L. Dai, J. J. Schlager and S. M. Hussain, *Advances in experimental medicine and biology*, 2012, **745**, 58-75.

37. Y. Yoshioka, T. Yoshikawa and Y. Tsutsumi, *Nihon eiseigaku zasshi. Japanese journal of hygiene*, 2010, **65**, 487-492.

38. X. Lu, Y. Liu, X. Kong, P. E. Lobie, C. Chen and T. Zhu, *Small*, 2013, **9**, 1654-1671.

39. I. Pacheco-Blandino, R. Vanner and C. Buzea, *Toxicity of nanoparticles*, 2012.

40. T. J. Brunner, P. Wick, P. Manser, P. Spohn, R. N. Grass, L. K. Limbach, A. Bruinink and W. J. Stark, *Environmental Science & Technology*, 2006, **40**, 4374-4381.

41. Q. Rahman, *Women in Biotechnology: Creating Interfaces*, 2008, 237-255.

42. N. Serpone, A. Salinaro and A. Emeline, 2001, Conference on Nanoparticles and Nanostructured Surfaces San Jose, California.

43. M. E. Burnett and S. Q. Wang, *Photodermatology Photoimmunology & Photomedicine*, 2011, **27**, 58-67.

44. B. Voit, *Journal of Polymer Science Part a-Polymer Chemistry*, 2000, **38**, 2505-2525.

45. G. C. Behera, A. Saha and S. Ramakrishnan, *Macromolecules*, 2005, **38**, 7695-7701.

46. N. Z. Qureshi, M. Rogunova, E. V. Stepanov, G. Capaccio, A. Hiltner and E. Baer, *Macromolecules*, 2001, **34**, 3007-3017.

47. A. W. Bosman, H. M. Janssen and E. W. Meijer, *Chemical Reviews*, 1999, **99**, 1665-1688.

48. F. Caruso, G. Qiao, A. R. Blencowe, T. K. Goh, L. A. Connal, G. K. Such, 2011, Patent number US2011250353-A1; US8496997-B2.

49. D. M. Knauss and T. Z. Huang, *Macromolecules*, 2002, **35**, 2055-2062.

50. R. Yoshida, K. Uchida, Y. Kaneko, K. Sakai, A. Kikuchi, Y. Sakurai and T. Okano, *Nature*, 1995, **374**, 240-242.

51. R. M. England and S. Rimmer, *Polymer Chemistry*, 2010, **1**, 1533-1544.

52. L. Niimi, K. Shiino, S. Hiraoka and T. Yokozawa, *Macromolecules*, 2002, **35**, 3490-3494.

53. L. Niimi, K. I. Serita, S. Hiraoka and T. Yokozawa, *Journal of Polymer Science Part a-Polymer Chemistry*, 2002, **40**, 1236-1242.

54. M. Colonna, C. Berti, E. Binassi, A. Celli, M. Fiorini, P. Marchese, M. Messori and D. J. Brunelle, *Polymer International*, 2011, **60**, 1607-1613.

55. J. Chiefari, Y. K. Chong, F. Ercole, J. Krstina, J. Jeffery, T. P. T. Le, R. T. A. Mayadunne, G. F. Meijs, C. L. Moad, G. Moad, E. Rizzardo and S. H. Thang, *Macromolecules*, 1998, **31**, 5559-5562.

56. X. Wang, X. Yuan, T. Qiang and L. Ren, *Journal of the Society of Leather Technologists and Chemists*, 2009, **93**, 61-66.

57. V. Uskokovic and T. A. Desai, *Journal of Biomedical Materials Research Part A*, 2013, **101A**, 1416-1426.

58. D. C. Pepper, *Quarterly Reviews*, 1954, **8**, 88-121.

59. G. Moad, Y. K. Chong, A. Postma, E. Rizzardo and S. H. Thang, *Polymer*, 2005, **46**, 8458-8468.

60. G. Moad, E. Rizzardo and S. H. Thang, *Chemistry-an Asian Journal*, 2013, **8**, 1634-1644.

61. B. M. Rosen and V. Percec, *Chemical Reviews*, 2009, **109**, 5069-5119.

62. K. Matyjaszewski, *Macromolecules*, 1993, **26**, 1787-1788.

63. J. Vandenbergh, T. d. m. Ogawa and T. Junkers, *Journal of Polymer Science Part a-Polymer Chemistry*, 2013, **51**, 2366-2374.

64. G. Moad, E. Bicciocchi, M. Chen, J. Chiefari, C. Guerrero-Sanchez, M. Haeussler, S. Houshyar, D. Keddie, E. Rizzardo, S. H. Thang and J. Tsanaktsidis, in *Progress in Controlled Radical Polymerization: Mechanisms and Techniques*, eds. K. Matyjaszewski, B. S. Sumerlin and N. V. Tsarevsky, 2012, vol. 1100, pp. 243-258.

65. V. Percec, T. Guliashvili, J. S. Ladislaw, A. Wistrand, A. Stjerndahl, M. J. Sienkowska, M. J. Monteiro and S. Sahoo, *Journal of the American Chemical Society*, 2006, **128**, 14156-14165.

66. Q. Lou and D. A. Shipp, *Chemphyschem*, 2012, **13**, 3257-3261.

67. G. Moad, G. Anderson Albert, F. Ercole, H. J. Johnson Charles, J. Krstina, L. Moad Catherine, E. Rizzardo, H. Spurling Thomas and H. Thang San, in *Controlled Radical Polymerization*, American Chemical Society, 1998, vol. 685, ch. 21, pp. 332-360.

68. G. Moad, E. Rizzardo and S. H. Thang, in *Fundamentals of Controlled/Living Radical Polymerization*, The Royal Society of Chemistry, 2013, pp. 205-249.

69. D. J. Keddie, G. Moad, E. Rizzardo and S. H. Thang, *Macromolecules*, 2012, **45**, 5321-5342.

70. E. Bicciocchi, Y. K. Chong, L. Giorgini, G. Moad, E. Rizzardo and S. H. Thang, *Macromolecular Chemistry and Physics*, 2010, **211**, 529-538.

71. J. Fu, Z. Cheng, N. Zhou, J. Zhu, W. Zhang and X. Zhu, *Polymer*, 2008, **49**, 5431-5438.

72. D. J. Keddie, C. Guerrero-Sanchez and G. Moad, *Polymer Chemistry*, 2013, **4**, 3591-3601.

73. C. Shang, J. Xu, X. Wang, X. Zhang, W. Zhang and T. Zhang, *Polymer*, 2013, **54**, 614-622.

74. X. Wang, J. Xu, Y. Zhang and W. Zhang, *Journal of Polymer Science Part a-Polymer Chemistry*, 2012, **50**, 2452-2462.

75. X. Wang, S. Li, Y. Su, F. Huo and W. Zhang, *Journal of Polymer Science Part a-Polymer Chemistry*, 2013, **51**, 2188-2198.

76. A. O. Moughton, J. P. Patterson and R. K. O'Reilly, *Abstracts of Papers of the American Chemical Society*, 2010, **240**.

77. J. M. J. Frechet, M. Henmi, I. Gitsov, S. Aoshima, M. R. Leduc and R. B. Grubbs, *Science*, 1995, **269**, 1080-1083.

78. Z. M. Wang, J. P. He, Y. F. Tao, L. Yang, H. J. Jiang and Y. L. Yang, *Macromolecules*, 2003, **36**, 7446-7452.

79. S. Carter, B. Hunt and S. Rimmer, *Macromolecules*, 2005, **38**, 4595-4603.

80. S. G. Roy and P. De, *Polymer Chemistry*, 2014, **5**, 6365-6378.

81. J. A. Alfurhood, P. R. Bachler and B. S. Sumerlin, *Polymer Chemistry*, 2016, **7**, 3361-3369.

82. J. S. Wang and K. Matyjaszewski, *Macromolecules*, 1995, **28**, 7572-7573.

83. Y. K. Chong, J. Krstina, T. P. T. Le, G. Moad, A. Postma, E. Rizzardo and S. H. Thang, *Macromolecules*, 2003, **36**, 2256-2272.

84. K. Matyjaszewski, B. Gobelt, H. J. Paik and C. P. Horwitz, *Macromolecules*, 2001, **34**, 430-440.

85. L. V. Zherenkova, P. V. Komarov and O. A. Guskova, *Journal of Structural Chemistry*, 2006, **47**, 156-162.

86. M. Muthukumar, *Journal of Chemical Physics*, 1997, **107**, 2619-2635.

87. J. Rosselgong, S. P. Armes, W. R. S. Barton and D. Price, *Macromolecules*, 2010, **43**, 2145-2156.

88. C. Holm, J. F. Joanny, K. Kremer, R. R. Netz, P. Reineker, C. Seidel, T. A. Vilgis and R. G. Winkler, in *Polyelectrolytes with Defined Molecular Architecture Ii*, ed. M. Schmidt, 2004, vol. 166, pp. 67-111.

89. I. Teraoka and P. Cifra, *Polymer*, 2002, **43**, 3025-3033.

90. N. D. Hann, *Journal of Polymer Science Part a-Polymer Chemistry*, 1977, **15**, 1331-1339.

91. G. Volet and J. Lesec, *Journal of Liquid Chromatography*, 1994, **17**, 559-577.

92. H. Mori, D. C. Seng, H. Lechner, M. F. Zhang and A. H. E. Muller, *Macromolecules*, 2002, **35**, 9270-9281.

93. R. Myers, *American Laboratory*, 2002, **34**, 58-62.

94. A. Katchalsky, *Biophysical Journal*, 1964, **4**, 9-17.

95. L. Wang and D. Cao, *Progress in Chemistry*, 2010, **22**, 905-915.

96. H. Heimo and I. Suominen, *Bioseparation*, 1995, **5**, 147-154.

97. V. A. Kabanov, *Polymer Science Series A*, 2004, **46**, 451-470.

98. L. Zhang and J. Sun, *Macromolecules*, 2010, **43**, 2413-2420.

99. R. J. Nap, S. H. Park and I. Szleifer, *Journal of Polymer Science Part B-Polymer Physics*, 2014, **52**, 1689-1699.

100. R. Ladj, A. Bitar, M. M. Eissa, H. Fessi, Y. Mugnier, R. Le Dantec and A. Elaissari, *International Journal of Pharmaceutics*, 2013, **458**, 230-241.

101. T. C. Johnstone, N. Kulak, E. M. Pridgen, O. C. Farokhzad, R. Langer and S. J. Lippard, *Acs Nano*, 2013, **7**, 5675-5683.

102. A. N. Kulak, M. Semsarilar, Y. Y. Kim, J. Ihli, L. A. Fielding, O. Cespedes, S. P. Armes and F. C. Meldrum, *Chemical Science*, 2014, **5**, 738-743.

103. S. H. Lee, M. C. Shin, S. J. Choi, J. H. Shin and L. S. Park, *Environmental Technology*, 1998, **19**, 431-436.

104. J. M. Ebeling, K. L. Rishel and P. L. Sibrell, *Aquacultural Engineering*, 2005, **33**, 235-249.

105. A. I. Zouboulis, P. A. Moussas and N. D. Tzoupanos, *Coagulation-flocculation processes applied in water or wastewater treatment*, 2009.

106. P. Somasundaran and V. Runkana, *Chemical Engineering Research & Design*, 2005, **83**, 905-914.

107. B. Wang, Y. Zhang and C. Miao, *Journal of Ocean University of China*, 2011, **10**, 42-46.

108. M. Mehdikhani-Nahrkhalaji, M. H. Fathi, V. Mortazavi, S. B. Mousavi, B. Hashemi-Beni and S. M. Razavi, *Journal of Materials Science-Materials in Medicine*, 2012, **23**, 485-495.

109. H.-W. Kim, J.-H. Song and H.-E. Kim, *Journal of Biomedical Materials Research Part A*, 2006, **79A**, 698-705.

110. H.-W. Kim, H.-H. Lee and G.-S. Chun, *Journal of Biomedical Materials Research Part A*, 2008, **85A**, 651-663.

111. G. Villalba, R. U. Ayres and H. Schroder, *Journal of Industrial Ecology*, 2007, **11**, 85-101.

112. G. I. o. America, *GIA Gem Reference Guide*, Gemological Institute of America, 1995.

113. B. J. Jeon, S. Y. Jeong, A. N. Koo, B.-C. Kim, Y.-S. Hwang and S. C. Lee, *Macromolecular Research*, 2012, **20**, 715-724.

114. D. W. Hutmacher, *Biomaterials*, 2000, **21**, 2529-2543.

115. A. N. Koo, I. K. Kwon, S. C. Lee, S.-K. Lee, H.-S. Kim, Y.-H. Woo, S.-H. Jeon, J.-H. Chae and K.-W. Kang, *Macromolecular Research*, 2010, **18**, 1030-1036.

116. S. Shekhar, A. Roy, D. Hong and P. N. Kumta, *Materials Science and Engineering: C*, 2016, **69**, 486-495.

117. J. A. Juhasz, S. M. Best and W. Bonfield, *Science and Technology of Advanced Materials*, 2016.

118. H. Shimizu, Y. Jinno, Y. Ayukawa, I. Atsuta, T. Arahira, M. Todo and K. Koyano, *Implant Dentistry*, 2016, **25**, 567-574.

119. M. P. Ferraz, F. J. Monteiro and C. M. Manuel, *Journal of applied biomaterials & biomechanics : JABB*, 2004, **2**, 74-80.

120. M. Senna, T. Isobe, M. Kanayama, 2000, Patent number WO200058209-A; WO200058209-A1; EP1110908-A1; JP2000607922-X; US6592989-B1.

121. V. N. Rudin, I. V. Melikhov, V. V. Minaev, A. Y. Orlov, V. E. Bozhevolnov, 2007, Patent number WO2007009477-A1; EP1909859-A1; US2009155320-A1.

122. W. T. Conner, D. D. Lee, 1999, Patent number US5958504-A.

123. M. Stigter, K. de Groot and P. Layrolle, *Biomaterials*, 2002, **23**, 4143-4153.

124. S. Itoh, M. Kikuchi, K. Takakuda, Y. Koyama, H. N. Matsumoto, S. Ichinose, J. Tanaka, T. Kawauchi and K. Shinomiya, *Journal of Biomedical Materials Research*, 2001, **54**, 445-453.

125. W.-E. Teo, W. He and S. Ramakrishna, *Biotechnology Journal*, 2006, **1**, 918-929.

126. L. M. Rodriguez-Lorenzo, J. N. Hart and K. A. Gross, *Biomaterials*, 2003, **24**, 3777-3785.

127. R. Surendran and K. Chinnakali, *Crystal Research and Technology*, 2008, **43**, 490-495.

128. G. W. C. Silva, L. Ma, O. Hemmers and D. Lindle, *Micron*, 2008, **39**, 269-274.

129. S. C. Mojumdar, J. Kozankova, J. Chocholousek, J. Majling and D. Fabryova, *Journal of Thermal Analysis and Calorimetry*, 2004, **78**, 73-82.

130. B. L. Riggs, S. F. Hodgson, D. L. Hoffman, P. J. Kelly, K. A. Johnson and D. Taves, *Jama-Journal of the American Medical Association*, 1980, **243**, 446-449.

131. M. E. Gomes, P. B. Malafaya and R. L. Reis, *Biopolymer Methods in Tissue Engineering*, 2003, **238**, 65-75.

132. F. Jakob, R. Ebert, A. Ignatius, T. Matsushita, Y. Watanabe, J. Groll and H. Walles, *Maturitas*, 2013, **75**, 118-124.

133. S. N. Parikh, *jour. Postgrad. Med.*, 2002, **48**, 142-148.

134. A. El-Ghannam, *Expert Review of Medical Devices*, 2005, **2**, 87-101.

135. P. Jayakumar and L. Di Silvio, *Proceedings of the Institution of Mechanical Engineers Part H-Journal of Engineering in Medicine*, 2010, **224**, 1415-1440.

136. H. J. Mankin, F. J. Hornicek, K. A. Raskin *Clin. Orthop. Related Res.*, 2005, **432**, 210-216.

137. J. C. Banwart, M. A. Asher, R. S. Hassanein *Spine*, 1995, **20**, 1055-1060.

138. G. Chiara, F. Letizia, F. Lorenzo, S. Edoardo, S. Diego, S. Stefano, B. Eriberto and Z. Barbara, *International Journal of Molecular Sciences*, 2012, **13**, 737-757.

139. X. Li, L. Wang, Y. Fan, Q. Feng, F.-Z. Cui and F. Watari, *Journal of Biomedical Materials Research Part A*, 2013, **101**, 2424-2435.

140. S. V. Dorozhkin, *Materials*, 2009, **2**, 399-498.

141. Z.-H. Li, J.-M. Wu, S.-J. Huang, J. Guan and X.-Z. Zhang, *Journal of Inorganic Materials*, 2011, **26**, 49-54.

142. M. Kikuchi, A. Yamazaki, M. Akao and H. Aoki, *Bio-Medical Materials and Engineering*, 1996, **6**, 405-413.

143. I. R. de Lima, G. G. Alves, C. A. Soriano, A. P. Campaneli, T. H. Gasparoto, E. S. Ramos Junior, L. A. de Sena, A. M. Rossi and J. M. Granjeiro, *Journal of Biomedical Materials Research Part A*, 2011, **98A**, 351-358.

144. Y. Z. Zhao, Y. Y. Huang, J. Zhu, S. H. Zhu, Z. Y. Li and K. C. Zhou, *Nanoscale Research Letters*, 2011, **6**.

Chapter 2 – General Materials and Instrumentation

2.1 Materials

Acrylic acid (Sigma Aldrich), methacrylic acid (Sigma Aldrich) and pyrrole (Sigma Aldrich) were distilled before use. Azobisisobutyronitrile (AIBN) (Sigma Aldrich) was recrystallised from methanol before use. 2-Acrylamido-2-methyl-1-propanesulfonic acid (Sigma Aldrich, ≥ 99.9%), sodium hydride (Sigma Aldrich, 60%), carbon disulfide (Sigma Aldrich, 99.9%), 4-vinyl benzyl chloride (Sigma Aldrich, 90%), magnesium turnings (Sigma Aldrich, 98%), bromobenzene (Sigma Aldrich, 99%), calcium hydroxide (Sigma Aldrich, ≥ 95%), phosphoric acid (Sigma Aldrich, 99.99%), calcium nitrate tetrahydrate (Sigma Aldrich, ≥ 99%), ammonium fluoride (Sigma Aldrich, ACS reagent > 98%), ammonia solution (Sigma Aldrich, 2.0M in methanol), diammonium hydrogen phosphate (Sigma Aldrich, ≥ 99%), methanol (Sigma Aldrich, ≥ 99.9%), DMSO (Sigma Aldrich, 99.9%), ethyl acetate (Sigma Aldrich, 99.7%), diethyl ether (VWR Chemicals, ≥ 99.9%), acetone (VWR Chemicals, ≥ 99.9%), dioxane (VWR Chemicals, 100%) and silica gel (Fluorochem, 60 Å, 40 – 63 μm mesh) were used as received.

Dry *N*,*N*-dimethylformamide (DMF) and tetrahydrofuran (THF) were obtained from the Grubbs dry solvent system (Puresolve, models SPS 400-6 and SPS200-6).[145] Untreated 'wet' solvent is contained in a reservoir and degassed by bubbling with argon. The solvent is forced out of the reservoir by argon gas pressure and into the rearmost column at its base; the solvent then passes upwards over a bed of activated alumina. The alumina is activated by heating to elevated temperature under an atmosphere of inert gas over several hours which dries it and causes charged groups to protrude from the surface. The charges associated with the groups on the surface are the opposite of those found in the water molecules within the solvent; hence when the 'wet' solvent comes into contact with the activated alumina the water within it is attracted to the alumina removing it from the solvent. The solvent then passes from the top of the rear column into the front column at its base via a length of stainless steel tubing where it passes over another bed of alumina before it emerges from the top of the column. The solvent then travels downwards through a length of stainless steel tubing which contains a seven micron inline filter in order to trap any solid matter which the solvent might contain. The now dry and filtered solvent then continues to a valving system at which point it can be dispensed into a suitable collecting vessel using a Schlenk line technique.

2.2 Instrumentation

2.2.1 Nuclear Magnetic Resonance (NMR)

^{1}H NMR spectra were recorded on a Bruker AV-400 instrument running at 400MHz at ambient temperature. 20 mg samples were dissolved in deuterated DMSO, filtered and placed into a 7 inch NMR tube. The NMR spectra were used to calculate the polymerisation yields by weight and the degree of branching. The NMR spectra were used to calculate the polymerisation yields by weight and the degree of branching. ^{1}H NMR spectroscopy was used to determine the percentage conversion of polymerisations by measuring the ratio of residual vinyl peaks to peaks of the polymer backbone. The technique was also used to confirm the synthesis of RAFT agents and determine the degree of branching in the polymers using known polymer peaks along with peaks corresponding to the RAFT agent end groups. The degree of branching (DB) describes the number of chain ends (H_{py}) compared to the total number of monomer units (H_{mono}) and branching agent units (H_{Bz}) incorporated in the polymer.[79] The DB can be calculated using equation 2.1.[79]

$$DB = \frac{H_{mono} + H_{Bz}}{H_{mono} + H_{Py} + H_{Bz}} \qquad \text{Eqn. 2.1}$$

^{13}C NMR spectra were recorded on a Bruker AV-400 instrument running at 400MHz at ambient temperature. 50 mg samples were dissolved in deuterated DMSO, filtered and placed into a 7 inch NMR tube. ^{13}C NMR was used to confirm the synthesis of RAFT agents.

Solid state ^{13}C, ^{19}F and ^{31}P NMR spectra were recorded on a Bruker AV-500 instrument running between 8-10 kHz at ambient temperature using cross polarisation Total Suppression of Spinning Sidebands (CP TOSS) using 'magic angle spinning' (MAS, 54.74 °). This technique was used in an attempt to determine differences between hydroxyapatite and fluorapatite samples. The resulting spectra were identical and therefore were of no use in the determination of differences between samples.

2.2.2 Elemental Analysis

The carbon, hydrogen, nitrogen and sulfur content of the RAFT agents were determined using a Perkin-Elmer 2400 CHNS/0 series 2 Elemental Analyser. Approximately 20 mg of RAFT agent sample was combusted completely in excess oxygen and combustion reagent. The levels of each element were detected using a thermal conductivity detector system.

2.2.3 Dynamic Light Scattering Particle Sizing

Particle sizes of pure hydroxyapatite and fluorapatite and polymer treated hydroxyapatite and fluorapatite were recorded using a Brookhaven instruments ZetaPALS Zeta Potential and Particle Sizing Analyser. Samples were dispersed in THF (pure samples and poly(acrylic acid) treated samples), DMF (pure samples, poly(methacrylic acid) and poly(2-acrylamido-2-methyl-1-propanesulfonic acid) treated samples), DMSO (hydroxyapatite added to poly(2-acrylamido-2-methyl-1-propanesulfonic acid) synthesis) and dioxane (hydroxyapatite added to poly(acrylic acid) and poly(methacrylic acid) synthesis) to give a count rate of between 0.5 – 1 Mcps. 5 'runs' lasting 2 minutes each were conducted for each experiment resulting in a mean effective diameter, standard error, half width, polydispersity and baseline index.

The ZetaPALS instrument assumes that the particle is spherical and moves through the solution via Brownian motion. The particle sizes are determined from the hydrodynamic radius of the particle using the Stokes-Einstein equation (equation 2.2):

$$D = \frac{kT}{6\pi\eta r_h} \qquad \text{Eqn. 2.2}$$

where D is the diffusion constant of the particle through the solvent, k is this Boltzmann constant, T is the absolute temperature, η is the viscosity of the solvent, and r_h is the radius of the spherical particle. This causes problems if the measured particles are not spherical as the equipment cannot accurately measure other particle morphologies. It is important to ensure accurate and stable temperature during measurements in order to ensure the correct solvent viscosity and hence diffusion constant. Viscosity is directly related to temperature and unstable temperatures can lead to convection currents that cause non-random movement through the solvent which will invalidate the particle size measurements.

2.2.4 Small Angle X-ray Scattering (SAXS)

Samples were run in either THF or DMF at 1 wt%. A dilute solution creates an environment where all the polymer chains are far away from each other. This removes any excess scattering caused by interactions of the polymer chains and allows specific size and shape analysis to be conducted. The samples were run for 30 minutes at a sample-to-detector distance of 1.46 m with a copper x-ray source ($\lambda = 1.54$ Å^{-1}), this equates to a q-range of 0.008 Å^{-1} to 0.2 Å^{-1}.

Firstly, the radius of gyration, R_g, of the polymer was estimated using the 'Unified fit' in the Irena package of Igor pro. This code was developed by Greg Beaucage to fit SAS data with levels composed of a Guinier part and a power law tail. The Unified fit code fits the scattering at low-q (Guinier region) with Guinier's law to estimate the size of the polymer chain, as well as fitting the slope of the scattering pattern in the higher-q section (Fourier region), which is related to the shape of the polymer chain. Guinier's law is used to fit the scattering intensity at low q (equation 2.3).

$$I(q) \approx I_e N_p n^2 . e^{-\left(\frac{{R_g}^2 q^2}{3}\right)} \qquad \text{Eqn. 2.3}$$

where, I_e is the scattering factor for a single electron, N_p is the number of particles in the scattering volume, n is the number of electrons in a particle, q is the scattering vector, and R_g is the radius of gyration. As I_e, N_p, and n^2 are all constants we can rewrite equation 2.3 as equation 2.4 where G is the classic Guinier prefactor.

$$I(q) \approx G . e^{-\left(\frac{{R_g}^2 q^2}{3}\right)} \qquad \text{Eqn. 2.4}$$

This can be used in summation with a structurally limited power law to fit the higher q region to create the Unified Guinier/poer-law equation developed by Greg Beaucage (equation 2.5)

$$I(q) \approx G . e^{-\left(\frac{{R_g}^2 q^2}{3}\right)} + B\left[\frac{\left(\operatorname{erf}\left(\frac{qR_g}{\sqrt{6}}\right)\right)^3}{q}\right]^P \qquad \text{Eqn. 2.5}$$

where B is a prefactor specific to the type of power-law scattering as determined by the regime in which P falls, and e r and f are constants. So for Porod's law (scattering from sharp interfaces, e.g. hard spheres), P = 4, whereas for Gaussian polymers, P = 2.

Secondly, it is important to note that the Rg is 'model-independent'. This means that it contains no information about the shape or the internal structure of the polymer chain. However, if the sample being measured is known to be spherical, the average size of the sphere (R_{sphere}) can be calculated using equation 2.6.

$$R_{Sphere} = \sqrt{\frac{4}{3}R_g} \qquad \text{Eqn. 2.6}$$

This relationship varies depending on the shape of the particle.

To obtain the molecular weight of the polymer from the radius of gyration we must assume ideal polymer chains. It is known that the ratio between the radius of gyration and the average end-to-end vector is 1/6 for ideal chains as shown in equation 2.7:

$$R_g{}^2 = \frac{1}{6}Nb^2 \qquad \text{Eqn. 2.7}$$

where N is the number of units and b is the unit length. However, non-ideal polymers have a certain stiffness, and this is accounted for using the Kuhn segment length l. This can now be written as equation 2.8:

$$R_g{}^2 = \frac{1}{6}Ll \qquad \text{Eqn. 2.8}$$

where L is the contour length and is equal to N × b. This equation can be rearranged in terms of N to give equation 2.9:

$$N = \frac{6R_g{}^2}{lb} \qquad \text{Eqn. 2.9}$$

Finally, in order to get the molecular weight of the polymer, you can simply multiply the number of segments N by the molecular weight of the monomer (equation 2.10).

$$M_w = \frac{6R_g{}^2}{lb}M \qquad \text{Eqn. 2.10}$$

Where M_w is the calculated weight average molecular weight of the polymer and M is the molar mass of the monomer repeat unit.

2.2.5 Attenuated Total Reflectance Fourier Transform Infrared Spectroscopy (ATR-FTIR)

ATR-FTIR spectra of pure hydroxyapatite and fluorapatite were recorded on a temperature controlled GoldenGate^{TM} single reflection ATR accessory (SpectraTech) coupled to a

ThermoNicolet Nexus FTIR spectrometer. Solid samples were placed in direct contact with the ATR crystal. Data were collected by averaging over 32 scans at 4 cm^{-1} resolution. The blank ATR crystal was used as a reference background.

2.2.6 Fourier Transform Infrared Spectroscopy – KBr disc

FTIR was used to study the crystal chemistry of FHA and HA and the chemical interactions between the ceramics and PAA by improving the resolution of the (F)HA spectra compared to the ATR-FTIR. Spectra were recorded using a Bruker Vertex 70 spectrometer (Ettlingen, Germany) in the range 400 - 4000 cm^{-1}. 1 mg of the sample was mixed with 50 mg KBr by hand using a pestle and mortar; the mixture was then pressed into a 12 mm diameter disk under a pressure of 60 MPa for 3 minutes. Samples were stored in a desiccator prior to analysis. Eight scans were recorded for each spectrum and all spectra were baseline corrected with the 'Opus' software package (version 7, Bruker) supplied with the spectrometer. A separate sample of pure KBr was used to create a reference spectrum to establish the background prior to each set of measurements. The spectra were overlaid and compared to determine if any difference was caused by the inclusion of PAA in the samples of FHA and HA.

Peak positions are caused by the bending and stretching of chemical bonds known as vibrations. These vibrations have definite energies which are inversely proportional to the wavelength of a photon of light as shown in equation 2.11:

$$E = \frac{hc}{\lambda} \qquad \text{Eqn. 2.11}$$

Where E is the photon energy, *h* is Planck's constant, *c* is the speed of light in vacuum and λ is the photon's wavelength. FTIR spectra are generally plotted using wavenumber, $\bar{\upsilon}$, which is the inverse of wavelength, hence giving equation 2.12:

$$E = hc\bar{\upsilon} \qquad \text{Eqn. 2.12}$$

FTIR measures the absorbance or transmittance of photons at wavenumbers in the mid-IR range of the infrared spectrum (~4000 cm^{-1}- 400 cm^{-1}). IR radiation does not have enough energy to induce electronic transitions, instead the absorbed photons' energy is deposited within the chemical bond as either a stretching or bending motion. Energy is conserved within the ‘reaction’ as the photon’s energy becomes vibrational energy within the chemical bond. For IR to be absorbed, a net change in dipole moment must occur within the molecule.

As the wavenumber is directly related to the energy of a photon, measurements can be made by passing a beam of infrared light through a sample and recording the absorbance which occurs when the photons are of the same energy as the vibrations of the chemical bonds. The absorbance of the photon is detected by decreased infrared intensity at the wavenumber of the light absorbed; this produces an absorption peak in the IR spectrum due to the dipole moment. Absorbance is related to the amount of light that is transmitted through the sample. If a sample is opaque then the transmittance will be 0 % as all the light is absorbed by the sample, conversely if a sample is completely transparent then the absorbance will be zero. Transmittance and absorbance can be calculated using equations 2.13 and 2.14 respectively:

$$T = \frac{I}{I_0} \qquad \text{Eqn. 2.13}$$

$$A = log\frac{1}{T} = log\frac{I_0}{I} \qquad \text{Eqn. 2.14}$$

Where T is transmittance, I is the intensity of the transmitted light, I_0 is the incidence light, and A is absorbance. If desired, these equations can be used alongside the Beer Lambert law (equation 2.15) in order to quantify the concentration of a sample if the molar absorption coefficient, ε, and path length, l, are known.

$$A = \varepsilon cl \qquad \text{Eqn. 2.15}$$

In practice quantification requires samples of high purity and low concentration in order to prevent intermolecular interactions and shifting chemical equilibrium. Quantification was no used during the present work.

2.2.7 X-ray Diffraction Spectroscopy (XRD)

X-ray diffraction patterns of hydroxyapatite, fluorhydroxyapatite and fluorapatite were recorded on a Bruker Instrument D8 Advance in flat plate mode using a copper radiation source. Powder samples were pressed into a flat plate holder and rotated at 45 rpm. Spectra were compared to known powder diffraction files to determine the composition of the ceramic particles and crystallinity of the sample and analysed using the TOPAS software supplied by Bruker to perform Rietveld and Pawley refinements.[146]

Dried powder samples of the composite samples detailed in Chapter 5 were also analysed using a Siemens D500 diffractometer (Munich, Germany) with Bragg-Brentano geometry and a CuKα source. 45 mg of sample was mixed by hand with 5 mg silicon to act as a reference and ground into a fine powder using a pestle and mortar. A small amount of Vaseline was placed in a circle on a microscope slide and inserted into the XRD holder. The powder sample was then placed on the Vaseline and smoothed until level using a second microscope slide. Analysis was undertaken using the angular range 20 – 60 ° 2θ. The step size and time per step were 0.04 ◦ and 3 s respectively. Rietveld refinement was performed on the XRD patterns using the MAUD refinement program[147].

Pawley and Rietveld refinements were conducted on the diffractograms collected from each sample. The main difference between these refinement techniques is that Pawley refinement looks to fit the correct unit cell parameters, while Rietveld refinement tries to determine the correct structure of the crystal lattice. Both techniques use a mathematical model to fit the collected data. The 'R factors' R_{wp} and R_{wpb} are the weighted profile residual and weighted profile residual without background respectively. These terms denote the 'goodness of fit' of the data to a known diffraction pattern of the same substance.[148] R_{wp} and R_{wpb} are calculated using equations 2.16 and 2.17 respectively.

$$R_{wp} = \left[\frac{\sum_{i=1}^{n} w_i \left(Y_i^{obs} - Y_i^{calc}\right)^2}{\sum_{i=1}^{n} w_i \left(Y_i^{obs}\right)^2}\right]^{1/2} \times 100\% \qquad \text{Eqn. 2.16}$$

$$R_{wpb} = \left[\frac{\sum_{i=1}^{n} w_i \left(Y_i^{obs} - Y_i^{calc}\right) \frac{\left(Y_i^{obs} - Y_i^{back}\right)}{Y_i^{obs}}}{\sum_{i=1}^{n} w_i \left(Y_i^{obs} - Y_i^{back}\right)^2}\right]^{1/2} \times 100\% \qquad \text{Eqn. 2.17}$$

Where n is the total number of points measured, w_i is the weight of the i^th^ data point (usually $w_i = 1/Y_i^{obs}$), Y_i^{obs} is the observed intensity of the ith data point, Y_i^{calc} is the calculated intensity of the ith point and Y_i^{back} is the background contribution to the diffraction pattern. Values of R_{wp} and R_{wpb} can give an indication of how well the collected diffraction pattern fits with the known profile for that material. There is no threshold to give a definitively good fit;

however, it is generally accepted that the lower the values of the residuals, the better the fit of the data, with the best fit occurring when R_{wp} equals one.[148]

Pawley refinement will always give a better fit than Rietveld refinement due to the different fitting parameters. Pawley refinement 'sees' reflections at particular angles and varies the intensity associated with the peak until the two overlap. Rietveld refinement on the other hand uses a structural model whereby the intensity of a peak is related to the electron density of the model of the crystal lattice; as a result, the Rietveld refinement will show how good the structural model is. A good fit will occur only when the diffraction peaks and electron density associated with the atomic position within the crystal model overlap effectively. Both Pawley and Rietveld refinements will produce axis parameters and give an idea of the size of the unit cell of the particles measured.

The main elements of a diffraction pattern are the peak position, peak intensity and peak broadening. Each of these factors is affected by separate variances within the unit cell which is directly related to Bragg's Law (equation 2.18).

$$2d \sin\theta = n\lambda \qquad \text{Eqn. 2.18}$$

Where d is the interplanar distance or 'd spacing' between atoms in the sample, θ is the scattering angle of the x-ray beam, n is a positive integer, and λ is the wavelength of the x-ray beam. Bragg diffraction causes constructive interference when x-rays, with a wavelength the same as the atomic spacing in the crystal structure, are scattered by atoms in a crystalline material. Constructive interference occurs when waves arrive at the detector in phase, in this instance the difference between the path lengths of the waves is an integer multiple of the wavelength. Conversely, destructive interference occurs when waves arrive out of phase and cancel each other out. Successive planes (miller indices) of the crystal lattice cause a cumulative effect which intensifies the interference effects. Bragg's law describes the scattering angle, θ, at which the constructive interference to be at its strongest. Diffraction patterns are produced by measuring the intensity of the scattered waves as a function of θ. The strongest peaks occur where θ satisfies Bragg's law and hence are known as Bragg peaks.

Peak position is affected by the unit cell length and the strain caused by structural variations; an increase in the angle of 2θ indicates a reduction in the strain of the unit cell. Peak intensity expresses the long-range order of the crystal lattice; larger crystals have greater long range order and as a result produce sharp peaks, this is also related to peak broadening. Peak broadening is most frequently associated with disruptions to the crystal lattice and nanoscale interactions within the unit cell. Broad peaks can indicate smaller particles but they can also be caused by the instrument the pattern was collected on. Different diffractometers will have differing optical configurations which will affect the height and shape of the peaks, while the overall area under the peak will remain constant. Other effects such as peak asymmetry, usually appearing below 30 ° 2θ and above 50 ° 2θ, are due to the instrument profile width and microstrain within the sample, both causing broadening. The area under peak remains constant when a sample is run under different conditions on the same instrument; hence sharper peaks show bigger crystallite sizes. Anisotropy can also have an effect on peak shape and height, depending on the dimensions of the particle. If crystallite sizes in the x and y directions are 100 times smaller than the size of the z direction, then the peaks corresponding to (h00) and (0k0) will be broader than (00l) peaks. Peak broadening of a single diffraction peak is caused by the dimensions of the particle perpendicular to the plane producing the diffraction peak. XRD analysis of crystallites with broad or polydisperse size distributions is difficult as the best diffraction patterns are formed when the particles of a sample are uniform in size and shape.

The unit cell is determined by the crystal lattice and the axis parameters. Hydroxyapatite has a hexagonal crystal lattice meaning that the cell parameters are as follows: a = b $\neq$ c with angles in between these axes consisting of $\alpha = \beta \neq \gamma$ where α and $\beta = 90$ ° and $\gamma = 120$ °. A schematic diagram of the unit cell of HA is shown in figure 2.1. Axis parameters *a* and *c* show the length and height of the unit cell. The axis parameters are proportional to the inverse square of the d spacing within the diffracted sample as described by equation 2.19.

$$\frac{1}{d^2} = \frac{4}{3}\frac{h^2+hk+k^2}{a^2} + \frac{l^2}{c^2} \qquad \text{Eqn. 2.19}$$

Equation 2.19 describes a hexagonal crystal lattice and can be used to manually derive axis parameters from a powder diffraction pattern.

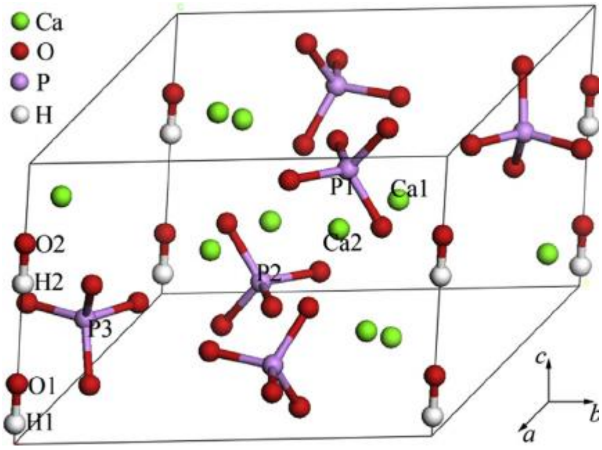

Figure 2.1. The conventional unit cell of hydroxyapatite.[149]

This is only possible if the powder pattern is very high quality and the miller indices corresponding to each peak are known. Alternatively, Pawley or Rietveld refinement can be used to determine the axis parameters using a known structure model. If the experimental parameters are well refined using a highly crystalline standard, then it may even be possible to determine crystallite sizes within the sample. This requires extremely accurate measurements and very crystalline samples. In practice this is very difficult to achieve with standard samples. However, refinement of powder patterns can give good quality information about the unit cell parameters of the sample, even if the sample isn't highly crystalline.

Any differences seen when comparing the lattice parameters of HA samples synthesised in the presence of polymers to the standard powder diffraction file (PDF) of pure HA can be used to determine differences in crystal dimension and atom placement within the sample. This can be used to indirectly determine lattice disruption and indicate whether the polymer has been incorporated into the unit cell, or is coating the particles instead.

2.2.8 Transmission Electron Microscopy (TEM)

TEM images were taken using a Philips CM-100 transmission electron microscope. Samples were prepared by adding approximately 20 mg of sample to 2 ml ethanol in a small vial, which were then sonicated for 15 minutes. The sonicated mixture was then dropped onto a carbon coated TEM grid using a Pasteur pipette and the ethanol was allowed to evaporate. Images were acquired at a range of magnifications and analysed using ImageJ software to determine the lengths and widths of (fluor)hydroxyapatite particles.[150]

2.2.9 Thermogravimetric Analysis (TGA)

Thermogravimetric analysis was conducted using a Perkin Elmer Pyris 1 Instrument. N_2 was used as purge gas with a flow rate of 60 ml/min. Calibration was carried out using the curie points of iron and alumel by burning a 10 mg weight of each solid. Any remaining impurities from previous runs were removed by heating the pan in a flame of a Bunsen burner before running the sample. The software Pyris Manager was used to program the furnace using the following parameters: the temperature was held at 25 °C for 5 minutes and then heated up to 800 °C using intervals of 10 °C per minute; finally, the temperature was held at 800 °C for another 5 minutes. The resulting thermograms were analysed using Pyris Manager.

2.2.10 Electron Ionisation Mass Spectrometry (EI-MS)

EI-MS was conducted on a VG AutoSpec magnetic sector mass spectrometer. 5 mg samples of the RAFT agents were dissolved in chloroform. Spectra were collected according to manufacturer's instructions.

2.3 References

1. A. B. Pangborn, M. A. Giardello, R. H. Grubbs, R. K. Rosen and F. J. Timmers, *Organometallics*, 1996, **15**, 1518-1520.
2. S. Carter, B. Hunt and S. Rimmer, *Macromolecules*, 2005, **38**, 4595-4603.
3. Bruker, *DIFFRACplus TOPAS 4.2 User ManualDIFFRACplus TOPAS 4.2 User Manual*, Bruker AXS GmbH, Karlsruhe, Germany., 2009.
4. L. Lutterotti, *Nuclear Instruments & Methods in Physics Research Section B-Beam Interactions with Materials and Atoms*, 2010, **268**, 334-340.
5. V. K. Pecharsky and P. Y. Zavalij, *Fundamentals of Powder Diffraction and Structural Characterization of Materials, Second Edition*, Springer US, 2009.
6. F. Ren, X. Lu and Y. Leng, *Journal of the Mechanical Behavior of Biomedical Materials*, 2013, **26**, 59-67.
7. C. A. Schneider, W. S. Rasband and K. W. Eliceiri, *Nature Methods*, 2012, **9**, 671-675.

Chapter 3 – Synthesis of highly branched polyelectrolytes

3.1 Chapter Summary

This chapter details the synthesis and analysis of hyperbranched polymers of poly(acrylic acid) (PAA), poly(methacrylic acid) (PMAA) and poly(2-acrylamido-2-methylpropane sulfonic acid) (PAMPS), as shown in figure 3.1, via RAFT polymerisation.

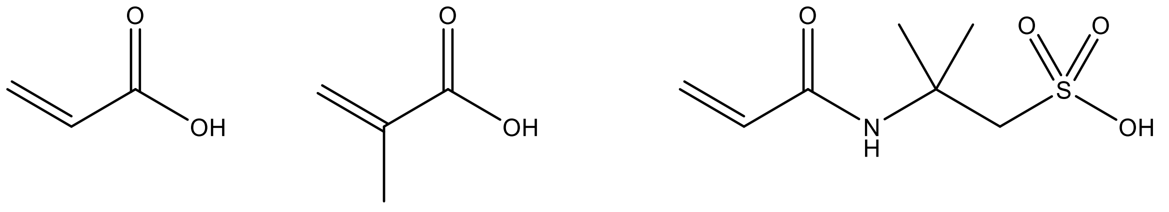

Acrylic acid Methacrylic acid 2-Acrylamido-2-methylpropane sulfonic acid

Figure 3.1. Molecular structures of acrylic acid, methacrylic acid and 2-acrylamido-2-methylpropane sulfonic acid.

The main aim was to determine the effect of the different Z groups of two RAFT agents on the formation of the polymers; the RAFT agents chosen for the polymer synthesis were 4-vinylbenzyl N-pyrrolecarbodithioate and 4-vinylbenzyl dithiobenzoate, shown in figure 3.2, as they are easily synthesised in a laboratory setting and suitable for the synthesis of polyelectrolytes.

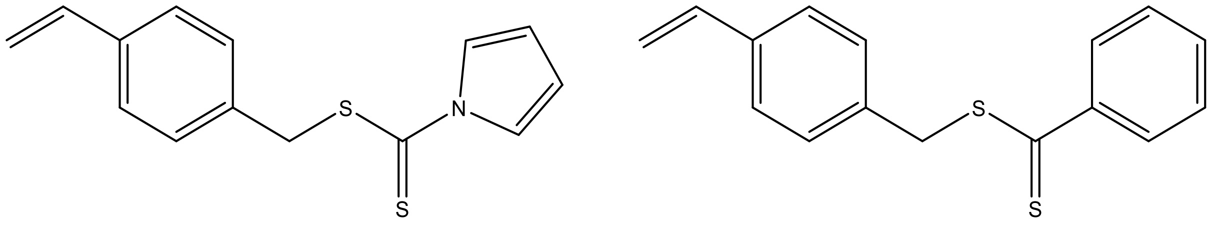

4-vinylbenzyl N-pyrrolecarbodithioate (VPC) 4-vinylbenzyl dithiobenzoate (VBD)

Figure 3.2. Molecular structures of the RAFT agents 4-vinylbenzyl N-pyrrolecarbodithioate (VPC) and 4-vinylbenzyl dithiobenzoate (VBD).

The second aim was to investigate the effect of the initiator on the polymer synthesis. Azobisisobutyronitrile (AIBN) and 4-4’azobis(4-cyanovaleric acid) (ACVA) were used to examine what effect, if any, the different side groups on the initiator had on the polymer synthesis. Figure 3.3 shows the structures of AIBN and ACVA. AIBN and ACVA are well known initiators; it was hypothesised that the variance in the groups adjacent to the N=N bond of the initiators would have an effect on the polymerisations.

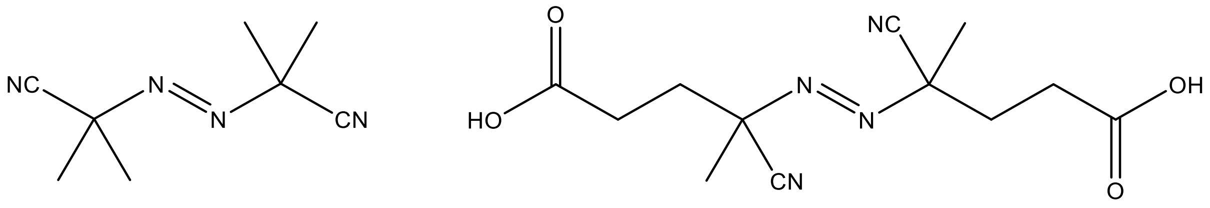

AIBN ACVA

Figure 3.3. The chemical structures of azobisisobutyronitrile (AIBN) and 4,4’-azobis(4-cyanovaleric acid) (ACVA) initiators used for the synthesis of hyperbranched polymers.

The COOH groups on the ACVA should allow more effective reactions with acid monomers due to the initiator being slightly solubilised by the monomer. The fact that the reaction is conducted in dioxane means that the AIBN will be more soluble in the solvent, while the acid end groups of the ACVA will make it more hydrophilic and therefore theoretically more likely to react with acidic monomers than the AIBN. Polymers were made in a ratio of 25:1 monomer to RAFT agent with the aim of producing highly branched polyelectrolytes. These polymers were chosen as they are negatively charged which should allow them to interact with the calcium ions of hydroxyapatite to form composite materials as detailed in subsequent chapters. Figure 3.4 shows a schematic diagram of the polymer synthesis.

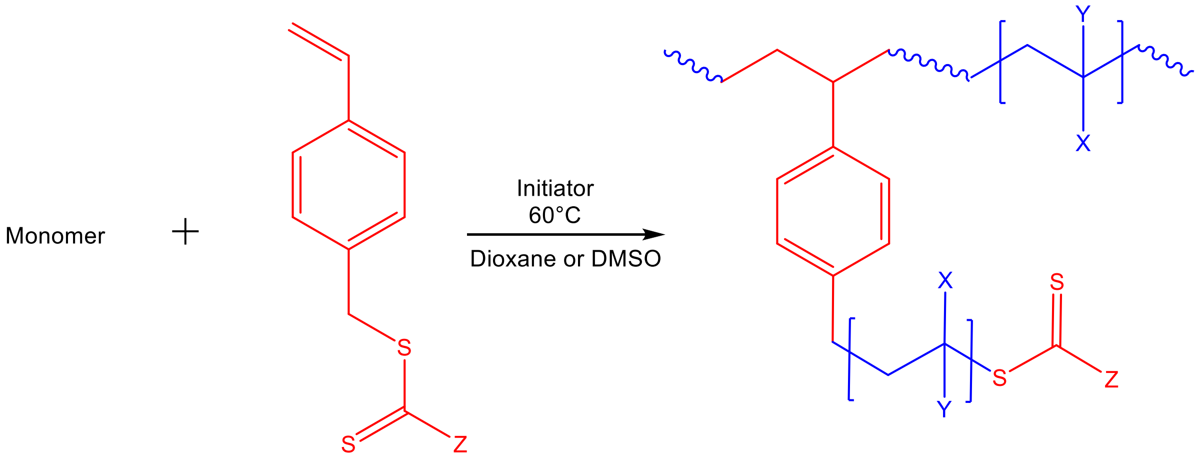

Acrylic acid: X= COOH, Y = H
Methacrylic acid: X = COOH, Y = Me
2-acrylamido-2-methyl propane sulfonic acid: X= CONHC$(CH_3)_2CH_2SO_3$H, Y = H

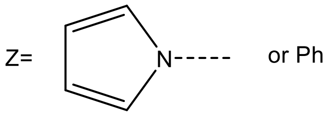

Figure 3.4. A schematic diagram of the RAFT polymerisations of acrylic acid, methacrylic acid and 2-acrylamido-2-methylpropane sulfonic acid using either azobisisobutyronitrile or 4-4’azobis(4-cyanovaleric acid) as an initiator and either 4-vinylbenzyl N-pyrrolecarbodithioate or 4-vinylbenzyl dithiobenzoate as a RAFT agent.

The synthesis of the polymers was complicated by the hygroscopic nature of the polymers which made purification difficult. The 'sticky' nature of some polymers meant that processing and in some cases analysis became near impossible. NMR spectroscopy was the main technique used to determine polymer conversion and degree of branching. The determination of molecular weight was extremely problematic due to the incompatibility of the polymers with certain solvents and columns, hence analysis via the usual method of GPC was not possible. Small angle x-ray scattering (SAXS) was used as an alternative method to determine the molecular weight of the polymers. After purification some polymers also became insoluble in many solvents. It was believed this was caused by cross linking within the polymers due to them being left in an acidic dry state which has previously been found to lead to decomposition producing irreversible cross-linking.[151] Several attempts to synthesise polymers using the same reactants, ratios and methods were carried out; in most cases the AMPS polymers degraded the RAFT agent during the polymerisation. Polymers that could be processed and purified were taken forward for use in the synthesis of composites and are detailed in this chapter. Unsuccessful polymers that could not be purified were analysed as far as possible but not taken forward.

3.2 Experimental

3.2.1 Synthesis of 4-vinylbenzyl N-pyrrolecarbodithioate (VPC) RAFT agent

Sodium hydride (6.032 g, 0.2513 mol) in dry DMF (160 ml) was placed in a degassed flask to give a grey suspension. Pyrrole (10.016 g, 0.1492 mol) in dry DMF (20 ml) was added drop-wise over 30 minutes to give a yellow foam. The solution was stirred for 30 minutes at room temperature then cooled to 0 °C with an ice bath. Carbon disulfide (9 ml, 0.1489 mol) in dry DMF (20 ml) was added drop-wise over 10 minutes giving a dark red solution. The solution was stirred at room temperature for 30 minutes then cooled to 0 °C with an ice bath. 4-vinylbenzyl chloride (22.271 g, 0.1459 mol) in dry DMF (20 ml) was added drop-wise over 20 minutes giving a brown solution then the solution was stirred overnight at room temperature. The crude product was extracted using diethyl ether (80 ml) and water (80 ml). The mixture was placed in a separating funnel, the top organic layer was collected and the aqueous layer was washed three times with diethyl ether (3 × 100 ml). The organic extracts were combined, dried over magnesium sulfate and filtered. Diethyl ether was removed via rotary evaporation giving a crude product of a brown oil. The crude product was purified via column chromatography eluted with petroleum ether, the first band was collected and rotary evaporated to give a yellow solid (35.022 g, 0.1350 mol). 4-vinylbenzyl N-pyrrolecarbodithioate (VPC) is light sensitive, mildly air sensitive and degrades over time at room temperature, the purified product was therefore stored under nitrogen, wrapped in foil at -20 °C.

Elemental analysis: Expected: C, 64.83 %; H, 5.05 %; N, 5.40 %; S, 24.72 %. Found: C, 64.87 %; H, 5.06 %; N, 5.42 %; S, 24.65 %.

*Mass spectroscopy***:** Expected m/z: 259.3, experimental m/z: 259.0.

^{1}H NMR: (400 MHz, $CDCl_3$) δ ppm: 4.62 (s, 2H, SC**H₂**Ar), 5.29 (d, 1H, $\mathbf{H}_2$C=CHAr), 5.78 (d, 1H, $\mathbf{H}_2$C=CHAr), 6.37 (m, 2H, $N(CH)_2(C\mathbf{H})_2$), 6.75 (dd, 1H, $H_2C=C\mathbf{H}Ar$), 7.45 (m, 4H, $H_2C=CH\mathbf{Ar}$), 7.75 (m, 2H, $N(C\mathbf{H})_2(CH)_2$).

^{13}C NMR: (400 MHz, $CDCl_3$) δ ppm 41.50 ($\mathbf{C}H_2$), 114.37 ($H_2\mathbf{C}=CHBz$), 126.01 – 137.36 ($H_2C=\mathbf{C}HBz$, $H_2C=CH\mathbf{Bz}$ and C(S)**Py**, multiplet), 199.28 (S**C**(S)Py).

FTIR: ν_{max} / cm^{-1}: 3290 (Py N-C), 2980 (CH_2), 2930 (CH_2), 2150 and 1980 (N-C(=S)S), 1730 (C=S), 1630 (C=S), 1540 and 1460 ($H_2C=C$), 1290 (Py, C=C), 870 and 760 (aromatic), 1040 (S-C=S), 910 (Bz, C=C), 690 (C-S).

3.2.2 Synthesis of 4-vinylbenzyl dithiobenzoate (VDB) RAFT agent

Magnesium turnings (1.8003 g, 0.150 mol) were gently heated and stirred under nitrogen for 40 minutes. The flask was left to cool to room temperature, then bromobenzene (7 ml, 0.066 mol) in THF (40 ml) was added drop-wise over 30 minutes. The reaction was gently heated to instigate the exothermic reaction; the reaction was cooled using an ice bath as required. A grey solution was formed, which was left to stir for 30 minutes at room temperature. Carbon disulfide (4 ml, 0.066 mol) in THF (30 ml) was then added drop-wise over 10 minutes; a reaction colour change of grey to yellow to dark red was observed. The reaction mixture was cooled to 0 ˚C using an ice bath and stirred for 30 minutes. 4-vinylbenzyl chloride (9.5 ml, 0.067 mol) in THF (30 ml) was added drop-wise over 10 minutes, the solution was allowed to warm to room temperature then stirred overnight. The reaction mixture was quenched using distilled water (80 ml) then the organic product extracted using diethyl ether (80 ml). The solutions were separated and the aqueous layer was washed with diethyl ether (3 × 100 ml). The organic extracts were combined and dried over magnesium sulfate then filtered and the solvent removed by rotary evaporation giving a red oil. The crude product was purified by flash column chromatography eluting with ethyl acetate. The solvent was removed via rotary evaporation to give a red oil (10.21 g, 0.037 mol). 4-vinylbenzyl dithiobenzoate (VBD) is light sensitive, mildly air sensitive and degrades over time at room temperature, therefore, the purified product was stored under nitrogen, wrapped in foil at -20 °C.

Elemental analysis: Found: C, 70.99 %; H, 5.24 %; S, 23.77 %. Expected: C, 71.06 %; H, 5.22 %; S, 23.72 %.

Mass spectroscopy: Expected m/z: 270.4, experimental m/z: 270.1.

^{1}H NMR: (400 MHz, $CDCl_3$) δ ppm 4.62 (s, 2H, $SC\mathbf{H_2}Ar$), 5.30 (m, 1H, $CH=C\mathbf{H}_2$), 5.79 (m, 1H, $CH=C\mathbf{H}_2$), 6.75 (m, 1H, $C\mathbf{H}=CH_2$), 7.20-7.63 (m, 7H, Ar) 8.04 (m, 2H, Ar).

^{13}C NMR: (400 MHz, $CDCl_3$) δ ppm 42.24 ($\mathbf{C}H_2$), 114.40 ($H_2\mathbf{C}=CHBz$), 126.74 – 144.96 ($H_2C=CH\mathbf{Bz}$, $H_2C=\mathbf{C}HBz$ and $C(S)\mathbf{Bz}$, multiplet), 227.75 ($S\mathbf{C}(S)Bz$).

FTIR: ν_{max} / cm^{-1}: 2980 (CH_2), 1730 (C=S), 1550 – 1460, 870 and 760 (Bz, aromatic), 1510 ($H_2C=C$), 1040 (S-C=S), 680 (C-S).

3.2.3 Synthesis of branched acrylic acid polymers using reverse addition fragmentation chain transfer (RAFT) polymerisation

Acrylic acid (AA) was mixed with the required amount of RAFT agent and initiator (See table 3.1.) in dioxane (30 ml). The reaction mixture was then transferred to an ampoule (50 ml) and subjected to 4 freeze-pump-thaw cycles. The ampoule was flame sealed and placed in a water bath to react at 60 ˚C for 24 hours. The thickened mixture was removed from the ampoule and precipitated into diethyl ether (500 ml). The solvent was decanted off and the polymer was washed with diethyl ether (100 ml) then dissolved in water and freeze dried to give a flaky powder. Masses of the products along with the RAFT agent and initiator used are given in table 3.1.

Table 3.1. Masses of initiator, RAFT agent and monomer used to synthesise acrylic acid polymers using different initiators and RAFT agents.

Sample	Ratio AA:RAFT	AA / g	AIBN / g	ACVA / g	VPC / g	VDB / g
PAA-VPC-AIBN	25:1	8.664	0.192	---	1.184	---
PAA-VPC	25:1	8.523	---	0.330	1.177	---
PAA-VBD-AIBN	25:1	8.790	0.199	---	---	1.319
PAA-VBD	25:1	9.048	---	0.354	---	1.344

PAA-VPC-AIBN: ^{1}H NMR (400 MHz, DMSO) δ ppm 12.29 (s, 1H, COO**H**), 7.77 (s, 2H, Py), 7.29 (s, 2H, Bz), 7.06 (s, 2H, Bz), 6.48 (s, 2H, Py), 2.22 (s, 1H, C**H**COOH), 1.74 (s, 2H, C**H**$_2$CHCOOH), 1.51 (s, 2H, backbone). M$_W$ determined by SAXS: 1.11 x 10^7 Da.

PAA-VPC: ^{1}H NMR (400 MHz, DMSO) δ ppm 12.30 (s, 1H, COO**H**), 7.77 (s, 2H, Py), 7.28 (s, 2H, Bz), 7.06 (s, 2H, Bz), 6.48 (s, 2H, Py), 2.21 (s, 1H, C**H**COOH), 1.74 (s, 2H, C**H**$_2$CHCOOH), 1.51 (s, 2H, backbone). M$_W$ determined by SAXS: 6.29 x 10^6 Da.

PAA-VBD-AIBN: ^{1}H NMR (400 MHz, DMSO) δ ppm 12.29 (s, 1H, COO**H**), 7.93 – 7.09 (m, 9H, Bz), 2.21 (s, 1H, C**H**COOH), 1.76 (s, 2H, C**H**$_2$CHCOOH), 1.52 (s, 2H, backbone). M$_W$ determined by SAXS: 1.13 x 10^7 Da.

PAA-VBD: ^{1}H NMR (400 MHz, DMSO) δ ppm 12.29 (s, 1H, COO**H**), 7.94 – 7.09 (m, 9H, Bz), 2.21 (s, 1H, C**H**COOH), 1.74 (s, 2H, C**H**$_2$CHCOOH), 1.51 (s, 2H, backbone). M$_W$ determined by SAXS: 1.19 x 10^7 Da.

3.2.4 Synthesis of branched methacrylic acid polymers using reverse addition fragmentation chain transfer (RAFT) polymerisation

Distilled methacrylic acid (MAA) was mixed with the required amount of RAFT agent and initiator (See table 3.2.) in dioxane (30 ml). The reaction mixture was then transferred to an ampoule (50 ml) and subjected to 4 freeze-pump-thaw cycles. The ampoule was flame sealed and placed in a water bath to react at 60 ˚C for 24 hours. The thickened mixture was removed from the ampoule and precipitated into diethyl ether (500 ml). The solvent was decanted off and the polymer was washed with diethyl ether (100 ml) then dissolved in water and freeze dried to give a flaky powder which became sticky on contact with the air. Masses of the products are given in table 3.2. along with the RAFT agent and initiator used.

Table 3.2. Masses of initiator, RAFT agent and monomer used to synthesise methacrylic acid polymers using different initiators and RAFT agents.

Sample	Ratio MAA:RAFT	MAA / g	AIBN / g	ACVA / g	VPC / g	VDB / g
PMAA-VPC-AIBN	25:1	9.177	0.174	---	1.035	---
PMAA-VPC	25:1	4.400	---	0.149	0.504	---
PMAA-VBD-AIBN	25:1	9.172	0.173	---	---	1.199
PMAA-VBD	25:1	9.220	---	0.304	---	1.157

PMAA-VPC-AIBN: ^{1}H NMR (400 MHz, DMSO) δ ppm 12.34 (s, 1H, COO**H**), 7.79 (s, 2H, Py), 7.29 (s, 2H, Bz), 7.06 (s, 2H, Bz), 6.44 (s, 2H, Py), 1.69 (s, 1H, C**H**$_2$C(CH$_3$)COOH), 1.01 (s, 2H, backbone), 0.92 (s, 2H, C(C**H**$_3$)COOH). M$_W$ determined by SAXS: 1.22 x 10^7 Da.

PMAA-VPC: ^{1}H NMR (400 MHz, DMSO) δ ppm 12.36 (s, 1H, COO**H**), 7.79 (s, 2H, Py), 7.29 (s, 2H, Bz), 7.03 (s, 2H, Bz), 6.44 (s, 2H, Py), 1.69 (s, 1H, C**H**$_2$C(CH$_3$)COOH), 1.01 (s, 2H, backbone), 0.91 (s, 2H, C(C**H**$_3$)COOH). M$_W$ determined by SAXS: 1.80 x 10^7 Da.

PMAA-VBD-AIBN: ^{1}H NMR (400 MHz, DMSO) δ ppm 12.34 (s, 1H, COO**H**), 7.94 – 7.03 (m, 9H, Bz), 1.69 (s, 1H, C**H**$_2$C(CH$_3$)COOH), 1.02 (s, 2H, backbone), 0.92 (s, 2H, C(C**H**$_3$)COOH). M$_W$ determined by SAXS: 1.06 x 10^7 Da.

PMAA-VBD: ^{1}H NMR (400 MHz, DMSO) δ ppm 12.35 (s, 1H, COO**H**), 7.96 – 7.04 (m, 9H, Bz), 1.69 (s, 1H, C**H**$_2$C(CH$_3$)COOH), 1.01 (s, 2H, backbone), 0.91 (s, 2H, C(C**H**$_3$)COOH). M$_W$ determined by SAXS: 1.52 x 10^5 Da.

3.2.5 Synthesis of branched 2-acrylamido-2-methyl-1-propanesulfonic acid polymers using reverse addition fragmentation chain transfer (RAFT) polymerisation

2-Acrylamido-2-methyl-1-propanesulfonic acid (AMPS) was mixed with the required amount of RAFT agent and initiator (See table 3.3.) in DMSO (30 ml). The reaction mixture was then transferred to an ampoule (50 ml) and subjected to 4 freeze-pump-thaw cycles. The ampoule was flame sealed and placed in a water bath to react at 60 ˚C for 24 hours. The thickened mixture was removed from the ampoule and precipitated into acetone (500 ml). The solvent was decanted off and the polymer was washed with acetone (100 ml) then dissolved in water and freeze dried to give a flaky powder which became sticky on contact with the air. Masses of the products are given in table 3.3. along with the RAFT agent and initiator used.

Table 3.3. Masses of initiator, RAFT agent and monomer used to synthesise 2-Acrylamido-2-methyl-1-propanesulfonic acid polymers using different initiators and RAFT agents.

Sample	Ratio AMPS:RAFT	AMPS / g	AIBN / g	ACVA / g	VPC / g	VDB / g
PAMPS-VPC-AIBN	25:1	10.096	0.083	---	0.493	---
PAMPS-VPC	25:1	14.788	---	0.201	0.688	---
PAMPS-VBD-AIBN	25:1	10.046	0.081	---	---	0.520
PAMPS-VBD	25:1	9.692	---	0.134	---	0.498

PAMPS-VPC-AIBN: ^{1}H NMR (400 MHz, DMSO) δ ppm 8.46 and 6.39 (s, 4H, Py), 7.74 and 7.01 (s, 4H, Bz) 4.45 (s, 1H, CON**H**), 3.05 (m, 2H, C(CH$_3$)C**H$_2$**), 1.48 (m, 6H, C(C**H$_3$**)CH$_2$). M$_W$ could not be determined by SAXS or GPC due to insolubility.

PAMPS-VPC: ^{1}H NMR (400 MHz, DMSO) δ ppm 8.46 and 6.39 (s, 4H, Py), 7.74 and 7.01 (s, 4H, Bz) 5.71 (s, 1H, CON**H**), 3.25 (m, 2H, C(CH$_3$)C**H$_2$**), 1.53 (m, 6H, C(C**H$_3$**)CH$_2$). M$_W$ determined by SAXS: 5.34 x 10^6 Da**.**

PAMPS-VBD-AIBN: ^{1}H NMR (400 MHz, DMSO) δ ppm 8.46 – 7.13 (m, 9H, Bz), 4.51 (s, 1H, CON**H**), 3.05 (m, 2H, C(CH$_3$)C**H$_2$**), 1.48 (m, 6H, C(C**H$_3$**)CH$_2$). M$_W$ could not be determined by SAXS or GPC due to insolubility.

PAMPS-VBD: ^{1}H NMR (400 MHz, DMSO) δ ppm 8.46 – 7.13 (m, 9H, Bz), 5.71 (s, 1H, CON**H**), 3.25 (m, 2H, C(CH$_3$)C**H$_2$**), 1.45 (m, 6H, C(C**H$_3$**)CH$_2$). M$_W$ determined by SAXS: 1.59 x 10^6 Da.

3.3 Results and discussion

3.3.1 Synthesis of 4-vinylbenzyl N-pyrrolecarbodithioate RAFT agent

4-vinylbenzyl N-pyrrolecarbodithioate (VPC) was synthesised in a one pot procedure. First pyrrole reacted with sodium hydride in dry DMF, carbon disulfide was then added to yield sodium N-pyrrolecarbodithioate. 4-vinylbenzyl chloride was then added to form 4-vinylbenzyl N-pyrrolecarbodithioate. The synthetic scheme of this reaction is given below in figure 3.5.

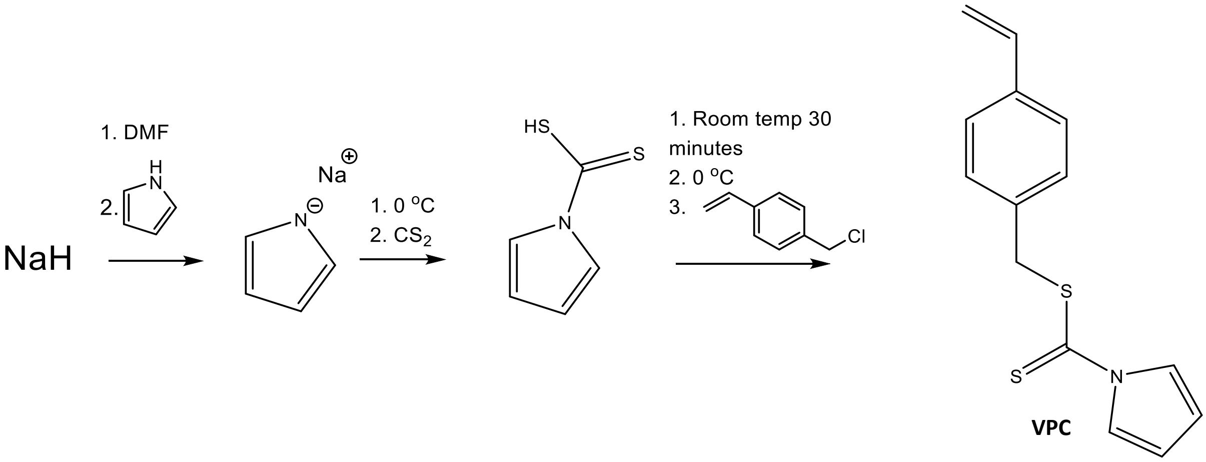

Figure 3.5. Schematic synthetic route for the synthesis of 4-vinylbenzyl N-pyrrolecarbodithioate (VPC).

Initial ^{1}H NMR spectra showed the inclusion of residual hexane from the purification of the product by column chromatography. As a result, the product was dried thoroughly *in vacuo* and reanalysed by ^{1}H NMR which showed no residual hexane. Further analysis by ^{13}C NMR, FTIR, elemental analysis and mass spectrometry proved that the yellow solid was pure VPC. The purified product was then used as a RAFT agent for the synthesis of polymers of acrylic acid, methacrylic acid and 2-acrylamido-2-methyl-1-propanesulfonic acid polymers via RAFT polymerisation.

3.3.2 Synthesis of 4-vinylbenzyl dithiobenzoate RAFT agent

4-vinylbenzyl dithiobenzoate (VBD) was synthesised in a one pot procedure. First magnesium turnings were heated slightly under a nitrogen atmosphere to activate the surface before bromobenzene in THF was added. Carbon disulfide was added to form dithiobenzoate, then 4-vinylbenzyl chloride was introduced to form 4-vinylbenzyl dithiobenzoate. The synthetic scheme of this reaction is given below in figure 3.6. Initial ^{1}H NMR spectra showed the inclusion of residual ethyl acetate from the purification of the product by column chromatography. As a result, the product was dried thoroughly *in vacuo* and reanalysed by ^{1}H NMR which showed no residual ethyl acetate. Further analysis by ^{13}C NMR, FTIR, elemental analysis and mass spectrometry proved that the orange / red oil was pure VBD. The purified product was then used as a RAFT agent for the synthesis of polymers of acrylic acid, methacrylic acid and 2-acrylamido-2-methyl-1-propanesulfonic acid polymers via RAFT polymerisation.

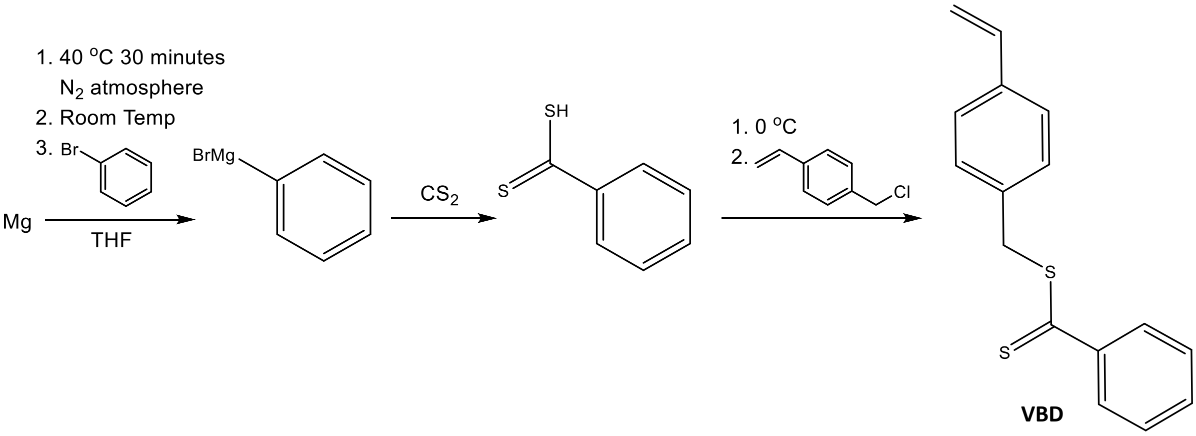

Figure 3.6. Schematic synthetic route for the synthesis of 4-vinylbenzyl dithiobenzoate (VBD).

3.3.3 Branched polymers via RAFT polymerisation

3.3.3.1 Poly(acrylic acid)

Branched poly(acrylic acid) (PAA) was synthesised using two different RAFT agents: 4-vinylbenzyl N-pyrrole carbodithioate (VPC) and 4-vinylbenzyl dithiobenzoate (VDB), and two different initiators: azobisisobutyronitrile (AIBN) and 4-azobiscyanovaleric acid (ACVA). The percentage weight yield of polymer obtained using ACVA as the initiator was greater in all cases than those initiated by AIBN. This was anticipated as the functional side groups of the ACVA initiator are more hydrophilic than those of AIBN, hence the ACVA is partly solubilised by the monomer producing a more favourable reaction. Analysis by ^{1}H NMR spectroscopy gave a degree of branching (DB) of between 2 and 6 as shown in table 3.4 below.

The degree of branching appeared to be reduced by the use of ACVA and VDB. However, the variance in the range of degree of branching is small suggesting that the difference is negligible.

Table 3.4. Percentage yield, degree of branching (DB) and colour of poly(acrylic acid) polymers synthesised using the RAFT agents VPC and VBD and initiators AIBN and ACVA.

Sample	RAFT / initiator	Percentage yield / %	DB / %	Product colour
PAA-VPC-AIBN	VPC / AIBN	75	6	Yellow
PAA-VPC	VPC / ACVA	86	5	Yellow
PAA-VBD-AIBN	VBD / AIBN	87	4	Orange/ pink
PAA-VBD	VBD / ACVA	93	2	Orange/ pink

The use of VPC as a RAFT agent produced polymers with a strong yellow colour while using VDB produced polymers with an orange/pink colour. ^{1}H NMR analysis also showed the presence of aromatic peaks between 7.94 – 6.48 ppm in all samples, showing the incorporation of the RAFT agent into the polymer, as expected from the colour of the samples. The choice of RAFT agent is important to allow control over the polymerisation. Vinyl acids are very active monomers and can self-polymerise under relatively mild conditions without an initiator. Acrylic acids are particularly difficult to polymerise by RAFT due to their ability to form a stable radical adduct which requires a strong chain transfer agent (CTA) to allow polymerisation. As such it is important to use a RAFT agent with a high chain transfer coefficient such as VPC or VBD.[60, 64, 68, 152, 153] Previous attempts to synthesise PAA by RAFT used a trithiocarbonate CTA to create low molecular weight PAAs with low dispersities.[151, 154] These studies determined that RAFT polymerisation of AA is hindered by transfer to solvent issues at high conversion and as such, low molecular weights should be targeted.

GPC analysis of the PAA polymers was not possible. Polyanions are especially difficult to analyse due to their affinity for charged surfaces;[155] as such, the use of GPC to analyse the poly(acrylic acid) samples alone was not possible, therefore the polymers were modified by methylation using trimethylsilyldiazomethane to cap the acidic end groups for size exclusion chromatography[156, 157]. However, the methylation caused the polymers to become insoluble in all solvents. It is believed this was due to the polymer crosslinking during methylation due to the presence of acidic and RAFT end groups which could have reacted via a radical pathway as has been reported previously.[151] Therefore, different methods were used to analyse the molecular weight of these polymers by indirect analysis to find the radius of gyration (R_g) and hence determine the molecular weight of the polymers.

Small angle x-ray scattering (SAXS) measurements at 1 wt% in THF determined that the PAAs had molecular weights upwards of 1 x 10^7 Da apart from PAA-VPC (ACVA) which had a molecular weight of 6.29 x 10^6 Da. These polymers are extremely large and therefore it is not surprising that they were insoluble in some solvents.

3.3.3.2 Poly(methacrylic acid)

Samples of branched poly(methacrylic acid) (PMAA) were also synthesised using VPC, VBD, ACVA and AIBN. Analysis of the polymers by ^{1}H NMR showed the presence of aromatic peaks between 7.94 – 6.48 ppm indicating that the RAFT agent was incorporated into the polymer in all cases. The degree of branching calculated ranged from 3 to 7 (table 3.5) which was slightly higher than the PAA polymers synthesised via the same method.

Table 3.5. Mass, degree of branching (DB) and colour of poly(methacrylic acid) polymers synthesised using the RAFT agents VPC and VBD and initiators AIBN and ACVA.

Sample	RAFT / initiator	Percentage yield / %	DB / %	Product colour
PMAA-VPC-AIBN	VPC / AIBN	87	7	Yellow
PMAA-VPC	VPC / ACVA	81	5	Yellow
PMAA-VBD-AIBN	VBD / AIBN	36	4	Orange/ pink
PMAA-VBD	VBD / ACVA	70	3	Orange/ pink

As with the PAA polymers described previously the samples synthesised using VPC as a RAFT agent showed a slightly higher degree of branching than those produced with VDB, but the variances between the degrees of branching of the samples are so low it was deemed that the difference was negligible. However, interestingly there was a marked difference between the synthesis of PAA and PMAA using AIBN and VBD. The percentage yield of PMAA-VBD-AIBN was extremely low compared to the other PMAA samples, although the PMAA-VBD sample prepare with ACVA also produced a smaller percentage yield than samples made with VPC. The synthesis was repeated several times and the same effect was seen in all cases. It is believed this was due to the MAA monomer being slightly bulkier than the PAA monomer; the additional methyl group may have prevented the slightly bulkier Z group of the VBD from polymerising the PMAA monomer. It is also possible that using AIBN as an initiator may have caused the low percentage yield due to the dissimilar functional side groups of the AIBN and MAA monomer causing an unfavourable polymerisation environment. Methylation of the polymers to allow GPC again caused the polymers to become insoluble in all solvents. As with the PAA samples it is believed this was due to the polymer crosslinking during methylation.

3.3.3.3 Poly(2-Acrylamido-2-methyl-1-propanesulfonic acid)

Branched 2-acrylamido-2-methyl-1-propanesulfonic acid polymers (PAMPS) were synthesised using VPC or VDB as RAFT agents, and AIBN or ACVA as initiators. The reactions yielded very small amounts of polymer; however, the degree of branching was much higher (as shown in table 3.6) than the PAA and PMAA samples made with the same ratio of monomer to RAFT agent.

Table 3.6. Mass, degree of branching (DB) and colour of poly(2-acrylamido-2-methyl-1-propanesulfonic acid) polymers synthesised using the RAFT agents VPC and VBD and initiators AIBN and ACVA.

Sample	RAFT / initiator	Percentage yield / %	DB / %	Product colour
PAMPS-VPC-AIBN	VPC / AIBN	36	21	Yellow
PAMPS-VPC	VPC / ACVA	47	15	Yellow
PAMPS-VBD-AIBN	VBD / AIBN	6	14	Orange/ pink
PAMPS-VBD	VBD / ACVA	27	12	Orange/ pink

As well as low percentage yields of polymer, analysis via ^{1}H NMR showed very low monomer to polymer conversions (table 3.7). The low yields and conversions of these reactions, along with the fact that the polymerisation mixtures turned brown or pale orange in the cases of VPC and VBD respectively, indicate that this was due to the strong acidity of the monomer causing the RAFT agent to degrade, hence preventing RAFT polymerisation from occurring. However, this should have left chain transfer radicals and initiator within the reaction solution which should have maintained uncontrolled radical polymerisation. As such it is likely that the destruction of the RAFT agent was not the cause of the low conversions.

Table 3.7. Percentage conversion of monomer to polymer calculated from NMR spectroscopy of a crude sample of polymer solution prior to precipitation.

RAFT agent	4-vinylbenzyl N-pyrrolecarbodithioate			4-vinylbenzyl dithiobenzoate		
Polymer	PAA	PMAA	PAMPS	PAA	PMAA	PAMPS
AIBN	74.6	81.4	25.7	73.6	32.4	3.8
ACVA	85.7	86.4	35.1	77.4	62.4	16.0

Recently the synthesis of linear block copolymers of AMPS have been reported using 2-dodecylsulfanylthiocarbonylsulfanyl-2-methyl propionic acid as a chain transfer agent.[158] The polymerisation was conducted in DMF as opposed to DMSO which was used to synthesise the AMPS polymers in this chapter. As both solvents are polar aprotic and miscible with water, it is not immediately obvious why the use of either of these solvents could affect the polymerisation of AMPS. However, DMSO can act as a mild oxidising agent which has an adverse effect on polymerisations.[159] As such it is likely that the use of DMSO as a reaction solvent was the cause of the low conversions of the AMPS polymers as opposed to the destruction of the RAFT agent.

As with the PMAA samples, the combination of monomer, AIBN and VBD produced the lowest percentage yield. AMPS is a much bulkier monomer than MAA and both are bulkier than AA, hence adding weight to the suggestion that the larger monomer molecules were hindered from interacting with the initiator and RAFT agent. The geminal dimethyl and sulfomethyl groups of the AMPS monomer cause steric hindrance to the amide group. [160-162] This makes the AMPS radical very large which will affect its ability to polymerise with chain transfer agents unless they are highly active. Another factor that makes the polymerisation of acidic monomers such as AMPS, AA and MAA difficult is that their respective radicals upon initiation are extremely reactive. This means that in order to carry out a successful RAFT polymerisation of these monomers, the synthesis would require a highly active RAFT agent to prevent uncontrolled homopolymerisation. Evidence from the literature suggests that the synthesis of acidic polymers is generally most successful when performed indirectly using protected monomers which are subsequently functionalised; for example tert-butyl acrylate deprotected with trifluoroacetic acid to form PAA.[163] The RAFT agents VPC and VBD would be suitable for polymerisations with the protected monomers; however, their use for the synthesis of acidic polymers by RAFT will always be hindered by the lack of reactivity in comparison to the acidic monomer radicals.[69]

^{1}H NMR analysis was used to provide a percentage conversion of monomer to polymer for all the polymers discussed in this chapter (table 3.7). The first point to notice is that the percentage conversion for the PAMPS samples is extremely low in all cases with the lowest conversion of 3.8 % being attributed to the combination of AMPS, AIBN and VBD. It is likely that the reason for the low percentage conversion and yield of the AMPS polymers is due to the acidity of the monomer causing the degradation of the RAFT agents during the polymerisation along with oxidation caused by the reaction solvent DMSO. As a result of this, no further AMPS polymers were synthesised but those that had been produced (see table 3.6) were taken forward to create composite particles as detailed in chapters 4 and 5.

In contrast to the AMPS polymers, polymers synthesised using AA and MAA responded well to VPC as shown by the high percentage conversions in each case. Interestingly the use of VBD lead to high percentage conversion and yield for PAA, yet the percentage conversion and yield for the PMAA was much lower when the reaction used AIBN as an initiator. This is the same trend seen with the percentage yields of the polymers stated earlier in the chapter. It is likely that this trend is due to the Z group of the RAFT agent which is not a strong enough radical to react with the AMPS or MAA radical and therefore prevents the progression of the polymerisations with AIBN and VBD. This suggests that VPC and VBD are not the optimal RAFT agents for synthesising AMPS polymers and VBD is not a suitable RAFT agent to synthesise PMAA. However, both VPC and VBD are suitable to produce PAA by RAFT polymerisation.

The AMPS monomer was particularly difficult to polymerise and process, four samples were successfully synthesised; however, after synthesis of PAMPS-VPC-AIBN, PAMPS-VPC, PAMPS-VBD-AIBN and PAMPS-VBD numerous attempts were made to repeat these polymerisations and all further attempts failed for various reasons. The main issues experienced were: the polymers gelled; the RAFT agent was destroyed by the monomer; and in some cases the polymers would not precipitate even with highly concentrated polymerisation mixtures. This resulted in the synthesis of PAMPS eventually being abandoned following the carousel reactions described in Chapter 4.

3.4 Conclusion

RAFT polymerisation was used to attempt to synthesise polymers of acrylic acid, methacrylic acid and 2-Acrylamido-2-methyl-1-propanesulfonic acid using two RAFT agents: 4-vinylbenzyl N-pyrrolecarbodithioate and 4-vinylbenzyl dithiobenzoate. The synthesis of PAA was successful with both RAFT agents, while the synthesis of PMAA was less successful using VBD and the AMPS polymers appeared to degrade both RAFT agents. This lead to the conclusion that RAFT polymerisation using VPC and VBD is not optimal for MAA and AMPS monomers and would require a more active RAFT agent such as a trithiocarbonate compound in future.[68-

[70, 81] However, the fact that DMSO was used as a polymerisation solvent and has been reported to act as a mild oxidising agent with adverse effects on polymerisations means there is a possibility that the AMPS polymers were unsuccessful due to the presence of oxygen in the reaction .[159] Hence, it is possible that the use of DMSO as a reaction solvent, rather than the destruction of the RAFT agent, was the cause of the low conversions of the AMPS polymers.

Some polymers were successfully synthesised using each monomer and carried forward to create composite materials. The successful polymers formed powders or solids which were water soluble making them useful for composite synthesis while those polymers that were unsuccessful were sticky and unmanageable. The unsuccessful polymers were insoluble in all solvents and could not be analysed; for this reason, it was decided they should be discarded in favour of the soluble polymers.

Analysis of the polymers by THF GPC was impossible as methylation of the polymers caused them to become insoluble in all solvents, it is likely that this was caused by radical crosslinking due to residual RAFT end groups during the methylation reaction. Analysis by ^{1}H NMR was conducted and showed that polymerisations of different conversions were successful in all cases. The degree of branching was calculated for each polymer and it was determined that the AMPS polymers produced the highest degree of branching with the lowest polymer conversion. The PAA and PMAA polymers produced the highest yields and percentage conversions and were deemed to be the most promising samples moving forward to the synthesis of composite materials.

3.5 References

1. J. Loiseau, N. Doerr, J. M. Suau, J. B. Egraz, M. F. Llauro and C. Ladaviere, *Macromolecules*, 2003, **36**, 3066-3077.
2. S. Carter, B. Hunt and S. Rimmer, *Macromolecules*, 2005, **38**, 4595-4603.
3. D. J. Keddie, *Chemical Society Reviews*, 2014, **43**, 496-505.
4. M. Benaglia, J. Chiefari, Y. K. Chong, G. Moad, E. Rizzardo and S. H. Thang, *Journal of the American Chemical Society*, 2009, **131**, 6914.
5. G. Moad, E. Bicciocchi, M. Chen, J. Chiefari, C. Guerrero-Sanchez, M. Haeussler, S. Houshyar, D. Keddie, E. Rizzardo, S. H. Thang and J. Tsanaktsidis, in *Progress in*

Controlled Radical Polymerization: Mechanisms and Techniques, eds. K. Matyjaszewski, B. S. Sumerlin and N. V. Tsarevsky, 2012, vol. 1100, pp. 243-258.

6. G. Moad, E. Rizzardo and S. H. Thang, in *Fundamentals of Controlled/Living Radical Polymerization*, The Royal Society of Chemistry, 2013, pp. 205-249.
7. G. Moad, E. Rizzardo and S. H. Thang, *Chemistry-an Asian Journal*, 2013, **8**, 1634-1644.
8. M. F. Llauro, J. Loiseau, F. Boisson, F. Delolme, C. Ladaviere and J. Claverie, *Journal of Polymer Science Part a-Polymer Chemistry*, 2004, **42**, 5439-5462.
9. V. Nikolaou, A. Simula, M. Droesbeke, N. Risangud, A. Anastasaki, K. Kempe, P. Wilson and D. M. Haddleton, *Polymer Chemistry*, 2016, **7**, 2452-2456.
10. E. Kuhnel, D. D. P. Laffan, G. C. Lloyd-Jones, T. Martinez Del Campo, I. R. Shepperson and J. L. Slaughter, *Angewandte Chemie (International ed. in English)*, 2007, **46**, 7075-7078.
11. L. Couvreur, C. Lefay, J. Belleney, B. Charleux, O. Guerret and S. Magnet, *Macromolecules*, 2003, **36**, 8260-8267.
12. W. M. Wan, P. D. Pickett, D. A. Savin and C. L. McCormick, *Polymer Chemistry*, 2014, **5**, 819-827.
13. W. W. Epstein and F. W. Sweat, *Chemical Reviews*, 1967, **67**, 247-260.
14. W. O. Parker and A. Lezzi, *Polymer*, 1993, **34**, 4913-4918.
15. Y. A. Aggour, *Polymer Degradation and Stability*, 1994, **45**, 273-276.
16. Y. A. Aggour, *Polymer Degradation and Stability*, 1994, **44**, 71-73.
17. R. McHale, F. Aldabbagh, W. M. Carroll and B. Yamada, *Macromolecular Chemistry and Physics*, 2005, **206**, 2054-2066.
18. D. J. Keddie, G. Moad, E. Rizzardo and S. H. Thang, *Macromolecules*, 2012, **45**, 5321-5342.
19. J. A. Alfurhood, P. R. Bachler and B. S. Sumerlin, *Polymer Chemistry*, 2016, **7**, 3361-3369.
20. E. Bicciocchi, Y. K. Chong, L. Giorgini, G. Moad, E. Rizzardo and S. H. Thang, *Macromolecular Chemistry and Physics*, 2010, **211**, 529-538.

Chapter 4 – Synthesis and characterisation of (fluor)hydroxyapatite nanoparticles with highly branched poly((meth)acrylic acid)s via the Prakash and Chen methods

4.1 Chapter Summary

This chapter explains the initial steps taken to form composite materials. The main objectives were to use the polymers discussed in chapter 3 either in the synthesis of hydroxyapatite (HA) and fluorapatite (FA) or as two separately synthesised entities to create coated HA or FA nanoparticles. Attempts were also made to form a polymer coating *in situ* by incorporating HA nanoparticles into small scale polymerisations.

A carousel reactor was chosen as a vessel to conduct small scale investigations into the merits of these different techniques. The carousel was chosen as it meant that up to 12 reactions could be conducted simultaneously under identical conditions to allow different polymer formulations to be utilised. The carousel reactions undertaken consisted of two main categories: 1) pre-synthesised HA particles in a polymerisation reaction and 2) pre-synthesised HA nanoparticles mixing with pre-synthesised polymers in solution. During these experiments, acidity levels became an issue hence a more acid stable analogue of HA, fluorapatite (FA) ($Ca_{10}(PO_4)_6F_2$) was synthesised and utilised to determine the viability of these methods.

The modified Prakash method,[1] developed by Caroline Wilcock, was used to synthesise HA nanoparticles as this method has been used very successfully to produce uniform HA particles in a variety of conditions. The Chen method was used to synthesise FA particles to test acid stability and hence the viability of the carousel reactions.[2]

The Prakash method was subsequently modified further by adding polymers directly to the synthesis of HA particles. This was in order to test whether a coating could be formed *in situ* and to determine the effect if any that the polymer would have on the crystal formation of HA nanoparticles. The particles were fully characterised using Fourier Transform Infrared spectroscopy (FTIR), x-ray diffraction (XRD), thermogravimetric analysis (TGA) and transmission electron microscopy (TEM).

Slight changes in particle size and morphology were observed and the inclusion of polymer in the synthesis of HA proved to have an interesting effect on the particles during characterisation. Analysis of the carousel reactions was extremely difficult and after some initial testing this method was abandoned in favour of single reactions which could be repeated, purified and analysed fully.

4.2 Experimental

4.2.1 Synthesis of hydroxyapatite nanoparticles via the Prakash method[1]

Calcium hydroxide ($Ca(OH)_2$, 1.85 g, 25 mmol) was suspended in distilled water (250 ml) on a stirrer hotplate at 400 rpm and stirred for 1 hour at 90 °C. Phosphoric acid (H_3PO_4, (1.73 g, 15 mmol) Sigma Aldrich) was dissolved in distilled water (250 ml). The phosphoric acid solution was added to the stirring calcium solution in one rapid pouring motion. The solution was stirred for 1 hour and then left to cool to room temperature overnight. The precipitate which had settled overnight was washed by decanting the clear liquid on top of the sediment and adding distilled water (500 ml). This was followed by stirring at 400 rpm for 1 minute and allowing the precipitate to settle over 2 hours. The washing procedure was repeated three times. The suspension was then dried at 60 °C in an oven, ground to a powder in an agate pestle and mortar, and half of the sample was sintered. The furnace (Lenton Thermal Designs UAF 15/5) was programmed to heat at 10 °C min^{-1} and then to maintain a temperature of 1000 °C for 2 hours before cooling to room temperature overnight. The powder was then stored in a vacuum desiccator.

4.2.2 Addition of hydroxyapatite nanoparticles during synthesis of branched polymers - carousel

Medical grade microparticles or nanoparticles of hydroxyapatite (approximately 0.01 g, 0.02 mmol) were placed in a carousel tube along with a mixture of initiator/monomer/RAFT agent in a suitable solvent (10 ml) (see table 4.1). The initiator used was 4,4'-azobis(4-cyanovaleric) acid (ACVA); the monomers used were acrylic acid (AA), methacrylic acid (MAA) and 2-acrylamido-2-methylpropanesulfonic acid (AMPS) and the RAFT agents used were 4-vinylbenzyl pyrrolecarbodithioate (VPC) and 4-vinylbenzyl dithiobenzoate (VBD). The reaction mixtures were placed in a carousel reactor and reacted for 24 hours at 60 °C under a nitrogen atmosphere. The resulting solutions were analysed using dynamic light scattering to

Table 4.1. Masses of Initiator, monomer and RAFT agent used in a carousel reaction to synthesise polymers around hydroxyapatite microparticles and nanoparticles.

Sample	ACVA / g	VPC / g	VDB / g	AA / g	MAA / g	AMPS / g	Solvent
AA/VPC/m	0.030	0.116	---	0.858	---	---	Dioxane
AA/VBD/m	0.034	---	0.124	0.846	---	---	Dioxane
MAA/VPC/m	0.029	0.104	---	---	0.882	---	Dioxane
MAA/VBD/m	0.029	---	0.108	---	0.871	---	Dioxane
AMPS/VPC/m	0.013	0.045	---	---	---	0.985	DMSO
AMPS/VBD/m	0.013	---	0.050	---	---	0.944	DMSO
AA/VPC/n	0.033	0.119	---	0.856	---	---	Dioxane
AA/VBD/n	0.033	---	0.131	0.845	---	---	Dioxane
MAA/VPC/n	0.029	0.106	---	---	0.874	---	Dioxane
MAA/VBD/n	0.029	---	0.110	---	0.870	---	Dioxane
AMPS/VPC/n	0.014	0.048	---	---	---	0.987	DMSO
AMPS/VBD/n	0.013	---	0.049	---	---	0.948	DMSO

determine the particle sizes, which were compared against samples of pure micro or nano hydroxyapatite in a suitable solvent.

4.2.3 Combination of hydroxyapatite nanoparticles with branched polymers

Medical grade microparticles or nanoparticles of hydroxyapatite was placed in a carousel tube along with a branched polymer, the synthesis of which was described in chapter 3, in a weight ratio of approximately 1:20, dissolved in a suitable solvent (4 ml) (see table 4.2).

Table 4.2. Masses of polymers and HA particles used to attempt to create a polymer coating around the HA micro- and nanoparticles in a 1:20 ratio of HA : polymer

Sample	Polymer	MicroHA / g	NanoHA / g	Polymer / g	Solvent
PAA-VPC/m	PAA-VPC	0.009	---	0.204	THF
PAA-VPC/n	PAA-VPC	---	0.010	0.205	THF
PMAA-VPC/m	PMAA-VPC	0.010	---	0.203	DMF
PMAA-VPC/n	PMAA-VPC	---	0.010	0.207	DMF
PAMPS-VPC/m	PAMPS-VPC	0.010	---	0.206	DMF
PAMPS-VPC/n	PAMPS-VPC	---	0.012	0.208	DMF
PAA-VBD/m	PAA-VBD	0.010	---	0.209	THF
PAA-VBD/n	PAA-VBD	---	0.010	0.206	THF
PMAA-VBD/m	PMAA-VBD	0.010	---	0.209	DMF
PMAA-VPC/n	PMAA-VBD	---	0.010	0.202	DMF
PAMPS-VBD/m	PAMPS-VBD	0.009	---	0.210	DMF
PAMPS-VBD/n	PAMPS-VBD	---	0.010	0.210	DMF

The reaction mixtures were placed in a carousel reactor and stirred for 24 hours at room temperature under a nitrogen atmosphere. The resulting solutions were analysed using dynamic light scattering to determine the particle sizes, which were compared against samples of pure hydroxyapatite in a suitable solvent. A second experiment using a weight ratio of HA to polymer of 1:2 was also conducted in a suitable solvent (4 ml) (See table 4.3).

Table 4.3. Masses of polymers and HA particles used to attempt to create a polymer coating around the HA micro- and nanoparticles in a 1:2 weight ratio of HA : polymer.

Sample	Polymer	MicroHA / g	NanoHA / g	Polymer / g	Solvent
m/PAA-VPC2	PAA-VPC	0.015	---	0.021	THF
m/PMAA-VPC2	PMAA-VPC	0.011	---	0.019	DMF
m/PAMPS-VPC2	PAMPS-VPC	0.010	---	0.018	DMF
m/PAA-VBD2	PAA-VBD	0.011	---	0.019	THF
m/PMAA-VBD2	PMAA-VBD	0.010	---	0.019	DMF
m/PAMPS-VBD2	PAMPS-VBD	0.010	---	0.019	DMF
n/PAA-VPC2	PAA-VPC	---	0.011	0.018	THF
n/PMAA-VPC2	PMAA-VPC	---	0.010	0.019	DMF
n/PAMPS-VPC2	PAMPS-VPC	---	0.010	0.018	DMF
n/PAA-VBD2	PAA-VBD	---	0.009	0.020	THF
n/PMAA-VBD2	PMAA-VBD	---	0.010	0.019	DMF
n/PAMPS-VBD2	PAMPS-VBD	---	0.010	0.019	DMF

The reaction mixtures were placed in a carousel reactor and stirred for 24 hours at room temperature under a nitrogen atmosphere. The resulting solutions were analysed using dynamic light scattering to determine the particle sizes, which were compared against samples of pure hydroxyapatite in a suitable solvent.

4.2.4 Synthesis of fluorapatite nanoparticles via the Chen method[2]

$$5Ca(NO_3)_{2\,(aq)} + 3(NH_4)_2HPO_{4\,(aq)} + NH_4F_{(aq)} + 3NH_4OH_{(aq)} \longrightarrow Ca_5(PO_4)_3F_{(s)} + 10NH_4NO_{3\,(aq)} + 3H_2O_{\,(l)}$$

Calcium nitrate (11.79 g, 50 mmol, Sigma Aldrich) was dissolved in distilled water (500 ml) and the pH adjusted to 11 via the drop-wise addition of ammonium solution. Diammonium hydrogen phosphate (3.98 g, 30 mmol, Sigma Aldrich) and ammonium fluoride (0.38 g, 10 mmol, Sigma Aldrich) were dissolved separately in distilled water (250 ml). The pH of both solutions was then adjusted to 10 via drop-wise addition of ammonium solution. The three solutions were then combined to give a white precipitate and stirred for 1 hour (combination gave a pH reading of 10.2) then left to settle over night at room temperature. The precipitate was then washed three times by pouring off the clear liquid on top of the precipitate and adding distilled water. Conductivity measurements were taken between washes and decreased after every wash suggesting that the free ion impurities in the solution were being removed. The conductivity measurement settled at 1.44 mScm^{-1} between the second and third washes and did not change after this. The precipitate was then dried in an oven at 60 °C overnight and then ground to a powder using an agate pestle and mortar. Half the sample was then sintered (Lenton Thermal Designs UAF 15/5). The furnace was programmed to heat at 10 °C/min and then to maintain a temperature of 700 °C for 2 hours before cooling to room temperature overnight. The powder was then stored in a vacuum desiccator. Transmission electron microscopy (TEM), fourier-transform infrared spectroscopy (FTIR) and X-ray diffraction (XRD) studies were conducted on both the unsintered and sintered samples.

4.2.5 Combination of fluorapatite nanoparticles with branched polymers

Fluorapatite (FA) was placed in a carousel tube along with a branched polymer, in a weight ratio of approximately 1:2, dissolved in a suitable solvent (4 ml) (see table 4.4). The reaction mixtures were placed in a carousel reactor and stirred for 24 hours at room temperature under a nitrogen atmosphere. The resulting solutions were analysed using dynamic light scattering to determine the particle sizes.

Table 4.4. Masses of polymers and FA particles used to attempt to create a polymer coating around the FA nanoparticles in a 1:2 ratio of FA : polymer. NanoFA (THF)and NanoFA (DMF) are control samples to allow comparison of treated and untreated FA nanoparticles in different solvents.

Sample	Polymer	NanoFA / g	Polymer / g	Solvent
F/PAA-VPC	PAA-VPC	0.011	0.022	THF
F/PMAA-VPC	PMAA-VPC	0.010	0.020	DMF
F/PAMPS-VPC	PAMPS-VPC	0.011	0.020	DMF
F/PAA-VBD	PAA-VBD	0.011	0.020	THF
F/PMAA-VBD	PMAA-VBD	0.011	0.024	DMF
F/PAMPS-VBD	PAMPS-VBD	0.011	0.022	DMF
NanoFA (THF)	---	0.011	---	THF
NanoFA (DMF)	---	0.011	---	DMF

4.2.6 Synthesis of hydroxyapatite nanoparticles with 1 wt% branched polymer additives via the modified Prakash method[1]

Synthesis was carried out in the same manner for all samples, see table 4.5 for masses of reactants. Calcium hydroxide ($Ca(OH)_2$, (50 mmol) Sigma Aldrich) was suspended in distilled water (250 ml) on a stirrer hotplate at 400 rpm and stirred for 1 hour at 90 °C. Phosphoric acid (H_3PO_4, (30 mmol) Sigma Aldrich) was dissolved in distilled water (250 ml) with 1 wt% of branched polymer (0.07 g). The phosphoric acid solution was added to the stirring calcium solution in one rapid pouring motion. The solution was stirred for 1 hour and then left to cool to room temperature and age overnight. The settled precipitate was washed by decanting the clear liquid on top of the sediment and adding distilled water (500 ml). This was followed by stirring at 400 rpm for 1 minute and allowing the precipitate to settle over 2 hours. This washing procedure was repeated three times. The suspension was then dried in a 60 °C oven, ground to a powder in an agate pestle and mortar and stored in a vacuum desiccator prior to analysis. Analysis of the samples was conducted using Fourier Transform Infrared Spectroscopy (FTIR), X-ray Diffraction (XRD), Thermogravimetric Analysis (TGA) and Transmission Electron Microscopy (TEM). Details of the experimental procedure for these techniques can be found in Chapter 2.

Table 4.5. Masses used in the synthesis of HA with 1 wt% branched polymer using the modified Prakash method.

Sample	$Ca(OH)_2$ / g	H_3PO_4 / g	Polymer / g
HA + 1 wt% PAA-VPC	3.707	3.451	0.069
HA + 1 wt% PAA-VBD	3.710	3.460	0.070
HA + 1 wt% PMAA-VPC	3.707	3.465	0.072
HA + 1 wt% PMAA-VBD	3.702	3.520	0.079

4.3 Results and Discussion

4.3.1 Synthesis of hydroxyapatite nanoparticles via the Prakash method[1]

Hydroxyapatite nanoparticles were synthesised using a variation on the Prakash suspension method[1] developed by Caroline Wilcock as described in section 4.2.1 of this chapter. TEM imaging and FTIR analysis were used to determine the size of the particles and assess whether hydroxyapatite had been synthesised. Visual inspection of the ceramic showed a dirty pale pink coloured solid after drying; when ground this became a cream coloured powder. Sintering the sample produced a white powder; the colour change during sintering was deemed unusual. Transmission electron microscopy (TEM) and fourier-transform infrared spectroscopy (FTIR) studies were conducted on both the unsintered and sintered samples to determine why the colour change occurred. FTIR analysis shown in figure 4.1 indicated that the sample may have degraded during the sintering process. The unsintered sample shows peaks from 3700 – 2660 cm^{-1} and 1640 cm^{-1}, corresponding to adsorbed water; peaks at 1440 cm^{-1} and 870 cm^{-1} correspond to CO_3^{2-} caused by absorption of carbon dioxide from the air; while the peaks at 1080 cm^{-1}, 1000 cm^{-1} and 960 cm^{-1} are due to the PO_4^{3-} group. The sintered sample shows peaks at 1085 cm^{-1}, 1020 cm^{-1} and 960 cm^{-1} which correspond to the PO_4^{3-} group. The lack of peaks in the regions of 3700 – 2660 cm^{-1} and 1650 – 1400 cm^{-1} shows that the adsorbed carbon dioxide and water was removed during the sintering process while the

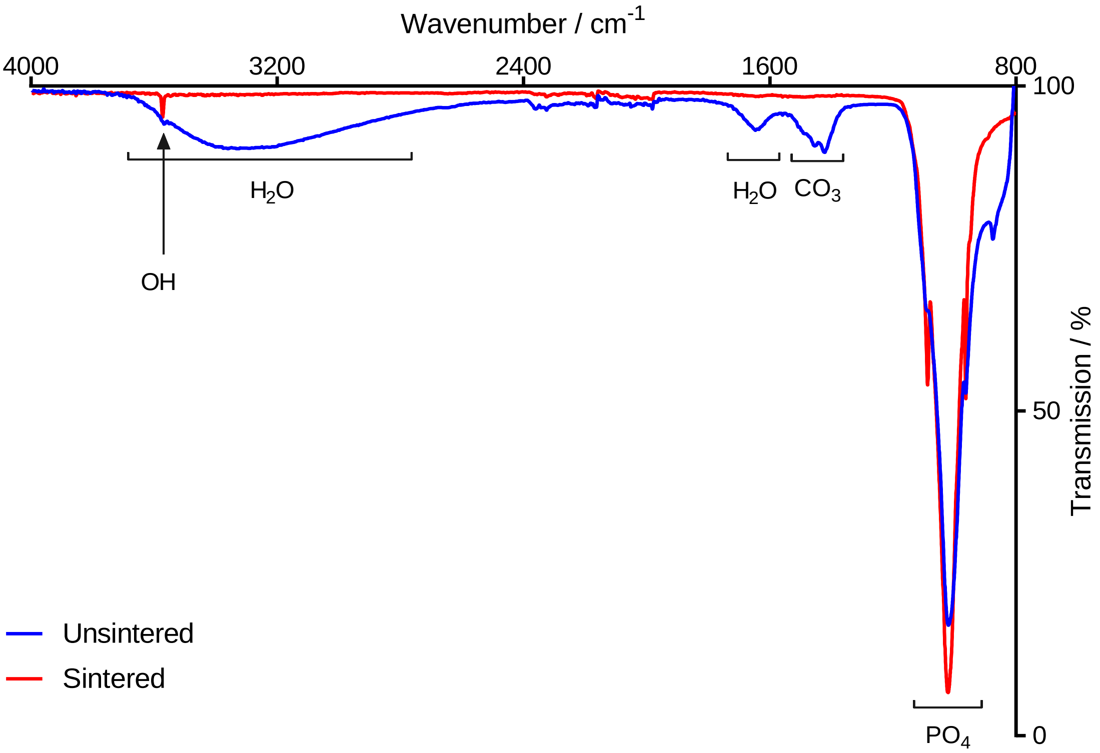

Figure 4.1. Overlaid ATR FTIR spectra of unsintered HA and HA sintered at 900 ˚C for 2 hours.

small peak at 3570 cm^{-1} could be due to the presence of the non-hydrogen bonded OH$^-$ ion within the crystal lattice. Looking at the FTIR spectrum of the sintered sample, it appears the sample degraded during the sintering process. The peak in the unsintered sample at 870 cm^{-1} could be used to explain this as it is characteristic of a calcium deficient hydroxyapatite[3] which is less stable at higher temperatures, hence supporting the theory that the sample degraded during sintering. TEM imaging (figure 4.2) also showed significant difference between the unsintered and sintered HA samples. The TEM images were compared to a control sample of HA prepared by the Prakash method by Caroline Wilcock (figure 4.2 e and f), a summary of the differences in particle size are shown below in table 4.6.

Table 4.6. A summary of the particle sizes of samples of hydroxyapatite synthesised via the modified Prakash method imaged using TEM and analysed using ImageJ software.

Sample	**Lengths / nm**			**Widths / nm**			**Aspect ratios**
	Mean	**SD**	**SE**	**Mean**	**SD**	**SE**	
Control	33.4	8.7	0.4	16.8	3.4	0.3	2.0
Sintered	106.9	28.4	3.7	54.6	9.0	0.9	2.0
Unsintered	34.9	6.6	0.7	14.8	3.6	0.4	2.4

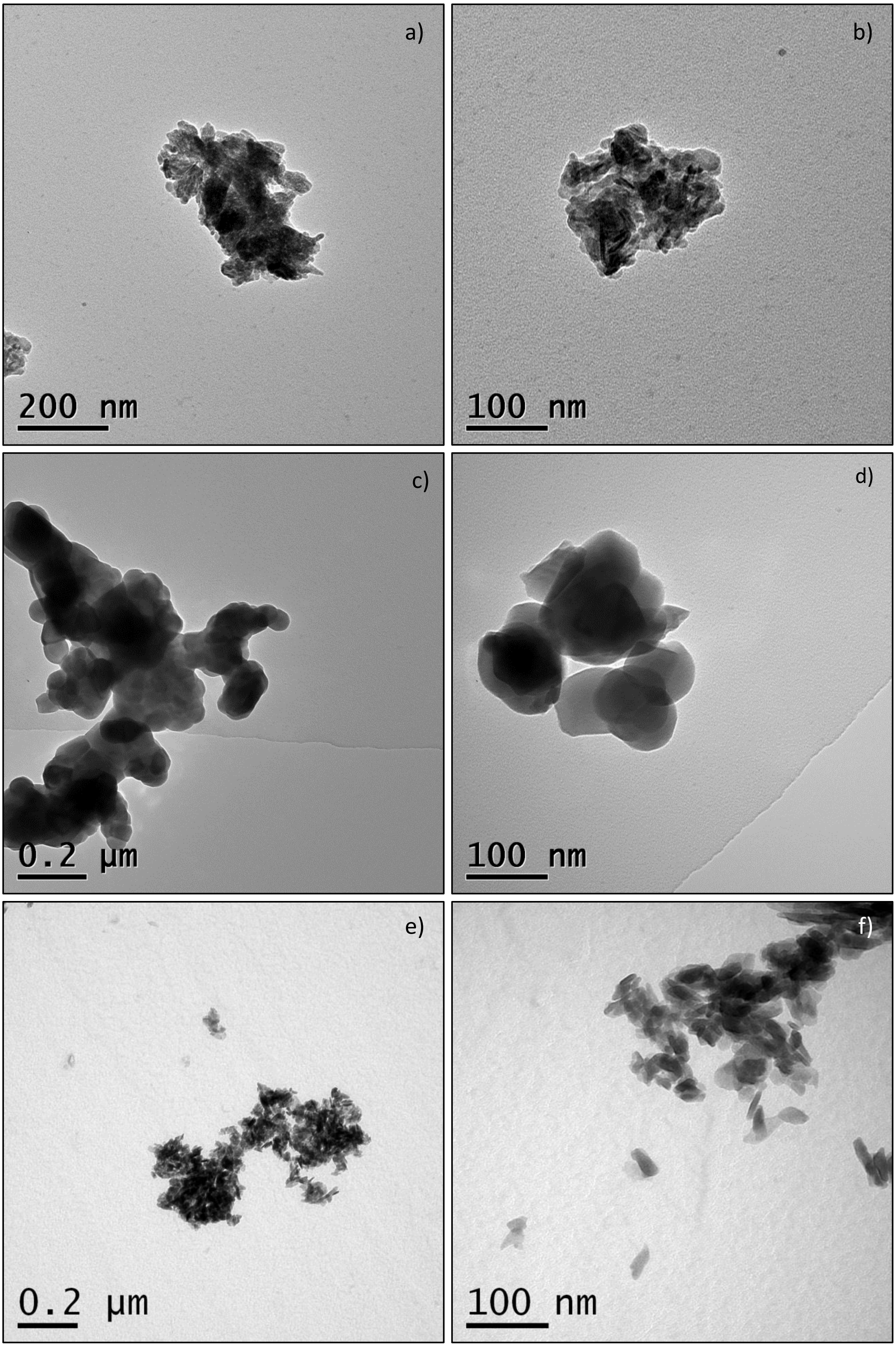

Figure 4.2. TEM images of unsintered hydroxyapatite (a and b), sintered hydroxyapatite (c and d) and a control sample of unsintered hydroxyapatite donated by Caroline Wilcock (e and f).

The unsintered samples appeared more crystalline as the particles have a much more defined morphology and are much smaller than the sintered samples as determined by particle sizing using ImageJ sizing software.[4] Increasing particle size is a known effect of sintering ceramics due to properties including, thermal heat capacity, thermal expansion coefficient and thermal conductivity.[5, 6] These properties determine the interaction of the particles during the sintering process. In bulk ceramic processing, sintering is used to turn a raw ceramic powder into a continuous solid network while nanoparticle sintering is used to improve the crystallinity of the final product by coalescing smaller particles together to form a low dispersity sample of marginally larger particles. A schematic diagram outlining this effect is shown in figure 4.3. [5, 6]

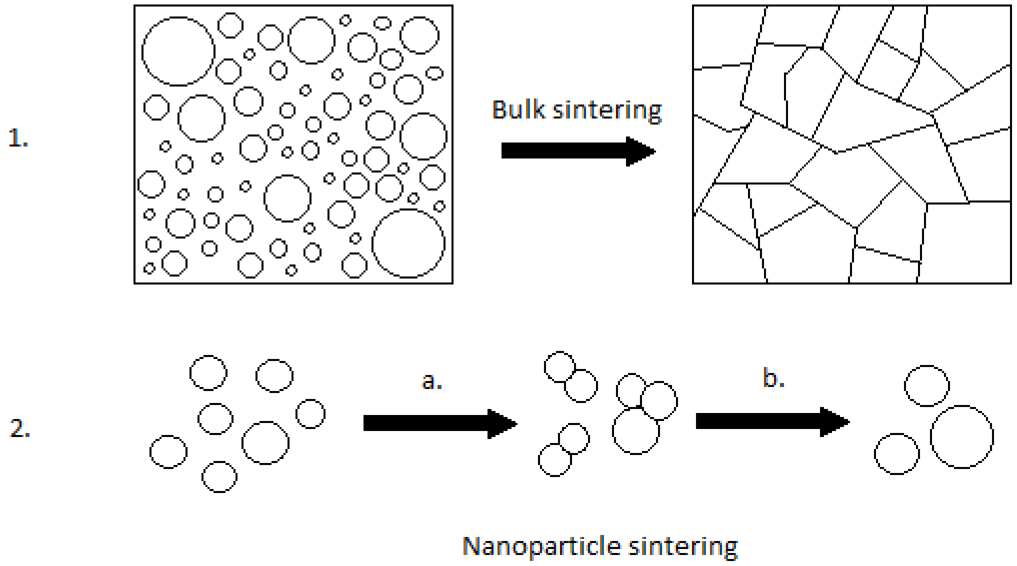

Figure 4.3. Sintering of bulk ceramics (route 1) and nanoparticles (route 2). In bulk sintering a raw powder is placed into a small container, the high temperatures of up to 1200 °C cause the raw powder to coalesce and form a continuous non porous network. During nanoparticle sintering, smaller particles aggregate due to the high surface area to volume ratio causing the nanoparticles to be extremely reactive which is then increased by the high temperatures of sintering (a). The reactivity of the particles once aggregated then causes structural changes to form slightly larger nanoparticles (b). Temperature has a large effect on the size of particles, longer sintering times at higher temperatures form larger particles.[5, 6]

The images of the unsintered sample when analysed with particle sizing software showed a mean particle length of 35 nm, while analysis of the sintered samples gave a mean particle length of 107 nm. However, the change in colour from cream to bright white during sintering, along with the apparent morphology change from small crystalline plates to large amorphous structures, suggests that the sintering process caused the sample to degrade as sintered samples usually become more crystalline during crystal growth[5]. As a result of the issues during the synthesis of the hydroxyapatite, medical grade microscale and nanoscale HA was sourced and used to test the polymers' suitability as coatings using a carousel reactor while the issues with the HA synthesis were investigated.

TEM images of the sourced medical grade microHA and nanoHA (figure 4.4) showed a significant difference between the morphology and size of the particles. The nanoHA particles are very uniform, while the microHA is much more varied in size and shape. For the purposes of initial testing of polymer coatings this was ideal as it gave an indication of the differences between coating on comparably large and small surface areas in terms of the micro and nanoHA respectively.

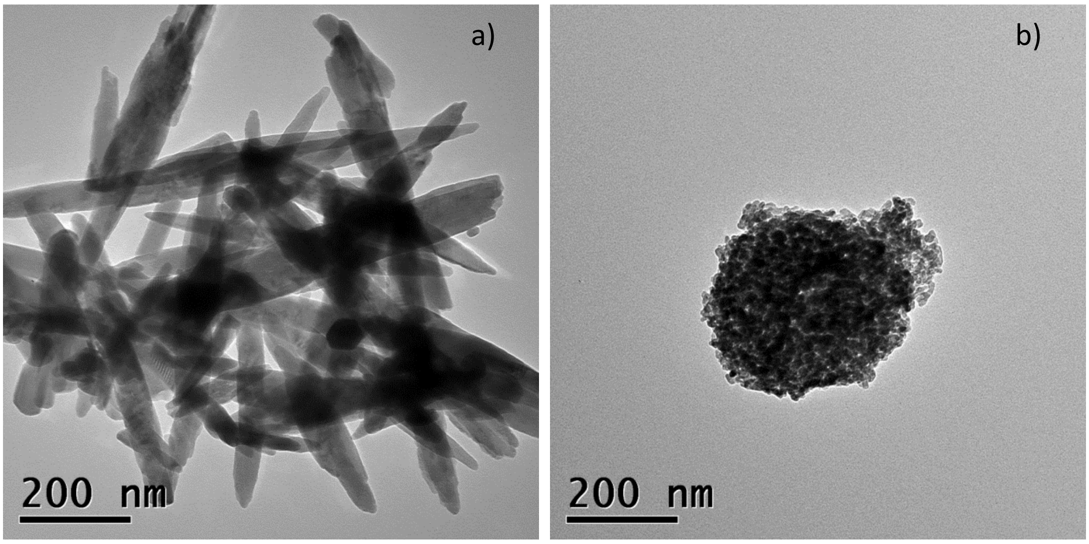

Figure 4.4. TEM images of medical grade a) microHA and b) nanoHA

4.3.2 Addition of hydroxyapatite nanoparticles during synthesis of branched polymers - carousel

Samples of micro and nano sized HA were added during the RAFT polymerisation of (meth)acrylic acid and AMPS with VPC and VBD as chain transfer agents. Specific reaction compositions are detailed in table 4.1 in section 4.2.2. The compositions for the reactions were chosen in order to mimic the polymer synthesises detailed in chapter 3 so as to be comparable to the polymers. Samples were then analysed by dynamic light scattering (DLS) to determine the size of the particles compared to a control sample of medical grade micro or nanoHA in the same solvent; this is summarised in table 4.7. The two acrylic acid polymerisations containing microHA (AA/VPC/m and AA/VBD/m) went cloudy overnight. Particle size analysis showed that overall the particles were smaller, AA/VPC/m = 1.23 mm, and AA/VBD/m = 0.91 mm than the control sample for both samples, there is an overlap of

Table 4.7. A summary of the mean effective diameter of PAA and PMAA synthesised in dioxane in the presence of micro or nanoHA particles and control samples of micro and nanoHA with no polymer. Negative differences with the control sample indicate the particles are smaller than the control sample. Issues with sample sedimentation during DLS measurements mean these data are not absolutely reliable and should be used as a guide only.

Sample	**Polymer / RAFT / HA**	**Mean Effective Diameter / mm**	**Standard error / mm**	**Difference with control / mm**
AA/VPC/m	PAA / VPC / microHA	1.23	0.01	-0.51
AA/VBD/m	PAA / VBD / microHA	0.91	0.15	-0.83
MAA/VPC/m	PMAA / VPC / microHA	1.17	0.13	-0.57
MAA/VBD/m	PMAA / VBD / microHA	2.51	0.48	0.77
MicroHA	--- / --- / microHA	1.74	0.19	---
AA/VPC/n	PAA / VPC / nanoHA	0.91	0.20	-0.38
AA/VBD/n	PAA / VBD / nanoHA	0.66	0.12	-0.63
MAA/VPC/n	PMAA / VPC / nanoHA	3.39	0.61	2.10
MAA/VBD/n	PMAA / VBD / nanoHA	1.14	0.14	-0.15
NanoHA	---/ --- / nanoHA	1.29	0.26	---

particle sizes, indicating that there is negligible difference between the particle sizes; it is possible that this is due to particle aggregation, or simply that the similar samples have formed particles with similar sizes.

Two methacrylic acid samples formed precipitates during the reaction to form a fine suspension. MAA with microHA and VBD (MAA/VBD/m) formed solid deposits which settled, while MAA with nanoHA and VPC (MAA/VPC/n) formed precipitates which, under stirring, reversibly aggregated into a ball and broke down into a powder. It is possible that the MAA/VPC/n coated the nanoHA particles causing all the particles to aggregate together which then reversibly broke up under sustained stirring while the MAA/VPC/m sample may have coated the particles to form a larger aggregate which could not be dispersed. Particle size analysis showed a distinct size increase of these two MAA samples compared to the control samples of nano and microHA. This indicates that a coating may have formed. However, it is more likely from the behaviour under stirring that the polymer and HA aggregated together rather than the polymer formed a coating.

The AMPS samples containing microHA (AMPS/VPC/m and AMPS/VBD/m) both showed an increase in size compared to the control sample. In contrast, neither of the two AMPS samples containing nanoHA (AMPS/VPC/n and AMPS/VBD/n) gave a reading during particle size analysis. Both samples were completely clear and showed no trace of nanoHA, hence it is believed that the polymerisation conditions were too acidic and the nanoHA degraded. This is an interesting result; if the polymerisation conditions were too strongly acidic for the nanoHA to survive then the fact that the microHA samples showed an increase in particle size is counterintuitive. It is possible that the increased size of the microHA in comparison to nanoHA allowed the microHA to act as a nucleation point for the polymerisation. As a result, this may have led to the formation of a polymer coating around the microHA particles hence leading to larger particles sizes when analysed in solution. This is summarised in table 4.8.

Table 4.8. A summary of the mean effective diameter of PAMPS synthesised in DMSO in the presence of micro or nanoHA particles and control samples of micro and nanoHA with no polymer. Negative differences with the control sample indicate the particles are larger than the control sample. Issues with sample sedimentation during DLS measurements mean these data are not absolutely reliable and should be used as a guide only.

Sample	**Polymer / RAFT / HA**	**Mean Effective Diameter / mm**	**Standard error / mm**	**Difference with control / mm**
AMPS/VPC/m	PAMPS / VPC / microHA	1.86	0.11	-0.45
AMPS/VBD/m	PAMPS / VBD / microHA	3.50	0.20	-2.14
MicroHA	--- / --- / microHA	1.41	0.17	---
AMPS/VPC/n	PAMPS / VPC / nanoHA	0.00	0.00	0.00
AMPS/VBD/n	PAMPS / VBD / nanoHA	0.00	0.00	0.00
NanoHA	--- / --- / microHA	1.36	0.17	---

In all cases, including the control samples, the particle size increased when sizing experiments were extended suggesting that the particles began aggregating after the solutions were no longer being stirred. This implies that the desired polymer coating to create the dispersion of the HA micro and nanoparticles was unsuccessful in this case. The lack of chemical analysis available due to the inability to purify the sample without potentially affecting the reaction mixture meant that this method was deemed unsuitable; it was impossible to calculate polymer conversion, molecular weight, degree of branching and polydispersity. The acidic conditions created by the free monomer in solution also mean that it is extremely difficult to gauge whether the HA is being coated or degraded. As a result, a different method using already synthesised polymers along with HA was investigated.

4.3.3 Combination of hydroxyapatite nanoparticles with branched polymers in a weight ratio of 1:20

To prepare samples, the polymers were dissolved in DMSO and medical grade HA was then added. Samples were stirred for 24 hours then analysed by DLS. The data collected from DLS analysis determined that in the cases of both medical grade micro and nanoHA, the acrylic acid polymers (PAA-VPC and PAA-VBD) and the poly(methacrylic acid) made with VBD (PMAA-VBD) gave particles with increased size when compared to the control sample, while the methacrylic acid made with VPC (PMAA-VPC) and both AMPS polymers (PAMPS-VPC and PAMPS-VBD) caused a size decrease compared to the control sample. The degree of branching for the three polymers that lead to a particle size increase was less than or equal to 5 in all cases, while the degree of branching in the case of the three polymers that lead to a particle size decrease was more than or equal to 5. This is described in table 4.9.

Table 4.9. A summary of mean effective diameter measurements from dynamic light scattering on medical grade microHA (m) and nanoHA (n) treated with polymers in a 1:20 weight ratio in DMSO. Issues with sample sedimentation during DLS measurements mean these data are not absolutely reliable and should be used as a guide only.

Sample	Polymer	DB	Effective Diameter / mm	Standard error / mm	Difference with control / mm
PAA-VPC/m	PAA-VPC	5	2.19	0.06	-0.44
PMAA-VPC/m	PMAA-VPC	5	1.40	0.29	0.34
PAMPS-VPC/m	PAMPS-VPC	15	1.22	0.22	0.52
PAA-VBD/m	PAA-VBD	2	2.54	0.61	-0.80
PMAA-VBD/m	PMAA-VBD	3	2.57	0.56	-0.83
PAMPS-VBD/m	PAMPS-VBD	12	1.35	0.22	0.40
MicroHA	---	---	1.74	0.19	---
PAA-VPC/n	PAA-VPC	5	2.01	0.17	-0.73
PMAA-VPC/n	PMAA-VPC	5	1.17	0.23	0.12
PAMPS-VPC/n	PAMPS-VPC	15	0.93	0.06	0.36
PAA-VBD/n	PAA-VBD	2	3.20	0.85	-1.91
PMAA-VBD/n	PMAA-VBD	3	2.01	0.49	-0.72
PAMPS-VBD/n	PAMPS-VBD	12	1.13	0.17	0.16
NanoHA	---	---	1.29	0.26	---

The standard error of most samples is rather large; however, they do provide an indication of the true particle size when compared to the control sample with no polymer. The overlap of the particle sizes by the standard error indicates that the samples may be closer in size to the untreated control. However, in every instance the effective diameter of the particles increased with subsequent ‘runs’. This indicates that the particles aggregate when the solution is not stirred. As a result, no true particle sizes can be taken from this data, however, the difference between the first and last ‘runs’ do give an indication on the level of aggregation caused by the lack of stirring.

4.3.4 Mixing medical grade HA with polymers in a ratio of 1:2

To prepare samples, the polymers were dissolved in THF (PAA samples) or DMF (PMAA and PAMPS samples) and medical grade HA was then added. Samples were stirred for 24 hours then analysed by DLS. The data collected from DLS analysis determined that in the cases of both medical grade micro and nanoHA, the acrylic acid polymers (PAA-VPC and PAA-VBD) gave particles with a very similar size to the control sample of nano or microHA in THF. However, the PMAA and PAMPS samples in all but the case of n/PAMPS-VPC2 all showed reduced size when compared to the control sample. The degree of branching for the two polymers that lead to a particle size increase was less than or equal to 5, while the degree of branching in the case of the four polymers that lead to a particle size decrease was more than or equal to 3. This is described below in table 4.10 (PAA samples in THF) and table 4.11 (PMAA and PAMPS samples in DMF).

Table 4.10. A summary of mean effective diameter measurements from dynamic light scattering on medical grade microHA and nanoHA treated with PAA in a 1:2 weight ratio in THF. Issues with sample sedimentation during DLS measurements mean these data are not absolutely reliable and should be used as a guide only.

Sample	Polymer	DB	Effective Diameter / mm	Standard error / mm	Difference with control / mm
m/PAA-VPC2	PAA-VPC	5	1.09	0.14	0.02
m/PAA-VBD2	PAA-VBD	2	1.14	0.20	-0.02
MicroHA	---	---	1.12	0.14	---
n/PAA-VPC2	PAA-VPC	5	1.25	0.28	0.40
n/PAA-VBD2	PAA-VBD	2	1.97	0.43	-0.32
NanoHA	---	---	1.65	0.24	---

Table 4.11. A summary of mean effective diameter measurements from dynamic light scattering on medical grade microHA and nanoHA treated with PMAA or PAMPS in a 1:2 weight ratio in DMF. Issues with sample sedimentation during DLS measurements mean these data are not absolutely reliable and should be used as a guide only.

Sample	Polymer	DB	Effective Diameter / mm	Standard error / mm	Difference with control / mm
m/PMAA-VPC2	PMAA-VPC	5	0.52	0.08	0.98
m/PAMPS-VPC2	PAMPS-VPC	15	0.49	0.07	1.01
m/PMAA-VBD2	PMAA-VBD	3	0.79	0.13	0.71
m/PAMPS-VBD2	PAMPS-VBD	12	0.39	0.05	1.12
MicroHA	---	---	1.50	0.27	---
n/PMAA-VPC2	PMAA-VPC	5	0.77	0.10	2.06
n/PAMPS-VPC2	PAMPS-VPC	15	26.45	4.98	-23.61
n/PMAA-VBD2	PMAA-VBD	3	0.69	0.12	2.15
n/PAMPS-VBD2	PAMPS-VBD	12	1.84	0.17	1.00
NanoHA	---	---	2.84	0.68	---

The particle size of the polymer treated HA appears to be independent of the degree of branching of the polymer. The standard errors associated with each sample are rather large again. However, they do provide an indication of the true particle size when compared to the control sample with no polymer. The PAA samples showed a good overlap with the particle size of the control sample in the case of both micro and nanoHA. However, the PMAA and PAMPS samples were far smaller than the control sample and showed no overlap at all when the standard error was taken into account. As with the 1:20 weight ratio of HA to polymer, in every instance the effective diameter of the particles increased with subsequent ‘runs’. This indicates that the particles aggregate when the solution is not stirred. It appears that the samples analysed in DMF aggregated to a lesser degree, or agglomerated more quickly when the stirring stopped than the samples run in THF. The values of the effective diameter of the particles are far more consistent than those analysed in THF. This may be due to the fact that DMF is more viscous than THF, hence the particles may not have the same freedom of movement through the solvent in DMF compared to THF. DLS analysis gives a comparison of the size of the particles in solution. However, in order to find the true particle sizes of the polymer treated HA, TEM analysis should be conducted.

4.3.5 Synthesis of fluorapatite nanoparticles via the Chen method[2]

Fluorapatite (FA) nanoparticles were synthesised using a variation on the Chen suspension method[2], as described in section 4.2.4 of this chapter. TEM imaging, XRD and FTIR analysis of the resultant particles determined the size and composition of the particles. Analysis of the FTIR spectrum of the sintered and unsintered samples confirmed that FA had been synthesised (figure 4.5).

Bands present from 3650 – 2600 cm^{-1} (broad) in the unsintered spectrum are characteristic of adsorbed water; this peak disappears when the sample is sintered showing the water is unbound and therefore not incorporated in to the FA structure.[2] The peak at 1020 cm^{-1} (sharp) is characteristic of the phosphate stretching vibration within the FA, while the peaks in the fingerprint region from 620 – 500 cm^{-1} (sharp) show the inclusion of fluoride ions within the FA structure alongside the phosphate bending vibration. A significant difference was also noticed when comparing TEM images (figure 4.6) of the FA sample with the HA sample. A rectangular morphology was seen, as opposed to the characteristic plate-like morphology of HA, indicating a difference in crystal structure; this suggests that fluoride has been successfully substituted into the unit cell to form fluorapatite. TEM images (Figure 4.6) show a distribution of sizes of FA particles across the sample. Particle sizing using ImageJ software gave a mean particle length of 45 nm. This is not in agreement with the particle sizing analysis using dynamic light scattering (DLS); however, as DLS is a ‘wet’ analysis technique whereas

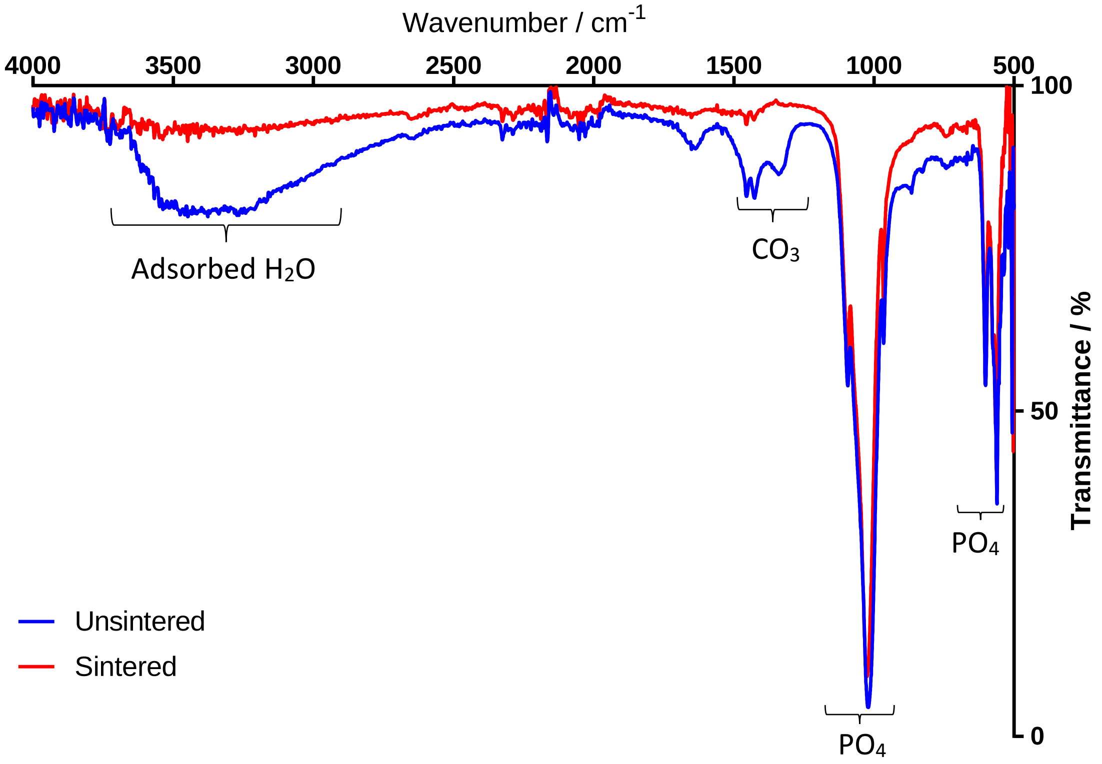

Figure 4.5. Overlaid ATR FTIR spectra of unsintered FA and FA sintered at 700 ˚C for 1 hour

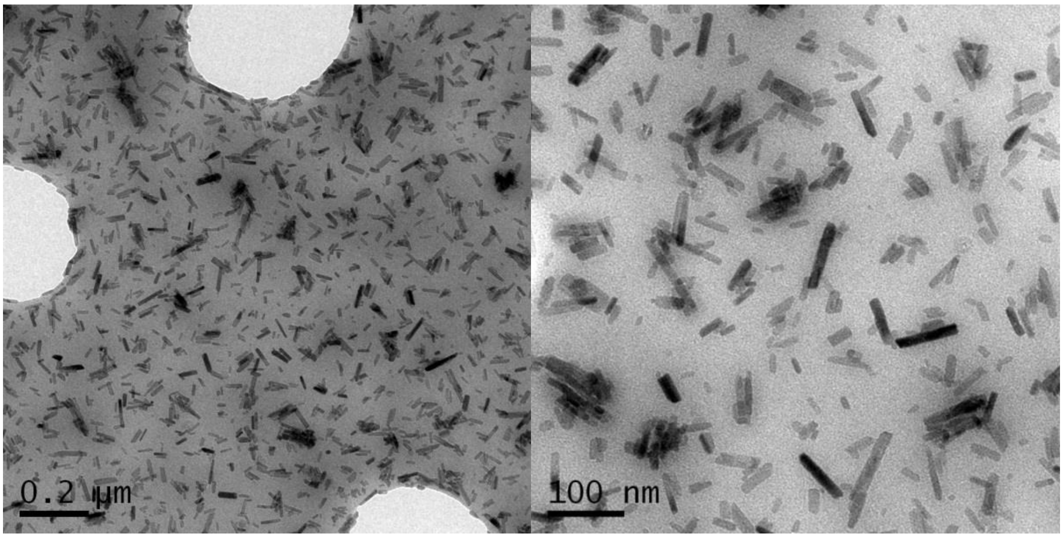

Figure 4.6. TEM images of FA.

samples are dry for TEM, the presence of solvent could allow particle aggregation hence increasing the particle size output. This could cause difficulties with the use of DLS for the analysis of polymer treated particles; if the presence of solvent causes particle aggregation, it is possible that this will give erroneous sizes of particles. This also suggests that the particles are not stable in solution; hence the best course of action could be to keep the samples dry.

Particle size analysis via DLS also assumes the particles are spherical; the fact that the particles are rectangular will therefore lead to erroneous results. As such no solid results can be taken from the DLS analysis.

Analysis of the XRD spectrum supports the evidence produced by the FTIR spectra and TEM imaging. The synthesised fluorapatite was overlaid with a star quality reference powder diffraction file (PDF) of fluorapatite as shown in figure 4.7.

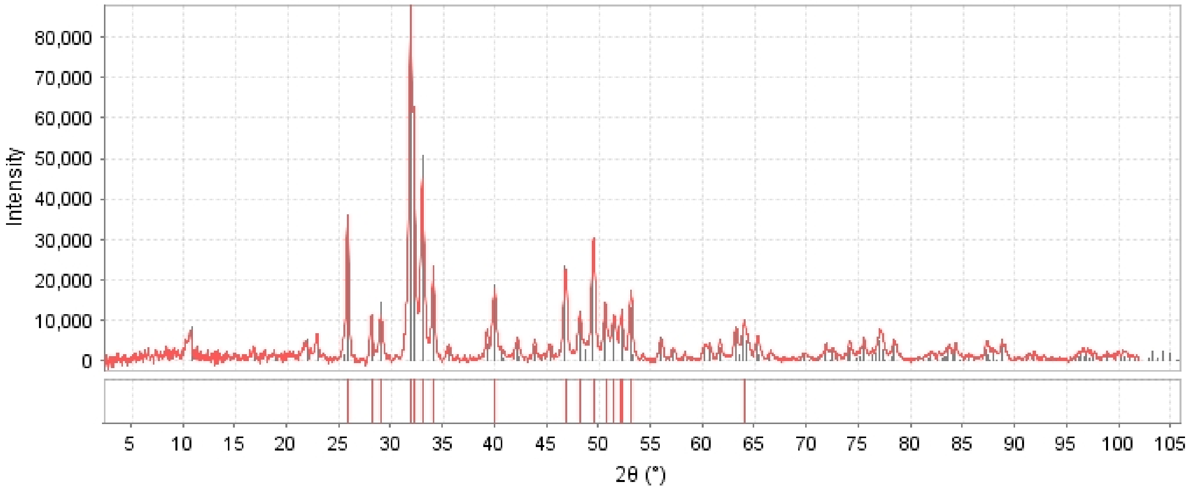

Figure 4.7. XRD spectrum of sintered fluorapatite overlaid with reference PDF 04-009-4021.

Comparison of the observed peaks from the sample and the reference spectrum showed a good overlap indicating a good fit. This supports the data gained by FTIR spectroscopy, hence providing convincing evidence that fluorapatite has been successfully synthesised. The reference spectrum matched the observed spectrum of synthesised fluorapatite. This, along with the FTIR spectrum and TEM imaging, provide good evidence that fluorapatite was successfully synthesised.

4.3.6 Combination of fluorapatite nanoparticles with branched polymers

Polymers of acrylic acid, methacrylic acid and 2-acrylamido-2-methylpropanesulfonic acid were synthesised in a 25:1 monomer: RAFT mixture as described in chapter 3 and mixed with fluorapatite (FA), as described in table 4.4 of section 4.2.5 of this chapter. To prepare samples, the polymers were dissolved in THF (PAA samples) or DMF (PMAA and PAMPS samples) (4 ml) and FA was then added. Samples were stirred for 24 hours then analysed by DLS. The data collected from DLS analysis determined that in all cases the particle sizes increased with the inclusion of polymer compared to the size of the control sample. This is described in table

4.12. FA is more acid stable than HA, hence it is possible that the increase in size of the particles is due to the polymers forming a coating, rather than dissolving the ceramic particles first.

Table 4.12. Mean effective diameter measurements from DLS analysis on fluorapatite treated with polymers in a 1:2 weight ratio.

Sample	Polymer	DB	Effective Diameter / mm	Standard error / mm	Difference with control / mm	Solvent
F/PAA-VPC	PAA-VPC	5	1.17	0.17	0.18	THF
F/PMAA-VPC	PMAA-VPC	5	0.65	0.02	0.42	DMF
F/PAMPS-VPC	PAMPS-VPC	15	0.48	0.02	0.25	DMF
F/PAA-VBD	PAA-VBD	2	1.45	0.25	0.46	THF
F/PMAA-VBD	PMAA-VBD	3	0.95	0.07	0.71	DMF
F/PAMPS-VBD	PAMPS-VBD	2	0.75	0.04	0.52	DMF
NanoFA (THF)	---	---	0.99	0.03	0.00	THF
NanoFA (DMF)	---	---	0.23	0.02	0.00	DMF

The PAA sample F/PAA-VPC showed some overlap with the pure FA sample when the standard error was taken into account. Both samples analysed in THF (F/PAA-VPC and F/PAA-VBD) gave the largest standard error values; it is therefore possible that solvent effects between the polymer and THF are causing the results to become skewed. All samples regardless of the solvent run in produced particle sizes that were larger than the control samples. Repeats of the DLS analysis provided a much smaller standard error in all cases and showed the same trend as the first experiment with the PAA samples producing the largest difference from the control sample. The particle sizes of the polymer treated samples were much larger with far smaller standard error values that did not overlap with the control samples. This is an interesting result which does not correlate with the data collected from DLS analysis of polymer treated HA. This supports the theory that the increased acid stability of the fluorapatite caused by fluoride substitution of the hydroxyl ion in hydroxyapatite allows the polymer to interact with the ceramic particles more easily. However, the DLS data also showed a similar trend to the HA DLS analysis that the particle sizes increased with further ‘runs’. This suggests that the particles are aggregating after the solution is stopped from stirring.

As with all the other carousel reactions, the results when measured with DLS were inconclusive. As the samples could not be effectively purified after the carousel reactions, it was decided that a new method would be introduced in order to form composite materials. As a result, the subsequent samples were produced by including pre-synthesised polymers in the reaction mixture to form hydroxyapatite nanoparticles.

4.3.7 Synthesis of hydroxyapatite nanoparticles with 1 wt% branched polymer additives via the modified Prakash method[1]

Hydroxyapatite nanoparticles were synthesised, as described in section 4.2.1, via the modified Prakash method with the addition of highly branched poly (acrylic acid) (PAA) synthesised as described in section 3.2 of chapter 3. Mixing the calcium hydroxide and phosphoric acid/ PAA solutions together formed a suspension which was then washed and dried. The resulting white solid was analysed using FTIR, XRD, TGA and TEM.

4.3.7.1 Fourier Transform Infra-red spectroscopy (FTIR)

The Prakash method of synthesising hydroxyapatite combines calcium hydroxide with phosphoric acid in a stoichiometric ratio to give a Ca/P ratio of 1.67. Alternate phases that can form during the synthesis of HA reduce this ratio producing calcium deficient HA which can be thermally treated with temperatures up to 1300 ^{o}C to produce pure HA.[3, 7] However, the inclusion of polymers within the synthesis of HA means that thermal treatment is impossible as this would destroy the organic constituent of the ceramic composite. Another method to ensure the formation of HA is the inclusion of an aging step during synthesis; this allows the calcium phosphate to reach the most favourable kinetic and thermodynamic phase possible, in this case hydroxyapatite. This means that the resulting composite materials should only contain HA and polymer, which is closer to the natural form of HA in the body. The substitution of Ca^{2+} by other ions such as Mg^{2+}, K^+ and Na^+ or the substitution of PO_4^{3-} by CO_3^{2-}, $H_2PO_4^-$ and HPO_4^{2-} for example, mean that HA found naturally in the body has a Ca/P ratio of between 1.5 – 1.67.[7] The substitution of other ions and infiltration of organic molecules into naturally occurring HA accounts for its versatile mechanical properties and bioactivity within the body. This also means that synthetic HA should include some level of ionic substitution to mimic natural HA when implanted in the body to have the best chance of being biocompatible.[3, 7]

FTIR is a powerful technique which can determine structural differences in ceramic materials through minute changes in vibrational frequency. As a result, it is commonly used to determine the purity of hydroxyapatite and note additional phases such as β–tricalcium phosphate (TCP) which may have formed during the synthetic process. Differing vibrational frequencies in these two calcium phosphate phases means they can be distinguished when analysing a FTIR spectrum. Figures 4.8 a and b show the overlaid and stacked normalised spectra of four samples of hydroxyapatite synthesised using a modified Prakash method respectively.

Overlaying the spectra shows the difference in peak intensity of the normalised spectra while the stacked spectra show the different peak shapes implying different crystal lattices due to differing vibrational frequencies. Comparing the overlaid spectra showed a change in the intensity and shape of the OH^- (approximately 3600 cm^{-1}) and PO_4^{3-} peaks (approximately 1030 cm^{-1} and 600 cm^{-1}). The same synthetic protocol was followed in the preparation of all samples; hence it is surprising that the peak intensities differ, indicating that the inclusion of different polymers in the sample synthesis has caused some disruption to the crystal lattice. The PO_4 peaks in all spectra are broad; this indicates the presence of amorphous material and a non-uniform distribution of particle sizes throughout the samples which suggests that there is some disruption in the ordering of the crystals. A summary of peak assignment of the FTIR spectra is given in table 4.13.

Table 4.13: Chemical groups and their corresponding wavenumbers in hydroxyapatite samples synthesised via the Prakash method containing 1 wt% PAA-VPC, PAA-VBD, PMAA-VPC and PMAA-VPC. Peak assignments were made using the reference data of Berzina-Cimdina and Borodajenko.[3]

Sample	**HA + 1 wt% PAA-VPC**	**HA + 1 wt% PAA-VBD**	**HA + 1 wt% PMAA-VPC**	**HA + 1 wt% PMAA-VBD**
Chemical Group	**Absorption bands / cm^{-1}**			
OH stretch	3568	3568	3570	3569
H_2O (adsorbed)	3690 - 2600, 1639	3690 - 2600, 1638	3690 - 2600, 1634	3690 - 2600, 1635
CO_2 (adsorbed)	2175 - 1975	2175 - 1975	2175 - 1975, 876	2175 - 1975, 876
COO^- (sym, asym)	1455, 1424	1455, 1424	1455, 1418	1456, 1418
PO_4 (v_3) bend	1094 - 1035	1094 - 1034	1094 - 1025	1093 – 1040
PO_4 (v_1)	962	962	963	962
OH bend	---	---	631	631
PO_4 (v_4) bend	602, 564	602, 564	603, 566	603, 566
PO_4 (v_2)	473	472	473	473

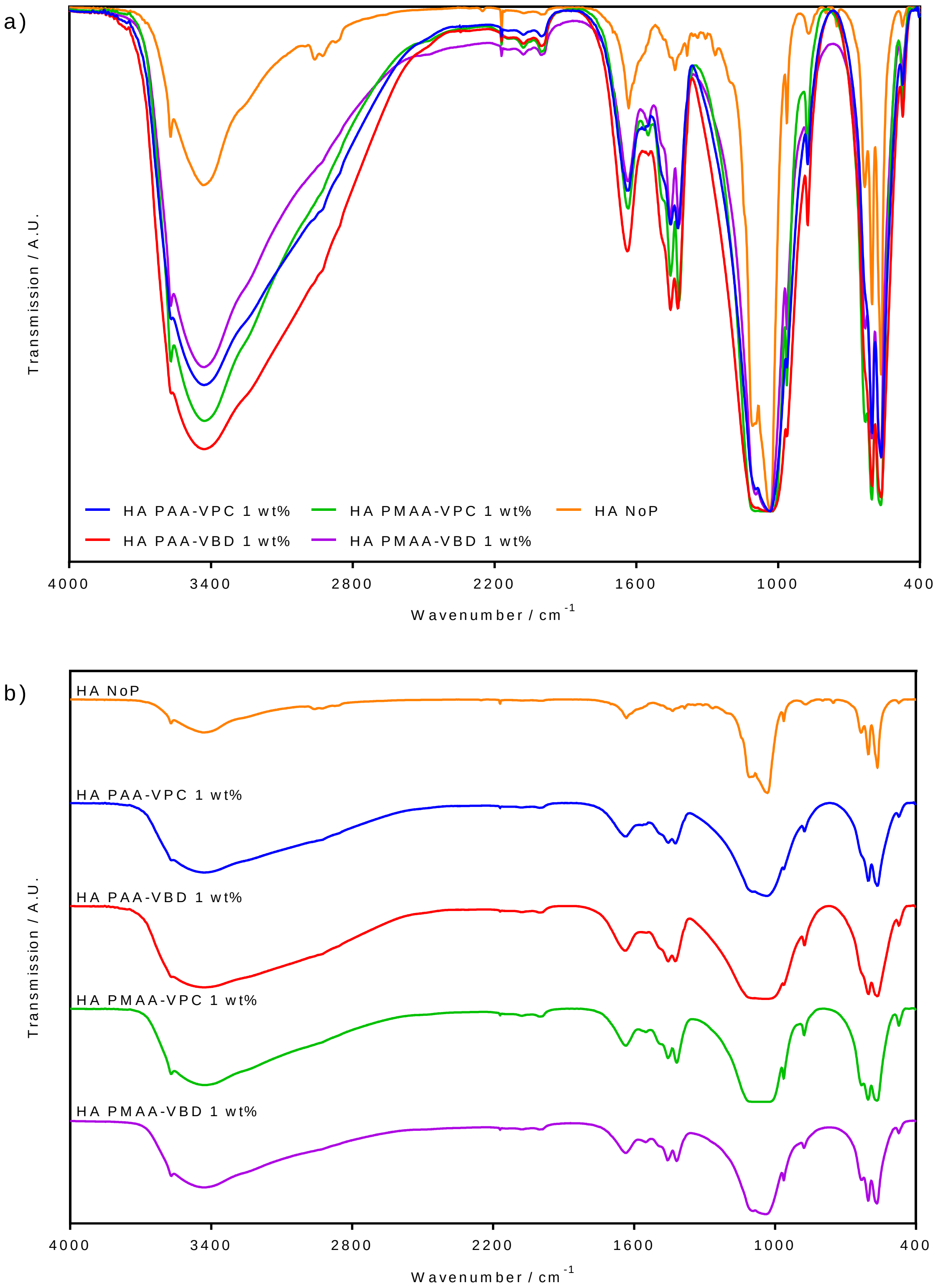

Figure 4.8 the normalised a) overlaid and b) stacked FTIR spectra of hydroxyapatite samples synthesised using the Prakash method containing 1 wt% PAA-VPC, PAA-VBD, PMAA-VPC and PMAA-VBD.

The inclusion of the polymer in the apatite particles is evident from the peaks between 1560 and 1410 cm^{-1} corresponding to the COO^{-} of the P(M)AA. Small shoulders in this region along with very weak peaks from 2100-1910 cm^{-1} correspond to CO_3 which occurs due to the adsorption of CO_2 from the atmosphere onto the particle surface during synthesis. Water is also adsorbed onto the surface of the particles during synthesis, along with KBr being extremely hygroscopic, this leads to the broad peak present from 3690 – 2600 cm^{-1} and the sharper peak at approximately 1640 cm^{-1}. The loss of peak sharpness seen in samples HA + 1 wt% PAA-VPC and HA + 1 wt% PAA-VBD implies a loss of long range order in the crystal structure. This along with the loss of peak intensity of the OH peak at 3568 cm^{-1}, within the extremely broad peak due to absorbed water from 3690 – 2600 cm^{-1}, suggests either the formation of a different calcium phosphate phase than hydroxyapatite such as calcium deficient hydroxyapatite, or disruption of the crystal lattice caused by the inclusion of PAA. The peak at 630 cm^{-1} corresponding to OH bend of hydroxyapatite appears as a shoulder for both HA + 1 wt% PAA-VPC and HA + 1 wt% PAA-VBD, which supports the theory that calcium deficient HA has been formed. However, another characteristic peak of adsorbed CO_2 also appears at 875 cm^{-1} hence, other characterisation techniques must be considered to fully determine which calcium phosphate phase has been formed.[3]

Peak broadening and differing peak shapes from approximately 1100 - 1020 cm^{-1} suggests a large degree of hydrogen bonding within the samples which can be attributed to the phosphate group interacting with the branched polymer.[3, 8-10] This is evident from all four spectra and along with the peaks between 1460 and 1410 cm^{-1} (corresponding to the COO^- of the P(M)AA) shows this inclusion of polymer in all samples. This causes disruption to the hydroxyapatite crystal lattice and introduces interactions between the acid groups of the polymer and phosphate groups of the HA which becomes evident as broad peaks when analysed by FTIR.[3, 8, 11] Other analytical techniques such as XRD can be used to support this.

4.3.7.2 X-ray powder diffraction (XRD)

Table 4.14 shows the *a* and *c* cell parameters of each sample determined through Pawley and Rietveld refinement of the XRD patterns. Lattice parameters determined by Pawley and Rietveld refinement differ slightly, but overall the parameters determined for each sample are reasonably consistent. However, it appears there are differences in the unit cell parameters when comparing each sample. This is to be anticipated due to the inclusion of polymer within the samples which could cause disruption to the crystal lattice as already stated.

Table 4.14. Cell parameters determined using Pawley refinement to fit the collected XRD diffractograms with powder diffraction files from the central database using the TOPAS software package from Bruker.

Sample	Pawley Refinement				Rietveld Refinement			
	a / Å	c / Å	R_{wp}	R_{wpb}	a / Å	c / Å	R_{wp}	R_{wpb}
HA + 1 wt% PAA-VPC	9.43(3)	6.87(2)	10.11	13.16	9.42(2)	6.87(2)	13.27	19.75
HA + 1 wt% PAA-VBD	9.40(1)	6.85(1)	10.08	10.77	9.41(3)	6.85(3)	14.48	21.79
HA + 1 wt% PMAA-VPC	9.402(2)	6.869(8)	9.13	12.30	9.41(1)	6.87(1)	12.87	18.43
HA + 1 wt% PMAA-VBD	9.41(1)	6.869(6)	11.38	13.00	9.42(1)	6.88(1)	16.84	25.11

The lattice parameters of HA + 1 wt% PAA-VPC are fairly consistent with those of pure HA (*a* = 9.432 Å, *c* = 6.881 Å)[12] while the other samples have *a* parameters which are smaller than those of pure HA. The smaller *a* parameter may indicate that an ion smaller than OH could have been substituted into the crystal lattice. Considering the chemicals used to synthesise the particles, $Ca(OH)_2$ and H_3PO_4 it is not obvious what this ion could be. However, considering the values for the goodness of fit it is possible that some elastic distortion has occurred within the crystal lattice leading to a change in the d spacing and hence the axis parameters. [13] When comparing the XRD patterns of the HA samples synthesised with branched PAA or PMAA via the Prakash method each sample shows some differences most likely caused by the inclusion of polymer during synthesis which could lead to crystal lattice disruption. The main difference seen between the samples is the difference in peak sharpness as shown by the powder patterns in figure 4.10.

The sharper peaks seen at 26.1 and 53.3 ° 2θ, indicating planes (002) and (004) respectively, in the diffraction patterns of HA + 1 wt% PMAA-VPC and HA + 1 wt% PMAA-VBD indicate an elongation of the particles along the c axis. Samples HA + 1 wt% PMAA-VPC and HA + 1 wt% PMAA-VBD have sharper peaks across the whole diffraction pattern compared to HA + 1 wt% PAA-VPC and HA + 1 wt% PAA-VBD suggesting that either the particles in the HA + 1 wt% PMAA-VPC and HA + 1 wt% PMAA-VBD samples are larger and more crystalline, or there are nanoscale interactions present within the HA + 1 wt% PAA-VPC and HA + 1 wt% PAA-VPC samples which do not occur in HA + 1 wt% PMAA-VPC and HA + 1 wt% PMAA-VBD. Peak broadening due to instrument parameters is unlikely as all samples were run on the same instrument with identical set up and timings. In order to say for sure whether the HA + 1 wt% PAA-VPC and HA + 1 wt% PAA-VBD are smaller than the HA + 1 wt% PMAA-VPC and HA + 1

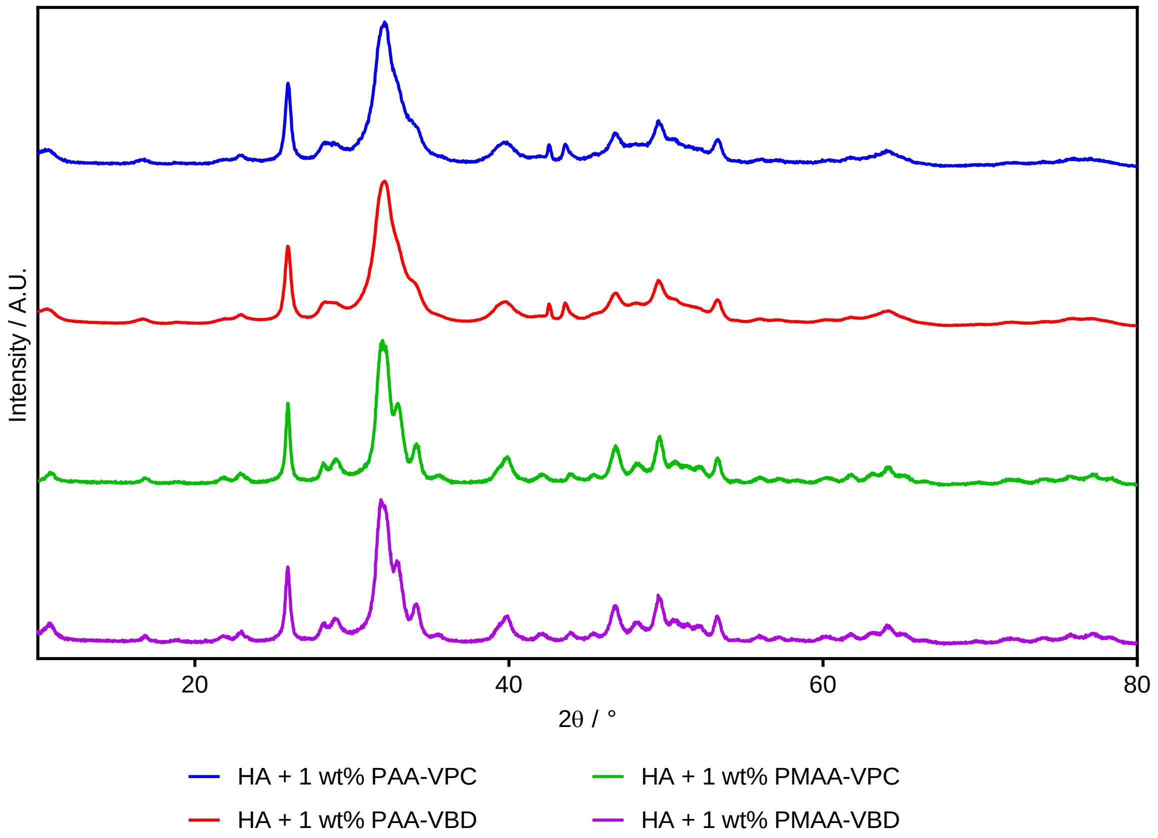

Figure 4.10. Powder diffraction patterns of samples of hydroxyapatite synthesised by the Prakash method in the presence of PAA or PMAA.

wt% PMAA-VBD samples, it is necessary to look at the TEM micrographs and particle sizes determined from them.

4.3.7.3 Thermogravimetric analysis (TGA)

TGA analysis was conducted to determine the percentage weight of polymer within the composite materials. Figure 4.11 shows the thermogravimetric curves for the PAA (HA + 1 wt% PAA-VPC and VBD) and PMAA samples (HA + 1 wt% PMAA-VPC and VBD) while table 4.15 shows the overall percentage mass loss of each sample.

Table 4.15. Mass loss calculated from the 320-420 °C region of the thermogravimetric curves of composite samples of hydroxyapatite synthesised using the Prakash method in the presence of 1 wt% P(M)AA to determine the percentage weight of polymer in the samples.

Sample	Initial weight %	Final weight %	Mass loss / %
HA + 1 wt% PAA-VPC	92.12	91.12	1.00
HA + 1 wt% PAA-VBD	91.59	90.75	0.84
HA + 1 wt% PMAA-VPC	97.37	96.37	1.00
HA + 1 wt% PMAA-VBD	96.94	95.80	1.14

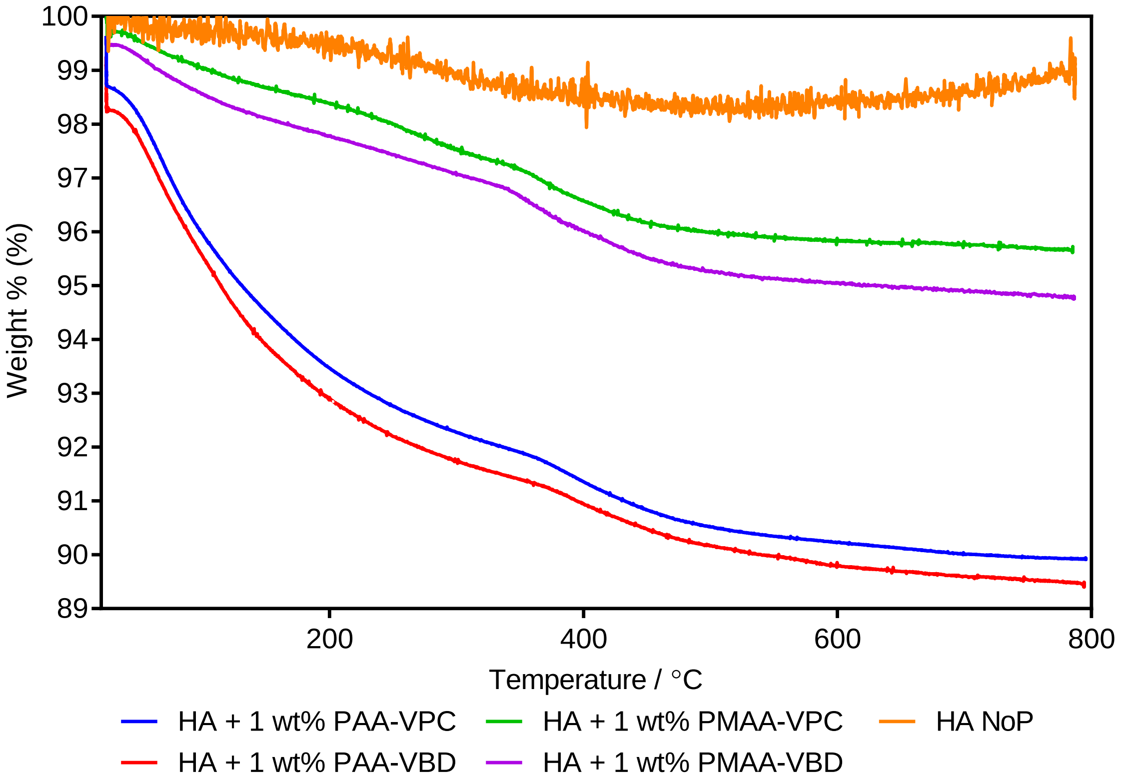

Figure 4.11. TGA thermogravimetric curves showing the mass lost with increasing temperature of composite samples of hydroxyapatite synthesised using the Prakash method in the presence of 1 wt% P(M)AA. A control curve showing HA with no polymer has been included for reference.

The mass loss seen in the samples containing PAA was almost double that of the PMAA samples. The reason for this is not immediately apparent. Drawing on evidence from the XRD analysis which suggests that the PMAA samples are more crystalline than the PAA samples, it could be that the polymer is so ingrained in the PMAA composite materials that it cannot be lost when the material is heated. However, the opposite may be true; it is possible that the PMAA was not incorporated at all into the composite material producing pure hydroxyapatite instead. This is unlikely as the FTIR spectrum of the PMAA samples showed the inclusion of the COO group which can only be attributed to the inclusion of polymer. The inflection between 320-420 °C can be attributed to the loss of polymer as this is a standard point at which organic material is lost during TGA and the sharp drop in mass in this temperature range shows that the material is lost quickly as would be expected when the polymer burns. The data in table 4.15 show approximately 1 wt% mass loss in this region which would also be expected from the amount of polymer included in the synthesis of the composite particles. The FTIR spectra of all samples also showed a large OH peak attributed to adsorbed water. The mass lost between 20-320 °C can be attributed to the loss of adsorbed water because HA nanoparticles are hygroscopic and as a result may have taken on extra moisture which could have resulted in differences in the percentage mass lost during thermogravimetric analysis. In order to test this, moisture analysis was conducted on the samples before they were re-analysed by TGA. Figure 4.12 shows the TGA thermogravimetric curves of the moisture analysed samples and Table 4.16 summarises the percentage mass loss of each sample following moisture analysis.

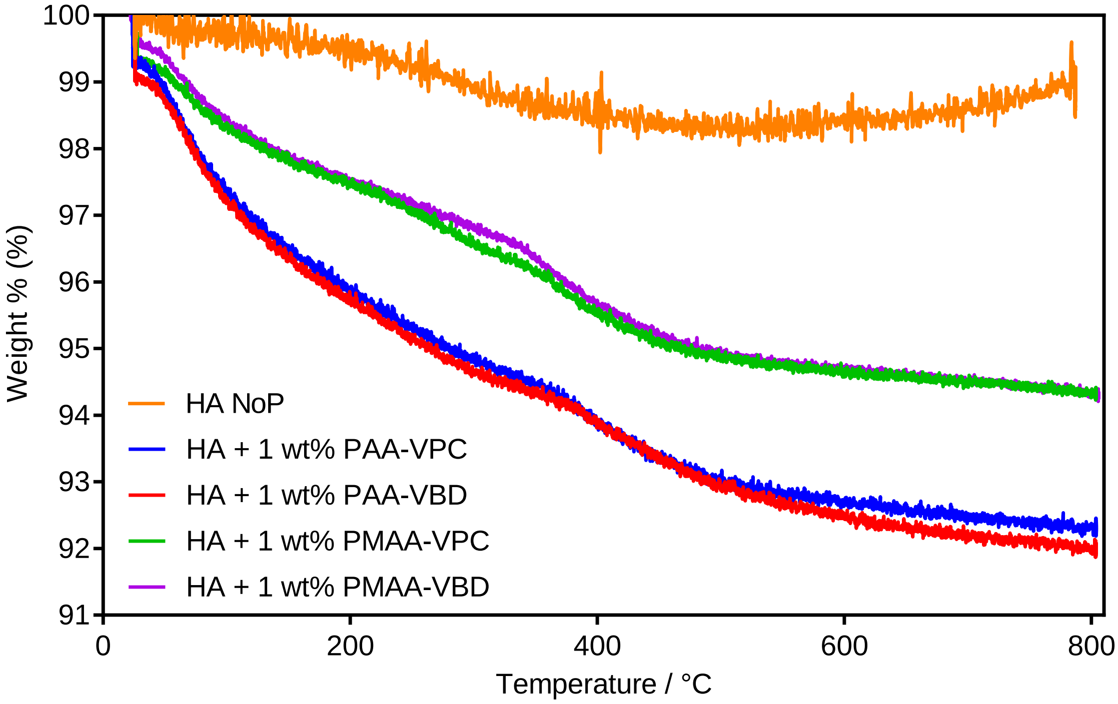

Figure 4.12. TGA thermogravimetric curves showing the mass lost with increasing temperature of composite samples of hydroxyapatite synthesised using the Prakash method in the presence of 1 wt% P(M)AA after moisture analysis. A control curve showing HA with no polymer has been included for reference.

Table 4.16 indicates that the mass lost during TGA after moisture analysis was very similar to the results when the samples were run without moisture analysis. However, samples HA + 1 wt% PMAA-VPC and HA + 1 wt% PMAA-VBD, still show a greater mass loss than the PAA samples, HA + 1 wt% PAA-VPC and HA + 1 wt% PAA-VBD whereas the TGA thermograms show an overall greater mass loss in the PAA samples.

This indicates that something intrinsic to the sample, such as crystallinity or the inclusion of polymer is more likely to be the cause of the discrepancy as opposed to the water content of the samples. This also proves that the mass loss during the TGA is not simply due to the loss of water, suggesting that the polymer has been incorporated into the sample either as a coating or within the crystal structure. Again, the evidence from the XRD analysis showing a

Table 4.16. Mass loss calculated from the 320-420 °C region of the TGA thermogravimetric curves of composite samples of hydroxyapatite synthesised using the Prakash method in the presence of 1 wt% P(M)AA after moisture analysis. Percentage mass lost during moisture analysis is also shown

Sample	TGA 320-420 °C		
	Initial weight / %	Final weight / %	Mass loss / %
HA + 1 wt% PAA-VPC	94.59	93.68	0.91
HA + 1 wt% PAA-VBD	94.51	93.71	0.80
HA + 1 wt% PMAA-VPC	96.44	95.33	1.11
HA + 1 wt% PMAA-VBD	96.64	95.49	1.15

lack of crystallinity in some samples and the elongation of the 00l plane implies that the polymer has been incorporated into the crystal lattice as opposed to coating the surface of the particles, hence causing differences in the crystal structure which make them more stable at higher temperatures.

4.3.7.4 Transmission Electron Microscopy (TEM)

Transmission Electron Microscopy was used to visualise the particles. From this the size, morphology and particle dispersion of the composite were analysed. Particle sizes were measured using ImageJ[4] and are quoted in table 4.17 while the TEM images are shown in figure 4.13.

Table 4.17. Particle lengths and widths measured using ImageJ software and the aspect ratios calculated as a result.

Sample	Lengths / nm			Widths /nm			Aspect ratios
	Mean	SD	SE	Mean	SD	SE	
HA + 1 wt% PAA-VPC	23.938	4.588	0.210	10.741	2.604	0.259	2.2
HA + 1 wt% PAA-VBD	20.784	4.124	0.193	7.464	1.874	0.186	2.8
HA + 1 wt% PMAA-VPC	34.075	5.448	0.271	11.571	1.764	0.176	2.9
HA + 1 wt% PMAA-VBD	30.496	5.118	0.294	11.201	2.046	0.204	2.7
Control	33.357	8.707	0.433	16.806	3.368	0.335	2.0

All of the micrographs in figure 4.13 show clear signs of aggregation even after sonication during the preparation of TEM grids. Particle sizes and aspect ratios were similar across all samples with the samples containing PAA measuring slightly smaller than those synthesised with PMAA. Samples containing PMAA also appeared to show less aggregation than the PAA samples. This may be related back to the marginally smaller size as smaller particles have a larger surface area to volume ratio which makes them more reactive; as a result, the smaller

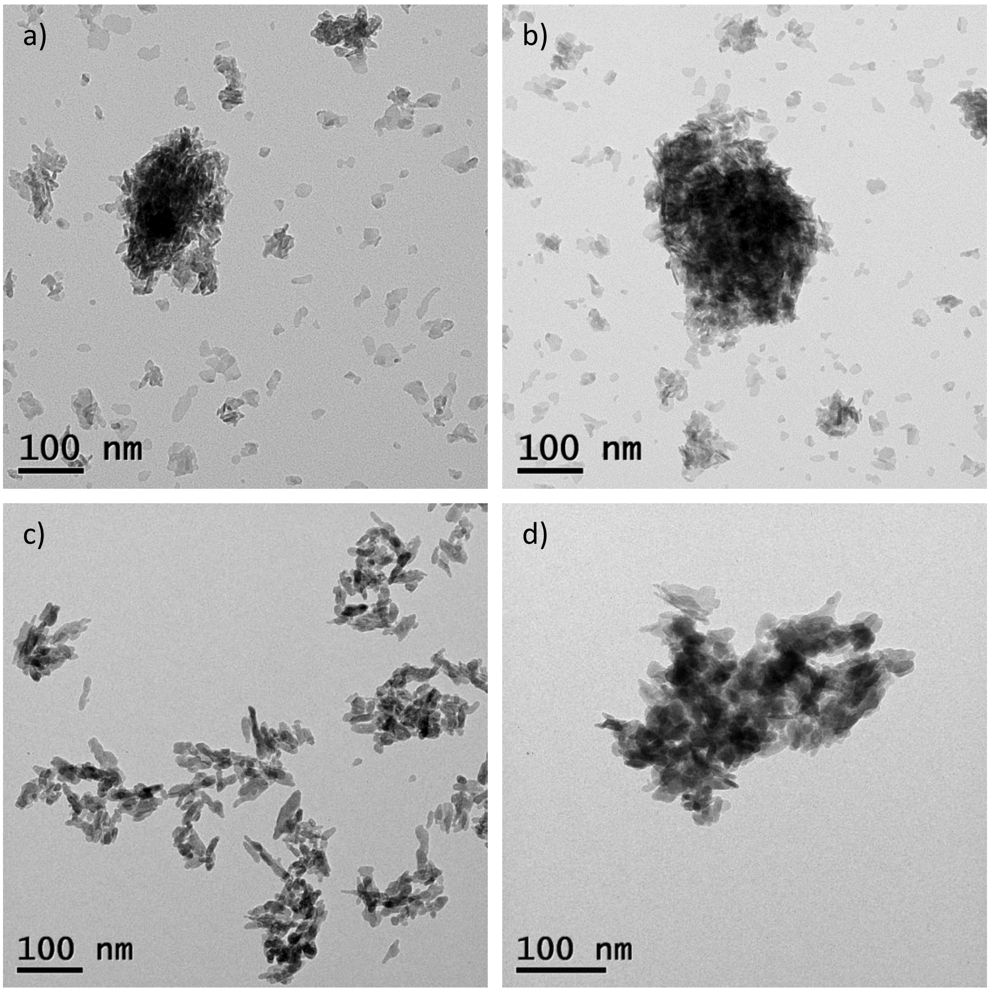

Figure 4.13. TEM micrographs of a) HA + 1 wt% PAA-VPC, b) HA + 1 wt% PAA-VBD, c) HA + 1 wt% PMAA-VPC and d) HA + 1 wt% PMAA-VBD.

particles are more likely to aggregate together than particles with larger dimensions. This has also been observed previously[14] and could also be due to the charged polymer forming conduits between particles causing them to flocculate. TEM images of the PAA treated HA were also compared with TEM images of pure HA donated by Caroline Wilcock (see figure 4.2 (e and f) earlier in the chapter). These showed a change in morphology from the plate-like shape seen in the pure HA sample to a needle-like morphology in the polymer treated HA samples as shown by the increase in aspect ratio; while the sizes of the particles remain relatively consistent. This is an interesting result as it suggested that the polymer binds to a specific face of the HA during the crystal formation causing elongation along one axis. This supports the XRD findings which suggested elongation of the crystal lattice along the 00l plane and is consistent with previous findings during similar investigations in the literature.[14, 15]

4.4 Chapter Conclusion

Calcium deficient hydroxyapatite was synthesised using the modified Prakash method of a wet precipitation of calcium hydroxide and phosphoric acid under basic conditions. The calcium deficient nature of the HA was investigated while medical grade micro and nanoHA were sourced for use in initial experiments to form coatings around the ceramic particles.

Using a carousel reactor, a method of including HA particles in a polymerisation solution was investigated. This method proved that the acidic conditions of the polymerisation degraded the HA particles. The resulting mixtures could not be purified and analysis of the crude mixtures was found to be inconclusive. For these reasons, this method was abandoned and an acid stability study was conducted on fluorapatite.

A second study using the carousel reactor to mix preformed particles with pre-synthesised polymers in solution faired marginally better as the particles were not degraded by an acidic environment. This approach was extended to test the more acid stable fluorapatite samples. Fluorapatite was successfully synthesised and characterised using the Chen method. Particles were then mixed with polymers in the same manner as the hydroxyapatite particles. Some evidence of particle coating was observed; however, the results were inconclusive due to the solvated method of analysis causing particle aggregation and causing erroneous readings as a result. The issues with purification also remained and no real evidence of coating was observed. In reaction to this, this method was abandoned in favour of incorporating polymers into the synthesis of HA nanoparticles.

The addition of polymers into the synthesis of HA was successful and the particles were able to be purified and characterised. Characterisation by FTIR, XRD, TGA showed that HA had formed with the inclusion of polymer in the crystal lattice creating a composite material rather than coated particles. Comparison of these particles by TEM with pure samples of HA showed some morphological differences which were attributed to the inclusion of polymer in the HA crystal lattice. With the success of this approach the idea of including the polymer in the synthesis of HA was taken further in order to test whether the same particles could be reached using a different, more robust protocol as outlined in the next chapter.

4.5 References

1. K. H. Prakash, R. Kumar, C. P. Ooi, P. Cheang and K. A. Khor, *Langmuir*, 2006, **22**, 11002-11008.
2. Y. M. Chen and X. G. Miao, *Biomaterials*, 2005, **26**, 1205-1210.
3. L. Berzina-Cimdina and N. Borodajenko, *Research of Calcium Phosphates Using Fourier Transform Infrared Spectroscopy InTech*, 2012.
4. C. A. Schneider, W. S. Rasband and K. W. Eliceiri, *Nature Methods*, 2012, **9**, 671-675.
5. E. Champion, *Acta Biomaterialia*, 2013, **9**, 5855-5875.
6. S. Nayar, M. K. Sinha, D. Basu and A. Sinha, *Journal of Materials Science-Materials in Medicine*, 2006, **17**, 1063-1068.
7. D. Shi, *Introduction to Biomaterials*, Tsinghua University Press, 2006.
8. M. Euvrard, A. Martinod and A. Neville, *Journal of Crystal Growth*, 2011, **317**, 70-78.
9. P. B. Y. Ofir, R. Govrin-Lippman, N. Garti and H. Furedi-Milhofer, *Crystal Growth & Design*, 2004, **4**, 177-183.
10. J. A. M. van der Houwen, G. Cressey, B. A. Cressey and E. Valsami-Jones, *Journal of Crystal Growth*, 2003, **249**, 572-583.
11. V. Uskokovic and T. A. Desai, *Journal of Biomedical Materials Research Part A*, 2013, **101A**, 1416-1426.
12. M. I. Kay, R. A. Young and A. S. Posner, *Nature*, 1964, **204**, 1050-1052.
13. T. Engelder, *Stress regimes in the lithosphere*, Princeton University Press., Princeton University Press., 2014.
14. K. J. Roche and K. T. Stanton, *Journal of Crystal Growth*, 2015, **409**, 80-88.
15. K. J. Roche and K. T. Stanton, *Journal of Fluorine Chemistry*, 2014, **161**, 102-109.

Chapter 5 – The effect of polymer architecture and molecular weight on the formation of (fluor)hydroxyapatite particles using poly(acrylic acid) additives

5.1 Chapter Summary

Following the issues with the Prakash method a new technique was sought to synthesise hydroxyapatite (HA) and fluorhydroxyapatite (FHA) which could be modified to include polymer additives. At the same time, a two-week placement was undertaken at University College Dublin (UCD).

The aim of the two week placement was to synthesise six different batches of apatite nanoparticles with varying levels of fluoride substitution and linear poly(acrylic acid) additives to determine their effects on the crystal size, morphology and unit cell of the apatite crystallites. The technique was then extended to test the hyperbranched polymers synthesised in chapter 3 to act as a comparison with HA and FHA produced using the Prakash method. The apatite samples were analysed using x-ray diffraction (XRD), fourier transform infrared spectroscopy (FTIR) and thermogravimetric analysis. The nanoparticles were also imaged via transmission electron microscopy (TEM) and size analysis was carried out using the software ImageJ[1, 2].

XRD and FTIR analysis was conducted on the linear and no polymer samples at UCD. This analysis was repeated upon returning to Sheffield in order to ensure that the samples could be directly compared to other samples produced using the Dublin methodology.

5.2 Experimental

5.2.1 Synthesis of fluorhydroxyapatite and hydroxyapatite varying linear poly(acrylic acid) additive addition (UCD)

Samples of fluorhydroxyapatite and hydroxyapatite were prepared with an aqueous solution of poly(acrylic acid) (PAA) with approximate molecular weights of either 9000 Da (E5) or 210000 Da (E11) to give an expected solids content of 4 wt% in the final composite. Control samples containing no PAA were also synthesised. Masses of chemicals used in each instance can be found in table 5.1, the synthetic protocol was identical in each instance.

A three necked round bottom flask (250 ml) was fitted with a condenser and a heat probe. The flask was charged with a solution of di-ammonium hydrogen orthophosphate ($(NH_4)_2HPO_4$, 4 g, 30 mmol) and poly(acrylic acid) 25 % solution of either E5 or E11 (0.8 g, 2×10^{-2} and 1×10^{-3} mmol respectively) in deionised water (100 ml) and heated to boiling while stirring. The solution was then adjusted to pH 10 by the addition of 32 % ammonium hydroxide solution and monitored with a pH probe. A solution of calcium chloride ($CaCl_2$, 5.5 g, 50 mmol) in deionised water (100 ml) was adjusted to pH 10 by the addition of 32 % ammonium hydroxide solution. The calcium solution was then added to the phosphate solution via a peristaltic pump over half an hour forming a milky suspension. The boiling suspension was left to stir for one hour at 85 ^{o}C, the heat was then turned off and the solution left to stir for 23 hours at room temperature. The suspension was then centrifuged at 20000 rpm until the solid had settled; the remaining solution was then decanted off and replaced with fresh deionised water. This washing step was repeated three times. Half of the sample was then resuspended in deionised water and stored while the other half was placed on a watch glass and dried overnight in an oven at 60 ^{o}C. The dried solid was ground in a pestle and mortar into a fine white powder then stored. Ammonium fluoride (NH_4F, 0.23 g, 6 mmol) was included in the initial phosphate solution when synthesising fluorhydroxyapatite. Poly(acrylic acid) was not included in samples of fluorhydroxyapatite and hydroxyapatite (sample name FHA-NoP and HA-NoP respectively) to act as a control.

Table 5.1. Masses of the chemicals used in the synthesis of six batches of substituted apatites using linear polymers of low and high molecular weight poly(acrylic acid) (E5 and E11 respectively).

Sample	$CaCl_2$ / g	$(NH_4)_2HPO_4$ / g	NH_4F / g	E5 / g	E11 / g
FHA-E5	5.551	3.993	0.234	0.812	---
FHA-E11	5.556	4.012	0.235	---	0.813
FHA-NoP	5.553	4.003	0.231	---	---
HA-E5	5.552	3.997	---	0.804	---
HA-E11	5.557	4.011	---	---	0.811
HA-NoP	5.555	4.001	---	---	---

5.2.2 Synthesis of fluorhydroxyapatite and hydroxyapatite with no polymer additives (UoS)

The method used was the same as described in section 5.2.1 for the synthesis of the (F)HA NoP samples. These samples were used as a control to determine whether the batches of chemicals used in the synthesis at UCD and UoS produced any major differences. Table 5.2 gives the masses used for the synthesis of the samples.

Table 5.2. Masses of the chemicals used in the synthesis of batches of fluorhydroxyapatite and hydroxyapatite with no polymer additives at UoS as a comparison to the (F)HA NoP samples synthesised at UCD.

Sample	$CaCl_2$ / g	$(NH_4)_2HPO_4$ / g	NH_4F / g
FHA NoP (S)	5.552	3.997	0.231
HA NoP (S)	5.551	4.002	---

5.2.3 Synthesis of fluorhydroxyapatite and hydroxyapatite varying highly branched poly(acrylic acid) additive addition

(F)HA samples were synthesised using the method described in section 5.2.1; with highly branched poly(acrylic acid)s made using RAFT polymerisation as described in chapter 3, PAA-VPC and PAA-VBD. Table 5.3 gives the masses used for the synthesis of each sample. Samples are labelled as either 0.2 wt% or 0.8 wt% which refer to the amount of polymer used in solution for the synthesis. These translate to 4 wt% and 16 wt% respectively of the maximum product yield. The actual value of the weight percentage of polymer incorporated into the composites will be calculated from the thermogravimetric analysis. Analysis by XRD, FTIR and TEM was also carried out to characterise the composite materials.

Table 5.3. Masses of the chemicals used in the synthesis of six batches of substituted apatites using hyperbranched polymers of poly(acrylic acid) made with either 4-vinylbenzyl pyrrolecarbodithioate (VPC) or 4-vinylbenzyl dithiobenzoate.

Sample	$CaCl_2$ / g	$(NH_4)_2HPO_4$ / g	NH_4F / g	PAA-VPC / g	PAA-VBD / g
HA PAA-VPC 0.2 wt%	5.543	3.999	---	0.203	---
HA PAA-VBD 0.2 wt%	5.577	3.987	---	---	0.208
FHA PAA-VPC 0.2 wt%	5.561	3.992	0.234	0.202	---
FHA PAA-VBD 0.2 wt%	5.546	4.031	0.232	---	0.207
HA PAA-VPC 0.8 wt%	0.556	0.395	---	0.0821	---
HA PAA-VBD 0.8 wt%	0.553	0.399	---	---	0.0814
FHA PAA-VPC 0.8 wt%	0.553	0.398	0.026	0.0824	---
FHA PAA-VBD 0.8 wt%	0.550	0.398	0.028	---	0.0810

5.2.4 Synthesis of fluorhydroxyapatite and hydroxyapatite varying highly branched poly(methacrylic acid) additive addition

The synthesis was carried out as described in section 5.2.1 using highly branched poly(methacrylic acid)s made using RAFT polymerisation, PMAA-VPC and PMAA-VBD. Table 5.4 gives the masses used for the synthesis of each sample. Samples are labelled as described in section 5.2.4 referring to the amount of polymer used in solution for the synthesis. The actual value of the weight percentage of polymer incorporated into the composites will be calculated from the thermogravimetric analysis. Further characterisation of the materials was carried out using XRD, FTIR and TEM.

Table 5.4. Masses of the chemicals used in the synthesis of six batches of substituted apatites using hyperbranched polymers of poly(methacrylic acid) made with either 4-vinylbenzyl pyrrolecarbodithioate (VPC) or 4-vinylbenzyl dithiobenzoate.

Sample	**$CaCl_2$ / g**	**$(NH_4)_2HPO_4$ / g**	**NH_4F / g**	**PMAA-VPC / g**	**PMAA-VBD / g**
HA PMAA-VPC 0.2 wt%	0.555	0.397	---	0.0215	---
HA PMAA-VBD 0.2 wt%	0.558	0.403	---	---	0.0209
FHA PMAA-VPC 0.2 wt%	0.553	0.397	0.0282	0.0215	---
FHA PMAA-VBD 0.2 wt%	0.558	0.395	0.0231	---	0.0210
HA PMAA-VPC 0.8 wt%	0.559	0.397	---	0.0812	---
HA PMAA-VBD 0.8 wt%	0.554	0.400	---	---	0.0813
FHA PMAA-VPC 0.8 wt%	0.553	0.400	0.024	0.0814	---
FHA PMAA-VBD 0.8 wt%	0.552	0.398	0.023	---	0.0816

5.3 Results and Discussion

5.3.1 Synthesis and characterisation of fluorhydroxyapatite and hydroxyapatite in the presence of linear poly(acrylic acid) additives

(Fluor)hydroxyapatite nanoparticles were synthesised with linear poly(acrylic acid) additives of low and high molecular weight 9000 Da (E5) and 210,000 Da (E11) respectively. The synthetic method used to produce the nanoparticles was different to that described in chapter 4. In this instance the synthesis of the (F)HA particles used a controlled addition method via a syringe pump. The method was developed by Dr Kevin Roche and uses aqueous solutions of all reactants as opposed to solids. The linear polymers were added to the synthesis as a 0.2 wt% solution which corresponded to 4 wt% of total output solids. An aqueous solution of $CaCl_2$ was added via syringe pump to an aqueous solution of $(NH_4)_2HPO_4$ and PAA; in the case of FHA synthesis a solution of NH_4F was added to the phosphate solution. Addition of the calcium solution to the phosphate solution produced a precipitate which was stirred overnight then washed and dried. The particles were analysed by XRD, FTIR, TGA and TEM.

As the F(HA) samples containing linear or no polymer (E5, E11 and NoP) were synthesised at UCD, analysis by XRD and FTIR was conducted twice using separate instrumentation at UCD and again at the University of Sheffield (UoS) so as to be comparable to the other samples described later in this chapter. The XRD analysis at UCD was used to determine crystallite sizes via Rietveld refinement using an internal silicon standard. FTIR measurements were conducted using precisely measured amounts of sample and KBr so as to be able to directly compare the spectra. Upon returning to UoS XRD analysis was conducted without an internal standard and an external standard was used in its place. This technique prevented crystallite sizes from being calculated; however, it allowed Pawley refinement to be conducted alongside Rietveld refinements using the TOPAS programme developed by Bruker. This method allowed the validity of the refinements conducted using the external standard method to be determined which improved confidence in the data. Rietveld refinements conducted using the internal standard method and MAUD refinement programme are valid on their own, yet the external standard method must be used to compare the data to samples synthesised at UoS using hyperbranched polymers. Internal standards could not be used during XRD analysis at UoS due to the time and resources needed to analyse and refine the internal standards before analysing the (F)HA particles. This was due to the lack of availability on the machines at UoS. As a result, the less time consuming external standard method was used in its place. Thermogravimetric analysis (TGA) and transmission electron microscopy (TEM) were also conducted on the samples at UoS to determine the percentage weight of polymer in the samples and the size and morphology of the particles respectively.

5.3.1.1 X-ray Diffraction with internal silicon standards

Rietveld refinement was performed on the XRD patterns collected at UCD with an internal silicon standard using the MAUD refinement program[3]. Rietveld refinement constructs a mathematical model of the crystal which accounts for the crystal space group, size and shape; lattice parameters, atomic positions and other parameters that can affect the diffraction pattern.[4] A pattern is then calculated based on this model and compared to the measured XRD pattern of the sample. The model can be refined by the least squares method until a good fit is produced at which point the calculated pattern is said to represent the sample. Care should be taken during the fitting process to ensure that the refined parameters are chemically and physically realistic. The fitting process is entirely mathematical and can refine parameters to give the best fit even if the parameters are physically impossible.[4, 5] As a result, some parameters must manually be set close to their true values before refinement begins to avoid unrealistic values. Estimated standard deviations (esd) of the parameters are calculated as part of the refinement process to represent the precision of the result. However, they do not include systematic errors and cannot be considered as a true estimate of the accuracy of the fit.[4, 5] The starting models for hydroxyapatite and fluorapatite were taken from Hughes *et al.*[6] and the background, phase composition, unit cell, and size-strain parameters were refined. Popa rules[7] were used for the size-strain parameters which limits the crystal shapes that can be modelled. This may lead to minor errors, but gives a more stable refinement and more reproducible comparison between samples due to the small number of fitting parameters.[4, 5, 7] A separate scan of lanthanum hexaboride (LaB_6) was used to calibrate the instrument parameters at UCD, which were then fixed for future refinements. The unit cell a-parameter for Si was fixed at 5.43088 Å using Powder diffraction file 00-027-1402: Silicon, 2011 as a reference to allow correction for peak-shift errors. The silicon peak shape parameters were determined using a scan of pure silicon and fixed for subsequent scans.

XRD samples were made up as described in chapter 2 with 45 mg of sample being mixed by hand with 5 mg silicon to act as an internal standard in the resulting pattern. Comparing the XRD patterns of each of the UCD sample shows some differences caused by the inclusion of fluoride ions and polymer. The main difference seen between the inclusion of fluoride and the lack thereof, FHA and HA samples respectively, is a difference in unit cell parameters. Table 5.5 shows the *a* and *c* cell parameters of each sample determined through Rietveld refinement of the XRD patterns.

Table 5.5. Unit Cell parameters and calculated sample weights of apatite samples. σ and R_W refer to the goodness of fit of the data to the refined model. A fit is considered 'good' when $\sigma < 2$ and $R_W < 15$. Rietveld refinement was carried out using the MAUD programme[3].

Sample	**Weight % Si**	**Weight % HA/FHA**	**Cell para *a* / Å**	**Cell para *c* / Å**	**Crystal size**		**σ**	**R_W**
					***h*00 / nm**	**00*l* / nm**		
FHA E5	12.57	87.43	9.4032	6.8849	14.554	47.637	1.5539	9.0030
FHA E11	12.38	87.62	9.4058	6.8843	13.712	42.854	1.5529	8.8311
FHA NoP	9.70	90.30	9.4022	6.8849	20.663	49.412	1.5650	9.0237
HA E5	12.03	87.97	9.4343	6.8806	24.860	61.631	1.4318	8.4563
HA E11	11.65	88.35	9.4361	6.8803	80.636	77.882	1.9855	11.5714
HA NoP	12.08	87.92	9.4339	6.8817	95.386	94.497	1.8659	10.9423

The values of the weight percentage of Si and (F)HA shown in the table give an indication of the crystallinity of the samples. Samples were precisely mixed in a 10:90 ratio of Si: (F)HA. Values of Si greater than 10 wt% indicate the presence of amorphous material in the sample which is invisible to XRD. The value of 9.7 wt% for the Si standard in the FHA NoP sample suggests the sample is fully crystalline as the ratio is in favour of the FHA rather than the Si.

The 0.3 wt% loss of Si is within experimental error and hence the ratio can be treated as 10:90 as initially prepared.

The HA E11 and HA NoP samples showed a much larger crystal size than all of the FHA and the HA E5 samples. This can be attributed to the fact that the OH^- is larger than the F^- ion and hence the crystal size increases in the HA samples. The difference in the size of the OH^- and F^- ions is also evident in the unit cell parameter *a* values which are larger for all the HA samples than the FHA samples. The 0.004 Å difference in the *c* parameter values for all samples showed the inclusion of polymer and substitution of OH^- for F^- had a very minor effect on the c axis of the cell parameter.

Interestingly, table 5.5 also shows that the HA E5 sample is smaller than the HA E11 and HA NoP samples and is more consistent in size with the FHA samples than the HA samples. This may indicate that E5 had some effect on the crystal growth of the HA during synthesis.

Comparing the XRD patterns of all the samples shows some differences. Both the HA and FHA samples containing no polymer showed sharper, more intense peaks when compared with samples containing E5 and E11 (figure 5.1). Peak intensity correlates to atom placement, atom size and occupancy within the unit cell while peak width indicates crystal size and strain.[5, 7] The higher intensity peaks seen in the patterns of samples containing no polymer implies more long range order within the crystals, hence suggesting that the inclusion of the polymer disrupts the packing within the unit cell.[5] Peak position is affected by changes in the unit cell.[5, 7] This is indicated when comparing FHA and HA samples as there is a slight offset of peak position between the two due to the F^- ion substitution into the crystal structure. The fact that the FHA peaks are shifted to a higher angle than the HA peaks shows that there is a smaller degree of strain within the crystal structure of the FHA. This suggests that the substitution of F^- reduces the strain within the crystal unit cell, most likely as the F^- is smaller and fits more easily into the vacant areas of the unit cell. This is supported by the fact that comparison of all the sample patterns shows a small increase in peak intensity in the FHA samples, implying greater long range order.[5]

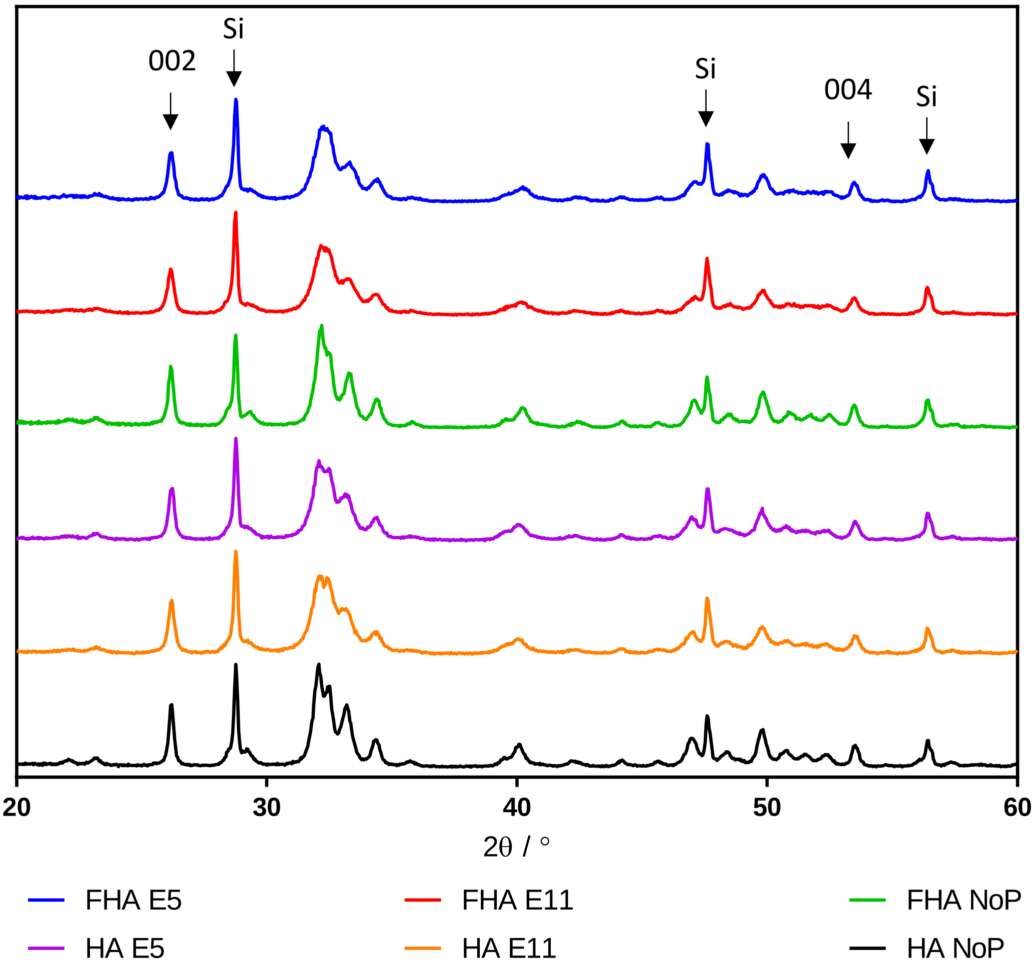

Figure 5.1. XRD patterns collected at UCD of (F)HA containing low molecular weight linear PAA (E5), high molecular weight linear PAA (E11) and no polymer (NoP) with an internal silicon standard to act as a reference.

5.3.1.2 X-ray diffraction with an external standard

XRD analysis was also conducted at the University of Sheffield using an external standard method so as to be comparable to other samples synthesised at UoS. The external standard method compares an unknown sample to a known reference sample and does not require the unknown sample to be mixed with any other materials.[8] The external standard method is therefore an attractive technique as it is none destructive. The patterns (figure 5.2) show a very similar trend to those run at UCD; however, there is an increase in sharpness evident in the samples run without the Si reference. This may be due the fact that samples were run for longer than the patterns collected at UCD producing more data points on the pattern. Alternatively, the fact that the samples were ground with the internal standard for the measurements at UCD may have made the particles smaller and hence caused peak broadening, although this is very unlikely.

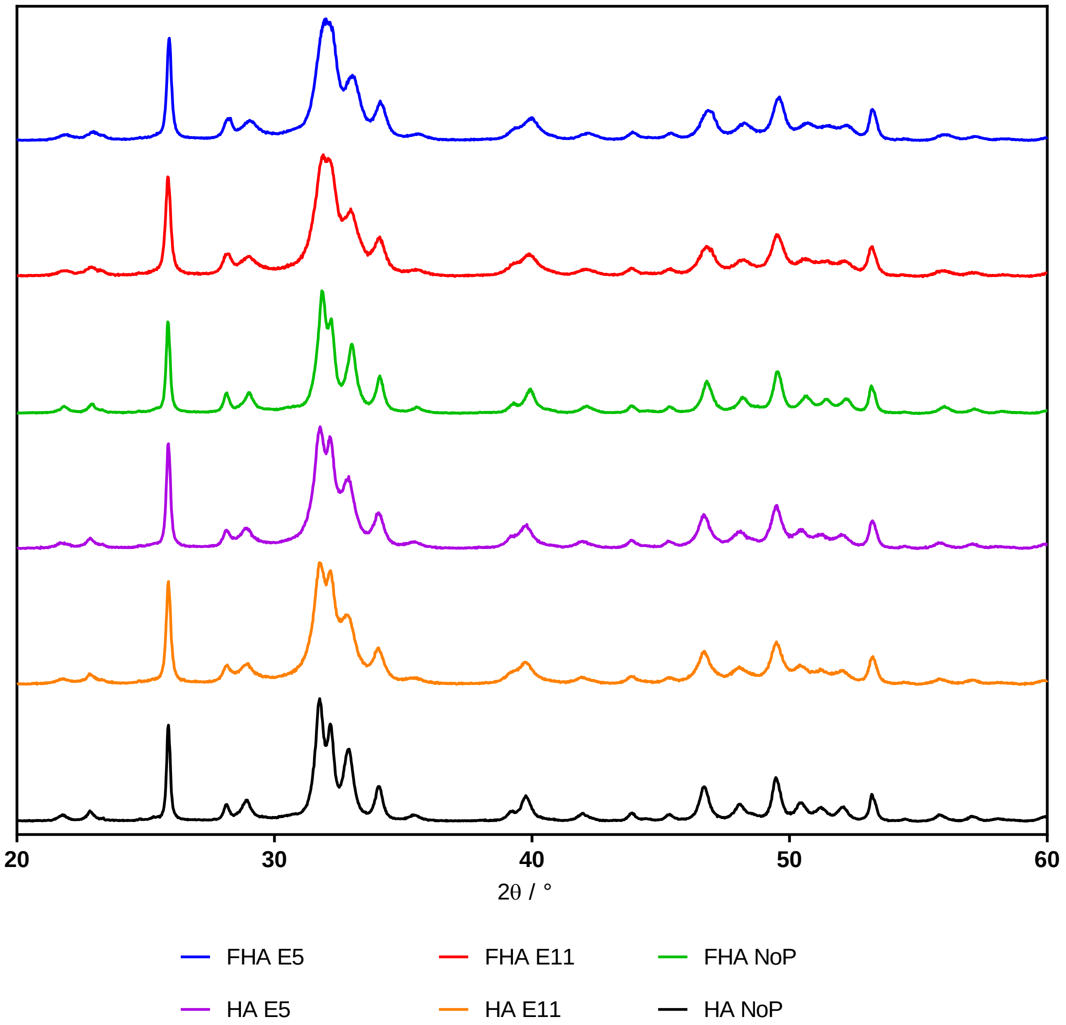

Figure 5.2. XRD patterns collected at UoS of (F)HA containing low molecular weight linear PAA (E5), high molecular weight linear PAA (E11) and no polymer (NoP).

A small peak is also evident at approximately 28° 2θ which was obscured by the Si peak in the previous pattern. Rietveld and Pawley refinements were conducted on the diffraction patterns using TOPAS, the data of which is summarise in table 5.6.[9] The values are very similar to those of the sample run at UCD with the FHA samples having a smaller *a* parameter value and larger *c* parameter value than the HA samples. The 'R factors' R_{wp} and R_{wpb} are the weighted profile residual and weighted profile residual without background respectively. These terms describe the 'goodness of fit' of the data to a known diffraction pattern of the same substance as described in chapter 4.[5] The goodness of fit is quite poor in all cases as denoted by the large R_{wp} and R_{wpb} values. This is to be expected due to the inclusion of the amorphous polymer which does not appear on the diffractograms but has an effect on the unit cell and hence causes changes to the sharpness and intensity of the (F)HA diffraction peaks.

Table 5.6. Cell parameters determined by Pawley and Rietveld refinement of the XRD patterns collected from (F)HA containing low molecular weight linear PAA (E5), high molecular weight linear PAA (E11) and no polymer (NoP). R_{wp} and R_{wpb} are measures of the goodness of fit. Values in brackets after the *a* and *c* axis parameters refer to the standard deviation of the last digit in the value calculated from the refinement.

Sample	Pawley Refinement				Rietveld Refinement			
	a / Å	c / Å	R_{wp}	R_{wpb}	a / Å	c / Å	R_{wp}	R_{wpb}
FHA E5	9.38(1)	6.875(2)	12.21	16.03	9.39(1)	6.88(1)	14.32	20.14
FHA E11	9.39(1)	6.88(1)	11.38	15.07	9.40(1)	6.88(1)	13.50	19.33
FHA NoP	9.39(1)	6.881(1)	11.48	14.79	9.401(4)	6.885(4)	13.51	18.50
HA E5	9.424(1)	6.87(1)	12.01	16.85	9.43(1)	6.88(1)	15.62	23.04
HA E11	9.43(2)	6.87(1)	11.10	15.70	9.44(1)	6.88(1)	14.86	22.21
HA NoP	9.43(1)	6.87(2)	11.52	15.44	9.43(1)	6.881(4)	15.64	22.20

While the peaks are rather broad, the shift in the value of 2θ shows that the compressive strain in the crystal lattice of the FHA samples is slightly greater than in the HA samples. This suggests that the PAA and or the fluoride substitution in the FHA samples causes the unit cell to be compressed in the 211 and 112 planes which is consistent with a smaller atom being placed in the centre of a trio of Ca ions within the crystal lattice as expected with fluoride substitution.

5.3.1.3 Fourier Transform Infrared Spectroscopy

FTIR was used to study the crystal chemistry of FHA and HA and the chemical interactions between the ceramics and PAA. Spectra were recorded using a Bruker Vertex 70 spectrometer (Ettlingen, Germany) in the range 400 - 4000 cm^{-1}. 1 mg of the sample was mixed with 50 mg KBr by hand using a pestle and mortar; the mixture was then pressed into a 12 mm diameter disk under a pressure of 60 MPa for 3 minutes. Samples were stored in a desiccator prior to analysis. Sixty-four scans were recorded for each spectrum and all spectra were baseline corrected with the 'Opus' software package (version 7, Bruker) supplied with the spectrometer. A separate sample of pure KBr was used to create a reference spectrum to establish the background prior to each set of measurements. The spectra were overlaid and compared to determine if any difference was caused by the inclusion of PAA in the samples of FHA and HA.

Samples were made up as stated previously with KBr being mixed with the sample to act as background reference which was removed from all spectra using the OPUS programme. OPUS was also used to normalise all spectra. Comparing the overlaid spectra of the HA and FHA samples (figure 5.3) showed a change in the intensity and shape of the OH^- (approximately

3400 cm^{-1}) and PO_4^{3-} peaks (approximately 1030 cm^{-1} and 600 cm^{-1}). As all samples were made in exactly the same manner, it is surprising that the peak intensities differ so greatly. This suggests that there is some disruption in the ordering of the crystals which supports the conclusions formed from the XRD data. Comparing the FHA and HA samples showed the apparent loss of peaks at approximately 3560 and 640 cm^{-1} corresponding to OH^-. The loss of this peak shows that the F^- substitution was successful. However, this is not exactly true as the mixture used created a 50:50 OH^- : F^- ratio in the apatite. The peak is not lost entirely however the intensity is reduced to such an extent with the fluoride substitution that it becomes lost in the baseline noise.

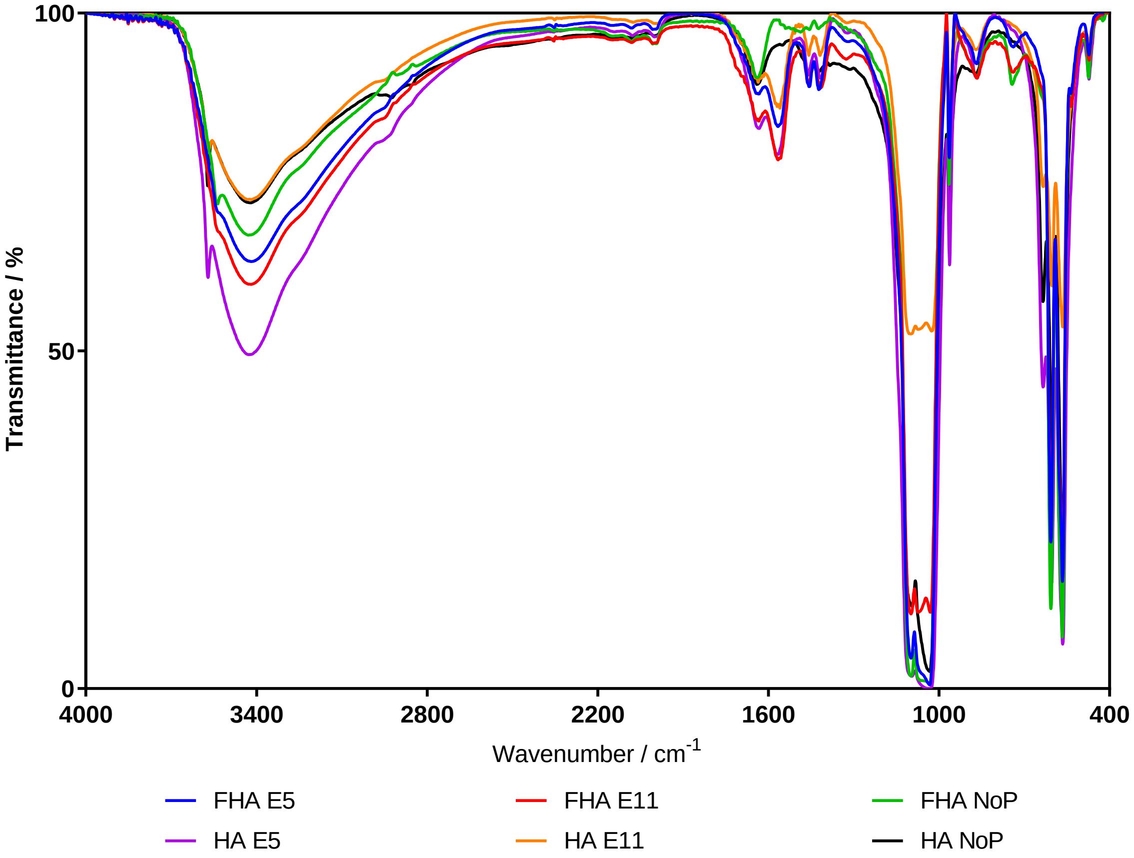

Figure 5.3. Overlaid FTIR spectra of HA and FHA samples treated with low molecular weight PAA (E5), high molecular weight PAA (E11) and no polymer (NoP).

The inclusion of the polymer in the apatite particles is evident from the peaks at 1560 cm^{-1} corresponding to the COO^- of the PAA. These peaks are not evident in the FHA and HA samples which do not contain polymer. Other peaks in this region correspond to CO_3^{2-} which occurs due to the adsorption of CO_2 from the atmosphere onto the particle surface during synthesis.

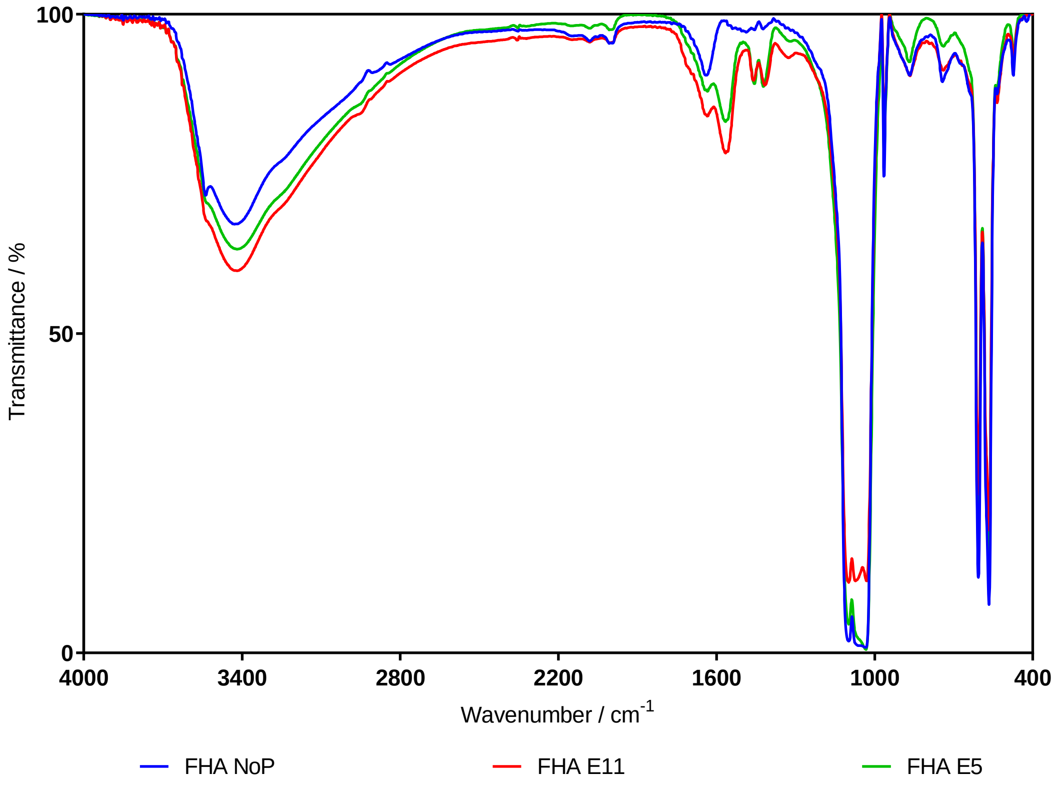

Figure 5.4. Overlaid FTIR spectra of FHA samples treated with low molecular weight PAA (E5), high molecular weight PAA (E11) and no polymer (NoP).

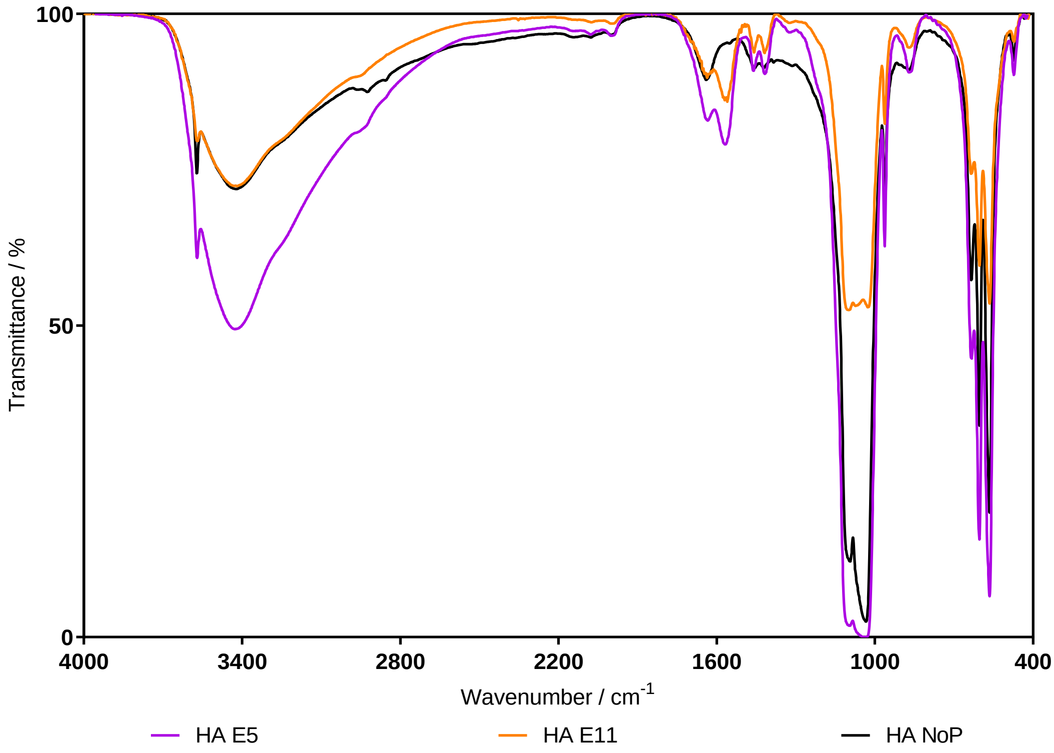

Figure 5.5. Overlaid FTIR spectra of FHA samples treated with low molecular weight PAA (E5), high molecular weight PAA (E11) and no polymer (NoP).

Comparing the FHA and HA samples to determine the change caused by the inclusion / exclusion of polymer (figures 5.4 and 5.5 respectively) showed a definitive difference between samples in the phosphate region of the spectrum (1030 cm^{-1}). The loss of peak sharpness seen in the samples containing E5 and E11 implies a loss of long range order in the crystal structure. Both the FHA and HA samples containing E11 showed a distinct loss in peak intensity and a large amount of peak broadening. This suggests a large degree of hydrogen bonding within the sample which, as it is not evident in the samples containing E5 or no polymer, can be attributed to the phosphate group interacting with the high molecular weight polymer.

An interesting result of comparing the HA samples is the distinct increase in intensity of the E5 sample. As all samples were made up in exactly the same manner this suggests an error in the equipment used. It is possible the balance had not been zeroed before the sample was weighed, or that more sample was in a certain area of the KBr disc increasing the intensity of the spectrum. Alternatively, looking at the crystallite sizes calculated by the Rietveld refinement for the HA samples, they are much smaller for the E5 sample than the samples containing E11 or no polymer. This could indicate that the low molecular weight polymer (E5) exerted some control over the growth of the particles during synthesis, while the high molecular weight polymer (E11) did not.

5.3.1.4 Thermogravimetric Analysis

Thermogravimetric analysis was conducted to determine the percentage weight of polymer within the composite materials. Figure 5.6 shows an overlay of the thermogravimetric curves collected, while table 5.7 summarises the weight loss of each sample. The weight loss calculated from the thermogravimetric curves and drawing on evidence from the XRD analysis suggests that the NoP samples are more crystalline than the E5 and E11 samples.

Table 5.7. Weight loss calculated from the region 320-420 °C of the TGA thermogravimetric curves of HA and FHA samples treated with low molecular weight PAA (E5), high molecular weight PAA (E11) and no polymer (NoP).

Sample	**Initial weight %**	**Final weight %**	**Weight loss / %**
FHA E5	96.40	94.19	2.21
FHA E11	97.04	93.93	3.11
FHA NoP	97.18	96.60	0.38
HA E5	96.60	94.72	1.88
HA E11	95.84	93.20	2.64
HA NoP	97.89	97.57	0.32

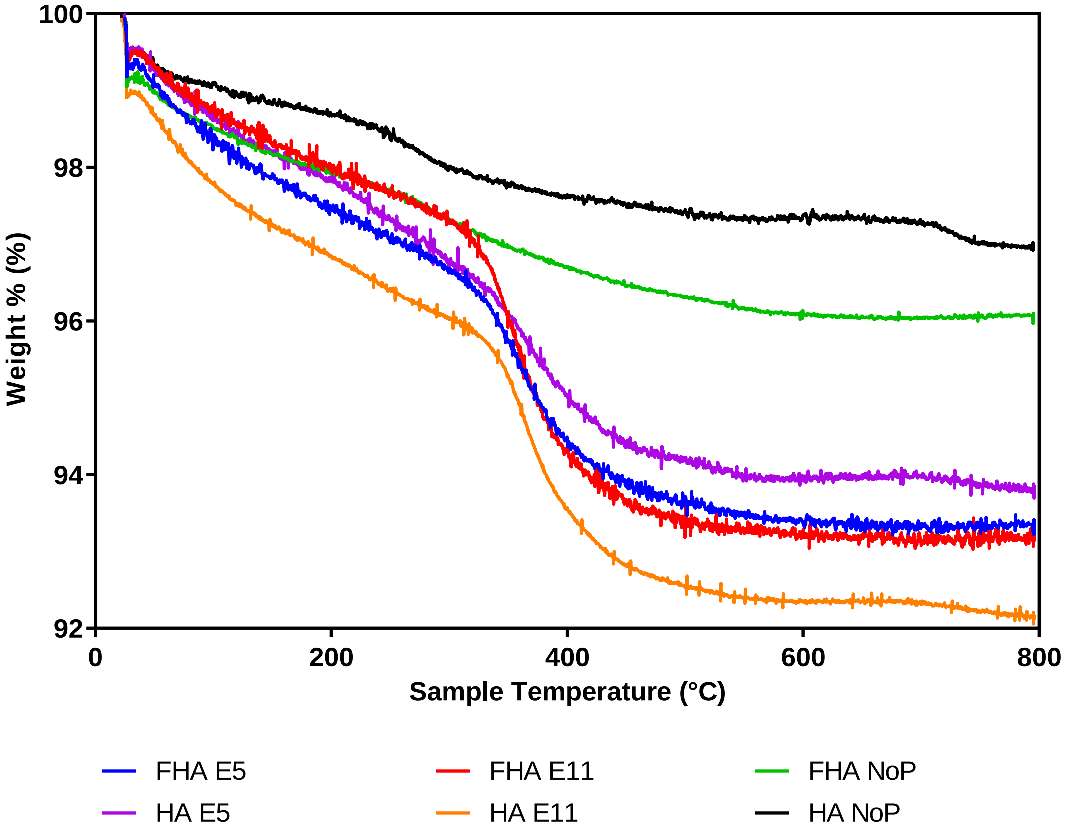

Figure 5.6. Overlaid TGA thermogravimetric curves of HA and FHA samples treated with low molecular weight PAA (E5), high molecular weight PAA (E11) and no polymer (NoP).

The minor weight loss seen in the NoP samples can be attributed to the loss of adsorbed water and CO_2 from the surface of the nanoparticles as the weight loss is consistent across the whole thermogravimetric curve. The weight loss ranging from 1.88 - 3.11 % across the E5 and E11 samples shows that polymer has been included in the samples. The inclusion of a 0.2 wt% solution of the E5 and E11 amounts to effectively 4 wt% of the total theoretical weight of the composite particles. The fact that the weight loss is less than 4 % is unsurprising as it is possible the PAA could have interacted with the calcium ions during the (F)HA synthesis and hence been washed out during processing. The FTIR spectra show a large OH peak across all samples suggesting that residual water is present in the samples even after drying, this is consistent with the sustained weight lost between 20 – 320 °C.

5.3.1.5 Transmission Electron Microscopy

In order to determine whether the linear polymers exerted any form of control over the growth of (F)HA the particles were imaged using transmission electron microscopy (TEM) and particle sizes were determined using ImageJ.[1, 2] These data were then compared to the XRD and FTIR obtained in this study to give a clearer picture of the effect of the PAA polymers on the formation of the FHA and HA particles. To confirm the changes in crystallite size measured by XRD, and determine any effects on crystallite morphology, the (F)HA samples were imaged using transmission electron microscopy. The resulting micrographs were analysed using ImageJ software[2] to determine the dimensions (lengths and widths) and resulting aspect ratios of the particles. The particle lengths, widths and aspect ratios are summarised in table 5.8 while the micrographs of the (F)HA samples are shown in figure 5.7.

Table 5.8. The lengths, widths and aspect ratios (length / width) determined using ImageJ imaging software on the TEM micrographs taken of (F)HA samples synthesised with low molecular weight PAA (E5), high molecular weight PAA (E11) and no polymer (NoP).

Sample	TEM widths / nm			TEM Lengths / nm			Aspect ratios
	Mean	SD	SE	Mean	SD	SE	
FHA E5	15.62	6.94	0.31	89.22	30.20	1.34	5.71
FHA E11	8.35	2.11	0.09	92.98	59.12	2.63	11.14
FHA NoP	17.03	6.75	0.30	81.27	27.34	1.22	4.77
HA E5	21.70	9.87	0.44	164.92	56.32	2.51	7.60
HA E11	20.61	7.83	0.35	167.58	59.44	2.65	8.13
HA NoP	24.84	12.27	0.55	163.48	57.64	2.56	6.58

From the data in table 5.8, it is evident that the HA particles were larger in all cases than the FHA samples. The images of pure FHA and HA showed far less aggregation than the PAA treated samples. This implies that the inclusion of polymer into the sample causes an adhesive effect which means the particles flocculate together. Interestingly, the samples containing no polymer were larger than the other samples with low aspect ratios suggesting their morphology was more plate-like than the needle-like particles seen in the TEM images of samples containing polymer. In contrast, the FHA E11 sample gave particles with a very high aspect ratio, implying the formation of needle like particles, as is evident in figure 5.7. This could be due to the inclusion of the polymer acting as a nucleation site and entering the (F)HA crystal structure causing disruption to the crystal lattice. This is consistent with the findings of Bertoni et al.[10] and Füredi-Milhofer et al.[11] that the inclusion of PAA during the synthesis of HA nanoparticles affects the degree of crystallinity and the morphology of the particles. This is due to the polymer entering the HA nanoparticles during their formation and altering the crystal packing, hence affecting crystal growth by elongating the *a* unit cell parameter and shrinking the *c* unit cell parameter and hence, the morphology of the

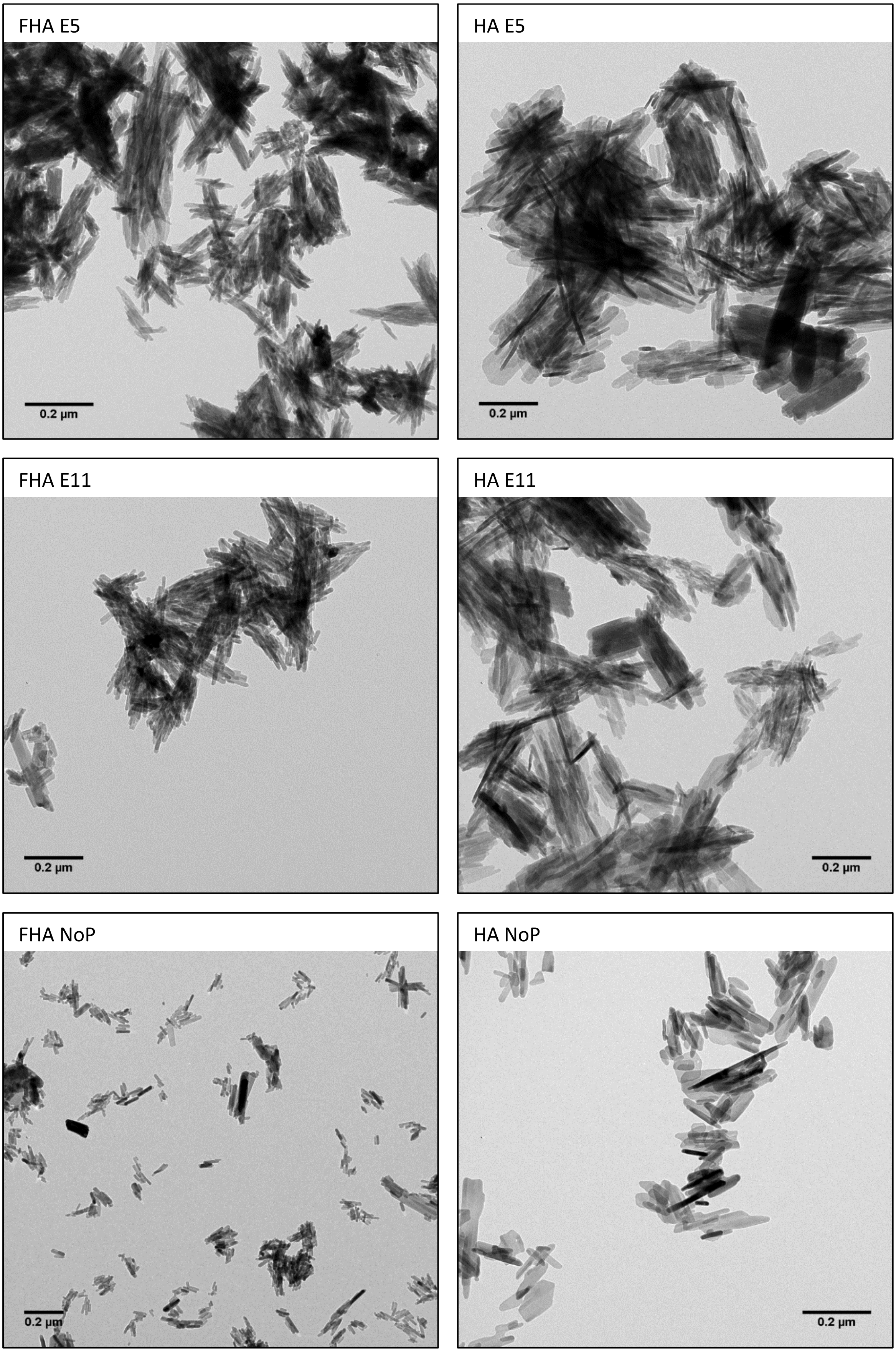

Figure 5.7 TEM micrographs of (F)HA samples synthesised with low molecular weight PAA (E5), high molecular weight PAA (E11) and no polymer (NoP).

particles. The substitution of hydroxyl with fluoride also has an effect on the crystal packing as the fluoride is smaller than the hydroxyl group, hence FHA cell parameters and particles are smaller than those of HA. This supports the evidence given by the XRD patterns of which the polymer substituted particles produce broader spectra than the particles with no polymer. This suggests that the particles are either smaller or less crystalline than the samples with no polymer, hence causing peak broadening. From the analysis conducted on the TEM images, it is more likely that smaller particles are the reason for this peak broadening.

5.3.2 Synthesis of fluorhydroxyapatite and hydroxyapatite without polymer additives (UoS)

In order to ensure the protocol used to synthesise the composite materials at UCD was viable upon return to UoS two samples of HA and FHA were synthesised without any additional polymer. Characterisation of the particles was conducted using XRD, FTIR, TGA and TEM analysis.

5.3.2.1 X-ray Diffraction

XRD analysis was conducted using an external standard method so as to be comparable to other samples described in this chapter, the diffraction patterns are shown in figure 5.8.

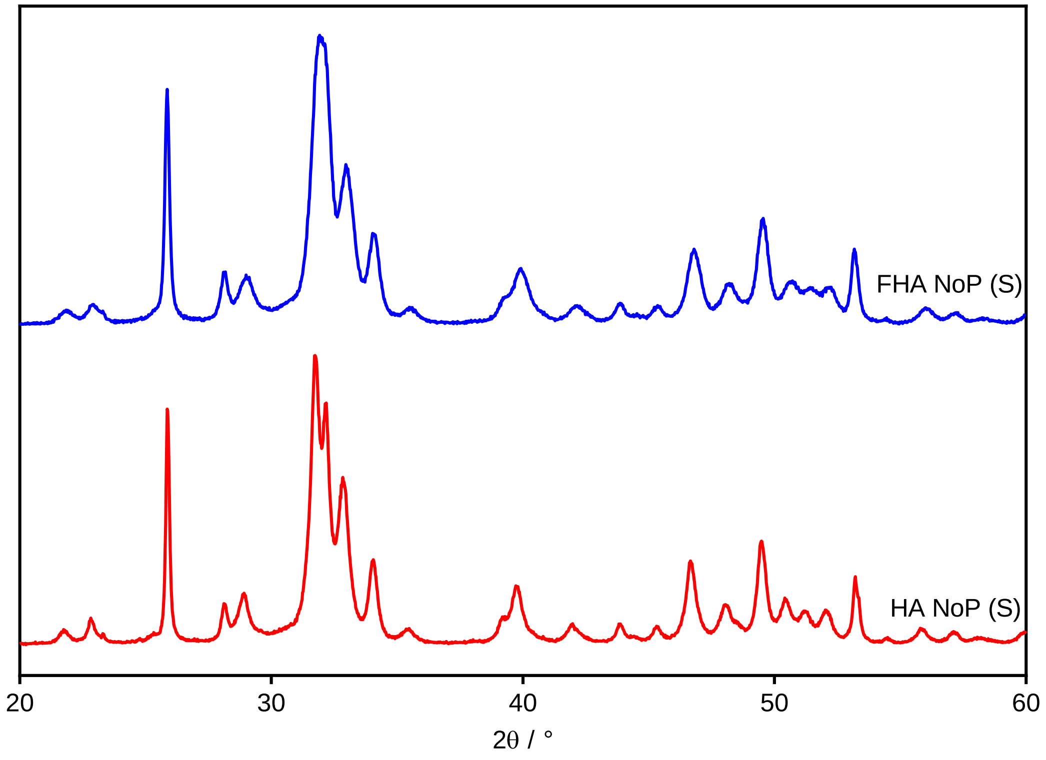

Figure 5.8. Stacked XRD patterns of HA and FHA samples synthesised without polymer at UoS

The pattern produced by the samples are very similar to the patterns of those synthesised at UCD; however, there is a slight increase in sharpness evident in the samples. This may be due the fact that samples were run for longer than the patterns collected using the internal standard method, producing more data points on the pattern. Rietveld and Pawley refinements were conducted on the diffraction patterns using TOPAS, the data of which is summarise in table 5.9.[9]

Table 5.9. Cell parameters determined by Pawley and Rietveld refinement of the XRD patterns collected of (F)HA containing no polymer, synthesised at UoS. R_{wp} and R_{wpb} are measures of the goodness of fit, values ≤ 10 and 12 respectively are deemed a good fit. Values in brackets after the a and c axis parameters refer to the standard deviation of the last digit in the value calculated from the refinement.

Sample	**Pawley Refinement**				**Rietveld Refinement**			
	a / Å	**c / Å**	**R_{wp}**	**R_{wpb}**	**a / Å**	**c / Å**	**R_{wp}**	**R_{wpb}**
FHA NoP (S)	9.399(1)	6.88(1)	12.51	16.21	9.40(1)	6.89(1)	15.34	21.70
HA NoP (S)	9.43(2)	6.877(5)	12.77	17.37	9.43(1)	6.88(1)	16.33	23.84

The values are very similar to those of the UCD samples with the FHA samples having a smaller *a* parameter value and larger *c* parameter value than the HA samples. The goodness of fit is quite poor in all cases, which is surprising given that the samples do not contain polymer. However, the UCD samples also showed a relatively poor fit due to the higher than expected intensity of the 002 and 004 peaks. It is possible that within the precipitation reaction to form these particles that some of the other ions in the mixture which do not appear in the final product act as nucleation points and cause the particles to grow preferentially along one axis of the unit cell.

5.3.2.2 Fourier transform infrared spectroscopy

FTIR was used to study the crystal chemistry of FHA and HA as before. The spectra were overlaid and compared to determine if any difference was evident between the FHA and HA samples synthesised at UCD and UoS. Figure 5.9 shows the FTIR spectra of The (F)HA NoP (S) samples. Comparing the overlaid spectra of the HA and FHA samples (figure 5.9) showed a change in the intensity and shape of the OH^- (approximately 3400 cm^{-1} and 680 cm^{-1}) and PO_4^{3-} peaks (approximately 1030 cm^{-1} and 600 cm^{-1}). This suggests that there is some disruption in the ordering of the crystals which supports the conclusions formed from the XRD data that the extra ions in the reaction mixture have had an effect on the particles formed in the reaction. Comparing the FHA samples with the HA samples showed the apparent loss of peaks at approximately 3560 and 640 cm^{-1}corresponding to non-hydrogen bonded OH^-.

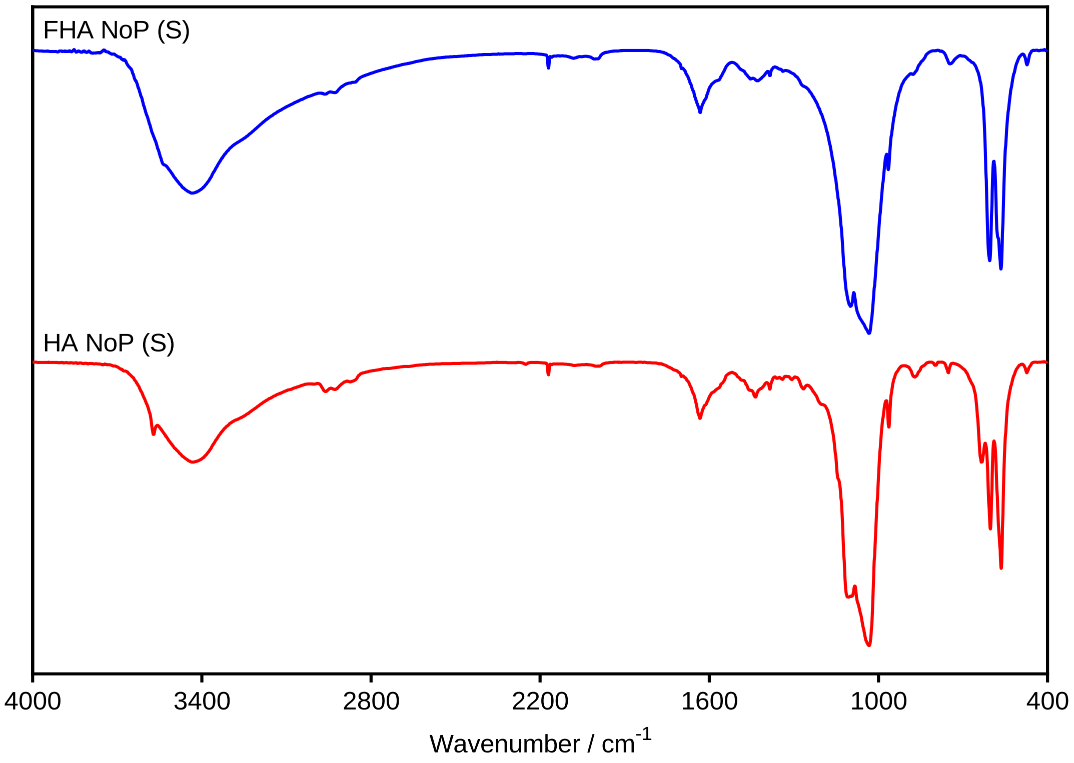

Figure 5.9. Stacked FTIR spectra of HA and FHA samples synthesised without polymer at UoS.

The loss of these peak shows that the F^- substitution was successful. The reaction mixture was intended to create a 50:50 OH^- : F^- ratio in the apatite. The peak is not lost entirely however the intensity is reduced to such an extent with the fluoride substitution that it becomes lost in the baseline noise.

Comparing these spectra with the (F)HA NoP samples synthesised at UCD shows that they are very similar. There is some excess water evident in both sets of spectra along with adsorbed CO_2 from the atmosphere (approximately 3400 cm^{-1} and 1660 cm^{-1} respectively). Otherwise the spectra are virtually identical.

5.3.2.3 Thermogravimetric analysis

TGA analysis was conducted to determine the percentage weight of material other than (F)HA in the samples and to get an idea of the thermal stability of the particles. Figure 5.10 shows an overlay of the thermogravimetric curves collected for the (F)HA NoP (S) samples. The weight loss calculated from the thermogravimetric curves and drawing on evidence from the XRD analysis suggests that the NoP samples are very crystalline samples. The minor weight loss seen in the NoP samples can be attributed to the loss of adsorbed water from the surface of the nanoparticles. The thermogravimetric curves both show an increase in weight

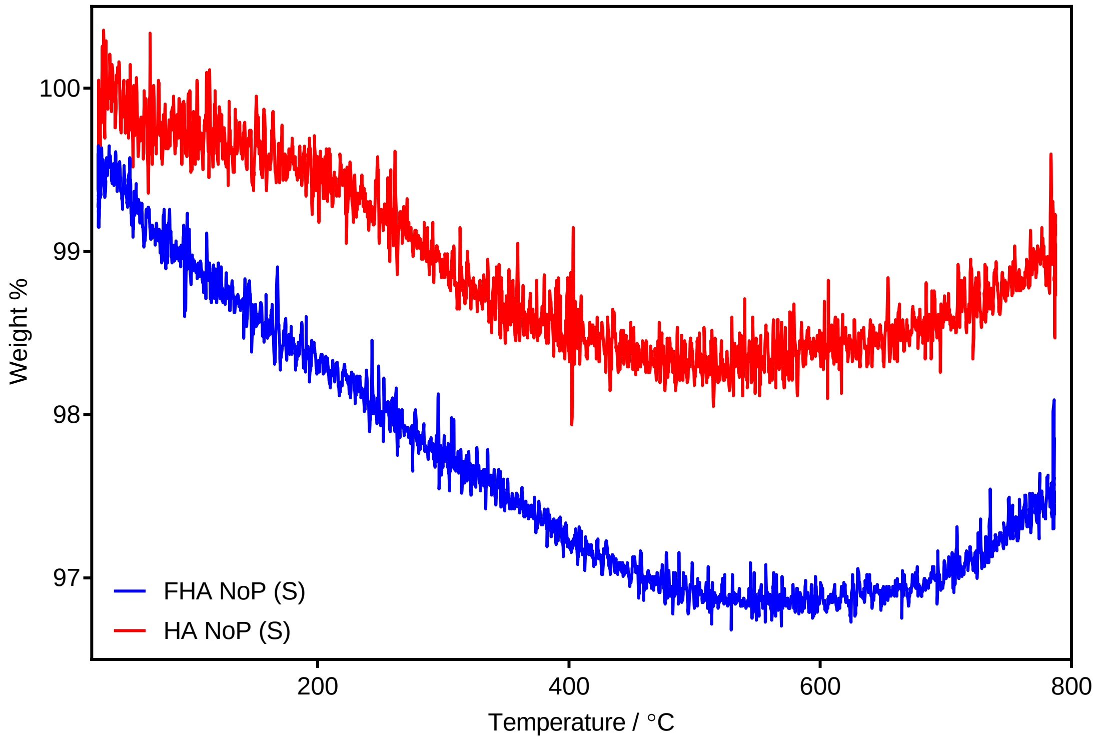

Figure 5.10. Overlaid TGA thermogravimetric curves of HA and FHA samples synthesised without polymer at UoS.

at higher temperatures after an initial weight loss. With the very small percentage loss in both samples and given how noisy the curves are, it is likely that this is caused by the TGA pan floating slightly in the furnace due to the presence of the flow of nitrogen during the data collection. As such the buoyancy of the pan leads to erroneous results. Table 5.10 shows the overall percentage weight loss of each sample.

Table 5.10. Weight loss calculated from TGA thermogravimetric curves of HA and FHA samples synthesised without polymer at UoS

Sample	Initial weight / %	Final weight / %	Overall weight lost / %
FHA NoP (S)	99.5	97.4	2.1
HA NoP (S)	99.7	98.5	1.2

These values are based on the first and last value produced by the data curve and hence do not take into account the slight increase in weight at the end of the run. As a result, the values of overall weight lost may be very slightly lower than they should be, but as the overall weight loss in each case is less than 3% this can be considered negligible. The curves also seem to suggest that the FHA loses more weight than the HA sample which could mean it is less stable than the HA sample. This is interesting as FHA is usually more thermally stable than HA. It is possible that this due to a higher residual water content in the FHA sample compared to the

HA; the FTIR spectra support this theory as the OH peak which accounts for the residual water is larger in the FHA NoP (S) spectrum than the HA NoP (S) sample.

5.3.2.4 Transmission electron microscopy

The (F)HA samples were imaged using transmission electron microscopy, the resulting micrographs were analysed using ImageJ software to determine the dimensions (lengths and widths) and resulting aspect ratios of the particles.[2] Micrographs of the (F)HA samples are given in figure 5.11.

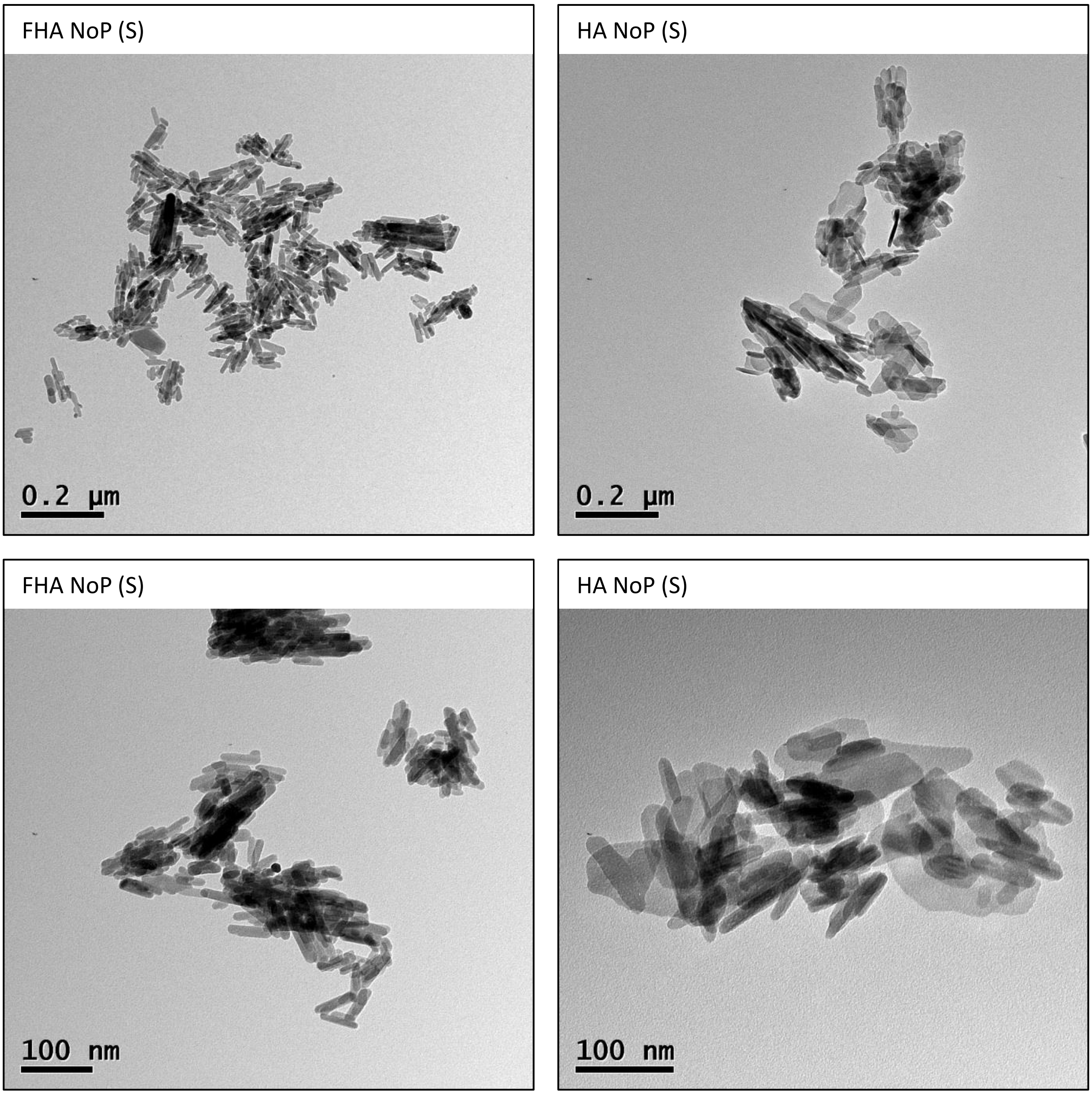

Figure 5.11. TEM micrographs of (F)HA containing no polymer synthesised at UoS.

The images of (F)HA NoP (S) show some aggregation; however, the overall picture is very similar to the (F)HA NoP synthesised at UCD. The particles have not formed large tight bundles but instead show discrete boundaries between each other which implies that the aggregation seen may be an artefact of the sample drying on the TEM grid. The particle lengths, widths and aspect ratios are summarised in table 5.11.

Table 5.11. Lengths, widths and resultant aspect ratios of (F)HA particles containing no polymer synthesised at UoS measured using ImageJ.

Sample	Lengths / nm			Widths / nm			Aspect ratios
	Mean	SD	SE	Mean	SD	SE	
FHA NoP (S)	50.29	12.72	0.57	10.78	2.25	0.22	4.66
HA NoP (S)	77.38	24.12	1.07	14.81	3.57	0.35	5.22

From the data in table 5.11, it is evident that the HA particle were larger than the FHA samples. The low aspect ratio of the HA sample suggests that their morphology was more plate-like than the FHA sample. Overall comparison of the FHA and HA samples without polymer synthesised at both UCD and UoS shows that the samples are very similar. Wet precipitation reactions will never give exactly the same particles twice due to the necessity for batch processing and hence minute differences between batches. As such, the similarity of the two sets of particles synthesised separately shows that the method was not affected by the location of the synthesis or the different batches of starting material used to produce that samples. Hence it was decided that the protocol for the synthesis could be used effectively at UoS to create new composite materials with different polymer additives.

5.3.3 Synthesis and analysis of fluorhydroxyapatite and hydroxyapatite synthesised in the presence of highly branched poly(acrylic acid) additives

Samples of HA and FHA were synthesised using the same method as those produced at UCD using samples of hyperbranched PAA instead of linear PAA. The polymers, described in section 3.2.3 of chapter 3, were included in the form of 0.2 wt% and 0.8 wt% solutions during the synthesis of the (F)HA particles. This equates to 4 wt% and 16 wt% of the maximum final yield of the particles. Samples were analysed using XRD, FTIR, TGA and TEM and compared to the UCD samples.

5.3.3.1 X-ray diffraction

XRD analysis was conducted using an external standard method. Figures 5.12 and 5.13 show the XRD diffraction patterns of the (F)HA samples synthesised in the presence of 0.2 wt% and 0.8 wt% solutions of hyperbranched PAA respectively. Rietveld and Pawley refinements

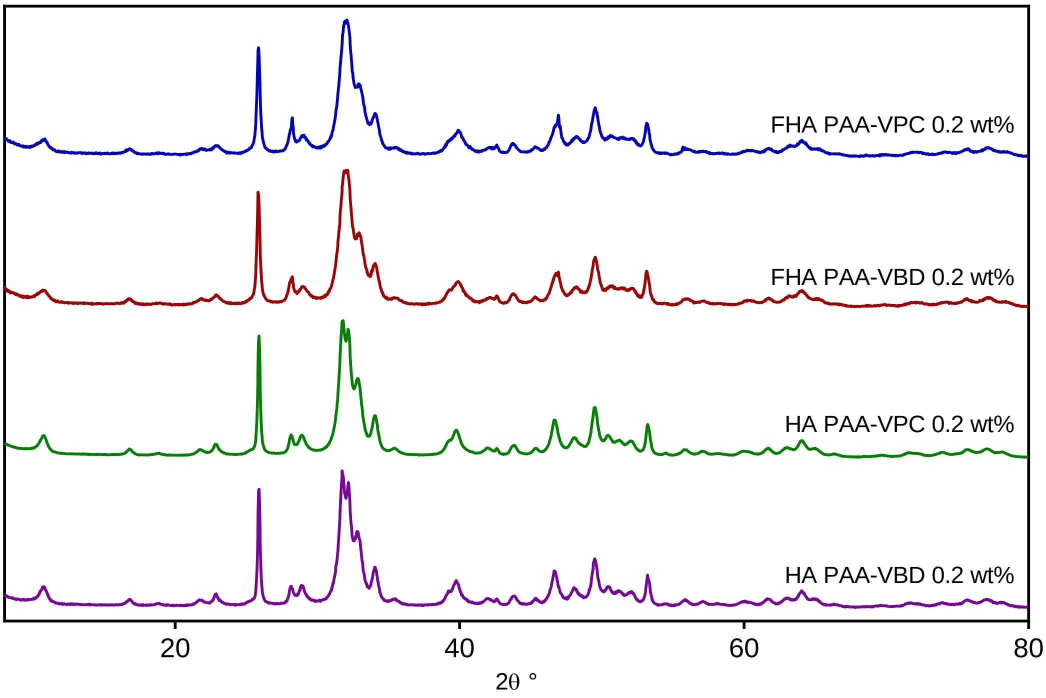

Figure 5.12. Stacked XRD patterns of (F)HA treated with a 0.2 wt% solution of hyperbranched PAA with either VPC or VBD as a RAFT agent.

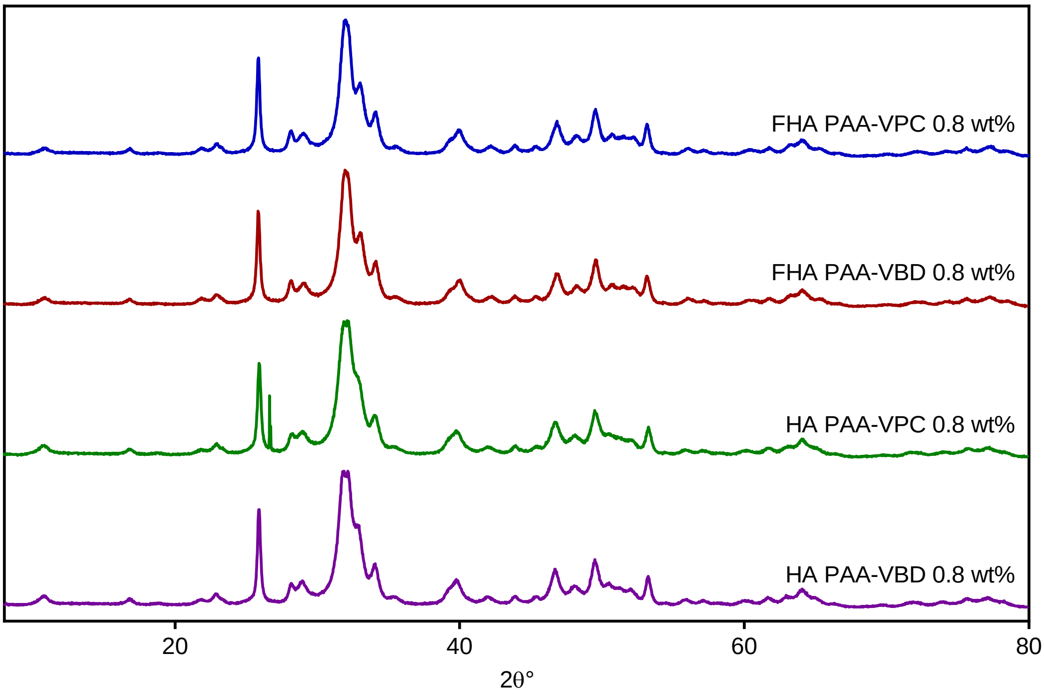

Figure 5.13. Stacked XRD patterns of (F)HA treated with a 0.8 wt% solution of hyperbranched PAA with either VPC or VBD as a RAFT agent.

were conducted on the diffraction patterns using TOPAS, the data of which is summarise in table 5.12. The diffraction patterns shown in figures 5.12 and 5.13 show an increase in peak sharpness in both the HA PAA-VPC 0.2 wt% and HA PAA-VBD 0.2 wt% samples yet the HA PAA-VPC 0.8 wt% and HA PAA-VBD 0.8 wt% samples both show far more amorphous peaks than the corresponding FHA samples. This suggests a critical level of PAA inclusion up to which increasing the concentration of PAA can produce more crystalline materials; after this point the composites become more amorphous. Another possibility to explain the loss of peak sharpness could be the size of the particles produced. As previously stated in chapter 4, nanoparticles below a certain size cause peak broadening in x-ray powder diffraction patterns due to the anisotropy of the scattering caused by the particles. The size of the particles cannot be determined by XRD, hence an imaging technique such as TEM must be implemented to determine whether particle size could account for the loss of peak sharpness. An extra peak is also evident at 26.2° 2θ in the diffraction pattern of the HA PAA-VPC 0.8 wt% sample. This peak does not correspond to any of the reactants used to synthesise the HA and does not appear on any other XRD diffraction patterns. As such it can be considered an impurity and excluded from further analysis. The values summarised in table 5.12 are similar to the samples containing linear PAA as described in section 5.3.1.

Table 5.12. Cell parameters determined by Pawley and Rietveld refinement of the XRD patterns collected of (F)HA treated with a 0.2 wt% or 0.8 wt% solution of hyperbranched PAA with either VPC or VBD as a RAFT agent. R_{wp} and R_{wpb} are measures of the goodness of fit. Values in brackets after the *a* and *c* axis parameters refer to the standard deviation of the last digit in the value calculated from the refinement.

Sample	**Pawley Refinement**				**Rietveld Refinement**			
	a / Å	**c / Å**	**R_{wp}**	**R_{wpb}**	**a / Å**	**c / Å**	**R_{wp}**	**R_{wpb}**
FHA PAA-VPC 0.2 wt%	9.40(1)	6.88(2)	8.81	9.33	9.39(3)	6.88(3)	18.10	19.17
FHA PAA-VBD 0.2 wt%	9.401(2)	6.881(3)	12.18	14.65	9.40(1)	6.88(1)	15.01	19.67
HA PAA-VPC 0.2 wt%	9.42(1)	6.87(3)	11.90	15.08	9.43(1)	6.87(1)	15.21	20.75
HA PAA-VBD 0.2 wt%	9.42(1)	6.87(1)	12.32	15.49	9.43(1)	6.87(1)	15.97	21.67
FHA PAA-VPC 0.8 wt%	9.38(1)	6.88(1)	9.89	13.48	9.39(1)	6.89(1)	12.50	17.90
FHA PAA-VBD 0.8 wt%	9.38(1)	6.883(4)	9.48	13.01	9.39(1)	6.89(1)	11.98	17.33
HA PAA-VPC 0.8 wt%	9.42(2)	6.869(1)	10.33	13.81	9.43(1)	6.87(1)	13.95	20.83
HA PAA-VBD 0.8 wt%	9.42(1)	6.87(1)	10.05	13.49	9.43(1)	6.88(1)	13.84	20.52

The axis parameters determined by both Pawley and Rietveld refinement are relatively similar. Both show that the inclusion of fluoride in the composite materials causes the *a* parameter to become smaller and the *c* axis parameter to become very slightly larger. Interestingly, the inclusion of 0.2 wt% PAA produced larger *a* axis parameters than the samples with 0.8 wt% PAA. This suggests a slight change in the crystal lattice which may be due to the larger quantity of PAA causing further elongation along the c axis. This is evident in the diffraction patterns as well; during Pawley and Rietveld refinement, peaks at 25.8 and 53.1° 2θ corresponding to (002) and (004) planes respectively were shown to be far larger than that expected by the fitting from the inputted crystal structures. Figure 5.14 demonstrates an example of the fitting and shows the difference between the peak ‘expected’ by the fitting programme (red line) and the actual peak collected in the diffraction pattern (blue line). The highlighted peaks correspond to the 002 and 004 planes of the HA crystal lattice.

The elongation of the 002 and 004 peaks suggests elongation of the crystal along the c axis. Previous studies by Roche *et al*.[12] and Liou *et al.*[13] also determined an elongation effect along the c axis with the inclusion of polymer additives. This is compatible with evidence from naturally occurring apatites, whereby collagen fibres align along the apatite crystals forming a uniform bioactive structure.[12-14] The goodness of fit is relatively good in all cases for the Pawley refinement except for the peaks corresponding to the 002 and 004 planes. The Rietveld refinement showed a similar fitting; however, the different natures of fitting lead to the differences in the goodness of fit. The fact that Pawley refinement ‘sees’ the peaks and varies the intensity of the fit to overlap with the peak, while the Rietveld refinement is dependent on the structural model, means that Pawley Refinement will always give a better fit than Rietveld refinement. But, if only the 002 and 004 peaks are prevented from being properly fitted using Rietveld refinement then this suggest the structural model of the apatite crystal is only affected in the direction of the c axis. This and the fact that that both the Pawley and the Rietveld refinement have difficulty fitting only the planes along the c axis (00l) due to an increase in peak intensity provides good evidence that the inclusion of polymer has a direct effect on the c axis of the crystal lattice. Further analysis by FTIR spectroscopy was conducted

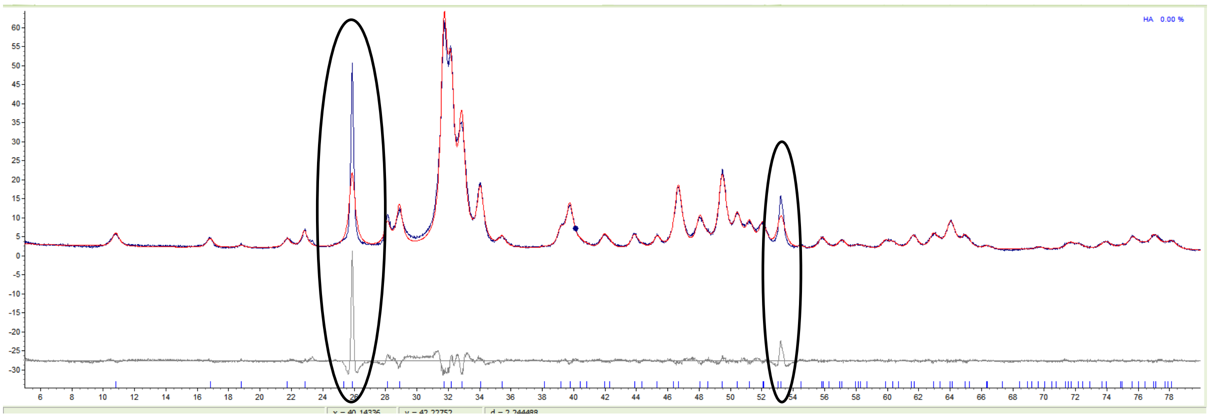

Figure 5.14. An example of fitting a composite sample to a CIF file of either HA or FHA. In this case fitting against the HA CIF produces large discrepancies at 25.8 and 53.1 ° 2θ corresponding to the (002) and (004) planes of the crystal, suggesting longer range order along these planes than in pure HA.

to determine any other effects on the intrinsic lattice structure while TGA and TEM were used to determine the amount of polymer in the composite and the size and morphology of the synthesised particles respectively.

5.3.3.2 Fourier transform infrared spectroscopy

FTIR spectra of polymer-(F)HA composites were recorded as before. Figures 5.15 and 5.16 show the collected FTIR spectra of the (F)HA PAA-VPC/VBD 0.2 wt% and 0.8 wt% samples respectively. In both figure 5.15 and 5.16 it is obvious that the HA samples show the extra peaks associated with non-hydrogen bonded OH at 3560 and 640 cm^{-1}.

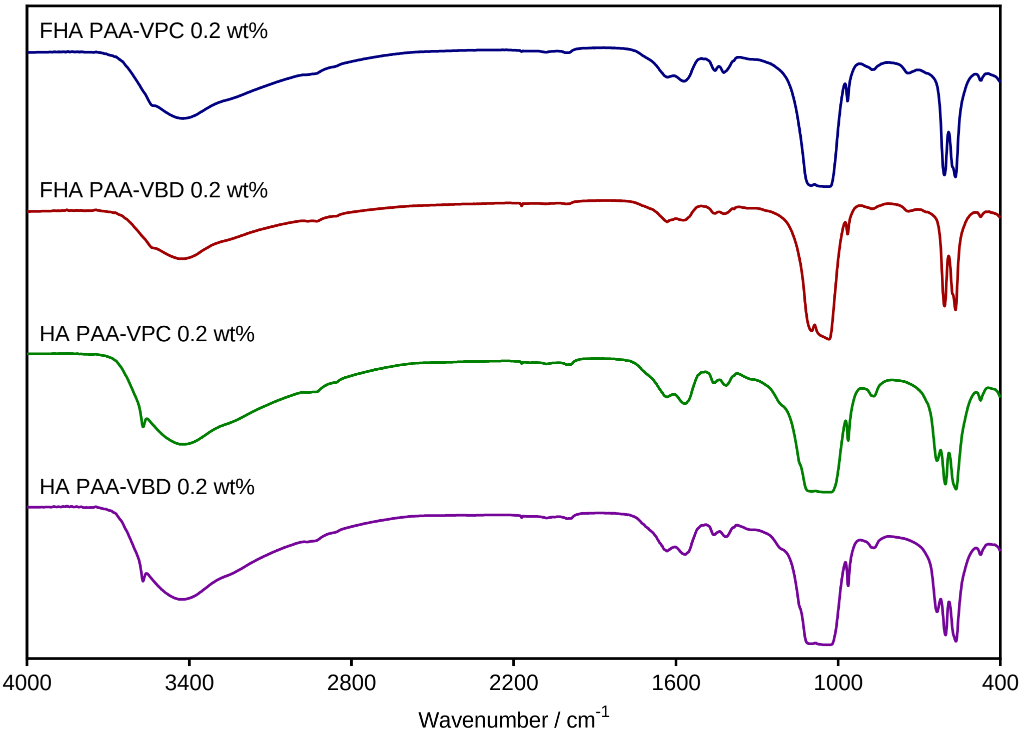

Figure 5.15. Stacked FTIR spectra of FHA and HA samples treated with a 0.2 wt% solution of hyperbranched PAA with either VPC or VBD as a RAFT agent.

The loss of these peaks in the FHA samples shows that the fluoride substitution was successful. However, as the mixture used was intended to create a 50:50 OH$^-$: F$^-$ ratio in the apatite the OH peak is not lost entirely but the intensity is reduced to such an extent with the fluoride substitution that it becomes lost in the baseline noise. This is the same result as the samples described previously in section 5.3.1. The inclusion of the polymer in the apatite particles is evident from the peaks at 1560 cm^{-1} corresponding to the COO$^-$ of the PAA. Interestingly these peaks are more pronounced in the HA samples than the FHA. Also the 0.8

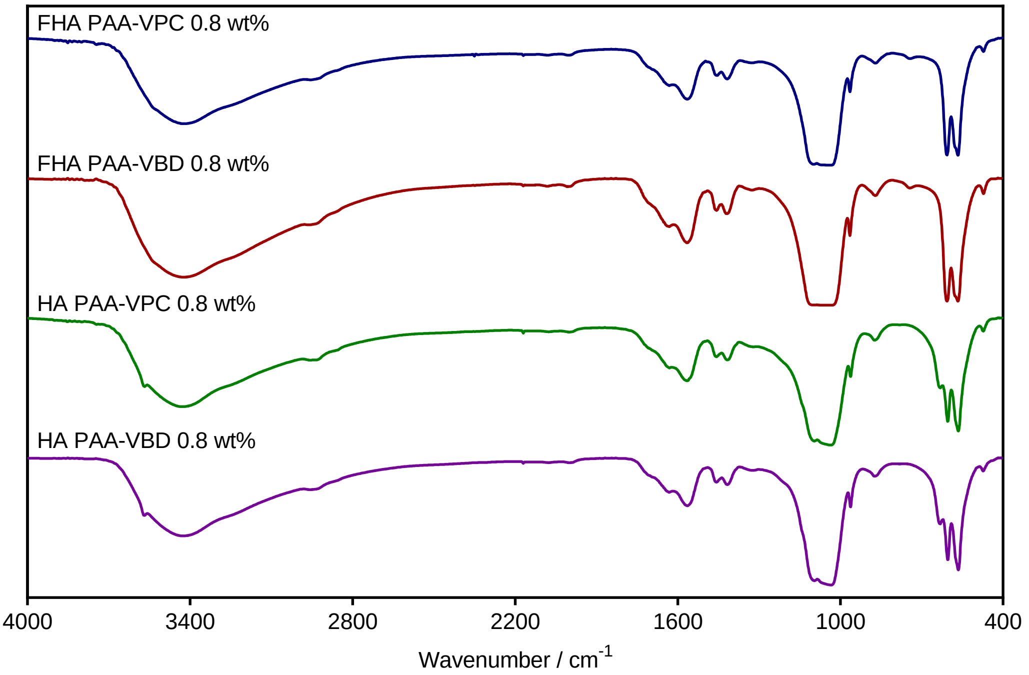

Figure 5.16. Stacked FTIR spectra of FHA and HA samples treated with a 0.8 wt% solution of hyperbranched PAA with either VPC or VBD as a RAFT agent.

wt% samples shown in figure 5.16 have larger peaks in this region suggesting an increase in the number of these bonds in the sample and hence an increase in the amount of polymer present as would be expected. Other peaks in this region correspond to CO_3^{2-} which occurs due to the adsorption of CO_2 from the atmosphere onto the particle surface during synthesis.

The phosphate region of the spectrum (1100 – 1000 cm^{-1}) shows a broad and quite flat peak across all the samples. The loss of peak sharpness seen in the samples implies a loss of long range order of the phosphate group in the crystal structure. This implies that the inclusion of the polymer within the samples has caused a change in the intrinsic crystal structure of the apatite composites. This supports the evidence seen by the XRD analysis that the 002 and 004 planes have been changed to provide longer range order. As the phosphate groups do not lie in the 00l plane of HA and FHA, but the calcium ions do, it is possible that the increased long range order of the 00l plane has caused the reconfiguration of the unit cell and hence the loss of long range order of the phosphate groups. This would also explain why it is the 00l plane that lengthens rather than the h00 or 0k0 plane as the negatively charged PAA will interact with the positively charged calcium ions as opposed to the net negatively charged phosphate or hydroxyl groups which do not reside in the 00l plane. Comparison of the peak intensities of the phosphate and hydroxyl groups in each spectrum, 1100 – 1000 cm^{-1} and 3400 cm^{-1}

respectively show very similar peak heights. This suggests a large amount of water remains within the sample even after drying and being stored in a desiccator. The broad peaks also suggest a large degree of hydrogen bonding within the samples which can be attributed to the phosphate groups interacting with the polymer. [15] The actual amount of polymer within the samples cannot be determined by FTIR hence further analysis of the samples was necessary to glean this information. As a result, thermogravimetric analysis was undertaken to examine the thermal stability and composition of the (F)HA samples.

5.3.3.3 Thermogravimetric analysis

Thermogravimetric analysis was conducted on the (F)HA PAA-VPC/VBD 0.2 wt% and 0.8 wt% samples, the resulting thermogravimetric curves are given in figure 5.17.

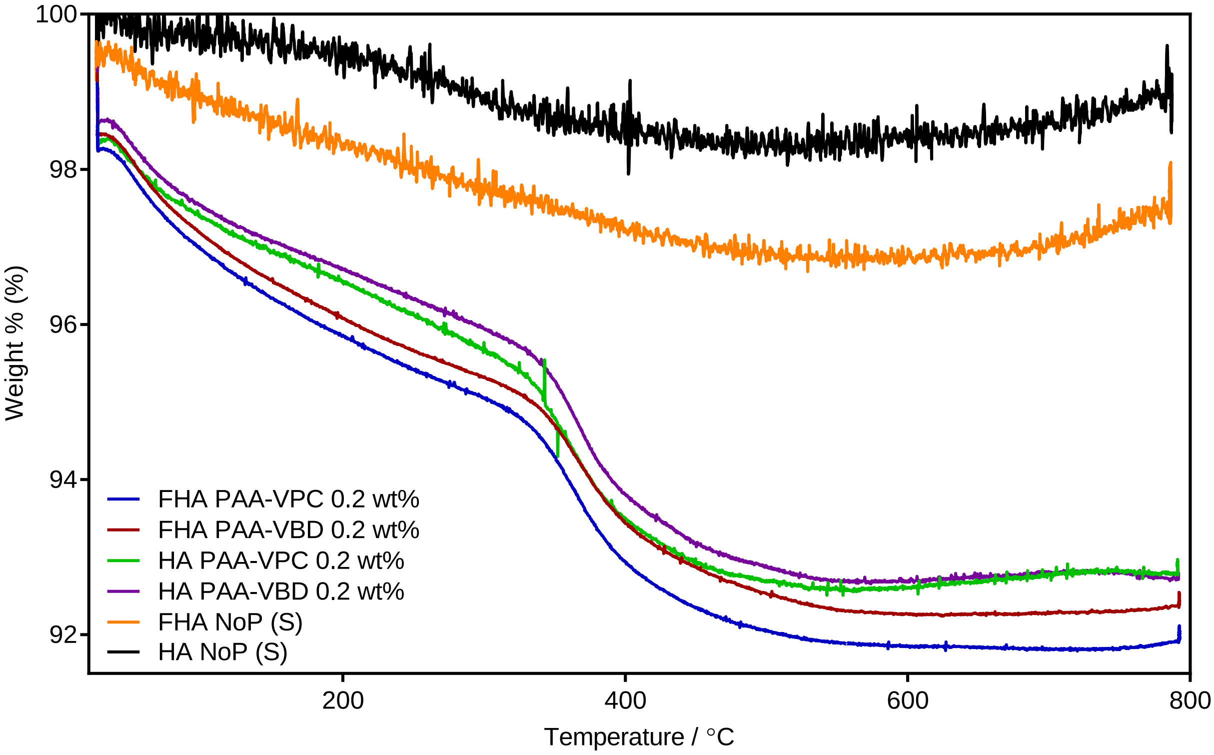

Figure 5.17. Overlaid TGA thermogravimetric curves of HA and FHA samples treated with a 0.2 wt% solution of hyperbranched PAA with either VPC or VBD as a RAFT agent.

The sharp drop in percentage weight at 20 °C is due to the buoyancy of the pan during the TGA runs. This is also evident in the noise seen throughout and at the end of each thermogravimetric curve. As such there is a certain amount of error associated with each measurement; however, the overall view of the thermogravimetric curves shows a distinct reduction in weight in all cases with a significant drop in weight from approximately 320 –

Table 5.13. Weight loss calculated from the region 320-420 °C of the TGA thermogravimetric curves of HA and FHA samples treated with low 0.2 wt% solutions of hyperbranched poly(acrylic acid)s PAA-VPC and PAA-VBD.

Sample	Initial weight / %	Final weight / %	Weight loss / %
FHA PAA-VPC 0.2 wt%	95.46	93.24	2.22
FHA PAA-VBD 0.2 wt%	95.78	93.53	2.25
HA PAA-VPC 0.2 wt%	94.87	92.65	2.22
HA PAA-VBD 0.2 wt%	95.14	93.17	1.97

420 °C. The overall weight lost by each sample is summarised in table 5.13. These values show a weight loss of between 1.97 – 2.25 % across the samples in the range 320-420 °C suggesting very similar levels of polymer in each sample. The inclusion of the 0.2 wt% solution of PAA in the reaction amounts to 4 wt% of the total amount of reactants used, therefore this suggests either a critical point after which no more PAA can be included, or the polymer interacted strongly with calcium ions in solution and was washed away during processing of the composite particles. Judging by the gradual decrease in weight in all samples when looking at figure 5.17 there is evidence of water loss during the temperature increase from 20 °C to approximately 350 °C. This theory is supported by the FTIR analysis which shows a large and broad OH peak in all the samples which can be attributed to retained moisture in the samples.

A similar result is seen in the thermogravimetric curves produced by the samples synthesised with 0.8 wt% solutions of PAA as shown in figure 5.18. A gradual decline in the percentage weight from approximately 20 – 350 °C is followed by a sharp drop in weight from 350 – 380 °C. Table 5.14 summarises the overall percentage weight lost by each sample in the region 320-420 °C. The sharp reduction in percentage weight from 350 – 380 °C is more pronounced in the thermogravimetric curves of the 0.8 wt% PAA samples. This is to be expected due to the higher levels of polymer theoretically contained within the samples of up to 16 wt% of the final composite.

Table 5.14. Weight loss calculated from the region 320-420 °C of the TGA thermogravimetric curves of HA and FHA samples treated with low 0.8 wt% solutions of hyperbranched poly(acrylic acid)s PAA-VPC and PAA-VBD.

Sample	Initial weight / %	Final weight / %	Weight loss / %
FHA PAA-VPC 0.8 wt%	96.85	92.39	4.46
FHA PAA-VBD 0.8 wt%	95.78	91.07	4.71
HA PAA-VPC 0.8 wt%	96.06	90.59	5.47
HA PAA-VBD 0.8 wt%	96.30	91.13	5.17

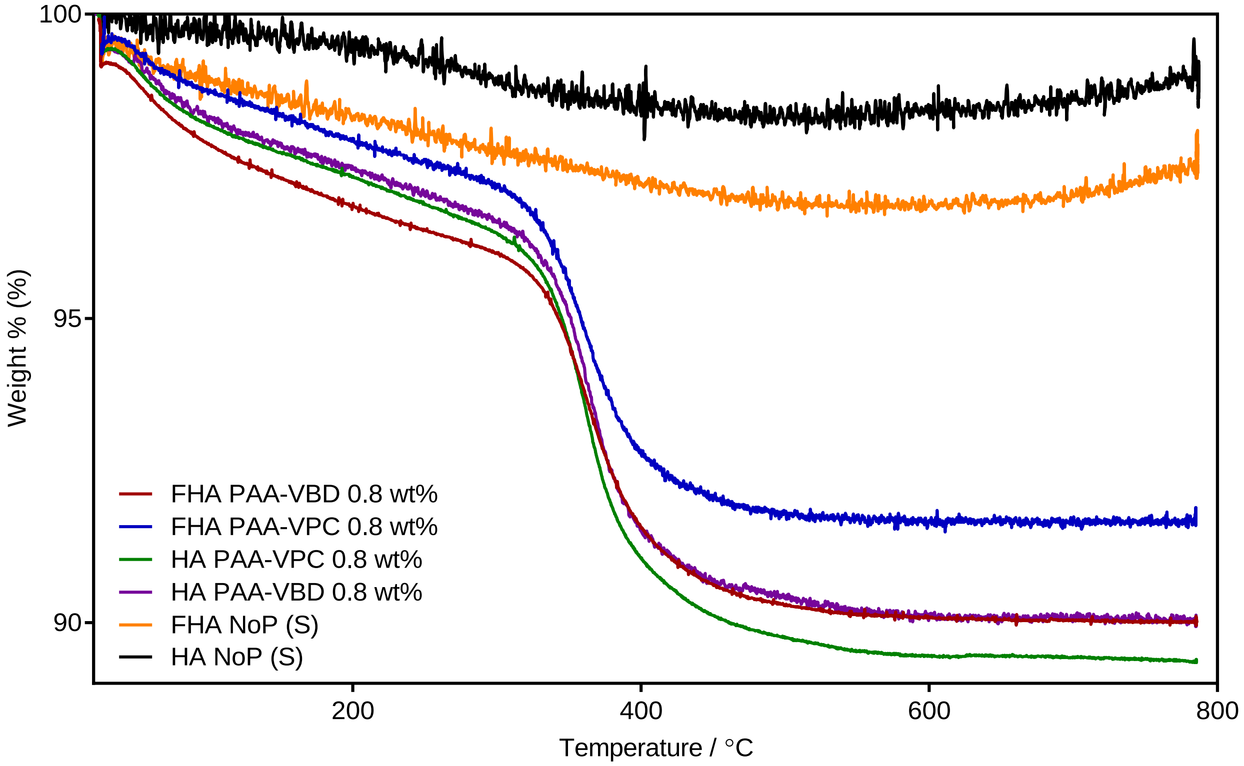

Figure 5.18. Overlaid TGA thermogravimetric curves of HA and FHA samples treated with a 0.8 wt% solution of hyperbranched PAA with either VPC or VBD as a RAFT agent.

The values given in table 5.14 of between 4.46 – 5.47 wt% show that the highest levels of polymer that could possibly be included in the composite were not achieved. This is an interesting result as it correlates well with natural bone mineral; the collagen present in the hydroxyapatite structures in natural bone is at a critical concentration, either side of which produces materials with less than optimal properties.[16] As such, it is possible that the PAA is acting in manner analogous to natural collagen in this instance and any polymer not included in the composite is instead removed during the washing stages of the material processing.

Also evident in figure 5.18 is the reduced weight loss of the FHA PAA-VPC sample, this could be due to a lack of polymer in the sample leading to less available material to be lost upon thermogravimetric analysis. However, FHA tends to be more thermally stable than HA; it is therefore possible that polymer may be unable to leave the sample upon heating due to being highly ingrained into the unit cell of the FHA. Unfortunately, this cannot be determined by simply looking at the thermogravimetric curve.

Further analysis was considered to determine whether the polymer was completely ingrained in the FHA. The considered method, inductively coupled plasma mass spectrometry (ICPMS), could be used to determine the amount of polymer present in the sample. However, as this is a destructive technique, there would be a limit on the information gleaned from this technique such as the structure of the unit cell. Neutral samples to act as standards are extremely difficult to find for samples with unknown carbon content. These factors and the many unknowns associated with them made ICPMS an unviable technique to determine the actual polymer content of the sample. As such the analytical techniques used to characterise the samples were maintained at XRD, FTIR, TGA and TEM.

5.3.3.4 Transmission electron microscopy

TEM images were collected and analysed using ImageJ software to determine the particle sizes and aspect ratios of the (F)HA PAA composite samples. TEM micrographs of the samples synthesised with 0.2 wt% PAA are shown in figure 5.19 and a summary of the particle sizes and aspect ratios is shown in table 5.15.

Table 5.15. Lengths, widths and resultant aspect ratios of (F)HA particles synthesised in the presence of a 0.2 wt% solution of poly(acrylic acid) made with either VPC or VBD as a branching RAFT agent, measured using ImageJ.

Sample	**Lengths / nm**			**Widths / nm**			**Aspect ratios**
	Mean	**SD**	**SE**	**Mean**	**SD**	**SE**	
FHA PAA-VPC 0.2wt%	52.21	18.23	0.81	8.44	2.88	0.13	6.19
FHA PAA-VBD 0.2wt%	59.87	19.76	0.88	9.50	2.56	0.11	6.30
HA PAA-VPC 0.2wt%	99.60	27.15	1.21	12.20	4.06	0.18	8.17
HA PAA-VBD 0.2wt%	100.12	32.54	1.45	14.09	6.39	0.28	7.11

The FHA samples are smaller than the HA samples as was determined earlier in the chapter with the linear polymers. Interestingly however the widths of all the particles are very similar causing the aspect ratios to suggest that the HA samples are longer and thinner than the FHA particles. Looking at the micrographs in figure 5.19, it is not immediately obvious whether the HA samples are more needle-like than the FHA as the aspect ratios in table 5.15 would imply. The micrographs themselves suggest that the FHA samples are actually more needle-like than the HA samples. However, the agglomeration of the particles evident in all the samples may have led to erroneous measurements as it is difficult to distinguish single particles. Inspection of the TEM micrographs of the samples synthesised with 0.8 wt% PAA (figure 5.20) shows a similar result. (table 5.16).

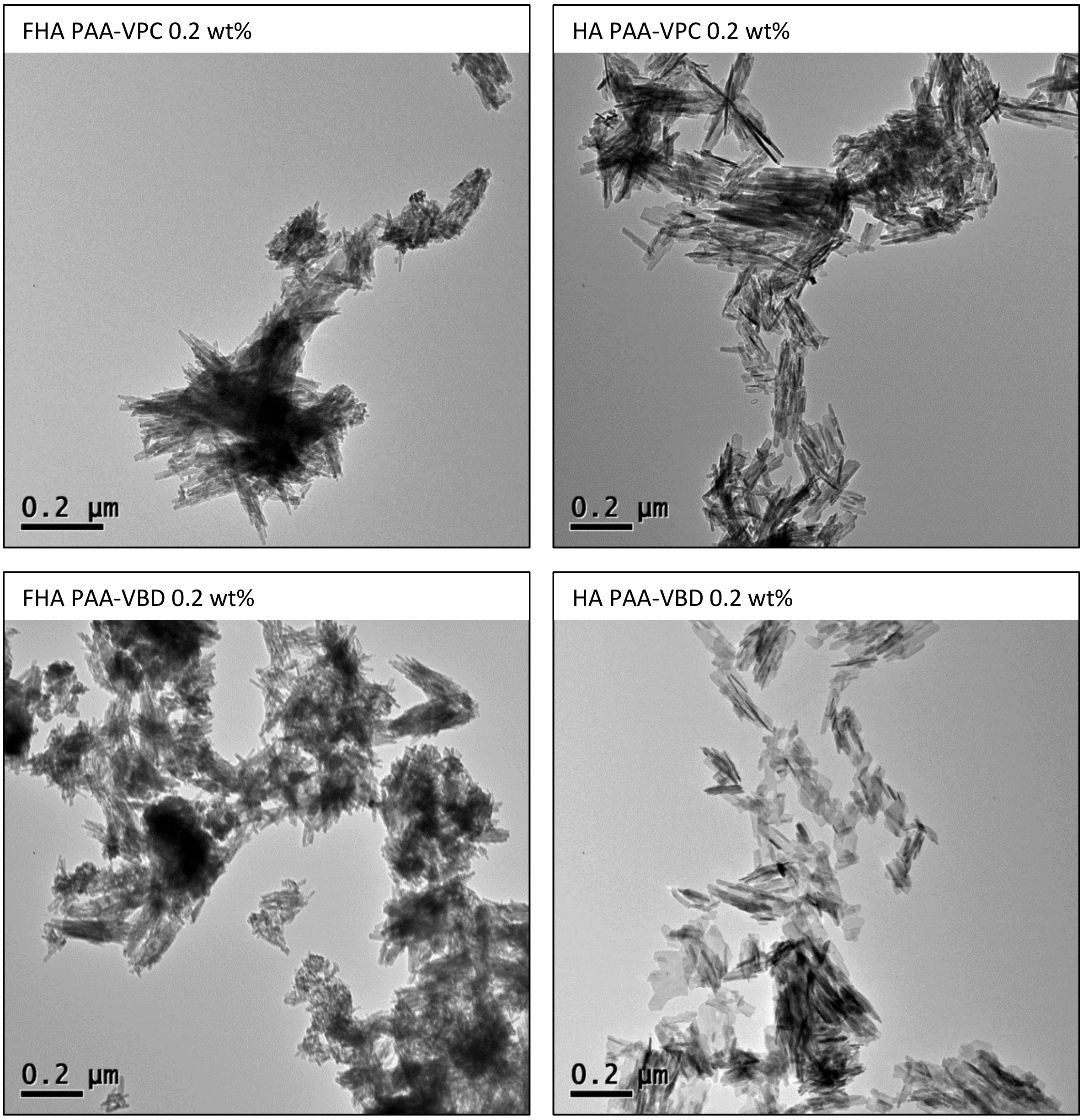
FHA PAA-VPC 0.2 wt%

HA PAA-VPC 0.2 wt%

FHA PAA-VBD 0.2 wt%

HA PAA-VBD 0.2 wt%

Figure 5.19. TEM micrographs of (F)HA synthesised in the presence of a 0.2 wt% solution of poly(acrylic acid) made with either VPC or VBD as a branching RAFT agent.

The micrographs of the 0.8 wt% PAA (F)HA samples show that the particles are highly aggregated, this makes measuring the particles difficult as the boundaries of the particles are obscured by overlapping. As a result of this, there is an error associated with the measured values of the lengths and widths of the particles which is unavoidable. Table 5.16 shows that, again, the FHA particles are smaller than the HA particles; however, the widths of the HA particles are very similar to the FHA samples suggesting again that the HA particles are more needle-like than the FHA particles. This is the opposite of that seen earlier in the chapter when

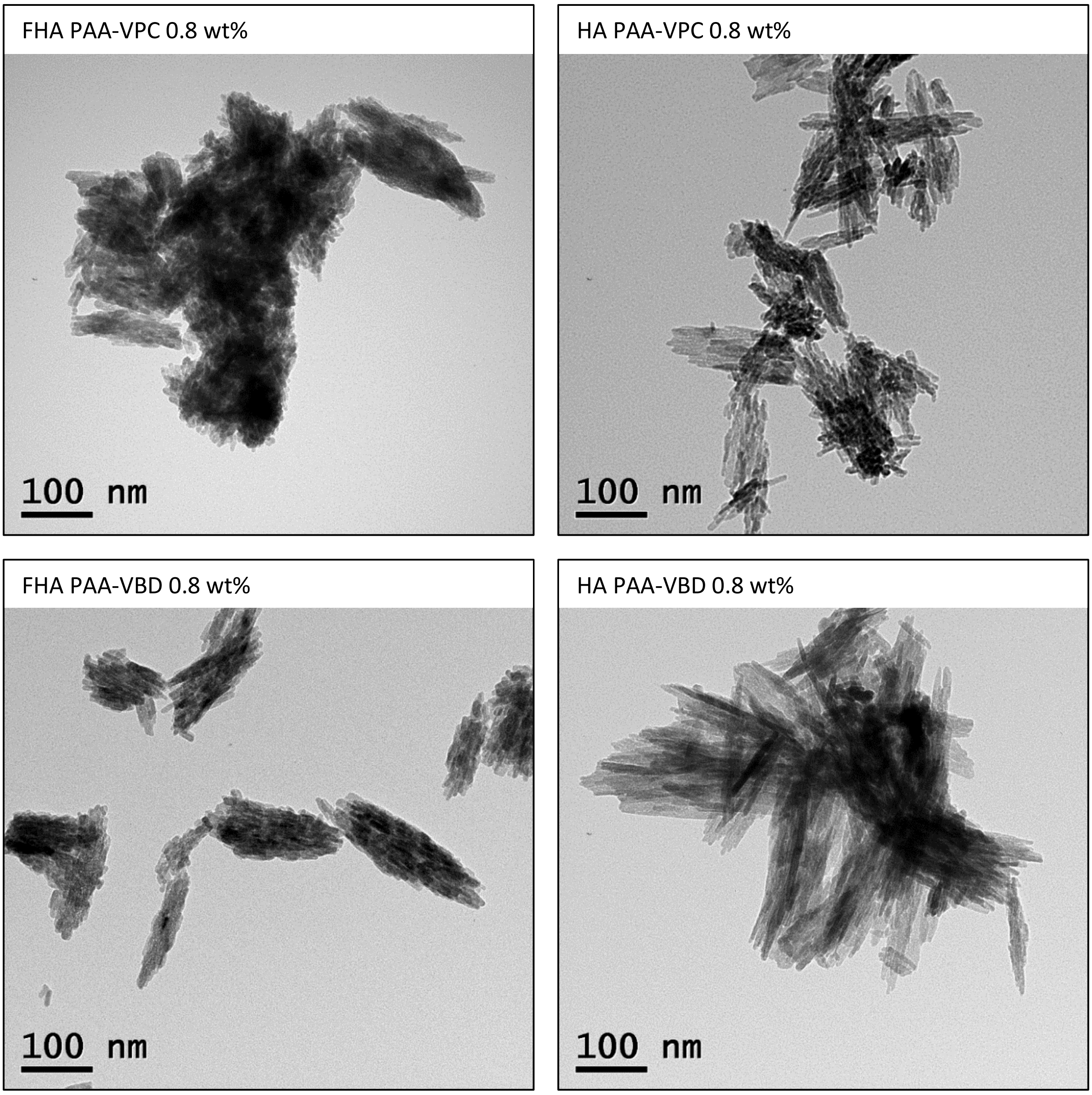

Figure 5.20. TEM micrographs of (F)HA synthesised in the presence of a 0.8 wt% solution of poly(acrylic acid) made with either VPC or VBD as a branching RAFT agent.

looking at the linear PAA samples in section 5.3.1. However, the same effect of the elongation of particles along one axis which was seen in the linear PAA samples is also apparent in the samples containing hyperbranched polymers. The amount of aggregation in the samples appears to increase with the amount of polymer included in the synthesis. Figure 5.20 shows the samples with 0.8 wt% PAA form small bundles of particles, while the samples synthesised with 0.2 wt% PAA are less aggregated. Poly(acrylic acid) is currently used in dental cements to enhance the mechanical strength of the material.[17, 18] As such it is not surprising that the inclusion of PAA in the synthesis of (F)HA particles leads to aggregation. However, previous

Table 5.16. Lengths, widths and resultant aspect ratios of (F)HA particles synthesised in the presence of a 0.8 wt% solution of poly(acrylic acid) made with either VPC or VBD as a branching RAFT agent, measured using ImageJ.

Sample	**Lengths / nm**			**Widths / nm**			**Aspect ratios**
	Mean	**SD**	**SE**	**Mean**	**SD**	**SE**	
FHA PAA-VPC 0.8 wt%	46.90	12.82	0.64	5.73	1.05	0.11	8.19
FHA PAA-VBD 0.8 wt%	60.70	10.19	0.51	5.89	0.96	0.10	10.31
HA PAA-VPC 0.8 wt%	76.60	12.84	0.64	5.91	1.39	0.14	12.96
HA PAA-VBD 0.8 wt%	81.36	14.09	0.70	6.12	1.00	0.10	13.30

studies have shown that PAA can have a nucleating and directing effect on the formation of HA particles. As such it is possible that there is a critical concentration of PAA where the directing effects of the PAA outweigh the aggregation of the particles by steric and electrostatic repulsion effects. This could prove interesting if taken on for further study; however, it will not be discussed here.

5.3.4 Synthesis of fluorhydroxyapatite and hydroxyapatite varying highly branched poly(methacrylic acid) additive addition

Other polymers similar to PAA could have a similar effect on the formation of (F)HA nanoparticles. As the studies discussed in chapters 3 and 4 showed, other candidates considered included poly(methacrylic acid) (PMAA). This was due to the fact that the acrylic acid and methacrylic acid monomers differ only by the inclusion of a methyl group giving the polymer a more rigid backbone, and hence should give relatively similar particles. However, the added steric hindrance provided by the addition methyl group on every repeat unit could have an effect on nucleation and particle growth alongside the electrostatic effects of the negatively charged polymers.

Samples of (F)HA were synthesised in the same manner as those discussed in section 5.3.3 using highly branched PMAA samples produced using RAFT polymerisation using VPC and VBD as RAFT agents. The polymers, described in section 3.2.3 of chapter 3, were included in the form of 0.2 wt% and 0.8 wt% solutions during the synthesis of the (F)HA particles. This equates to 4 wt% and 16 wt% of the maximum final yield of the particles. Samples were analysed using XRD, FTIR, TGA and TEM and compared to the UCD and PAA samples.

5.3.4.1 X-ray diffraction

XRD analysis was conducted using an external standard method as with the PAA samples in section 5.3.2. Figures 5.21 and 5.22 show the XRD diffraction patterns of the (F)HA samples

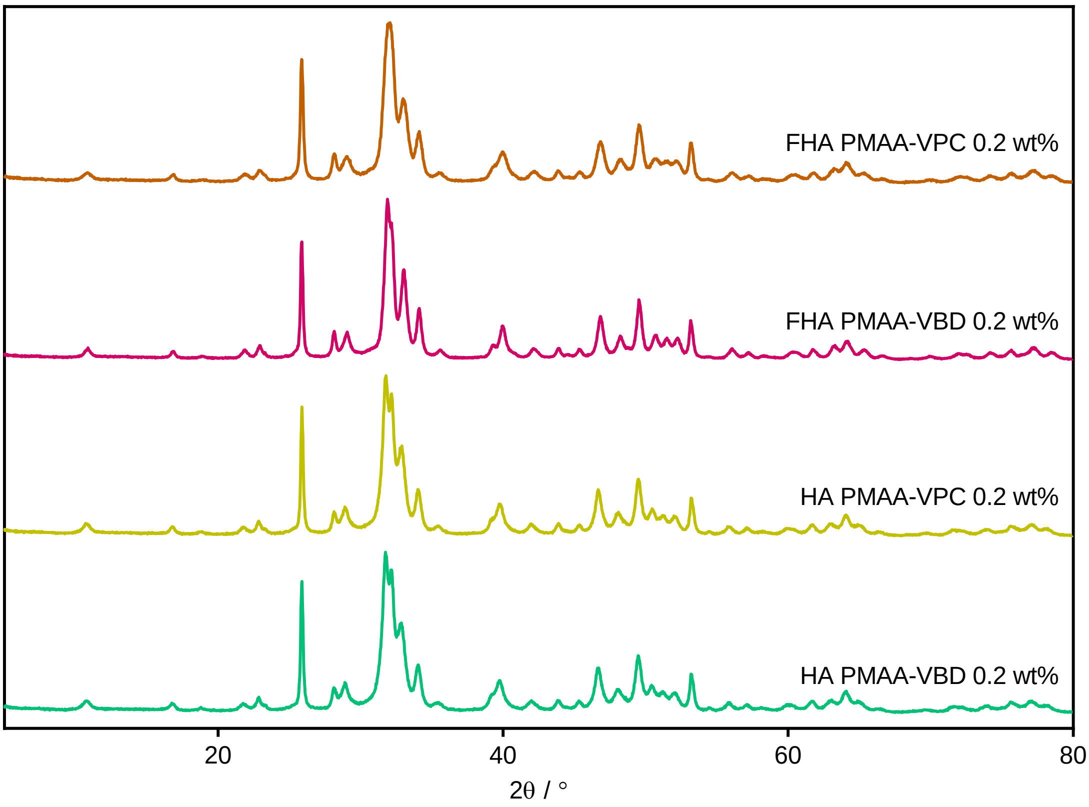

Figure 5.21. Stacked XRD patterns of (F)HA treated with a 0.2 wt% solution of hyperbranched PMAA with either VPC or VBD as a RAFT agent.

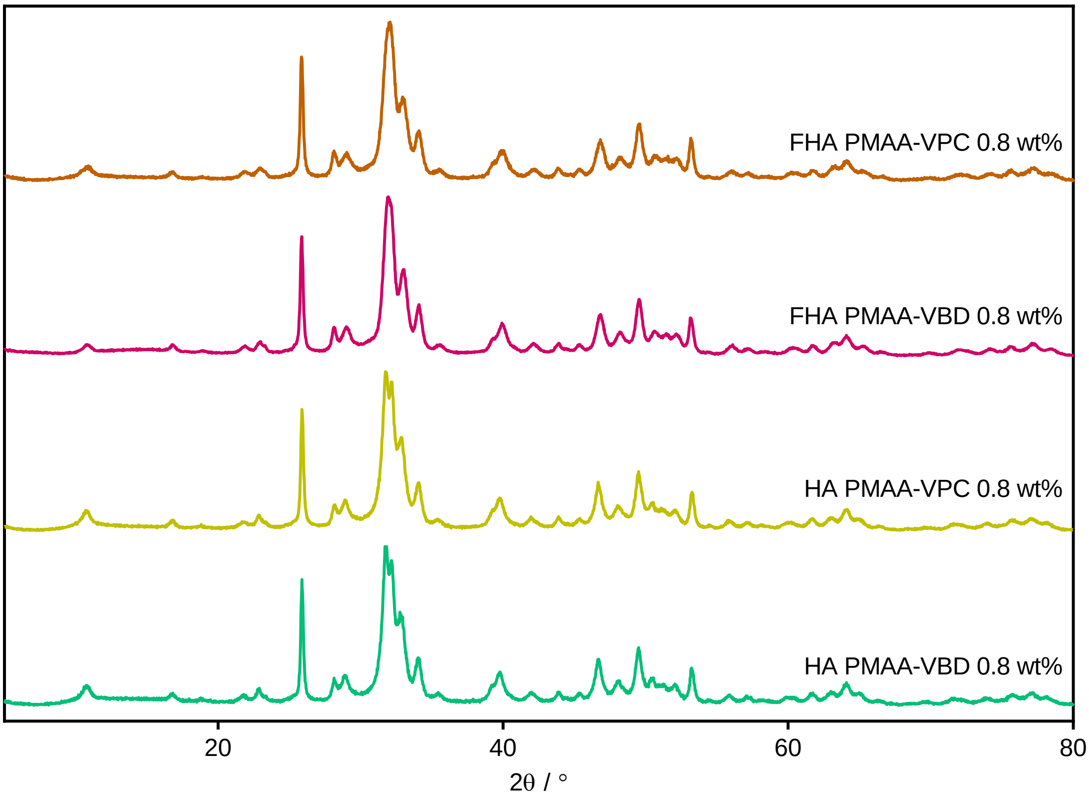

Figure 5.22. Stacked XRD patterns of (F)HA treated with a 0.8 wt% solution of hyperbranched PMAA with either VPC or VBD as a RAFT agent.

synthesised in the presence of 0.2 wt% and 0.8 wt% solutions of hyperbranched PMAA respectively. Rietveld and Pawley refinements were conducted on the diffraction patterns using TOPAS, the data from which is summarise in table 5.17.

Table 5.17. Cell parameters determined by Pawley and Rietveld refinement of the XRD patterns collected of (F)HA treated with a 0.2 wt% or 0.8 wt% solution of hyperbranched PMAA with either VPC or VBD as a RAFT agent. R_{wp} and R_{wpb} are measures of the goodness of fit, values ≤ 10 and 12 respectively are deemed a good fit. Values in brackets after the a and c axis parameters refer to the standard deviation of the last digit in the value calculated from the refinement.

Sample	**Pawley Refinement**				**Rietveld Refinement**			
	a / Å	**c / Å**	**R_{wp}**	**R_{wpb}**	**a / Å**	**c / Å**	**R_{wp}**	**R_{wpb}**
FHA PMAA-VPC 0.2 wt%	9.391(1)	6.886(3)	11.38	14.88	9.39(1)	6.89(1)	14.23	19.30
FHA PMAA-VBD 0.2 wt%	9.387(4)	6.885(5)	10.85	14.57	9.387(4)	6.885(4)	13.36	18.05
HA PMAA-VPC 0.2 wt%	9.43(1)	6.88(1)	11.61	16.68	9.43(1)	6.88(1)	15.95	23.18
HA PMAA-VBD 0.2 wt%	9.431(6)	6.878(2)	11.43	15.59	9.44(1)	6.88(1)	15.82	22.69
FHA PMAA-VPC 0.8 wt%	9.390(1)	6.8827(2)	13.02	16.60	9.40(1)	6.89(1)	15.08	20.28
FHA PMAA-VBD 0.8 wt%	9.390(2)	6.882(5)	11.21	15.73	9.40(1)	6.89(1)	13.72	19.89
HA PMAA-VPC 0.8 wt%	9.435(1)	6.8774(5)	12.51	18.54	9.44(1)	6.88(1)	15.11	21.93
HA PMAA-VBD 0.8 wt%	9.427(4)	6.874(2)	12.57	15.64	9.44(1)	6.88(1)	16.36	23.74

In all cases the *a* parameter is smaller when looking at the FHA samples compared to the HA samples. Interestingly the *c* parameter values are very similar across all samples when looking at both the Pawley and Rietveld refinement. The diffraction patterns shown in figures 5.21 and 5.22 show an increase in peak sharpness in all the HA PMAA-VPC and HA PMAA- VBD samples yet the FHA PMAA-VPC and FHA PAA-VBD samples all show much broader peaks than the corresponding HA samples. However, the FHA samples with both 0.2 and 0.8 wt% PMAA show more definition in the peak shapes. Again the peaks are rather broad, with a shift in the value of 2θ showing that the compressive strain in the crystal lattice of the FHA samples is slightly greater than in the HA samples as seen previously. This suggests that the PMAA and or the fluoride substitution in the FHA samples causes the unit cell to be compressed in the 211 and 112 planes which is consistent with a smaller atom being placed in the centre of a trio of Ca ions within the crystal lattice as expected with fluoride substitution. Peak sharpness could be affected by the size of the particles produced during synthesis. Nanoparticles below a 100 nm begin to cause peak broadening in x-ray powder diffraction patterns due to the anisotropy of the scattering caused by the particles. The values of the FHA samples summarised in table 5.17 are smaller than the samples containing linear PAA as described in section 5.3.1 and the branched PAA samples described in section 5.3.3. This suggests that the inclusion of the methyl group on the methacrylic acid monomer causes the interactions between the polymer and (F)HA to change slightly. At present it is not obvious what this change may be. The axis parameters determined by both Pawley and Rietveld refinement are relatively similar. Both show that the inclusion of fluoride in the composite materials causes the *a* parameter to become smaller and the *c* axis parameter to become very slightly larger. Similarly, with the PAA samples, the fitting of the 00l peaks in the (F)HA samples containing PMAA was poor due to the higher intensity 00l peaks than the pure HA diffraction pattern that the fitting programme compares it to. This suggests that the c axis has been elongated as seen previously with the PAA samples. This implies that even with the additional methyl group on the monomer, the electrostatic effects of the polymer are not affected and hence the polymer can bind with the Ca ions along the c axis causing the polymer to act as a template for the formation of (F)HA nanoparticles.

5.3.4.2 Fourier transform infrared spectroscopy

To determine the effect on the chemistry of the (F)HA crystals, FTIR spectroscopy was conducted on the composite samples as before. Figures 5.23 and 5.24 show the collected FTIR spectra of the (F)HA PMAA-VPC/VBD 0.2 wt% and 0.8 wt% samples respectively.

In both figure 5.23 and 5.24 it is obvious that the HA samples show the extra peaks associated with non-hydrogen bonded OH at 3560 and 640 cm^{-1} with the loss of these peaks in the FHA samples showing that the fluoride substitution was successful. The reaction mixture used to synthesise the particles was intended to create a 50:50 OH^- : F^- ratio in the apatite; as described previously. The inclusion of the polymer is evident from the peaks at 1560 cm^{-1} corresponding to the COO^- of the PMAA. A very small and broad peak at approximately 2950 cm^{-1} which is nearly lost in the major hydrogen bonded OH peak from 3400 – 2900 cm^{-1} corresponds to the C-H bond of the methyl group on the methacrylic acid repeat unit. These peaks are slightly more pronounced in the FHA samples than the HA samples, which is the opposite to that seen with the PAA samples (section 5.3.3). Similarly, the 0.8 wt% samples have larger peaks in these regions (figure 5.24), suggesting an increase in the number of these bonds in the sample and hence an increase in the amount of polymer present as would be expected. The phosphate region of the spectrum (1100 – 1000 cm^{-1}) shows a broad double peak across all the samples. The peaks in this region are slightly sharper than those seen in the samples made with highly branched PAA (section 5.3.3). This suggests greater long range order in the PMAA samples and more crystalline samples than the PAA analogues.

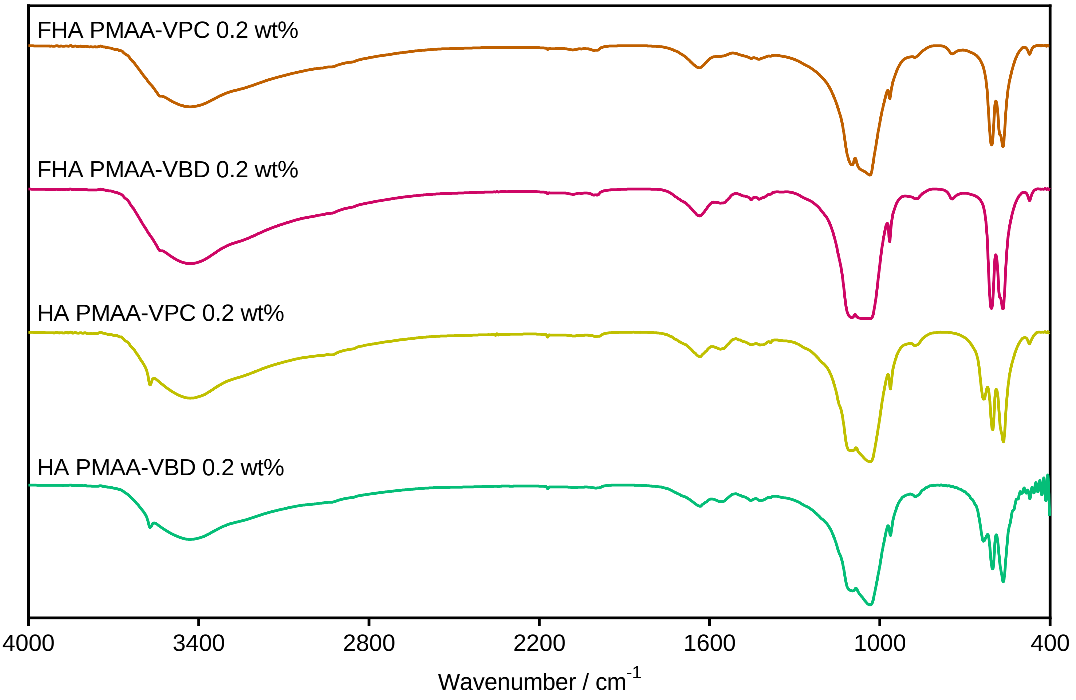

Figure 5.23. Stacked FTIR spectra of FHA and HA samples treated with a 0.2 wt% solution of hyperbranched PMAA with either VPC or VBD as a RAFT agent.

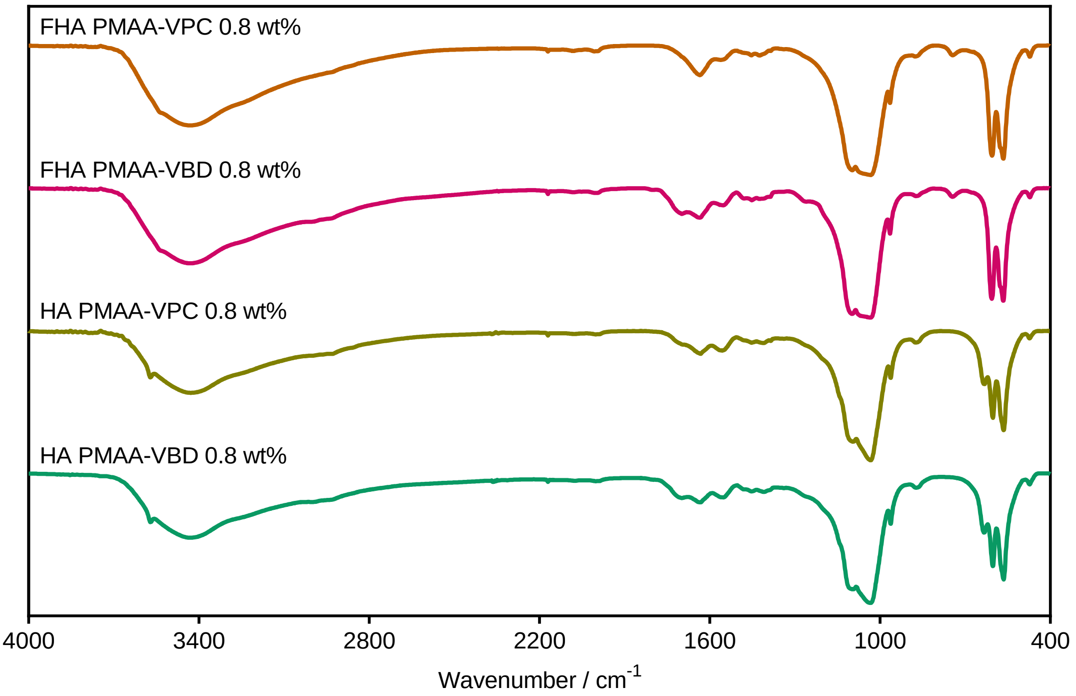

Figure 5.24. Stacked FTIR spectra of FHA and HA samples treated with a 0.8 wt% solution of hyperbranched PMAA with either VPC or VBD as a RAFT agent.

The lack of peak sharpness seen in the phosphate region implies a loss of long range order of the phosphate group in the crystal structure. This indicates that the inclusion of the polymer within the samples has again caused a change in the intrinsic crystal structure of the apatite composites, as did the PAA samples discussed previously. This supports the evidence given by the XRD analysis that the 002 and 004 planes have been elongated to produce longer range order along the *c* axis by reconfiguring the unit cell to reduce the long range order of the phosphates in the h00 and 0k0 planes and increase the order of the Ca ions along the 00l plane.[5, 7] This explains why it is that the 00l plane lengthens rather than the h00 or 0k0 plane as the negatively charged PMAA will interact with the positively charged calcium ions as opposed to the net negatively charged phosphate or hydroxyl groups which do not reside in the 00l plane.[19, 20]

Comparison of the peak intensities of the phosphate (1100 – 1000 cm^{-1}) and hydroxyl (3400 cm^{-1}) regions in each spectrum show that the phosphate region has produced more intense peaks than the hydroxyl region. This suggests some water may still remain within the sample even after drying and being stored in a desiccator.[21, 22] The peak broadness also suggests a large degree of hydrogen bonding within the samples which can be attributed to the phosphate and hydroxyl groups interacting with the polymer.[15]

5.3.4.3 Thermogravimetric analysis

To quantify the extent of polymer inclusion, samples were analysed with thermogravimetric analysis (figure 5.25). The noise seen throughout and at the end of each thermogravimetric curve along with the sharp drop at the beginning of some curves is due to buoyancy of the pan as described previously. As such there is a certain amount of error associated with each measurement; however, the overall view of the thermogravimetric curves shows a distinct loss in weight in all cases with a significant drop in weight from approximately 320 – 380 °C. The overall weight lost by each sample is summarised in table 5.18.

Table 5.18. Weight loss calculated from the region 320-420 °C of the TGA thermogravimetric curves of HA and FHA samples treated with low 0.2 wt% solutions of hyperbranched poly(methacrylic acid)s PMAA-VPC and PMAA-VBD.

Sample	Initial weight / %	Final weight / %	Weight loss / %
FHA PMAA-VPC 0.2 wt%	96.71	95.73	0.98
FHA PMAA-VBD 0.2 wt%	98.29	96.31	1.98
HA PMAA-VPC 0.2 wt%	97.32	95.68	1.64
HA PMAA-VBD 0.2 wt%	97.22	95.10	2.12

The inclusion of the 0.2 wt% solution of PAA in the reaction corresponds to 4 wt% of the total solids content of reactants used. These values show an overall weight loss of between 0.98 –

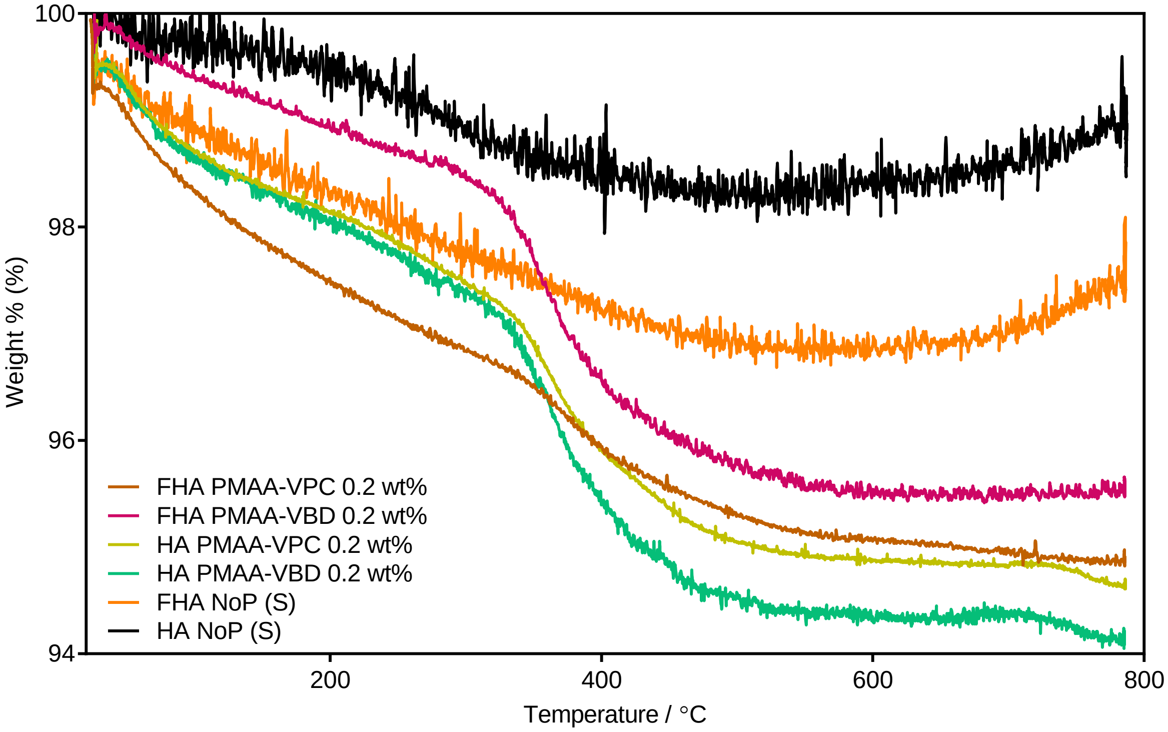

Figure 5.25. Overlaid TGA thermogravimetric curves of HA and FHA samples treated with a 0.2 wt% solution of hyperbranched PMAA with either VPC or VBD as a RAFT agent.

2.12 wt% across the samples which is lower than the 4 wt% that would be expected from the maximum yield of the reaction conditions. Judging by the gradual decrease in weight in all samples when looking at figure 5.25 there is evidence of water loss during the temperature increase from 20 °C to approximately 350 °C. Comparing the (F)HA-PMAA samples with the (F)HA NoP (S) samples shows that the drop in weight % of the (F)HA-PMAA samples does not appear in the (F)HA NoP (S) samples confirming the presence of polymer. This suggests that the lower than expected values of percentage weight loss produced from the analysis can be explained by the loss of polymer during washing as it may have complexed with calcium ions in solution. Alternatively, during heating PMAA will gradually lose water by forming anhydrides then will undergo decarboxylation to release CO_2. This would explain the gradual loss of weight before the drop off at 350 °C[23, 24].

The curves themselves are interesting as there is a considerable difference between samples. The FHA PMAA-VPC sample shows a very gradual decline in weight throughout the TGA run; while the HA PMAA-VPC thermogravimetric curve shows a definitive drop in weight from 350 – 380 °C which is similar to both the FHA and HA PMAA-VBD samples. However, the overall percentage weight loss is relatively consistent across each sample which suggests that similar amounts of polymer are included in the composites. The (F)HA samples containing PMAA-VBD are almost identical in shape with an initial drop in weight in the HA curve explained by the buoyancy of the TGA pan. The FHA PMAA-VPC curve is an anomaly in this instance as there is only a very small change in gradient at 350 – 380 °C compared to the other samples; it is possible that the gradual and consistent weight loss of the FHA PMAA-VPC sample means that the polymer is very well ingrained in the composite and is therefore lost as the outside of the sample is burned. In contrast, thermogravimetric analysis of samples synthesised with 0.8 wt% solutions of PMAA (figure 5.26) show no consistency across the samples. Data is summarised in Table 5.19.

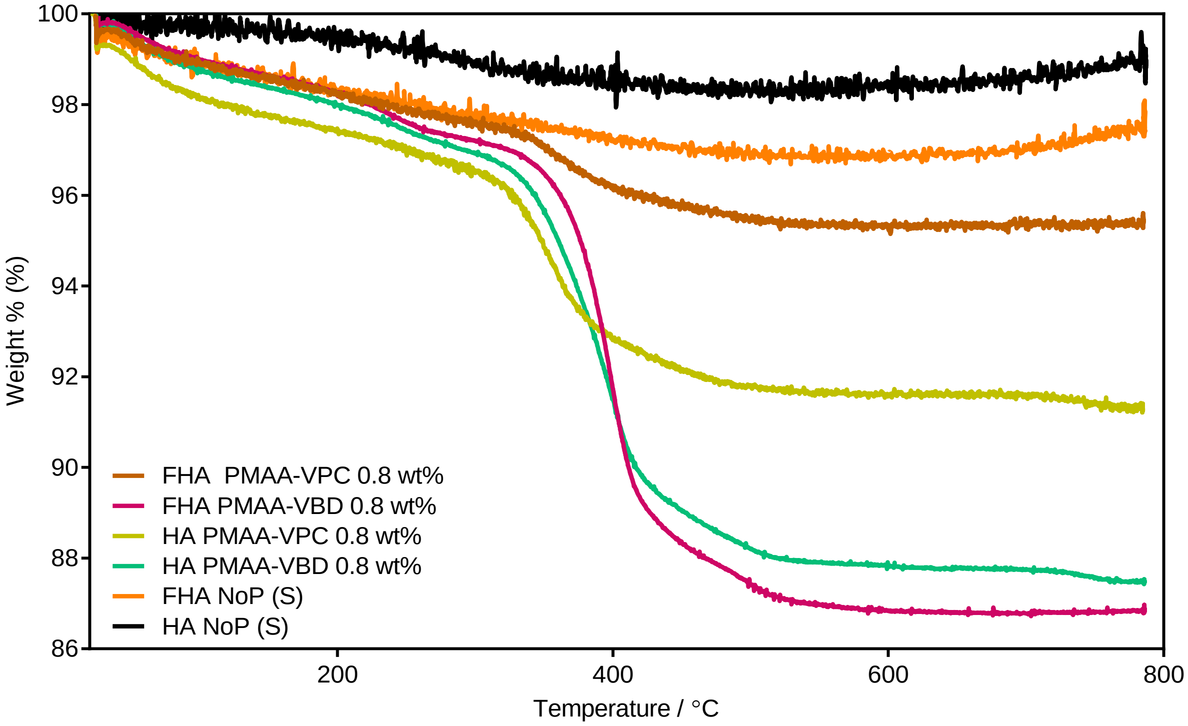

Figure 5.26. Overlaid TGA thermogravimetric curves of HA and FHA samples treated with a 0.8 wt% solution of hyperbranched PMAA with either VPC or VBD as a RAFT agent.

Table 5.19. Weight loss calculated from the region 320-420 °C of the TGA thermogravimetric curves of HA and FHA samples treated with low 0.8 wt% solutions of hyperbranched poly(methacrylic acid)s PMAA-VPC and PMAA-VBD.

Sample	Initial weight / %	Final weight / %	Weight loss / %
FHA PMAA-VPC 0.8 wt%	97.47	95.99	1.48
FHA PMAA-VBD 0.8 wt%	97.04	89.31	7.73
HA PMAA-VPC 0.8 wt%	96.26	92.60	3.66
HA PMAA-VBD 0.8 wt%	96.68	89.84	6.84

Weight losses of between 1.48 and 7.73 wt% show that the theoretical levels of polymer inclusion were not achieved, and there are inconsistencies between the overall weight loss in the samples. The sharp reduction in percentage weight from 350 – 380 °C is more pronounced in the curves of the (F)HA PMAA-VBD samples. A gradual decline in the percentage weight from approximately 20 – 350 °C is followed by a sharp drop in weight from 350 – 380 °C. The HA PMAA-VPC sample shows this to an extent with a much less pronounced decrease in weight between 350 – 380 °C than the PMAA-VBD samples. In contrast, the FHA PMAA-VPC 0.8 wt% sample shows a very gradual decline in weight and overall produced a smaller loss in weight than the 0.2 wt% sample. It is difficult to explain why this is; it is possible that the polymer did not fully dissolve into the solution and hence was not incorporated into the composite in the intended levels. Going back to the XRD and FTIR measurements which show very similar diffraction patterns and spectra respectively across all samples, it is not immediately obvious whether low levels of polymer have been included in the FHA PMAA-VPC 0.8 wt% sample. FHA tends to be more thermally stable than HA; it is therefore possible that polymer degradation products may be unable to leave the sample upon heating due to being highly ingrained into the unit cell of the FHA. Alternatively, it is possible that the PMAA-VPC has been incorporated to a critical level. This is again analogous to natural bone mineral as the collagen present in the hydroxyapatite structures in natural bone is at a critical concentration as stated previously.[16] As such, it is possible that the PMAA is acting in the same manner as natural collagen in this instance and any polymer not included in the composite is instead removed during the washing stages of the material processing.

5.3.4.4 Transmission electron microscopy

TEM images were collected and subsequently analysed using ImageJ software to determine the particle sizes and aspect ratios of the (F)HA PMAA composite samples. TEM micrographs of the samples synthesised with 0.2 wt% PMAA are shown in figure 5.27 and a summary of the particle sizes and aspect ratios is shown in table 5.20. As before, FHA samples were found to be smaller than the HA samples. The widths of the FHA particles are also smaller than the HA samples, while the aspect ratios suggest that the particles have a needle-like morphology rather than a plate morphology. Interestingly, the HA samples have larger aspect ratios than the FHA samples suggesting they are more needle-like than the FHA samples. However, as the HA samples are also larger in all dimensions than the FHA particles the aspect ratios are not large enough to show a significantly different morphology between the HA and FHA particles. Upon analysis of the micrographs (figure 5.27), it is not immediately obvious

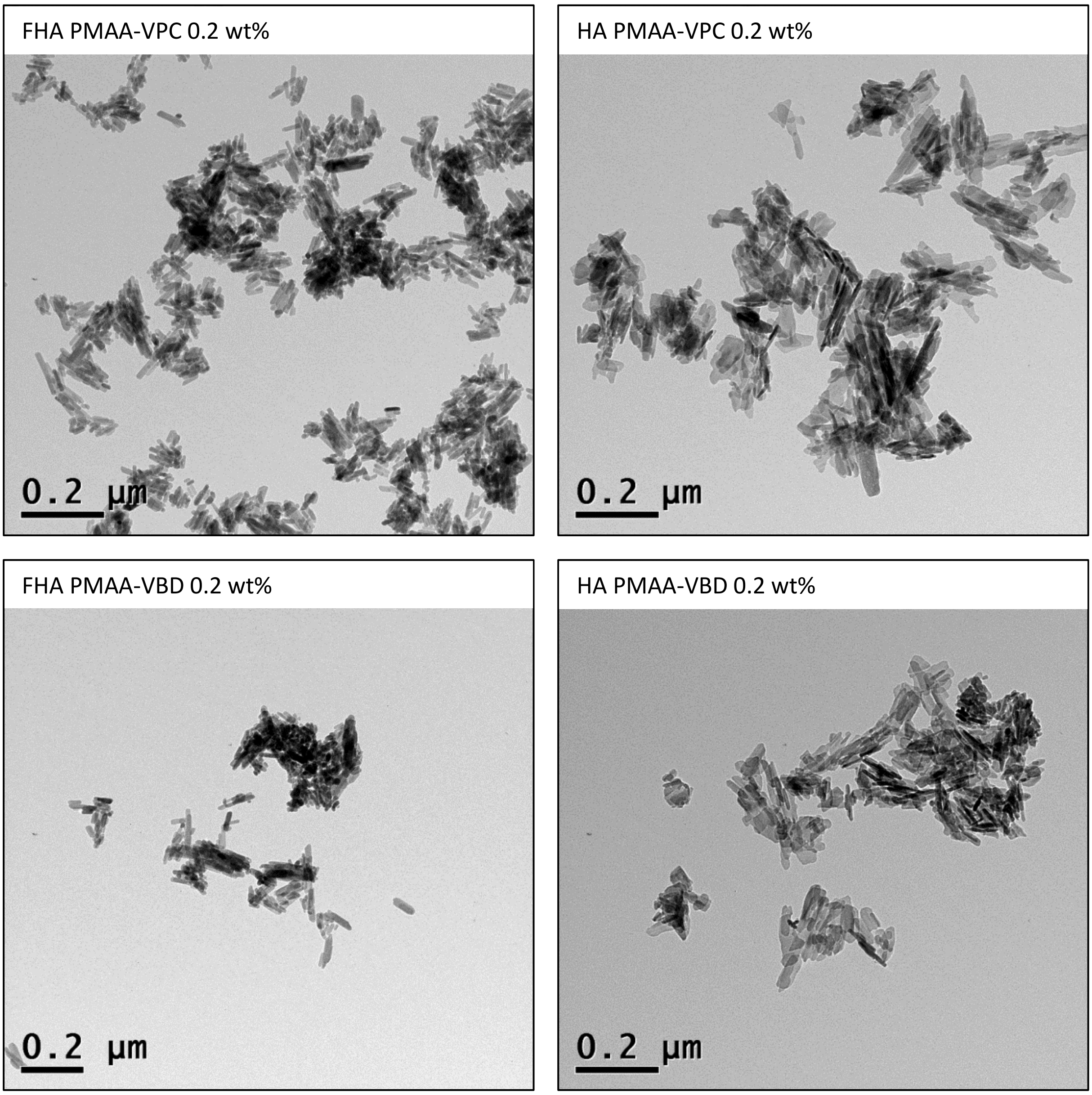

FHA PMAA-VPC 0.2 wt%

HA PMAA-VPC 0.2 wt%

FHA PMAA-VBD 0.2 wt%

HA PMAA-VBD 0.2 wt%

Figure 5.27. TEM micrographs of (F)HA synthesised in the presence of a 0.2 wt% solution of poly(methacrylic acid) made with either VPC or VBD as a branching RAFT agent.

Table 5.20. Lengths, widths and resultant aspect ratios of (F)HA particles synthesised in the presence of a 0.2 wt% solution of poly(methacrylic acid) made with either VPC or VBD as a branching RAFT agent, measured using ImageJ.

Sample	**Lengths / nm**			**Widths / nm**			**Aspect ratios**
	Mean	**SD**	**SE**	**Mean**	**SD**	**SE**	
FHA PMAA-VPC 0.2 wt%	42.52	8.57	0.43	9.09	2.31	0.23	4.68
FHA PMAA-VBD 0.2 wt%	43.06	7.87	0.39	9.86	1.91	0.19	4.37
HA PMAA-VPC 0.2 wt%	99.45	15.88	0.79	14.42	3.97	0.40	6.90
HA PMAA-VBD 0.2 wt%	95.85	17.75	0.88	17.11	4.72	0.47	5.60

whether the HA samples are more needle-like than the FHA as the aspect ratios are not much larger than the FHA samples (table 5.20). The micrographs suggest that the FHA samples are actually more needle-like than the HA samples; however, the aggregation of the particles evident in all the samples may have led to erroneous measurements as it is difficult to distinguish single particles. Looking at the TEM micrographs of the samples synthesised with 0.8 wt% PMAA shown in figure 5.28 a similar picture can be seen. A summary of the particle sizes and aspect ratios of the (F)HA 0.8 wt% PMAA samples is shown in table 5.21.

Table 5.21. Lengths, widths and resultant aspect ratios of (F)HA particles synthesised in the presence of a 0.8 wt% solution of poly(methacrylic acid) made with either VPC or VBD as a branching RAFT agent, measured using ImageJ.

Sample	**Lengths / nm**			**Widths / nm**			**Aspect ratios**
	Mean	**SD**	**SE**	**Mean**	**SD**	**SE**	
FHA PMAA-VPC 0.8wt%	46.59	9.33	0.46	9.26	1.23	0.12	5.03
FHA PMAA-VBD 0.8wt%	54.85	10.09	0.50	11.08	1.45	0.14	4.95
HA PMAA-VPC 0.8wt%	56.31	12.06	0.60	10.11	1.93	0.19	5.57
HA PMAA-VBD 0.8wt%	58.63	12.56	0.63	12.33	2.88	0.29	4.75

The micrographs of the 0.8 wt% PMAA (F)HA samples show that the particles are highly aggregated. The most notable feature of these particles is that the values of the mean particle sizes and aspect ratios shown in table 5.21 are almost identical in all samples. This is very different to all the other samples analysed in this chapter. It is possible that steric and or electrostatic effects produced by the addition of 0.8 wt% PMAA have caused the particles to reach a critical size with a critical concentration of PMAA.[25] These nanoparticle systems are fundamentally colloidal and therefore the addition of charged entities will reach a saturation point after which the size and or stability of the system will not improve.[25] The micrographs show that the particles all have some particles with a needle-like morphology. The HA samples show a slightly different morphology with some particles appearing to be more plate-like. This is not reflected in the aspect ratios given in table 5.21 however it is consistent with the other particles discussed in this chapter. The same effect of the elongation of particles along one axis which was seen in the PAA and 0.2 wt% PMAA samples is also apparent in the samples containing 0.8 wt% PMAA. The amount of aggregation in the samples appears to remain the same between the 0.2 and 0.8 wt% PMAA samples. There is some evidence of alignment in the FHA PMAA-VBD 0.8wt% sample; however, upon inspection of other micrographs of the same sample there is little to suggest that any true particle alignment has occurred.

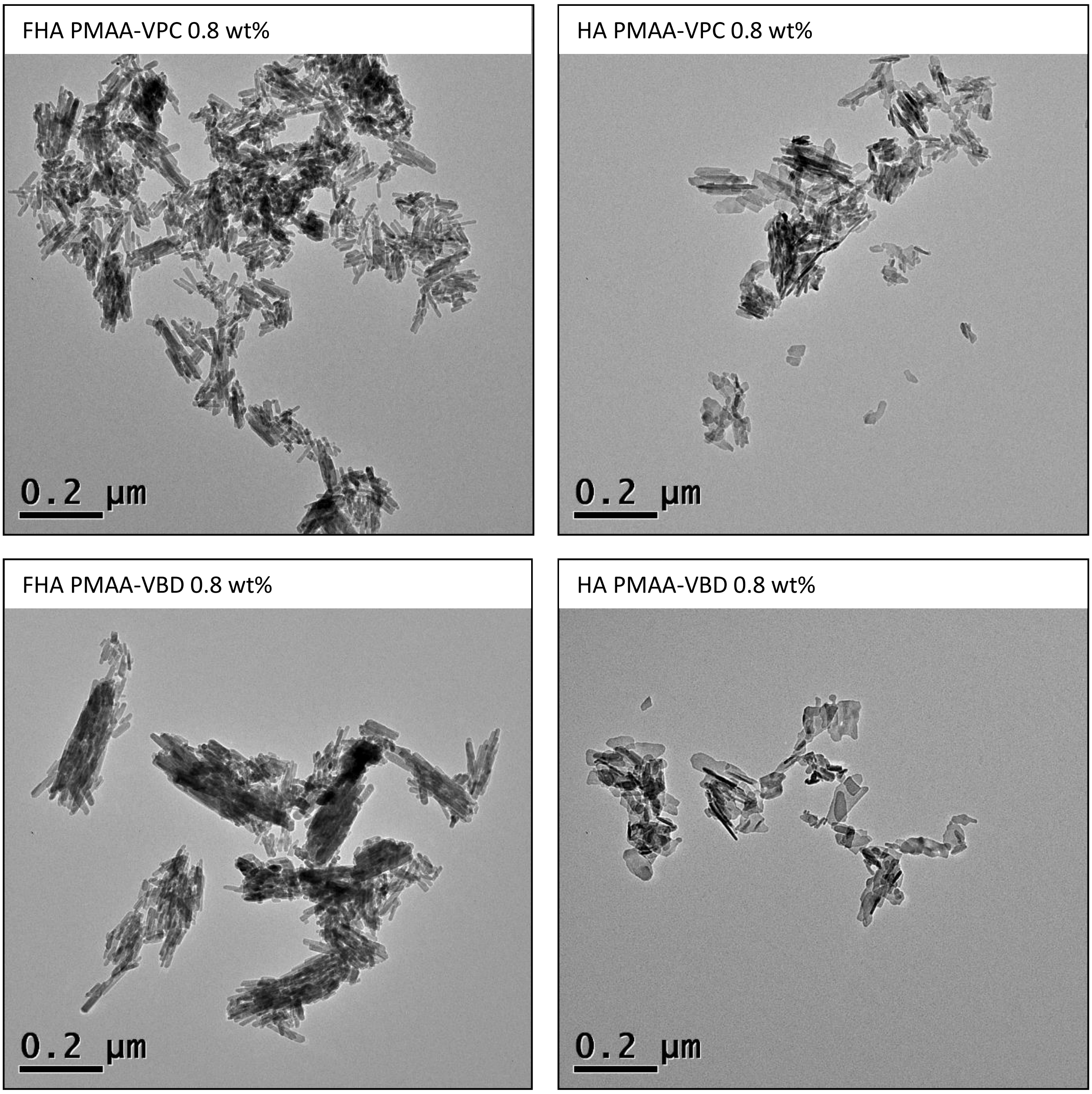

Figure 5.28 TEM micrographs of (F)HA synthesised in the presence of a 0.8 wt% solution of poly(methacrylic acid) made with either VPC or VBD as a branching RAFT agent.

5.4 Conclusion

5.4.1 Synthesis of fluorhydroxyapatite and hydroxyapatite varying linear poly(acrylic acid) additive addition

During a placement at University College Dublin samples of hydroxyapatite and fluorapatite were successfully synthesised with samples of low and high molecular weight linear poly(acrylic acid), E5 and E11 respectively. Samples were also synthesised without polymer to act as a control to compare to the composite samples.

Analysis and characterisation of the particles by TEM showed that the inclusion of fluoride in the samples had an effect on the size and morphology of the particles making them smaller and more needle-like than the HA samples which were found to have a plate-like morphology. Characterisation by TGA showed that the inclusion of a 0.2 wt% solution of E5 or E11 during the synthesis produced composite particles with a polymer content of less than 4 wt%. The inclusion of the PAA produced particles which were more needle-like and showed a higher degree of aggregation than the pure FHA and HA samples. This implies that the polymer may have acted as a nucleation point for the formation of (F)HA particles and the many COO^- side groups then acted as a template for the composite particles to grow along. The aggregation is likely due to increased charge attraction between the Ca^{2+} ions and COO^- in the (F)HA particles causing inter-particle attraction.

XRD analysis showed that the pure (F)HA particles were more crystalline than the E5 and E11 composite particles while FTIR showed that the chemical interactions of the phosphate groups were interrupted in the E5 and E11 samples. Both XRD and FTIR analysis showed a loss of long range order in the phosphate region of the particles with an increase in long range order along the c axis of the unit cell perpendicular to the phosphate groups.

5.4.2 Synthesis of fluorhydroxyapatite and hydroxyapatite without polymer additives

Samples of (F)HA were synthesised without polymer at the University of Sheffield to test the validity of the protocol used at UCD. The (F)HA NoP (S) were found to be almost identical to those synthesised at UCD allowing for negligible differences between the batch wet precipitation synthesis. With the successful recreation of the (F)HA NoP samples at UoS the protocol was then taken further to determine the effect of highly branched polymers on the synthesis of (F)HA.

5.4.3 Synthesis of fluorhydroxyapatite and hydroxyapatite varying highly branched poly(acrylic acid) additive addition

Samples of (F)HA were synthesised in the presence of 0.2 or 0.8 wt% solutions of highly branched poly(acrylic acids) produced by RAFT polymerisation. The particles were characterised using XRD and FTIR which determined that the particles were not fully crystalline and the polymer had been successfully included in the particles.

Characterisation by TGA showed that the particles synthesised using a 0.2 wt% solution, which corresponds to 4 wt% of the maximum particle yield, contained between 6 – 7 wt% of extra material in total, but only ~2 wt% was determined to be polymer. When compared to the samples containing no polymer which contained 2 – 3 wt% extra material determined to be water and adsorbed CO_2, it was concluded that the excess extra material in the highly branched PAA samples was also water and CO_2; this was confirmed by analysis of the FTIR spectra. Samples synthesised with a 0.8 wt% solution, which corresponds to 16 wt% of the maximum particle yield contained between 4 - 5 wt% of extra material. The difference between the maximum yield and experimental yield was thought to be due to a critical concentration of polymer in the composite particles, after which the polymer begins binding to other starting material such as Ca^{2+} ions in the reaction mixture.

Analysis of the micrographs collected by TEM showed that the 0.2 wt% samples were less aggregated than the 0.8 wt% samples with all particles appearing needle-like. The particles appear to agglomerate to form small bundles of aligned particles, suggesting that the polymer acted as a template for the (F)HA to grow along. XRD analysis determined an elongation of the 00l plane of these particles which is consistent with the needle-like particles seen in the TEM micrographs.

5.4.4 Synthesis of fluorhydroxyapatite and hydroxyapatite varying highly branched poly(methacrylic acid) additive addition

Samples of (F)HA synthesised in the presence of 0.2 or 0.8 wt% solutions of highly branched poly(methacrylic acid) to determine the effect of the extra methyl group in the repeat unit. Characterisation using XRD and FTIR determined that the particles were not fully crystalline and the polymer had been successfully included in the particles. FTIR analysis also showed excess water and adsorbed CO_2 in all samples.

Characterisation by TGA showed that the particles synthesised using a 0.2 wt% solution, corresponding to 4 wt% of the maximum particle yield, contained between approximately 1 - 2 wt% of polymer material. When compared to the samples containing no polymer which contained 2 – 3 wt% extra material determined to be water and adsorbed CO_2 and cross examining the TGA result with the FTIR spectra, it was concluded that the excess extra material in the highly branched PMAA samples lost outside of the 320 – 420 was also water and CO_2. Samples synthesised with a 0.8 wt% solution, corresponding to 16 wt% of the maximum particle yield contained between approximately 1.5 – ~ 8 wt% of polymer. The difference between the maximum possible yield and experimental yield was thought to be due to a critical concentration of polymer in the composite particles, after which the polymer begins binding to other starting material such as Ca^{2+} ions in the reaction mixture.

Analysis of the micrographs collected by TEM showed that the 0.2 wt% samples were less aggregated than the 0.8 wt% samples with all particles appearing needle-like. However, the 0.8 wt% samples proved to be extremely similar sizes across both the FHA and HA samples. The HA 0.8 wt% PMAA particles were smaller than the 0.2 wt% samples. This is in line with the suggestion that there is a critical concentration of PMAA that can be included in the (F)HA particles, after which the polymer begins to bind with other ionic species in the reaction mixture. As with the highly branched PAA samples, the (F)HA PMAA particles appear to agglomerate to form small bundles of aligned particles, suggesting that the polymer acted as a template for the (F)HA to grow along. XRD analysis again determined an elongation of the 00l plane of these particles which is consistent with the needle-like particles seen in the TEM micrographs.

With the success of the synthesis of these particles with P(M)AA, these composite particles were taken on for cell testing, as detailed in the next chapter. The protocol for the synthesis of (F)HA particles was also extended further to include other polymers. The synthesis of these polymers will be discussed in chapter 7.

5.5 References

1. R. Lind, *Open Source Software in Life Science Research: Practical Solutions in the Pharmaceutical Industry and Beyond*, 2012, 131-149.
2. W. S. Rasband, *Astrophysics Source Code Library*, 2012.
3. L. Lutterotti, *Nuclear Instruments & Methods in Physics Research Section B-Beam Interactions with Materials and Atoms*, 2010, **268**, 334-340.
4. H. M. Rietveld, *Journal of Applied Crystallography*, 1969, **2**, 65-&.
5. V. K. Pecharsky and P. Y. Zavalij, *Fundamentals of Powder Diffraction and Structural Characterization of Materials, Second Edition*, Springer US, 2009.

6. J. M. Hughes, M. Cameron and K. D. Crowley, *American Mineralogist*, 1989, **74**, 870-876.
7. N. C. Popa, *Journal of Applied Crystallography*, 1998, **31**, 176-180.
8. P. K. Mehta and M. J. Shah, *Journal*, 1969.
9. Bruker, *DIFFRACplus TOPAS 4.2 User ManualDIFFRACplus TOPAS 4.2 User Manual*, Bruker AXS GmbH, Karlsruhe, Germany., 2009.
10. E. Bertoni, A. Bigi, G. Falini, S. Panzavolta and N. Roveri, *Journal of Materials Chemistry*, 1999, **9**, 779-782.
11. H. FurediMilhofer and S. Sarig, *Progress in Crystal Growth and Characterization of Materials*, 1996, **32**, 45-74.
12. K. J. Roche and K. T. Stanton, *Journal of Crystal Growth*, 2015, **409**, 80-88.
13. S. C. Liou, S. Y. Chen and D. M. Liu, *Journal of Biomedical Materials Research Part B-Applied Biomaterials*, 2005, **73B**, 117-122.
14. S. C. Liou, S. Y. Chen and D. M. Liu, *Biomaterials*, 2003, **24**, 3981-3988.
15. L. Berzina-Cimdina and N. Borodajenko, *Research of Calcium Phosphates Using Fourier Transform Infrared Spectroscopy InTech*, 2012.
16. F.-Z. Cui and J. Ge, *Journal of Tissue Engineering and Regenerative Medicine*, 2007, **1**, 185-191.
17. J. Zhao, Y. Weng and D. Xie, *Journal of Biomedical Science and Engineering*, 2010, **3 (11)**, 11.
18. K. Arita, A. Yamamoto, Y. Shinonaga, K. Harada, Y. Abe, K. Nakagawa and S. Sugiyama, *Dental Materials Journal*, 2011, **30**, 672-683.
19. M. Corno, A. Rimola, V. Bolis and P. Ugliengo, *Physical Chemistry Chemical Physics*, 2010, **12**, 6309-6329.
20. M. I. Kay, R. A. Young and A. S. Posner, *Nature*, 1964, **204**, 1050-1052.
21. A. J. Freemont, *Current Orthopaedics*, 1998, **12**, 181-192.
22. T. Lemaire, T. T. Pham, E. Capiez-Lernout, N. H. de Leeuw and S. Naili, *Journal of Biomechanics*, 2015, **48**, 3066-3071.
23. A. Kubotera and R. Saito, *Polymer Journal*, 2016, **48**, 611-619.
24. Y. Inai, S. Kato, T. Hirabayashi and K. Yokata, *Polymer Journal*, 1995, **27**, 196-200.
25. D. J. Shaw, *Introduction to colloid and surface chemistry*, 1966, 186.

Chapter 6 – Cell culture of MG63 cells with (fluor)hydroxyapatite / poly(acrylic acid) nanocomposites

6.1 Chapter Summary

This chapter describes the tissue culture of human fibroblast cells from a cell line of human osteosarcoma cells (MG63 cells) with the (F)HA samples containing 0.2 wt% poly(acrylic acid)s (PAA) described in chapter 5. Concentrations of 1 mg ml^{-1} and 10 mg ml^{-1} of (F)HA particles in cell culture media were used to determine the effect of the particles on the metabolic activity and cell membrane permeability of the MG63 cells. Assays were conducted using a PrestoBlue® (PB) Cell Viability Reagent to determine the metabolic activity of the MG63s after culture for 72 hours in direct contact with the (F)HA particles. A Pierce ™ LDH (lactate dehydrogenase) Cytotoxicity Assay Kit was used to determine the effect of the (F)HA particles on the cell membrane of the MG63 cells. Live/dead staining was also used to image the cells to determine cell viability when subjected to the (F)HA particles. The PB and LDH assays were analysed by fluorescence measurements using a plate reader, while the live/dead staining was analysed using a fluorescence microscope.

6.2 Experimental

6.2.1 Material sterilisation

(F)HA particles were weighed out at the required concentrations, e.g. 100 mg particles weighed out for a 10 ml suspension of 10 mg ml^{-1} particles in media. The particles were suspended in isopropyl alcohol (IPA) and shaken for 30 minutes. The suspensions were centrifuged for 5 minutes at 1000 rpm and the supernatant was removed. The particles were resuspended in phosphate buffered saline (PBS) and shaken for 5 minutes. The suspension was centrifuged for 5 minutes at 1000 rpm and the supernatant removed; this washing procedure was repeated three times. After the final centrifugation, the PBS supernatant was removed and the particles were resuspended in minimum essential medium-A (α-MEM) containing 10 % fetal bovine serum (FBS), 1 % penicillin/streptomycin (P/S), 1 % non-essential amino acids (NEAA), and 1 % L-glutamine (L-glu). These suspensions were then added to the culture cells at the appropriate time point.

6.2.2 Cell Passage

Firstly, the media was removed from a T75 flask of confluent MG63 cells. The cells were washed three times with PBS, then trypsin-EDTA solution (0.05 % trypsin/ 0.02 % EDTA, 3 ml) was added and the flask was incubated for 5 minutes at 37 °C in a 5 % CO_2 atmosphere. 1 ml FBS was added to quench the trypsin and the flask was gently tapped to encourage cell detachment. The cell suspension was transferred to a centrifuge tube and centrifuged at 1000 rpm for 5 minutes. The supernatant was removed and the cell pellet was resuspended in 10 ml media (α-MEM, 10 % FBS, 1 % NEAA, 1 % P/S, 1 % L-glu). 10 μl cell suspension was added to a haemocytometer for cell counting. 200,000 cells were seeded in a clean sterile T75 culture flask and incubated at 37 °C in a 5 % CO_2 atmosphere until confluent. The same procedure was used for cell seeding onto well plates.

6.2.3 PrestoBlue Metabolic Assay

50,000 MG63 cells were seeded in triplicate in 24 well plates and the volume of media in each well was made up to 1 ml. The well plates were incubated at 37 °C in a 5 % CO_2 atmosphere for 24 hours to allow cell attachment. The media was then removed and suspensions of the relevant concentration of sterilised particles in media (1 ml) were added to the appropriate cell wells in triplicate. Additional wells containing no particles were also seeded in triplicate to act as positive and negative controls. The plates were incubated for 72 hours incubated at 37 °C in a 5 % CO_2 atmosphere with the cells in direct contact with the (F)HA particles. After 72 hours a solution of 2 % sodium dodecyl sulfate (SDS) in media was added to the negative control wells and incubated for 15 minutes. In the absence of light 100 μl of media was removed from each well and PrestoBlue® Cell Viability Reagent (100 μl, Thermo Fisher Scientific) was added to each well. The plates were wrapped loosely in foil and incubated at 37 °C in a 5 % CO_2 atmosphere with time points being taken at 30 minutes and 90 minutes after the addition of PB. For each time point 200 μl of media was transferred to a 96 well plate from each cell well. The fluorescence of the solutions was read by a fluorescent plate reader with excitation and emission wavelengths of 535 nm and 590 nm respectively. Plates containing particles, positive control (media and media without serum) and negative control (SDS) wells with no cells were also produced to give a background reading and determine whether the (F)HA particles had an effect on the fluorescence readings.

6.2.4 LDH Assay

A Pierce™ LDH Cytotoxicity Assay Kit (Thermo Fisher Scientific) was used to conduct the chemical compound mediated cytotoxicity assay according to the manufacturer's instructions. 8500 MG63 cells were seeded in triplicate in 96 well plates, the volume of media was made up to 200 µl in each well and the plates were incubated at 37 °C in a 5 % CO_2 atmosphere for 24 hours to allow cell attachment. Additional wells were prepared in the same manner to act as controls. The media was then removed and 200 µl of particle suspensions of the appropriate concentration was added to each well, the plates were then incubated for a further 72 hours at 37 °C in a 5 % CO_2 atmosphere. Triplicate wells of control samples were made up as follows: positive control (1 µl LDH positive control solution in 1 % bovine serum albumin (BSA) in PBS); no cells with media and serum; no cells with media only; spontaneous LDH activity (10 µl sterile DI water); maximum LDH activity (negative control). To start the reaction 10 µl lysis buffer was added to the maximum LDH activity wells and the plate was incubated at 37 °C in a 5 % CO_2 atmosphere for 45 minutes. 50 µl of each sample was transferred to a new 96 well plate and 50 µl of the 'start' reaction mixture from the assay kit was added to each well and mixed using a multi-channel pipette. The plate was loosely wrapped in foil and incubated at room temperature for 30 minutes. 50 µl of 'stop' solution was added to each well and mixed by gentle tapping. The absorbance of the samples at 490 nm and 680 nm was measured using a fluorescent plate reader. % cytotoxicity was calculated according to manufacturer's instructions.

6.2.5 Live/Dead Staining

25,000 MG63 cells were seeded in duplicate in a 48 well plate and the volume of each well made up to 500 µl with media. The plates were incubated at 37 °C in a 5 % CO_2 atmosphere for 24 hours to allow cell attachment. The media was then removed from the wells and 500 µl of particle suspension of the appropriate concentration was added to each well, positive and negative control wells were left with cells in media without particles. The plates were then incubated for a further 72 hours at 37 °C in a 5 % CO_2 atmosphere. A LIVE/DEAD® Viability/Cytotoxicity Kit, for mammalian cells (Thermo Fisher Scientific) was used according to the manufacturer's instructions. 10 µl of 2 mM ethidium homodimer-1 in DMSO/H_2O 1:4 (v/v) (EthD-1) was added to 990 µl PBS and mixed using a Vortex Mixer (Stuart Equipment). 5 µl of 4 mM Calcein AM was added to the EthD-1 solution to give a final concentration of approximately 2 μM of both stains in solution, which was wrapped in foil to protect the solution from light. A negative control was created by adding media with 15 % ethanol to the negative control wells and incubated for 15 minutes then washed with PBS. Media was removed from each cell well and the wells were washed gently with PBS three times. 100 μl of the stain solution was added to just cover the surface of each well. The plates were wrapped loosely in foil and incubated at room temperature for 30 minutes. The plates were viewed under a fluorescent microscope using the green channels to visualise the live cells and red channel to view the dead cells. The resulting images were given false colour using Fiji software[1] and overlaid to view the live and dead cells.

6.3 Results and Discussion

Metabolic assays are a useful method in the determination of the cytotoxic effects of new materials. Commonly used assays include the use of resazurin dye which reacts with nicotinamide adenine dinucleotide (NADH) to form resorufin undergoing a colour change from blue to red in the process.[2-4] This provides a simple assay which is non-toxic to cells and a direct method of measuring cell viability through fluorescence measurement.

Other assays to determine the cytotoxic effect of materials include measuring the release of lactate dehydrogenase (LDH) which gives information on the cell membrane and live/dead staining. LDH assays also use a colour change to indicate the release of LDH which mediates a redox reaction between the oxidised and reduced forms of NADH. The NADH then reacts with a tetrazolium salt 2-(4-iodophenyl)-3-(4-nitrophenyl)-5-phenyl-2*H*-tetrazolium (INT) which is reduced to formazan, a red dye. The accompanying colour change from colourless to red again provides a direct method of measuring LDH release by absorbance measurement at 490 nm.[5]

Live/dead staining is a useful method of determining cell viability as it uses two dyes which selectively stain either living or dead cells. The most commonly used dyes used are calcein-AM (green) and ethidium homodimer-1 (EthD-1, red) which stain living and dead cells respectively. Other dyes are available for staining with the many requirement being that one dye is membrane permeable which can then be metabolised within the living cells while the other is membrane impermeable and binds with DNA from damaged or dead cells.[6] Live/dead staining can produce quantitative data by counting cells on a haemocytometer and determining the ratio of living a dead cells. This method is not always possible due to the constraints of some cells culture techniques including direct methods in which cells are in contact with materials in culture whereby removing cells from culture and placing them on a haemocytometer would negate the results of the assay.[3, 7]

6.3.1 PrestoBlue® Metabolic Assay

A PrestoBlue® metabolic assay was undertaken using MG63 cells cultured in the presence of (F)HA particles at a concentration of 1 mgml^{-1} or 10 mgml^{-1}. PB was added to the cell culture wells at a concentration of 10 % PB in media and time points were taken 30 minutes and 90 minutes after the stain was added to the wells. Fluorescence measurements were obtained using a plate reader with excitation and emission wavelengths of 535 nm and 590 nm respectively. The PrestoBlue® assay proceeds via the irreversible redox reaction between the resazurin stain in the PB and the reduced form of the mitochondrial coenzyme nicotinamide adenine dinucleotide (NADH) found in cells.[8] The redox reaction causes the resazurin to be reduced to resorufin causing a colour change from blue to red. This is mediated by the NADH coenzyme which is oxidised during the reaction as shown in scheme 6.1.[2, 8-10]

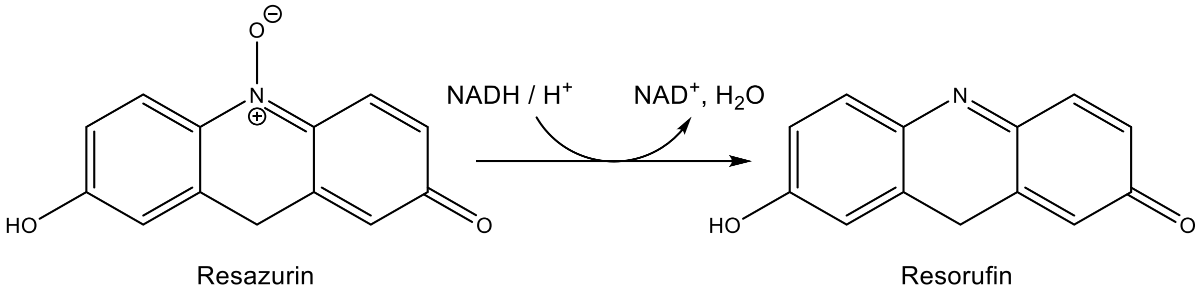

Scheme 6.1. A schematic showing the redox reaction between resazurin and the reduced form of nicotinamide adenine dinucleotide (NADH) to produce resorufin.

Fluorescence measurements were obtained from the cell samples containing (F)HA particles at a concentration of either 1 mg ml^{-1} and 10 mg ml^{-1}; control samples containing particles but no cells were also measured. These measurements were taken in order to account for any fluorescence emitted by the (F)HA particles or media. The raw fluorescence data obtained for all samples is shown in figure 6.1.

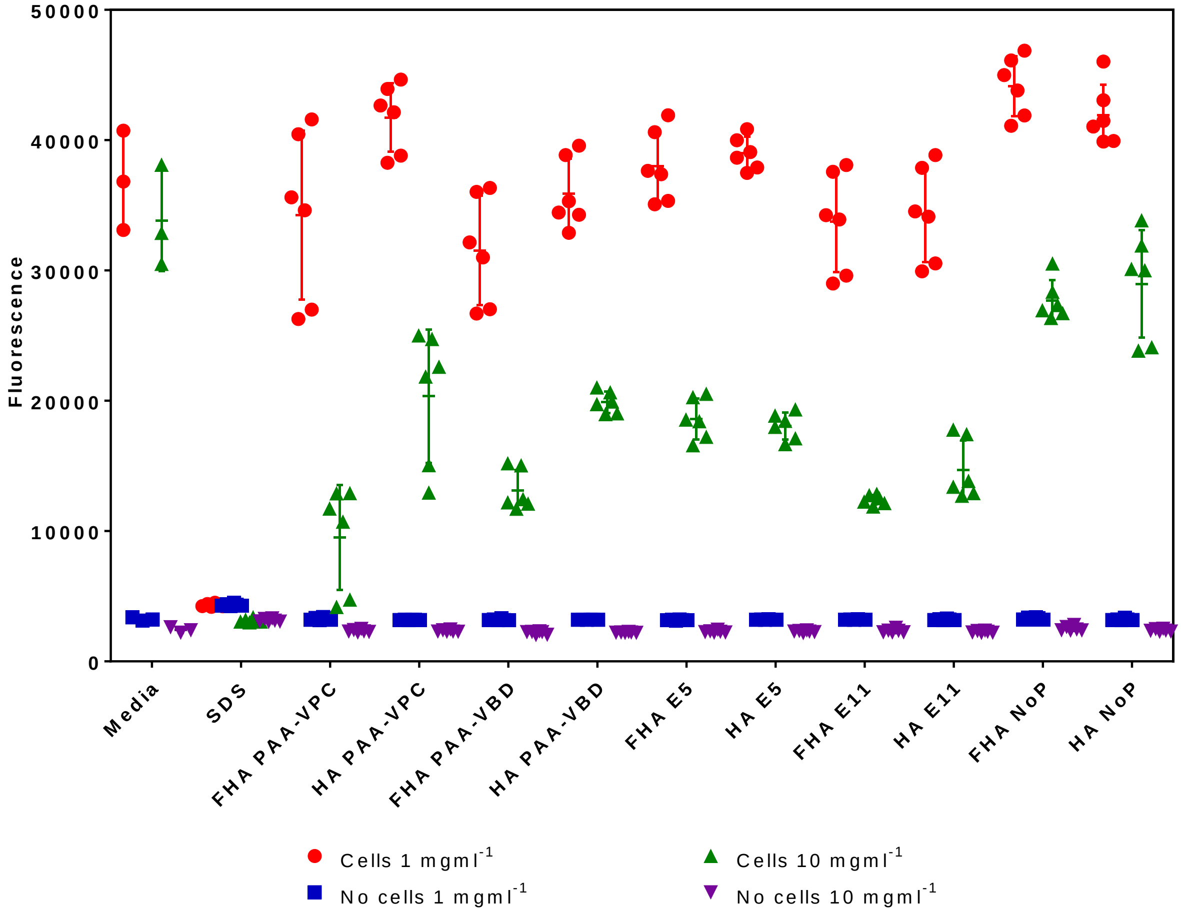

Figure 6.1. A graph showing the measured fluorescence at 90 minutes after the addition of PB stain to (F)HA particles in media only and MG63 cells cultured for 72 hours in direct contact with 1 mg ml^{-1} (F)HA particles. Error bars indicate the standard deviation of the raw fluorescence values.

The raw data shows a spread of values for each data set. In order to make this data more meaningful, the fluorescence measurements from the cell samples were normalised by taking the mean fluorescence of the cell sample and subtracting the mean fluorescence of the corresponding no cell sample containing (F)HA particles. This way the fluorescence emitted by the PB stain, media and (F)HA particles is removed and the value which remains is the mean fluorescence for the cultured cells only.

Figure 6.2 shows the mean fluorescence for the MG63 cells loaded with 1 mgml^{-1} (F)HA particles at 90 minutes after incubation with the PB stain. The greater the fluorescence output means more NADH is in the system producing resorufin, hence there are more living cells in the system. The irreversible reduction of resazurin to resorufin is therefore directly proportional to aerobic respiration of cells and hence can be used as a quantifiable method of assessing cell viability.[2, 8-11] The data shown in figure 6.2 suggests that at a concentration

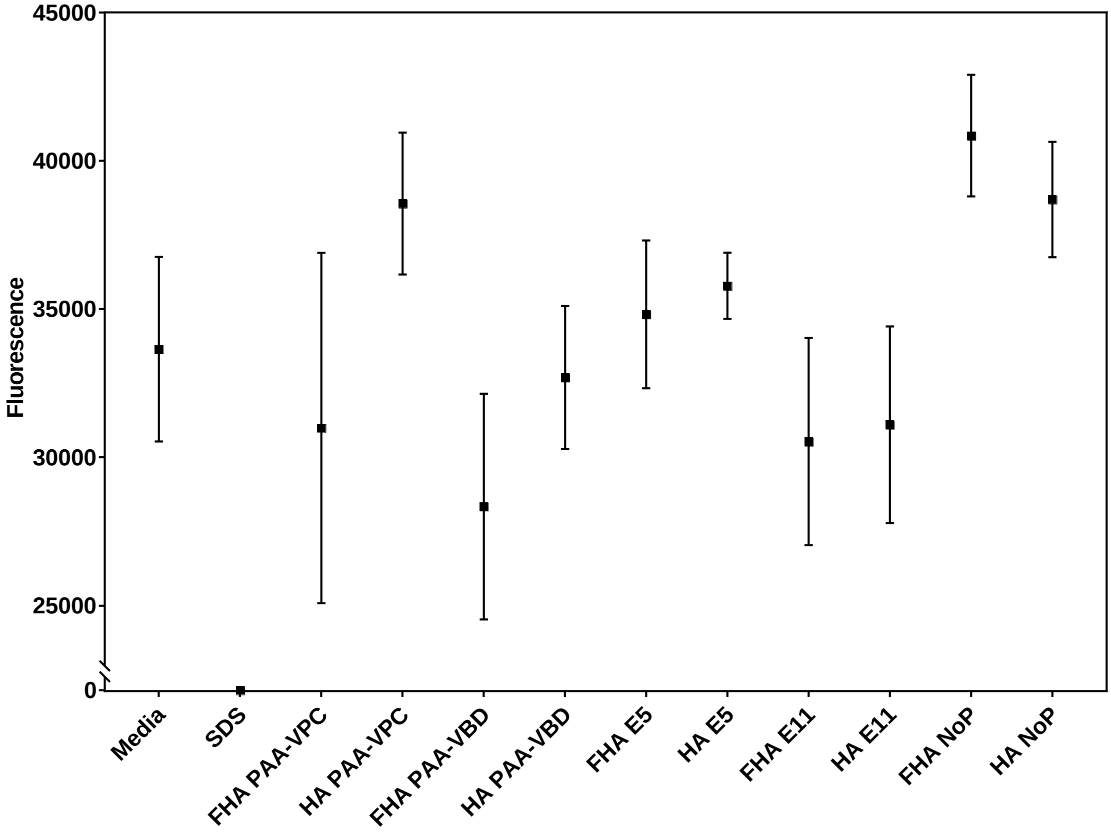

Figure 6.2. A graph showing the mean measured fluorescence at 90 minutes after the addition of PB stain to MG63 cells cultured for 72 hours in direct contact with 1 mg ml^{-1} (F)HA particles. Error bars indicate the standard deviation associated with the mean values of fluorescence.

of 1 mg ml^{-1} of (F)HA particles, the cells are not largely affected by the (F)HA particles. The negative control of SDS shows that none of the particle suspensions are completely cytotoxic, while the positive control indicates that the particles have some effect on cell viability. It appears that the particles containing no polymer (NoP) and the HA with branched poly(acrylic acid) containing pyrrole end groups (PAA-VPC) particles had the least cytotoxic effect on the MG63 cells and may have even encouraged cell growth due to the higher fluorescence measurement than the positive control. However, this cannot be determined for certain without further rigorous assessment. It also appears that the FHA samples may be marginally more cytotoxic than the HA samples as overall the FHA samples show a lower fluorescence output. To determine the effect of the concentration of particles loaded onto the cells, a second experiment using particle suspension at a concentration of 10 mgml^{-1} was conducted. Figure 6.3 shows the measured fluorescence for the MG63 cells loaded with 10 mgml^{-1} (F)HA particles at 90 minutes after incubation with the PB stain.

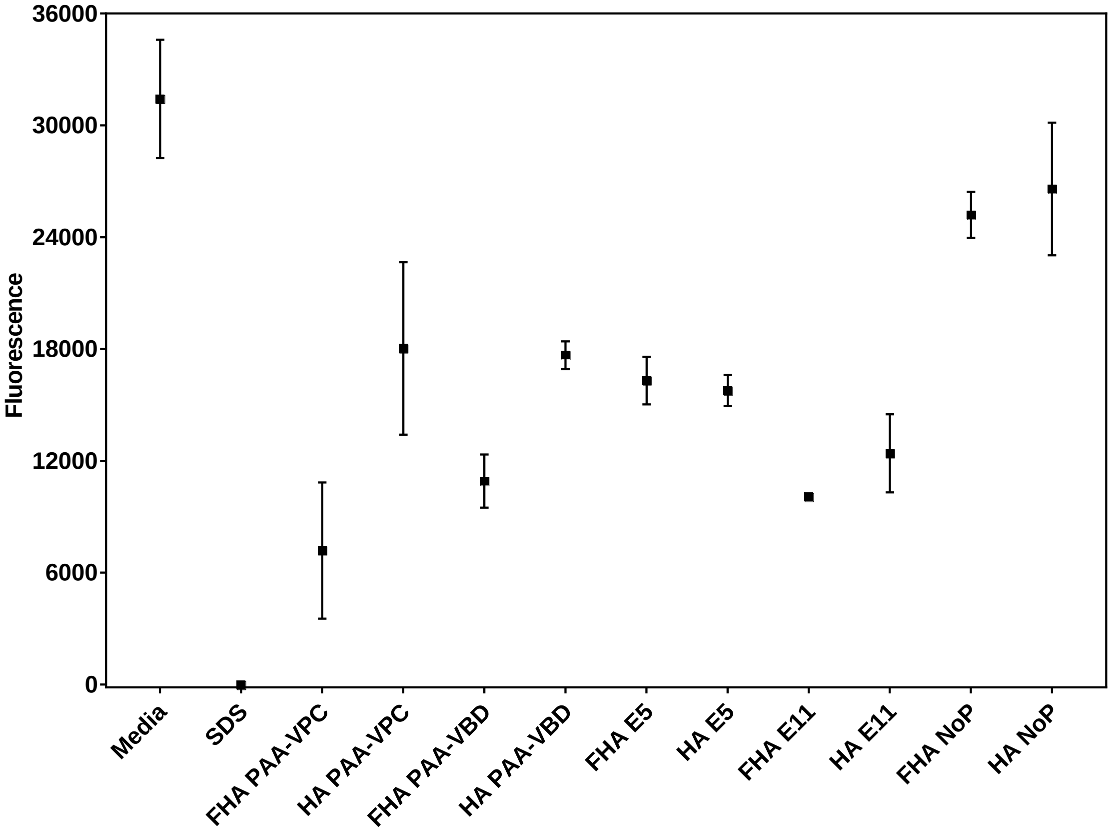

Figure 6.3. A graph showing the mean measured fluorescence at 90 minutes after the addition of PB stain to MG63 cells cultured for 72 hours in direct contact with 10 mg ml^{-1} (F)HA particles. Error bars indicate the standard deviation associated with the mean values of fluorescence.

It is immediately obvious when viewing figure 6.3 that the concentration of the particles in media loaded onto the cells has a direct effect on cell viability. In all cases the measured fluorescence output is far lower than the measurements at 1 mgml^{-1} indicating that increasing the concentration of particles in the cell well increases the cytotoxic effect of the particles. However, the overall fluorescence measurements are far lower than those observed for the 1 mgml^{-1} samples hence showing there is less NADH in the system and the increased particle concentration has had a more cytotoxic effect than the lower concentration of particles.

6.3.2 LDH Assay

A second assay to determine the effect of the (F)HA particles on the cell membrane of the MG63 cells was also conducted. This assay measures the level of lactate dehydrogenase (LDH) released into the cell culture media when the cell membrane is damaged. The LDH released can be quantified through an enzymatic reaction which transforms lactate into pyruvate; the reaction is catalysed by free LDH in the system. A schematic diagram of the assay mechanism is shown in scheme 6.2.

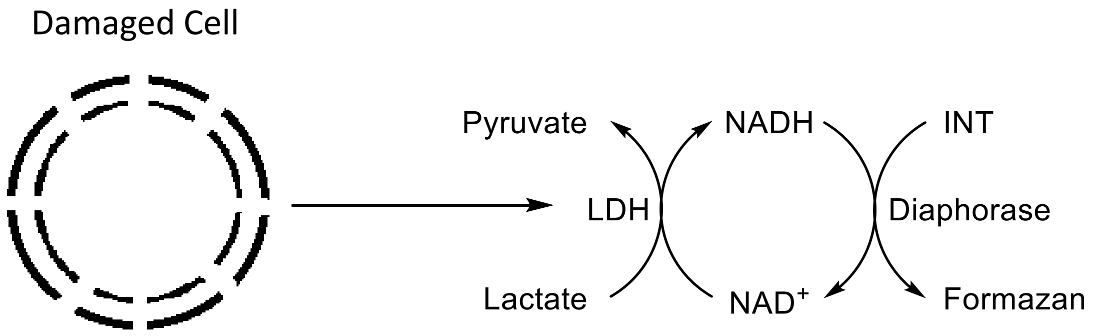

Scheme 6.2. Schematic mechanism of the LDH cytotoxicity assay reproduced from the Pierce LDH Cytotoxicity Assay Kit (Thermo Scientific) instructions.[12]

2-(4-iodophenyl)-3-(4-nitrophenyl)-5-phenyl-2*H*-tetrazolium (INT) is a tetrazolium salt commonly used in redox assays as its reduced form formazan is a red dye which can be used quantitatively to assess LDH release. During the assay LDH released by damaged cells reduces NAD^+ to NADH which then reacts with the INT to form formazan. The reaction can be followed visually via a colour change from colourless to red indicating the presence of formazan and hence LDH. In order to quantitatively measure LDH release, absorbance measurements at 490 nm and 680 nm can be obtained using a plate reader. The reading at 680 nm gives a background absorbance signal from the instrument, subtracting this value from the corresponding 490 nm absorbance value gives the absorbance output for a particular well. This can then be used in conjunction with the control samples and equation 6.1 to determine % cytotoxicity of the compound used to treat the cells.

$$\%\,Cytotoxicity = \frac{Compound\ treated\ LDH\ activity - Spontaneous\ LDH\ activity}{Maximum\ LDH\ activity - Spontaneous\ LDH\ activity} \times 100 \qquad \text{Eqn. 6.1}$$

Equation 6.1 normalises the data by taking maximum LDH activity as 100 % cytotoxicity and spontaneous LDH activity as 0 % cytotoxicity, this means that the value left directly corresponds to the % cytotoxicity of the compound used to treat the cells. Tables 6.1 and 6.2 give the mean absorbance, corresponding % cytotoxicity and standard deviation of (F)HA particles included in the cell culture of MG63 cells for 72 hours at concentrations of 1 mg ml^{-1} and 10 mg ml^{-1} respectively. For these calculations two measurements from three cell wells were made, hence n = 6.

Table 6.1. Normalised mean absorbance values measured at a wavelength of 490 nm for MG63 cells cultured in direct contact with 1 mgml^{-1} (F)HA particles for 72 hours to measure LDH released by cells and determine the % cytotoxicity of the (F)HA particles. The % cytotoxicity was calculated according to equation 6.1, the corresponding standard deviation of % cytotoxicity measurements is also shown. Negative values indicate less LDH is present in the sample than the measured spontaneous LDH released by cells.

Sample	Mean Absorbance	% Cytotoxicity	Standard deviation
FHA PAA-VPC	0.30	-0.47	0.21
HA PAA-VPC	0.26	-2.04	0.52
FHA PAA-VBD	0.33	0.97	0.62
HA PAA-VBD	0.28	-1.06	1.23
FHA NoP	0.32	0.64	1.04
HA NoP	0.29	-0.75	0.49
FHA E5	0.32	0.41	0.52
HA E5	0.35	1.89	0.04
FHA E11	0.27	-1.68	1.08
HA E11	0.32	0.49	1.842
Media + serum	0.40	4.11	1.14
Media	0.10	-9.25	0.43
Positive control	0.31	-0.14	0.87
Spontaneous LDH	0.31	0.00	0.41
Max LDH	2.61	100.00	46.64

Table 6.2. Normalised mean absorbance values measured at a wavelength of 490 nm for MG63 cells cultured in direct contact with 10 mgml^{-1} (F)HA particles for 72 hours to measure LDH released by cells and determine the % cytotoxicity of the (F)HA particles. The % cytotoxicity was calculated according to equation 6.1, the corresponding standard deviation of % cytotoxicity measurements is also shown. Negative values indicate less LDH is present in the sample than the measured spontaneous LDH released by cells

Sample	Mean Absorbance	% Cytotoxicity	Standard deviation
FHA PAA-VPC	0.92	20.59	5.79
HA PAA-VPC	0.32	2.14	0.49
FHA PAA-VBD	0.68	13.03	2.18
HA PAA-VBD	0.27	0.54	0.97
FHA NoP	0.35	2.93	2.13
HA NoP	0.31	1.68	0.20
FHA E5	0.48	7.10	1.05
HA E5	0.41	4.77	1.07
FHA E11	0.31	1.85	1.28
HA E11	0.42	5.05	1.57
Media and serum	0.15	-3.18	0.95
Media	0.04	-6.60	0.03
Positive control	0.00	-7.68	0.06
Spontaneous LDH	0.25	0.00	1.35
Max LDH	3.50	100.00	0.58

In some cases, a negative value of % cytotoxicity was determined for samples indicating less LDH was released than the control sample of spontaneous LDH release in which cells were treated with deionised water. The large standard deviation seen in the maximum LDH sample for the 1 mg ml^{-1} may have been due to pipetting errors when adding the 'start' or 'stop' solutions to the wells. Overall, the data for LDH released by cells treated with 1 mg ml^{-1} (F)HA particles were very low, showing that at this concentration the particles are not particularly cytotoxic. Increasing the concentration of particles to 10 mg ml^{-1} showed an increase in the levels of LDH released and hence % cytotoxicity associated with the particles responsible. Interestingly the % cytotoxicity measured for the 10 mg ml^{-1} samples was positive in all cases for the particle samples, this suggests that there is a maximum loading of particles after which their therapeutic potential is surpassed by the cells' ability to effectively metabolise the material. Figure 6.4 shows a graphical representation of the 1 mg ml^{-1} and 10 mg ml^{-1} LDH release data in order to compare the % cytotoxicity of the particle and control samples at the two different concentrations.

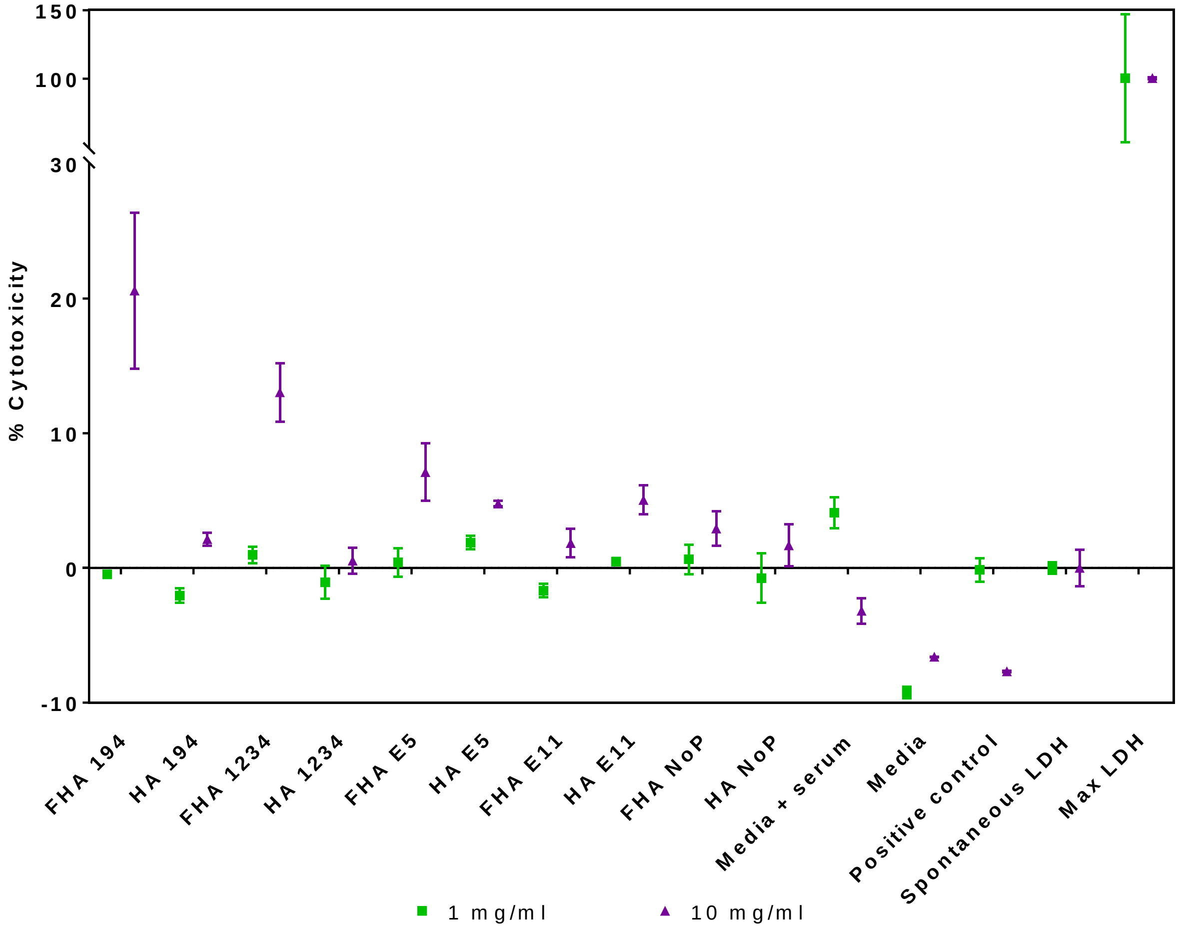

Figure 6.4. Normalised % cytotoxicity values determined by absorbance measurements at a wavelength of 490 nm for MG63 cells cultured in direct contact with 1 mgml^{-1} or 10 mgml^{-1} (F)HA particles for 72 hours to measure LDH released by cells. The % cytotoxicity was calculated according to equation 6.1, error bars indicate the standard deviation of % cytotoxicity measurements. Negative values indicate less LDH is present in the sample than the measured spontaneous LDH released by cells.

In all cases the media only and positive control samples produced a negative % cytotoxicity response showing that the cells were healthy. Oddly, the media and serum control in the 1 mgml^{-1} data set appears to show around 4 % cytotoxicity. This may be due to issues with pipetting which may have led to more or less than 150 μl of material being added to the well causing erroneous results. It is also possible that the cells were damaged by some other means, possibly the addition of the 'start' solution and subsequent mixing may have caused some minor damage to cells in that well. The graph appears to show that increasing the concentration of particles in the cell wells increases the % cytotoxicity of the particles. FHA PAA-VPC appears to be the most cytotoxic judging by the LDH assay, while the FHA samples in general appear to be marginally more cytotoxic than the HA samples. Live/dead staining was conducted in order to determine whether these levels of cytotoxicity were accurate.

6.3.3 Live/Dead Staining

Live/dead staining was undertaken using a solution of calcein AM (CAM) to stain living cells and ethidium homodimer-1 (EthD-1) to stain dead cells. The stained cells were then imaged using a fluorescence microscope via green and red channels. Figures 6.5 and 6.6 show the composite images of the live/dead stained MG63 cells treated with FHA and HA respectively. Particle suspension concentrations were maintained at 1 mg ml^{-1} and 10 mg ml^{-1} to be comparable to the PB and LDH assays already discussed.

The first point of interest to note about these images is that the levels of cells seeding appear to be very different across all samples. Some images such as FHA E5 10 mg ml^{-1}, FHA NoP 10 mg ml^{-1} and HA E5 10 mg ml^{-1} appear to have much greater cell densities than the other samples. In contrast to this the HA PAA-VPC 1 mg ml^{-1} and FHA PAA-VPC 10 mg ml^{-1} appear to have particularly low seeding densities. This is unexpected as the same number of cells were seeded in each well. It is possible this was caused by the cell suspension settling even with resuspension between the cells being seeded into wells.

The second point of interest is the fact that the (F)HA particles appear to be stained by the EthD-1 stain as is evident in the (F)HA PAA-VBD 10 mg ml^{-1} images. These images also show that the cells are capable of growing in direct contact with the (F)HA particles as the living cells are in the same area as the particles. It is not obvious however whether the cells are growing on the particles or below them on the tissue culture plastic as the overlaid stained

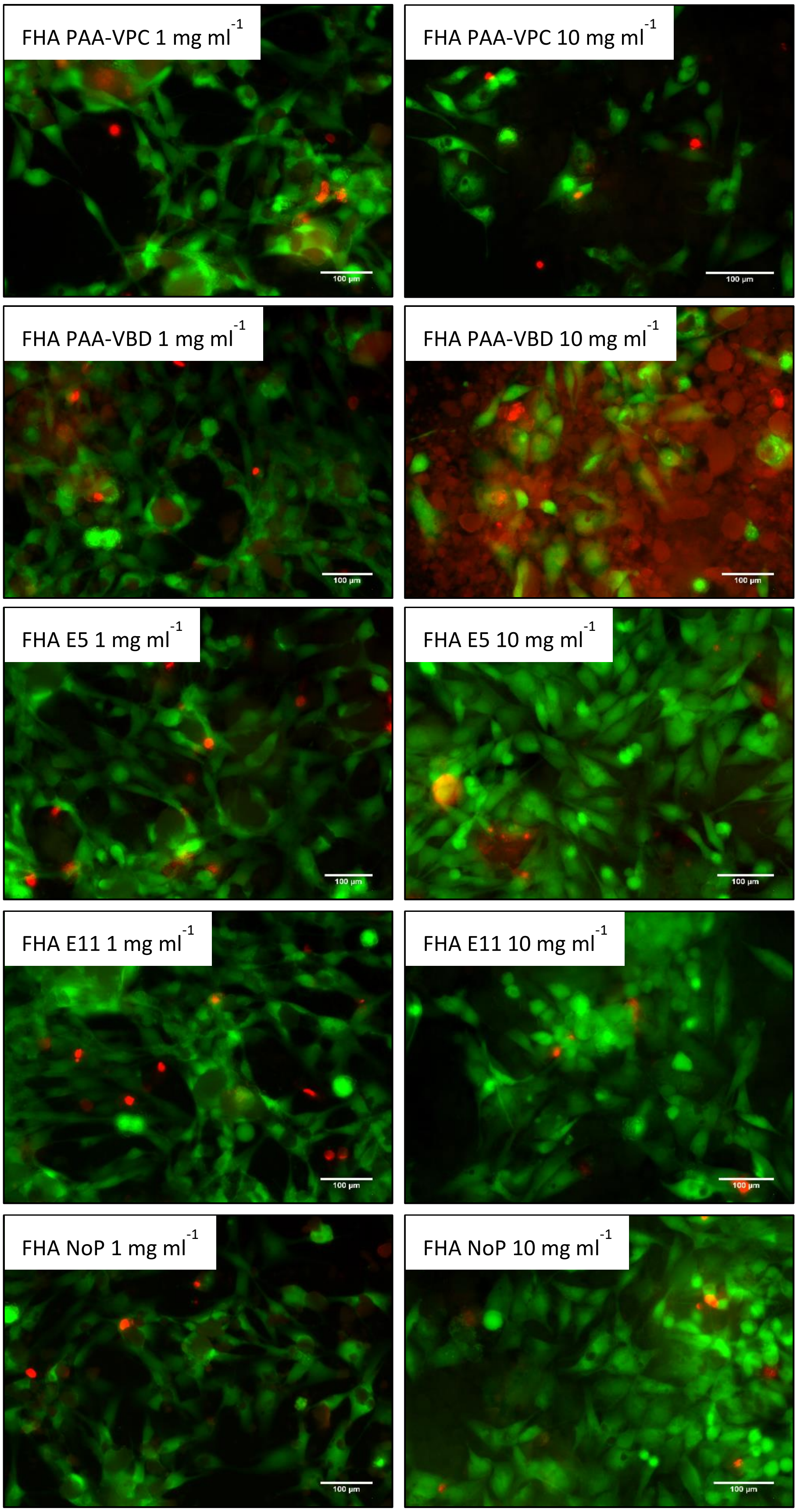

Figure 6.5. False colour fluorescence microscope images of MG63 cells treated with FHA samples at concentrations of 1 mgml^{-1} and 10 mgml^{-1}. The live and dead cells were stained using Calcein AM (green) and ethidium homodimer-1 (red) respectively.

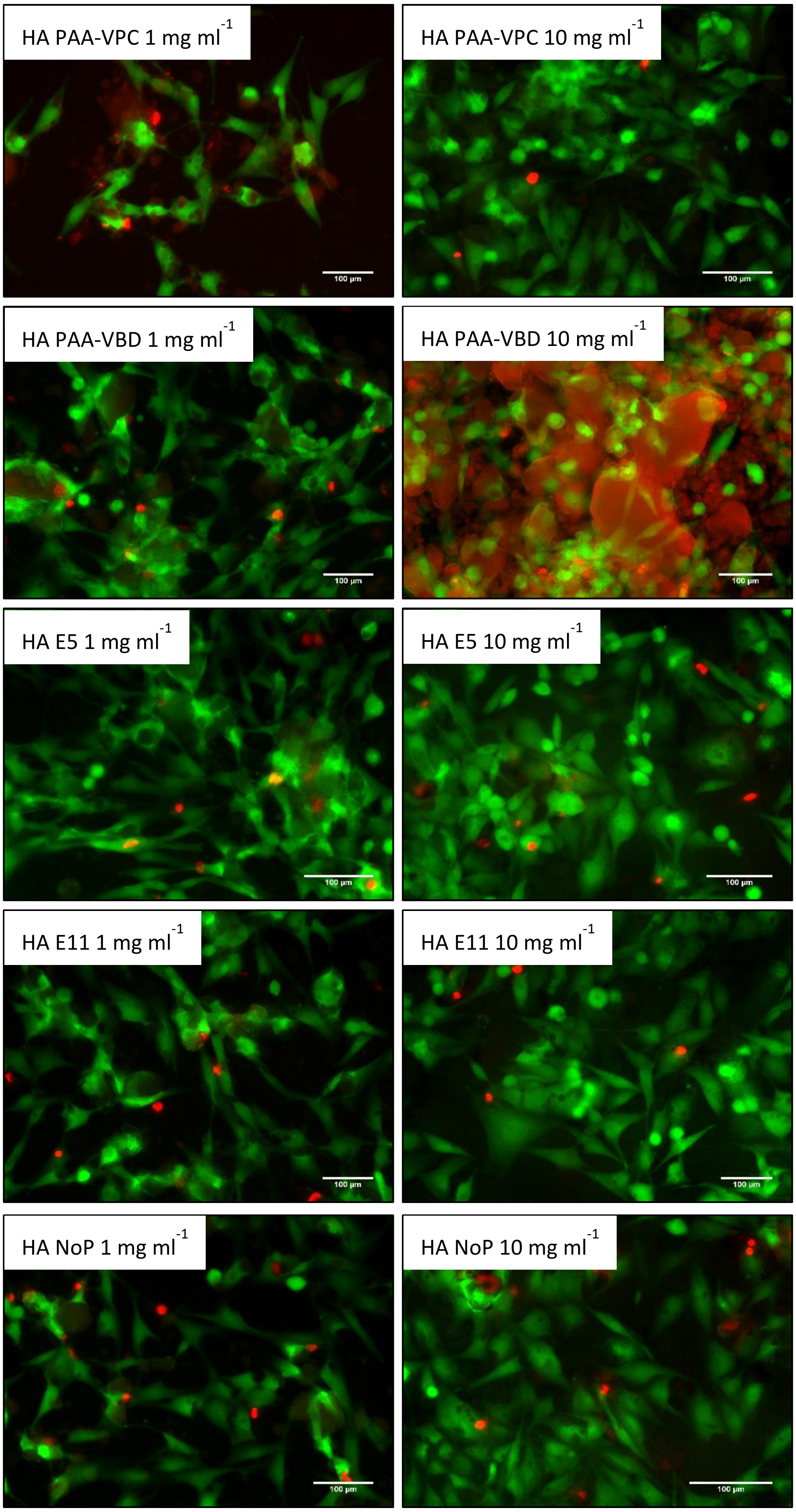

Figure 6.6. False colour fluorescence microscope images of MG63 cells treated with HA samples at concentrations of 1 mgml^{-1} and 10 mgml^{-1}. The live and dead cells were stained using Calcein AM (green) and ethidium homodimer-1 (red) respectively.

images show only the fluorescence output of that channel rather than the three-dimensional position of the cells.

Also evident is the fact that there appears to be no significant difference between the number of living and dead cells in any of the images. This may be due to the limited area available for imaging, or it is possible that the cells were largely unaffected by the presence of the (F)HA particles. Overall it was not possible to determine any cytotoxic effects of the (F)HA particles using this technique. However, the live/dead staining does appear to indicate that the cells can grow and survive in the presence of the (F)HA particles to a certain extent. In all the images there are living (green) and dead (red) cells present. The number of living and dead cells varies with each sample due to the apparent cell density.

6.4 Conclusion

Several assays were conducted to determine the impact of adding (F)HA particles to MG63 cells in culture. Cell viability, damage to the cell membrane and numbers of live and dead cells were measured after cells had been cultured for 72 hours with (F)HA particles at a concentration of either 1 mgml^{-1} or 10 mgml^{-1}. Actual concentrations of particles were extremely difficult to maintain in terms of consistency due to the sterilisation process and the fact that the particles settled very quickly in media. This meant that resuspension was conducted within the pipette during addition to the cell well which clogged the pipette and caused inconsistencies in the volumes of media added to the cell wells.

PrestoBlue assays using MG63 cells cultured with (F)HA particles at a concentration of either 1 mgml^{-1} or 10 mgml^{-1} determined that the FHA samples had a marginally greater impact on the cell viability than the HA samples. This was determined by fluorescence measurements using a plate reader which showed that HA samples produced a higher level of fluorescence which is directly proportional to cell viability. Cells cultured with particles at a concentration of 1 mgml^{-1} showed greater cell viability than cells cultured with particles at a concentration of 10 mgml^{-1}. This was expected as the greater particle loading almost completely covered the cells in culture and hence may have prevented cells from growing normally.

LDH assays conducted on MG63 cells cultured in the same manner outlined above determined that the (F)HA particles had very little impact on cell membranes at a concentration of 1 mgml^{-1} but the % cytotoxicity increased when the particles were introduced at a concentration of

10 mgml^{-1}. Again, this is likely due to the particles smothering the cells at the higher concentration. Both concentrations showed relatively low levels of % cytotoxicity in comparison with the negative control (100 % cytotoxicity) suggesting that the particles had little effect on the cell membranes.

Live/dead staining showed that the cell coverage in the wells was slightly uneven and may have been caused by pipetting errors due to cells settling in between seeding even with resuspension of the cells between wells being seeded. Some samples containing the higher concentration of (F)HA particles showed large numbers of particles surrounding the cells as the (F)HA particles absorbed the EthD-1 (red) dye along with the dead cells. Living and dead particles were seen in all samples and the fact that living cells definitely outnumbered the dead cells shows that the (F)HA particles are not inherently cytotoxic. The cytotoxicity levels could not be quantified by live dead staining due to the limited number of cells in each image.

6.5 References

1. J. Schindelin, I. Arganda-Carreras, E. Frise, V. Kaynig, M. Longair, T. Pietzsch, S. Preibisch, C. Rueden, S. Saalfeld, B. Schmid, J.-Y. Tinevez, D. J. White, V. Hartenstein, K. Eliceiri, P. Tomancak and A. Cardona, *Nature Methods*, 2012, **9**, 676-682.
2. T. Dienstknecht, K. Ehehalt, Z. Jenei-Lanzl, J. Zellner, M. Mueller, A. Berner, M. Nerlich and P. Angele, *Bulletin of Experimental Biology and Medicine*, 2010, **150**, 157-159.
3. H. H. J. Gerets, S. Dhalluin and F. A. Atienzar, *Mammalian Cell Viability: Methods and Protocols*, 2011, **740**, 91-101.
4. S. N. Rampersad, *Sensors*, 2012, **12**, 12347-12360.
5. K. Jaehn and M. J. Stoddart, in *Mammalian Cell Viability: Methods and Protocols*, ed. M. J. Stoddart, 2011, vol. 740, pp. 141-148.
6. M. J. Stoddart, *Mammalian Cell Viability: Methods and Protocols*, 2011, **740**, 1-6.
7. B. Gantenbein-Ritter, C. M. Sprecher, S. Chan, S. Illien-Juenger and S. Grad, in *Mammalian Cell Viability: Methods and Protocols*, ed. M. J. Stoddart, 2011, vol. 740, pp. 127-140.
8. M. Boncler, M. Rozalski, U. Krajewska, A. Podsedek and C. Watala, *Journal of Pharmacological and Toxicological Methods*, 2014, **69**, 9-16.
9. E. G. M. Lemos and L. M. Carareto-Alves, *World Journal of Microbiology & Biotechnology*, 1998, **14**, 139-141.

10. J. O'Brien, I. Wilson, T. Orton and F. Pognan, *European Journal of Biochemistry*, 2000, **267**, 5421-5426.

11. R. Gonzalez-Pinzon, R. Haggerty and D. D. Myrold, *Journal of Geophysical Research-Biogeosciences*, 2012, **117**.

12. T. Decker and M. L. Lohmannmatthes, *Journal of Immunological Methods*, 1988, **115**, 61-69.

Chapter 7 – Synthesis and characterisation of (fluor)hydroxyapatite nanoparticles with poly(ethylene glycol – *co* – *N*-(2-hydroxyethyl) acrylamide) copolymers

7.1 Chapter Summary

This chapter describes the synthesis and analysis of (fluor)hydroxyapatite ((F)HA) composite samples produced using the poly(ethylene glycol – *co* – *N*-(2-hydroxyethyl)acrylamide) (PEG-co-HEA) polymers provided by Sarah-Franziska Stahl. Composite samples were synthesised using the Dublin method with PEG-co-HEA polymers in place of the poly[(meth)acrylic acid] samples used previously. It was hypothesised that the PEG block would act as a steric stabiliser while the HEA block would interact with the forming apatite particles; this would then lead to discrete dispersed nanoparticles with PEG stabilisers on the outside of the particles.

The donated polymers were synthesised as a series using two different length PEG blocks, 1900 Da and 5000 Da while the targeted degree of polymerisation ($DP_{targeted}$) for the HEA block was varied to determine the effect on particle size. The two different molecular weights of PEG blocks were used to determine the effect of increasing the molecular weight of the stabiliser block. The variation of the $DP_{targeted}$ of the HEA block, from 10 to 100, was used to determine the effect of hydrogen bonding on the growth of the apatite particles. It was believed that longer HEA blocks would cause the apatite particles to elongate during growth as the polymer could act as a templating nucleation point for the apatite crystals to grow along. This would be consistent with the results seen in chapter 5 whereby the higher molecular weight acrylic acid samples (E11) produced very long thin particles when added to the synthesis of (F)HA.

The apatite samples were analysed using X-ray diffraction (XRD), fourier transform infrared spectroscopy (FTIR) and thermogravimetric analysis (TGA). The nanoparticles were also imaged via transmission electron microscopy (TEM) and size analysis was carried out using the software ImageJ.[1]

7.2 Experimental

7.2.1 Synthesis of HA with 10 wt% PEG-co-HEA polymers of varying HEA block lengths

PEG-co-HEA block copolymers were added to synthesis of hydroxyapatite nanoparticles at 10 wt% of the total solid contents. The typical synthesis of a HA PEG-co-HEA sample was conducted as follows. Diammonium hydrogen phosphate (0.377 g, 2.85 mmol) and PEG-co-HEA polymer (0.1 g, 10 wt% total solids) were dissolved in deionised water (10 ml). The solution was heated to reflux and the pH adjusted using ammonium hydroxide (30-35 % solution). Calcium chloride (0.523 g, 4.71 mmol) was dissolved in deionised water (10 ml) and transferred into a syringe. The calcium chloride solution was added dropwise via a syringe pump at a rate of 3.33 ml min^{-1} to the diammonium hydrogen phosphate / PEG-co-HEA solution forming a white precipitate. The heat was switched off after 1 hour of aging and the suspension stirred for 24 hours at room temperature. The suspension was centrifuged for 15 minutes at 20000 rpm, the supernatant was decanted off and the solid resuspended in deionised water. The washing was then repeated three times. The white solid was then transferred onto a glass petri dish and dried in an oven at 70 °C overnight. The dried solid was transferred to a pestle and mortar and ground into a powder. Characterisation was then conducted using FTIR, XRD, TGA and TEM analysis. Exact masses of reactants used in the synthesis are given in table 7.1.

Table 7.1. Masses of reactants used to synthesise HA samples containing 10 wt% by solid mass of PEG-co-HEA block copolymers synthesised with a PEG macroinitiator. The polymers have varying HEA block lengths via targeted degree of polymerisation and differing molecular weights of PEG depending which macroinitiator was used during the polymer synthesis: 1900 Da or 5000 Da PEG-isobutyryl bromide.

Sample	$CaCl_2$ / g	$(NH_4)_2HPO_4$ / g	Polymer / g	HEA $DP_{targeted}$	PEG block
HA PEG-co-HEA 1	0.535	0.379	0.102	10	1900
HA PEG-co-HEA 2	0.522	0.379	0.105	10	5000
HA PEG-co-HEA 3	0.529	0.375	0.098	50	1900
HA PEG-co-HEA 4	0.522	0.378	0.098	50	5000
HA PEG-co-HEA 5	0.521	0.376	0.102	100	1900
HA PEG-co-HEA 6	0.525	0.372	0.099	100	5000
HA PEG-co-HEA 7	0.520	0.375	0.103	90	1900
HA PEG-co-HEA 8	0.521	0.378	0.100	90	5000
HA PEG-co-HEA 9	0.523	0.376	0.102	80	1900
HA PEG-co-HEA 10	0.524	0.378	0.102	80	5000
HA PEG-co-HEA 11	0.523	0.378	0.102	70	1900
HA PEG-co-HEA 12	0.523	0.377	0.101	70	5000

7.2.2 Synthesis of FHA with 10 wt% PEG-co-HEA polymers of varying HEA:PEG ratios

Synthesis of fluorhydroxyapatite samples containing 10 wt% of solid of PEG-co-HEA polymers was conducted in the same manner as described in section 7.2.1 except that a sample of ammonium fluoride (0.021 g, 3.1 mmol) was added to the phosphate solution before the addition of the calcium chloride solution. Characterisation was conducted using FTIR, XRD, TGA and TEM analysis. Exact masses of reactants used in the synthesis are given in table 7.2.

Table 7.2. Masses of reactants used to synthesise FHA samples containing 10 wt% by solid mass of PEG-co-HEA block copolymers synthesised with a PEG macroinitiator. The polymers have varying HEA block lengths via targeted degree of polymerisation and differing molecular weights of PEG depending which macroinitiator was used during the polymer synthesis: 1900 Da or 5000 Da PEG-isobutyryl bromide.

Sample	$CaCl_2$ / g	$(NH_4)_2HPO_4$ / g	NH_4F / g	Polymer / g	HEA $DP_{targeted}$	PEG block
FHA PEG-co-HEA 1	0.513	0.367	0.025	0.099	10	1900
FHA PEG-co-HEA 2	0.516	0.364	0.020	0.110	10	5000
FHA PEG-co-HEA 3	0.515	0.372	0.020	0.101	50	1900
FHA PEG-co-HEA 4	0.513	0.364	0.020	0.098	50	5000
FHA PEG-co-HEA 5	0.519	0.368	0.021	0.103	100	1900
FHA PEG-co-HEA 6	0.509	0.362	0.021	0.101	100	5000
FHA PEG-co-HEA 7	0.509	0.368	0.022	0.101	90	1900
FHA PEG-co-HEA 8	0.510	0.311	0.021	0.104	90	5000
FHA PEG-co-HEA 9	0.511	0.367	0.020	0.104	80	1900
FHA PEG-co-HEA 10	0.514	0.367	0.021	0.100	80	5000
FHA PEG-co-HEA 11	0.511	0.366	0.023	0.105	70	1900
FHA PEG-co-HEA 12	0.510	0.366	0.021	0.102	70	5000

7.3 Results and Discussion

7.3.1 Synthesis of HA with 10 wt% PEG-co-HEA polymers of varying HEA block lengths and PEG molecular weights

PEG-co-HEA block copolymers provided by Sarahfranziska Stahl were added as 10 wt% of output solids to the synthesis of hydroxyapatite nanoparticles. The donated polymers were synthesised as a series with various targeted degrees of polymerisation ($DP_{Targeted}$) for the HEA block. The PEG blocks of the copolymer were achieved using a PEGylated macroinitiator during the HEA polymerisation; the macroinitiator contained a PEG chain of either 1900 Da or 5000 Da. These polymers were then added to the synthesis of HA nanoparticles in order to determine the effect of non-charged polymers on the growth of the particles. HEA has the ability to hydrogen bond while PEG has been used previously as a steric stabiliser and masking agent for colloids in biological systems.[2-6] It was believed that the differing nature of the two blocks would mean the HEA block would interact with the HA as it formed due to the ability of HEA to form a high energy hydration layer around hydroxyl groups[3] while the PEG block would act as a steric stabiliser to control particle dispersion and prevent aggregation.[5, 6] Analysis and characterisation of the particles was conducted using XRD, FTIR, TGA and TEM.

7.3.1.1 X-ray diffraction

X-ray diffraction was conducted on all HA samples containing the block PEG-co-HEA polymers. The resulting diffraction patterns were fitted using Pawley and Rietveld refinement to produce cell parameter information for the samples using TOPAS software.[7] Figure 7.1 shows the normalised XRD diffraction patterns of all samples, while table 7.3 shows the cell parameter determined by Pawley and Rietveld refinement.

Table 7.3 Cell parameters of HA samples synthesised using PEG-co-HEA copolymers of varying HEA block lengths and PEG molecular weights due to the use of either PEG 1900 Da or 5000 Da macroinitiators. Values in brackets denote the standard deviation of the final value of the measurement.

Sample	**Pawley Refinement**				**Rietveld Refinement**			
	a / Å	*c* / Å	R_{wp}	R_{wpb}	*a* / Å	*c* / Å	R_{wp}	R_{wpd}
HA PEG-co-HEA-1	9.432(1)	6.880(1)	13.47	18.26	9.43(1)	6.88(1)	16.46	24.94
HA PEG-co-HEA-2	9.433(2)	6.881(1)	13.72	19.18	9.43(1)	6.88(1)	16.53	24.86
HA PEG-co-HEA-3	9.434(1)	6.88(1)	13.41	18.43	9.43(1)	6.88(1)	16.24	24.56
HA PEG-co-HEA-4	9.44(1)	6.87(1)	12.79	17.88	9.45(1)	6.87(1)	15.62	23.55
HA PEG-co-HEA-5	9.43(1)	6.881(1)	13.71	18.46	9.43(1)	6.88(1)	16.52	25.12
HA PEG-co-HEA-6	9.429(1)	6.878(3)	13.07	17.97	9.43(1)	6.88(1)	15.93	24.11
HA PEG-co-HEA-7	9.43(1)	6.879(1)	12.41	16.47	9.43(1)	6.88(1)	16.21	23.84
HA PEG-co-HEA-8	9.428(4)	6.88(2)	12.81	17.30	9.43(4)	6.880(4)	16.28	23.54
HA PEG-co-HEA-9	9.43(1)	6.878(1)	13.30	17.22	9.43(1)	6.88(1)	16.66	22.97
HA PEG-co-HEA-10	9.43(3)	6.877(3)	13.82	18.07	9.43(4)	6.880(4)	17.06	23.44
HA PEG-co-HEA-11	9.44(1)	6.88(2)	13.36	17.38	9.44(1)	6.88(1)	17.04	23.57
HA PEG-co-HEA-12	9.43(3)	6.881(2)	13.94	17.86	9.43(1)	6.88(1)	16.99	23.35

The 'R factors' R_{wp} and R_{wpb} denote the weighted profile residual and weighted profile residual without background respectively. These terms denote the 'goodness of fit' of the data to a known diffraction pattern of the same substance.[8] There is no threshold to give a definitively good fit; however, it is generally accepted that the lower the values of the residuals, the better the fit of the data, with the best fit occurring when R_{wp} equals one.[8] All of the collected diffraction patterns look very similar and fitted well to a known sample of HA during refinement. This suggests that hydroxyapatite was formed in all cases. The sharpness of all

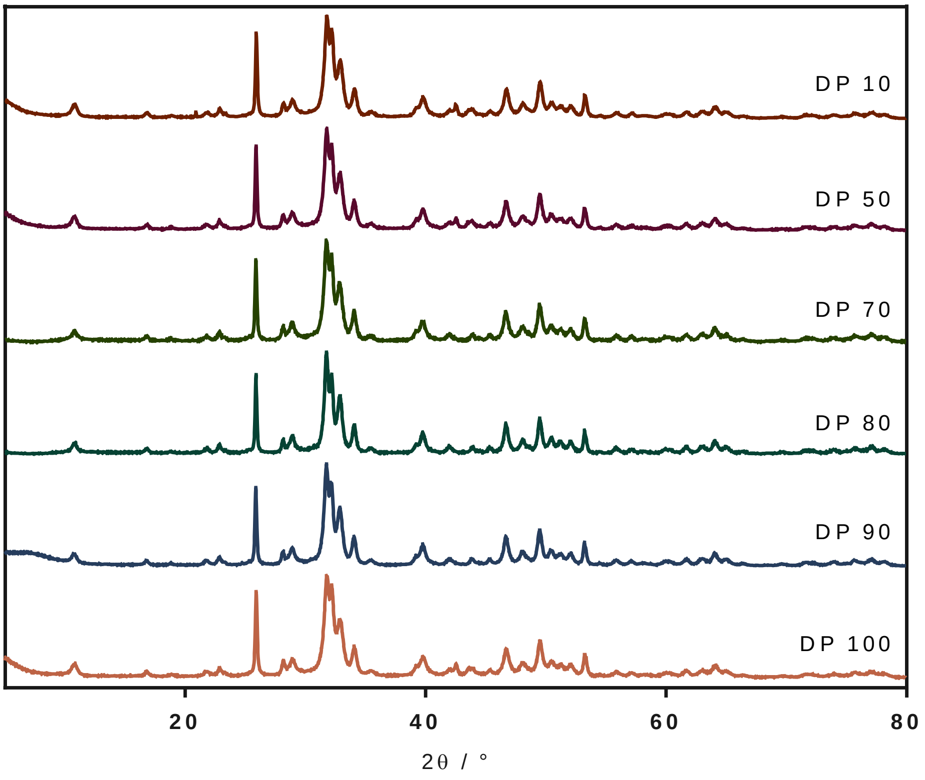

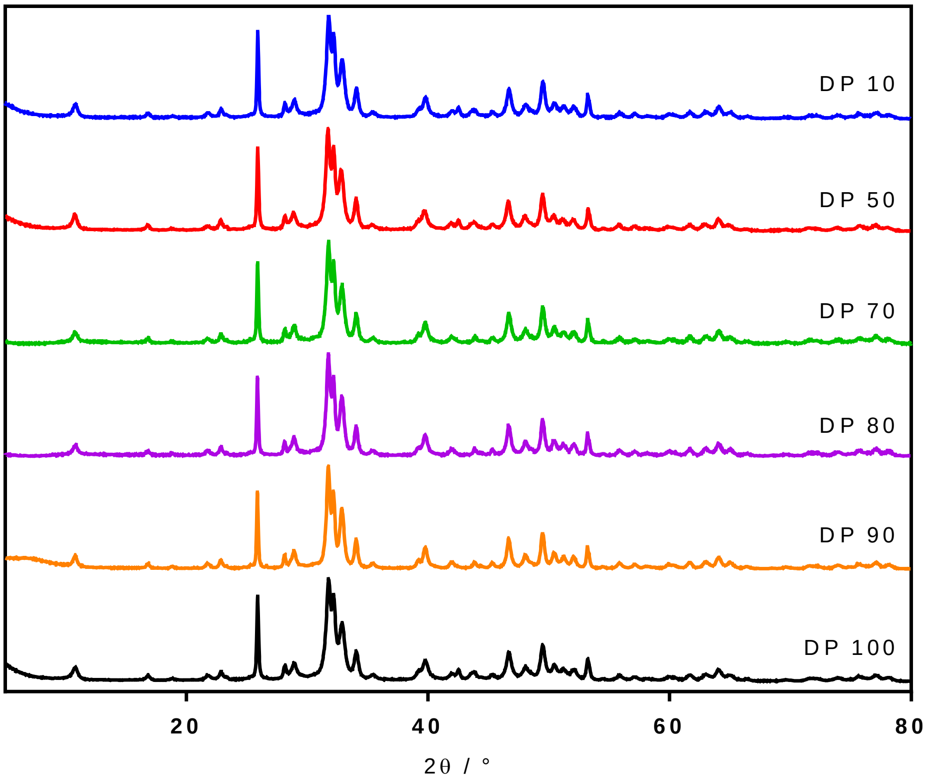

Figure 7.1. Overlaid normalised x-ray diffraction patterns of HA samples prepared with a range of polymers with varying HEA block lengths and PEG molecular weights. Samples synthesised with PEG 1900 macroinitiator are shown in the top figure while those produced using the PEG 5000 macroinitiator are shown in the bottom.

the XRD patterns shows that the samples are crystalline. The relative intensities of the peaks at approximately 26 and 33° 2θ show that there is elongation along the c axis. The peak at 26° 2θ corresponds to the 002 plane while the peak at 33° 2θ corresponds to the 300 plane, the peak corresponding to the 300 plane is approximately two thirds of the height of the peak corresponding to the 002 plane which indicates that the 002 plane has more long range order and hence there is elongation along the c axis.[8]

The axis parameters determined by Pawley and Rietveld refinement are very similar across all samples. In all cases the fitting of the diffraction patterns to a known standard of HA were poor as shown by the large R_{wp} and R_{wpb} values which denote goodness of fit. This is due to the elongation of the peak at 26° 2θ which corresponds to the 002 plane. As the peak had a greater intensity than pure HA diffraction pattern it meant that the fitting was distorted to account for the increased intensity, and hence reduced the goodness of fit in all cases. It was not possible to determine crystallite sizes from these samples as the inclusion of polymer creates an unknown phase. While the polymer phase is amorphous and hence does not appear in the HA diffraction patterns, the fact that it is shown to disrupt the crystal lattice by the elongation of the 002 plane means it has an effect on the crystal lattice and would need to be included as a separate phase in order to determine crystallite size. As such, the XRD analysis showed that HA had been formed in all cases, but further analysis was needed to determine the effect of the polymer on the unit cell.

7.3.1.2 Fourier transform infrared spectroscopy

FTIR was used to study the crystal chemistry of HA and the chemical interactions between the ceramics and PEG-co-HEA. Comparing the overlaid spectra of the HA (Figure 7.2) showed a change in the intensity and shape of the OH (approximately 3400 cm^{-1}) and PO_4 peaks (approximately 1030 cm^{-1} and 600 cm^{-1}). The difference in the OH peaks between samples can be attributed to adsorbed water on the sample surface along with the fact that KBr is extremely hygroscopic hence it retains water even after storage in a desiccator. The small peak at 3570 cm^{-1} protruding from the broad OH peak corresponds to non hydrogen bonded OH which is characteristic of HA.[9]

The peaks corresponding to the phosphate groups at approximately 1030 cm^{-1} and 600 cm^{-1} are strong and broad in all cases. This is likely due to disruption of the crystal lattice caused

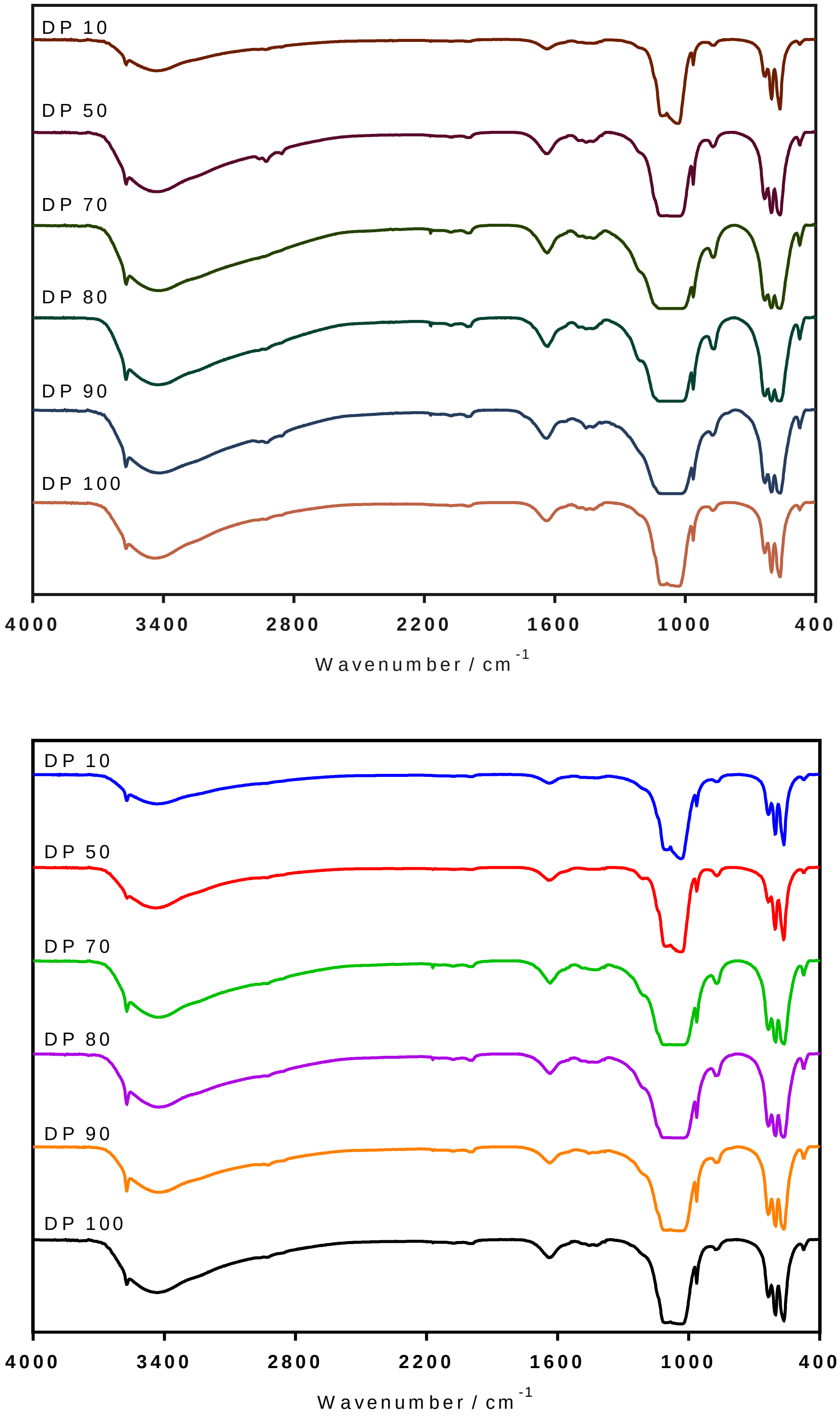

Figure 7.2. Overlaid normalised FTIR spectra of HA samples prepared with a range of polymers with varying PEG:HEA ratios and PEG weights. Samples synthesised with PEG 1900 macroinitiator are shown in the top figure while those produced using the PEG 5000 macroinitiator are shown in the bottom figure.

by the inclusion of polymer as seen in the XRD analysis which showed an elongation of the *c* axis. As the phosphate group lies perpendicular to the *c* axis in the unit cell, increased long range order along the *c* axis will mean loss of long range order along the *a* axis which will mean disruption to the phosphate group alignment within the crystals. [8, 9]

Comparison of the shape and position of the peaks shows the characteristics of hydroxyapatite showing that the synthesis of HA was successful in all cases. Extra peaks around 1640 cm^{-1} correspond to the polymer and adsorbed carbonate groups on the surface of the apatite particles showing that the PEG-co-HEA polymers have been incorporated into the crystal structures of HA in all cases.

7.3.1.3 Thermogravimetric analysis

Thermogravimetric analysis was conducted to determine whether the polymer had been incorporated into the composite material and, if so, the percentage weight of polymer ingrained in each sample of HA. Figure 7.3 shows the TGA traces of all samples while table 7.4 describes the percentage weight lost during the thermogravimetric analysis.

Table 7.4: A summary of the results from the thermogravimetric analysis of HA samples synthesised using PEG-co-HEA polymers of varying HEA degree of polymerisation and molecular weights of PEG. The percentage weight of polymer present in each HA sample is listed alongside the targeted and actual DP of the HEA block and molecular weight of the PEG macroinitiator used during the polymer synthesis.

Sample	HEA $DP_{targeted}$	HEA DP_{actual}	PEG	Wt% $_{Initial}$	Wt% $_{Final}$	Wt% $_{Polymer}$
HA PEG-co-HEA 1	10	13	1900	99.7	96.9	2.8
HA PEG-co-HEA 2	10	11	5000	99.7	96.8	2.9
HA PEG-co-HEA 3	50	53	1900	99.4	95.9	3.5
HA PEG-co-HEA 4	50	51	5000	99.7	96.8	2.9
HA PEG-co-HEA 5	100	110	1900	99.3	95.8	3.5
HA PEG-co-HEA 6	100	107	5000	99.6	96.4	3.2
HA PEG-co-HEA 7	90	98	1900	100.0	96.6	3.4
HA PEG-co-HEA 8	90	94	5000	100.0	98.1	1.9
HA PEG-co-HEA 9	80	85	1900	100.0	99.1	0.9
HA PEG-co-HEA 10	80	89	5000	100.0	97.8	2.2
HA PEG-co-HEA 11	70	84	1900	100.0	96.4	3.6
HA PEG-co-HEA 12	70	88	5000	100.0	97.3	2.7

As weight was lost from all samples when viewed alongside the analysis by FTIR which showed the inclusion of polymer, it was determined that polymer had successfully been incorporated into all samples. However, the amount of polymer which was incorporated into the HA samples seemed to differ greatly across the samples. It is also evident that the final weight

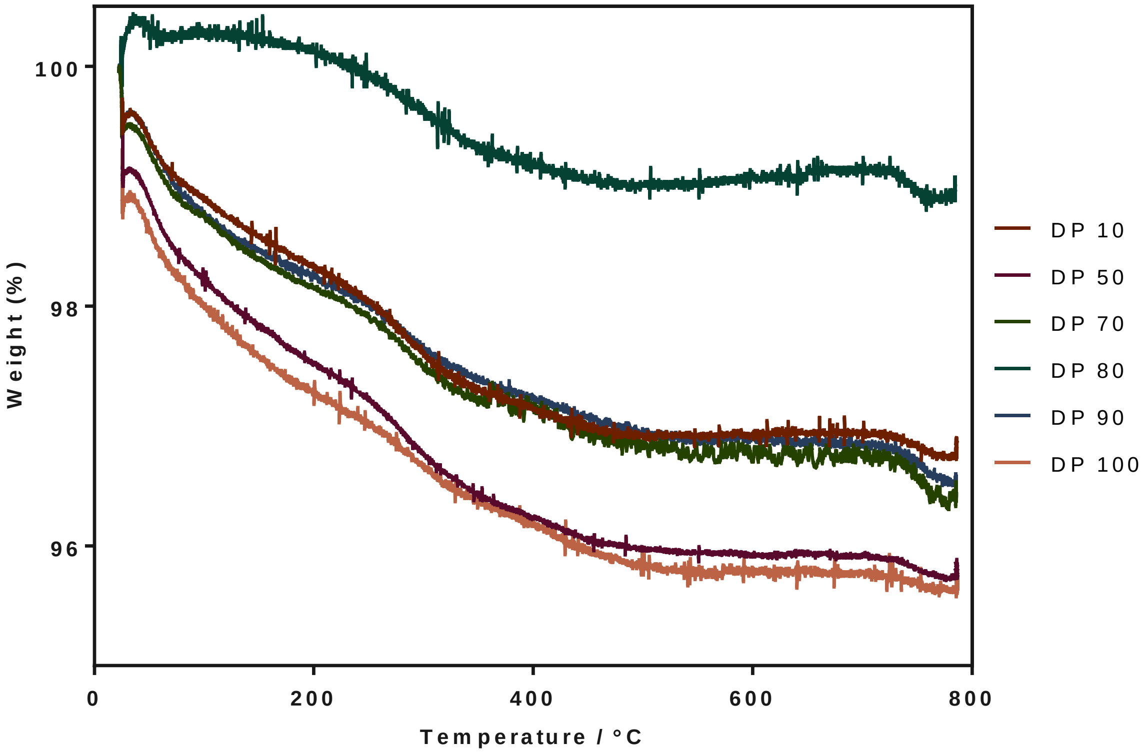

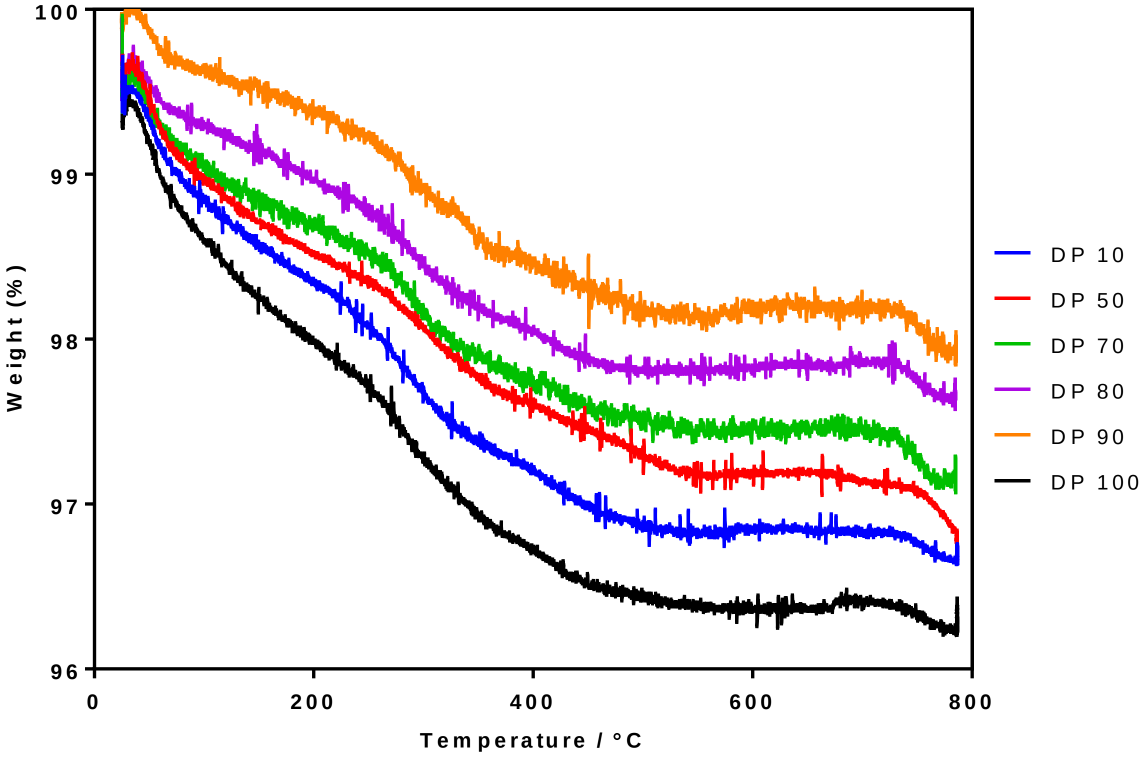

Figure 7.3. Overlaid normalised thermogravimetric curves of HA samples prepared with a range of polymers with varying $DP_{targeted}$ of the HEA block and PEG molecular weights. Samples synthesised with PEG 1900 macroinitiator are shown in the top figure while those produced using the PEG 5000 macroinitiator are shown in the bottom figure.

percentage of polymer in the samples is far less than the 10 wt% which was originally added to the HA synthesis. It is possible that this was due to the polymer being water soluble and hence it may have been washed away during the material processing steps.

In general, the total percentage weight loss during the TGA is fairly consistent across all samples. Two anomalies are apparent in terms of the samples 8 and 9 (90:1 PEG 5000 and 80:1 PEG 1900 respectively) as these samples lost 1.93 and 0.95 wt% respectively. This low weight loss is potentially due to the polymer being washed away during processing. Looking back at the FTIR spectra for both samples shows that the peak around 1690 cm^{-1} corresponding to the polymer is much smaller when compared to all the other samples. As FTIR is not a quantitative technique, this cannot be said for certain; however, the combination of the data collected from the FTIR and TGA measurements appears to suggest that far less polymer was incorporated into samples 8 and 9 than all other samples.

Other than the two anomalies the weight loss in all other samples was relatively consistent allowing for the error of the instrument. The fact that such small amounts were lost from all samples increases the error associated with the measurement due to the prevalence of pan buoyancy which can have an adverse effect on the measurements.[10] This is evident in all samples as can be seen by the levels of noise in the thermogravimetric curves shown in figure 7.3. Looking at the thermogravimetric curves shows that while the PEG 5000 samples (bottom figure) were relatively consistent in shape, the PEG 1900 samples (top figure) were far more varied. The 90:1 PEG1900 sample (HA PEG-co-HEA 9) trace is especially different due to the difference in weight loss with all other samples. However, the shape of the curves is relatively consistent in terms of the temperatures at which the greatest weight loss occurs.

There appears to be no correlation between the percentage weight lost and the molecular weight of the PEG block or the DP of the HEA block. As such it is likely that the polymers interact differently with the apatite crystals compared to the polymers tested in previous chapters. In all cases, it appears that polymer has been included into all of the composite samples when considering the TGA, FTIR and XRD results all together.

7.3.1.4 Transmission electron microscopy

In order to determine what effect the polymer inclusion had on the hydroxyapatite crystals, transmission electron microscopy (TEM) was conducted to image the particles. Transmission electron microscopy was used to image the particles to determine their size and morphology. Figure 7.4 shows TEM micrographs of the HA samples prepared with the PEG 1900 co-HEA polymers, while figure 7.5 shows the TEM micrographs of the composite sample prepared with PEG 5000 co-HEA polymers.

Upon visual inspection of the TEM micrographs it is evident that the particles are all fairly consistent in terms of size and shape. There are a range of particle sizes within all samples with very large particles visible alongside much smaller particles. All samples appear to show particle aggregation indicating that the PEG group of the copolymers incorporated into the samples has not acted as a steric stabiliser. ImageJ was used to determine the particle sizes and aspect ratios,[1] a summary of the results for the HA PEG 1900 HA samples are shown in table 7.5.

Table 7.5 A summary of the particle sizes and aspect ratios of HA particles synthesised in the presence of 10 wt% PEG 1900-co-HEA polymers varying the DP of the HEA block. $DP_{targeted}$ and DP_{actual} of the HEA blocks are given in the table alongside particle sizes, standard deviation, standard error of measurement and aspect ratios of the respective HA particles measured by ImageJ.[1]

Sample	HEA DP		Lengths / nm			Widths / nm			Aspect ratios
	Targeted	Actual	Mean	SD	SE	Mean	SD	SE	
HA PEG-co-HEA 1	10	13	77.38	23.46	0.95	16.77	3.94	0.39	4.61
HA PEG-co-HEA 3	50	53	87.44	29.75	1.32	26.95	6.23	0.62	3.24
HA PEG-co-HEA 11	70	84	73.64	14.47	0.72	20.65	5.78	0.57	3.57
HA PEG-co-HEA 9	80	85	75.04	12.78	0.57	28.46	5.81	0.58	2.64
HA PEG-co-HEA 7	90	98	75.10	20.59	1.02	26.57	4.54	0.45	2.83
HA PEG-co-HEA 5	100	110	79.95	20.05	1.00	21.44	4.71	0.47	3.73

These values show that the particle sizes are very similar across all samples regardless of the polymer used in the composite synthesis. This implies that the HEA block length does not have an effect on the apatite particles. Plotting DP_{actual} against mean particle length (figure 7.6) shows that the HA PEG 1900-co-HEA particle sizes have very little variance, especially when the standard deviation is taken into account. Interestingly, this is not the case for the composite particle synthesised with PEG 5000 polymers; a summary of the results for the HA PEG 5000 HA samples are shown in table 7.6.

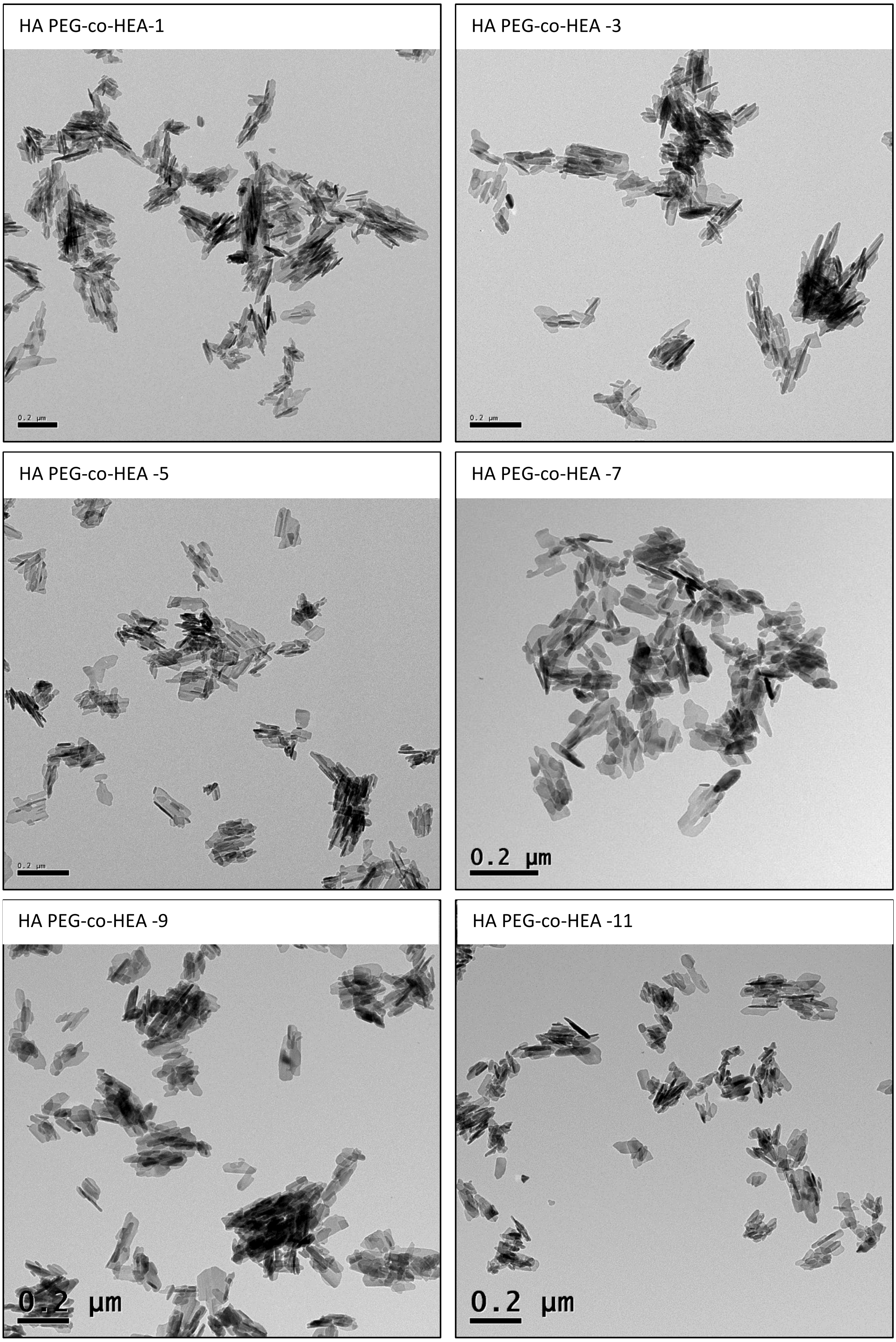
HA PEG-co-HEA-1

HA PEG-co-HEA -3

HA PEG-co-HEA -5

HA PEG-co-HEA -7

HA PEG-co-HEA -9

HA PEG-co-HEA -11

Figure 7.4. Transmission electron micrographs of HA samples prepared with 10 wt% PEG-co-HEA polymers synthesised using the macroinitiator PEG 1900 isobutyryl bromide with varying HEA $DP_{targeted}$. The $DP_{targeted}$ of the HEA blocks are as follows: 1 = 10, 3 = 50, 5 = 100, 7 = 90, 9 = 80 and 11 = 70.

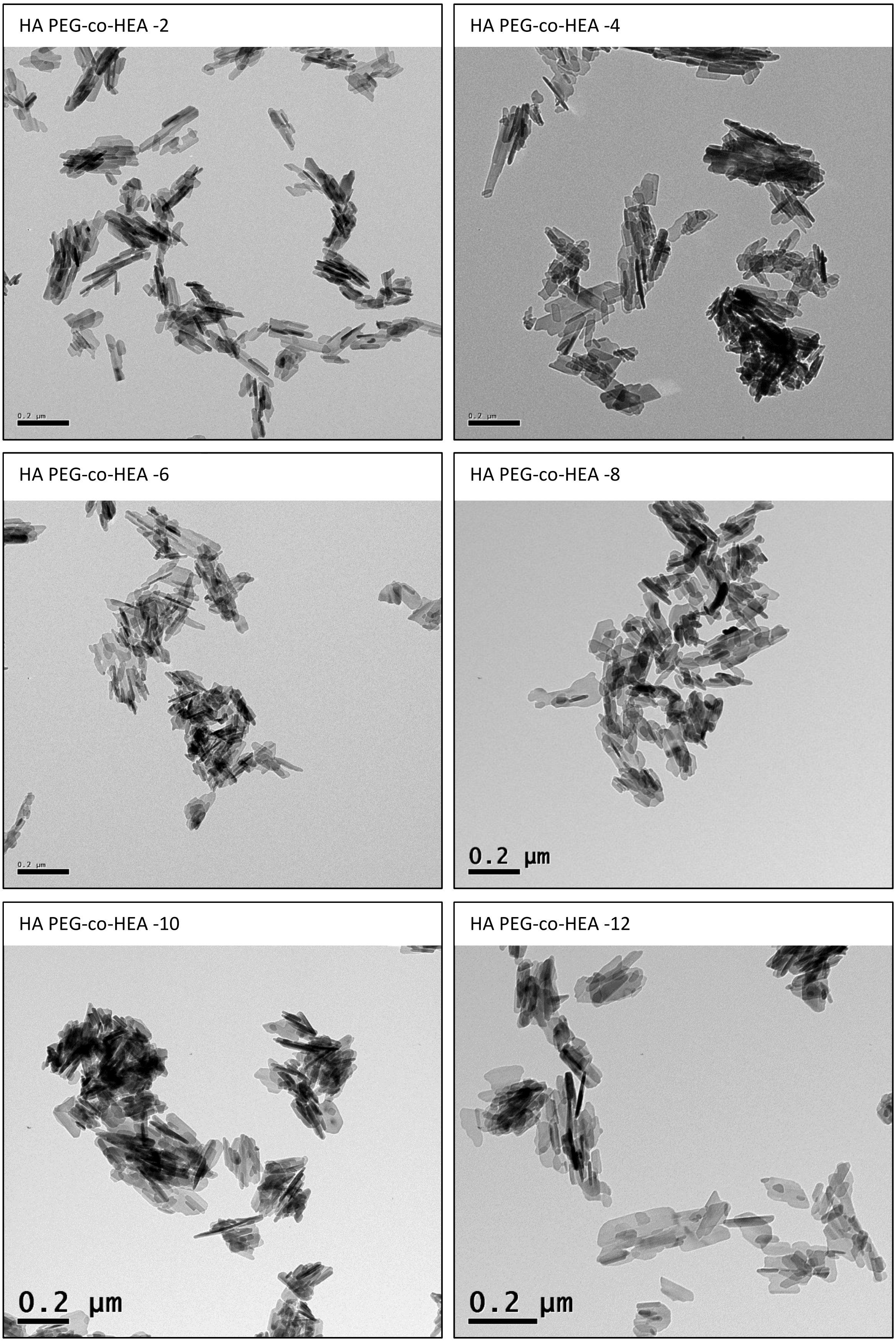

HA PEG-co-HEA -2

HA PEG-co-HEA -4

HA PEG-co-HEA -6

HA PEG-co-HEA -8

HA PEG-co-HEA -10

HA PEG-co-HEA -12

Figure 7.5. Transmission electron micrographs of HA samples prepared with 10 wt% PEG-co-HEA polymers synthesised using the macroinitiator PEG 5000 isobutyryl bromide with varying HEA $\mathrm{DP}_{\mathrm{targeted}}$. The $\mathrm{DP}_{\mathrm{targeted}}$ of the HEA blocks are as follows: 2 = 10, 4 = 50, 6 = 100, 8 = 90, 10 = 80 and 12 = 70.

Table 7.6 A summary of the particle sizes and aspect ratios of HA particles synthesised in the presence of 10 wt% PEG 5000-co-HEA polymers varying the DP of the HEA block. $DP_{targeted}$ and DP_{actual} of the HEA blocks are given in the table alongside particle sizes, standard deviation, standard error of measurement and aspect ratios of the respective HA particles measured by ImageJ.[1]

Sample	HEA DP		Lengths / nm			Widths / nm			Aspect ratios
	Targeted	Actual	Mean	SD	SE	Mean	SD	SE	
HA PEG-co-HEA 2	10	11	112.83	29.03	1.18	25.72	10.22	1.02	4.39
HA PEG-co-HEA 4	50	51	108.74	30.33	1.35	38.60	7.38	0.73	2.82
HA PEG-co-HEA 12	70	88	100.92	23.96	1.19	27.08	6.54	0.65	3.73
HA PEG-co-HEA 10	80	89	98.35	16.55	0.82	27.31	6.55	0.65	3.60
HA PEG-co-HEA 8	90	94	96.62	26.74	1.33	30.47	6.98	0.69	3.17
HA PEG-co-HEA 6	100	107	86.87	22.48	1.00	19.80	6.12	0.61	4.39

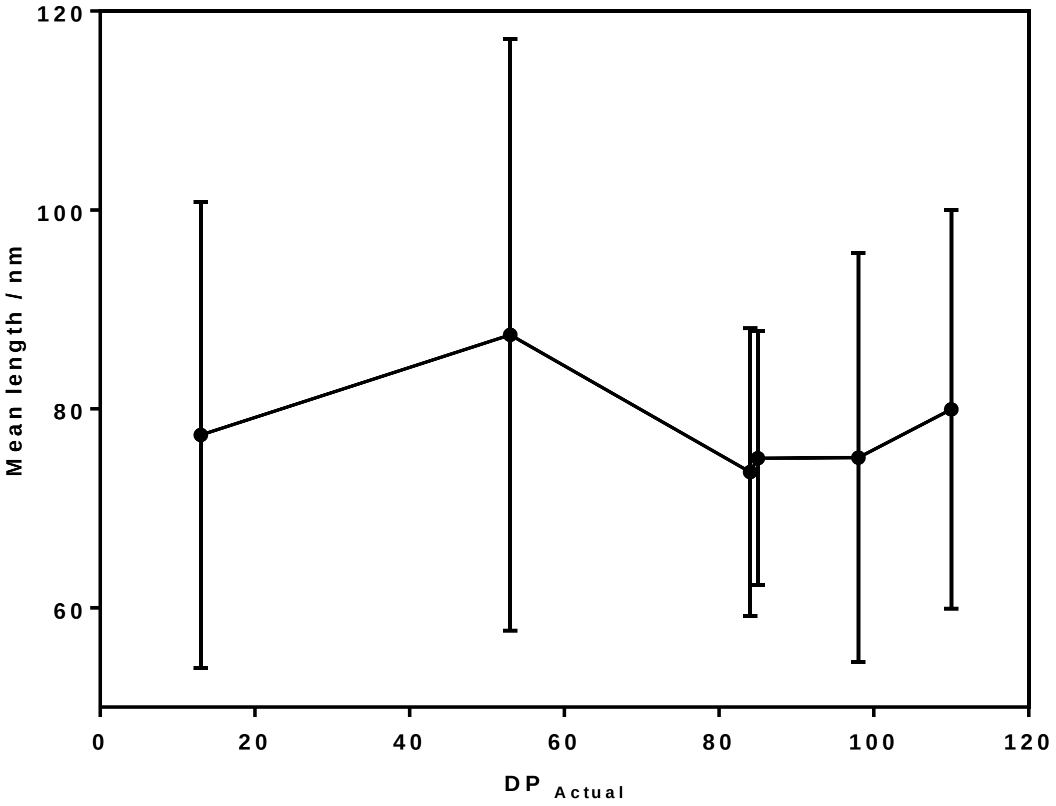

Figure 7.6. A plot showing the lack of correlation between mean particle length and r_{actual} of HA particles synthesised in the presence of PEG1900-co-HEA polymers. Error bars are the calculated standard deviation of the particle mean lengths measured using ImageJ.[1]

Table 7.6 shows that as the DP of the HEA block increases the size of the composite particles synthesised decreases. Figure 7.7 shows a plot of actual ratio against mean particle length of the HA PEG 5000-co-HEA composites. This plot suggests that even when the standard deviation of the mean particle size is taken into account, the particle length decreases with the increased ratio of HEA in the polymer used to form the composite particles. The trend is particularly interesting when looking at samples 12, 10 and 8 where $DP_{Targeted}$ = 70, 80 and 90 respectively while DP A$_{\mathrm{ctual}}$ = 88, 89 and 94 respectively. The similarity in particle sizes and DP $_{\mathrm{Actual}}$ while still maintaining the trend of increasing HEA ratio leading to decreasing particle size suggests that the amount of HEA in the polymers used to create the composite particle has a direct impact on particle formation and therefore it is likely that the HEA block of the copolymer acts as a nucleation point for the growth of HA particles.[2, 3] It is not clear why the same trend is not seen for the PEG1900 polymers. The large standard deviations show a large variation in particle size across the composite samples, hence it is possible that human error when measuring the particles was the cause of the differences in trends

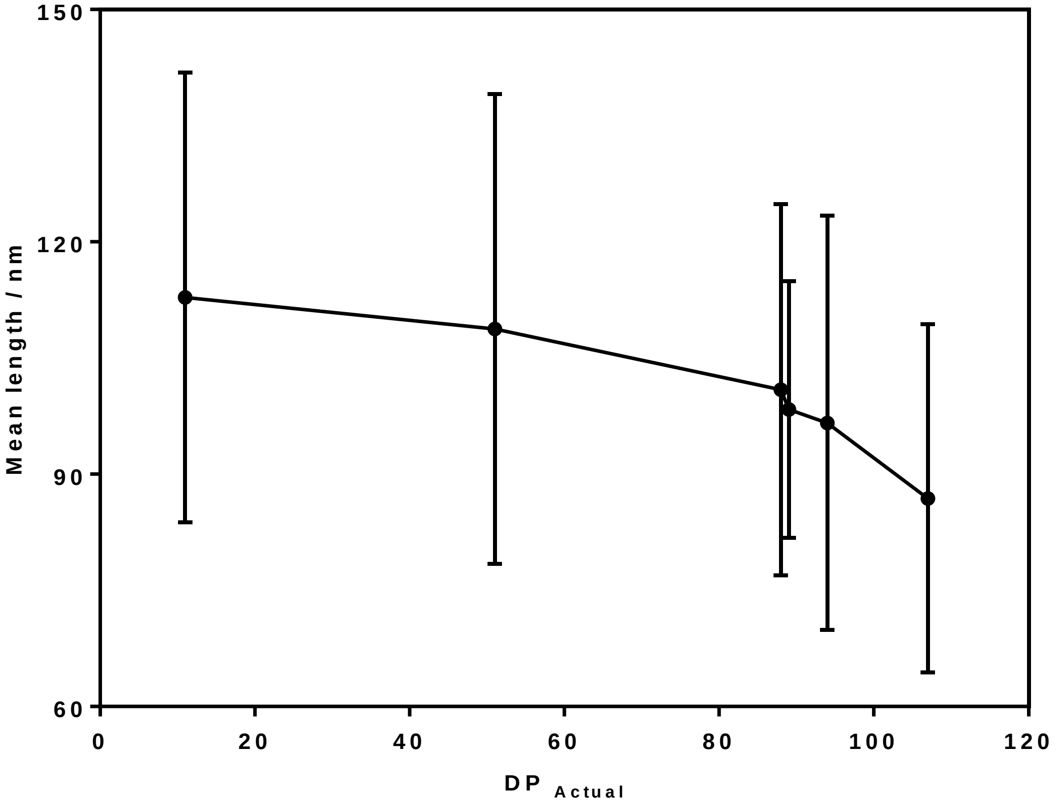

Figure 7.7. A plot showing the decrease in particle size of synthesised composite particles with increasing ratio of HEA in the PEG5000-co-HEA polymers used to produce the composite particles. Error bars are the calculated standard deviation of the particle mean lengths measured using ImageJ.[1]

between the PEG 1900 and PEG 5000 samples. In order to test this, the same polymers were used to synthesise fluorhydroxyapatite composite samples using the exact same reaction conditions to make them comparable the HA samples discussed so far.

7.3.2 Synthesis of FHA with 10 wt% PEG-co-HEA polymers of varying HEA block lengths and PEG molecular weights

Fluorhydroxyapatite (FHA) samples were synthesised as described in section 7.2.2 using 10 wt% of the PEG-co-HEA block copolymers mentioned in section 7.3.1 which were donated by Sarahfranziska Stahl. Samples were characterised and analysed using X-ray diffraction (XRD), fourier transform infrared (FTIR) spectroscopy, thermogravimetric analysis (TGA) and transmission electron microscopy (TEM). These samples were then compared to the HA sample discussed previously to determine the effect of fluoride substitution.

7.3.2.1 X-ray diffraction

X-ray diffraction was conducted on the samples and the resulting patterns were fitted as before. Figure 7.8 shows the normalised XRD diffraction patterns of all samples, while table 7.7 shows the cell parameter determined by Pawley and Rietveld refinement.

Table 7.7 Cell parameters of FHA samples synthesised using PEG-co-HEA copolymers of varying HEA block lengths and PEG molecular weights due to the use of either PEG 1900 Da or 5000 Da macroinitiators. Values in brackets denote the standard deviation of the final value of the measurement.

Sample	**Pawley Refinement**				**Rietveld Refinement**			
	a / Å	*c* / Å	R_{wp}	R_{wpb}	*a* / Å	*c* / Å	R_{wp}	R_{wpb}
FHA PEG-co-HEA-1	9.395(3)	6.889(2)	12.06	15.66	9.39(1)	6.89(1)	14.54	19.57
FHA PEG-co-HEA-2	9.395(2)	6.885(1)	11.79	15.35	9.40(1)	6.89(1)	14.19	19.21
FHA PEG-co-HEA-3	9.40(1)	6.89(1)	11.79	15.27	9.40(1)	6.89(1)	14.63	19.88
FHA PEG-co-HEA-4	9.397(4)	6.886(4)	11.71	15.34	9.40(1)	6.89(1)	14.27	19.28
FHA PEG-co-HEA-5	9.394(1)	6.886(2)	11.45	14.85	9.39(1)	6.89(1)	14.31	19.36
FHA PEG-co-HEA-6	9.396(2)	6.89(1)	11.54	15.06	9.40(1)	6.89(1)	14.22	19.25
FHA PEG-co-HEA-7	9.398(1)	6.890(1)	11.74	15.33	9.39(1)	6.89(1)	14.35	19.26
FHA PEG-co-HEA-8	9.398(1)	6.889(1)	11.71	15.12	9.40(1)	6.89(1)	14.42	19.38
FHA PEG-co-HEA-9	9.401(1)	6.888(5)	11.82	15.23	9.40(1)	6.89(1)	14.38	19.40
FHA PEG-co-HEA-10	9.400(1)	6.890(3)	11.72	15.25	9.40(1)	6.89(1)	14.43	19.43
FHA PEG-co-HEA-11	9.392(4)	6.886(1)	11.60	15.14	9.39(1)	6.89(1)	14.47	19.51
FHA PEG-co-HEA-12	9.394(4)	6.887(1)	11.69	15.15	9.39(1)	6.89(1)	14.44	19.45

All diffraction patterns look very similar and fitted well to a known sample of FHA during refinement, suggesting that fluorhydroxyapatite was formed in all cases. The peaks across all samples are slightly broad, indicating that either the samples are not very crystalline or that the particle sizes are very small and hence diffract the x-rays differently causing peak broadening. The relative intensities of the peaks at approximately 26 and 33° 2θ show that there is elongation along the *c* axis as seen previously with the HA samples synthesised with the same polymers. The peak at 26° 2θ corresponds to the 002 plane while the peak at 33° 2θ

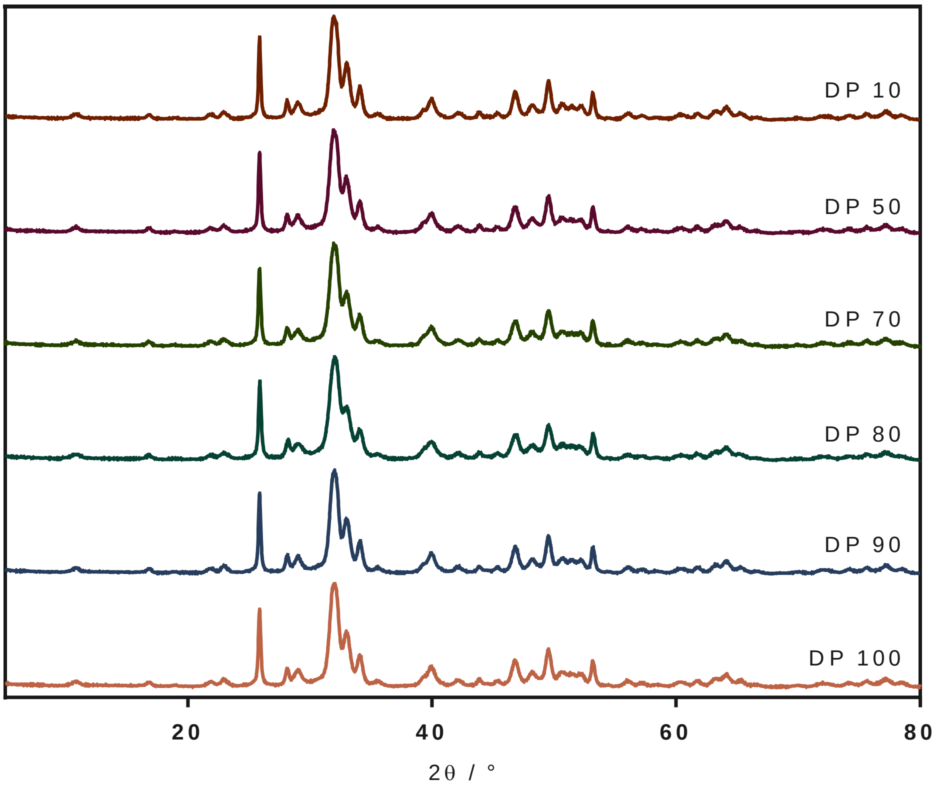

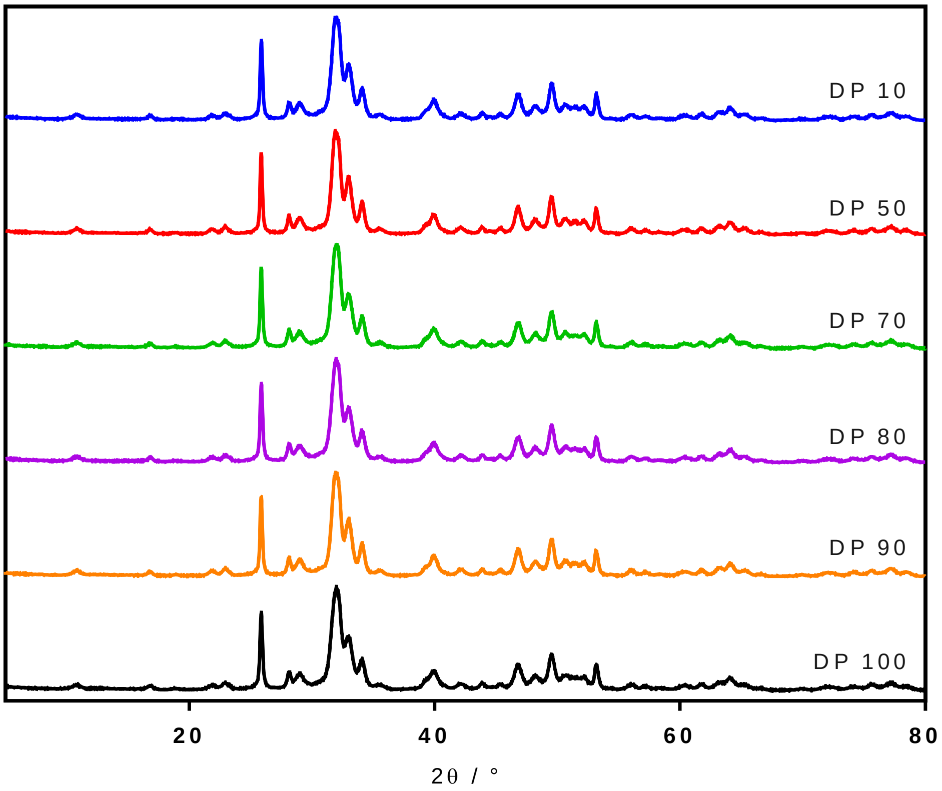

Figure 7.8. Overlaid normalised x-ray diffraction patterns of FHA samples prepared with a range of polymers with varying HEA DP $_{\text{targeted}}$ and PEG molecular weights. Samples synthesised with PEG 1900 macroinitiator are shown in the top figure while those produced using the PEG 5000 macroinitiator are shown in the bottom figure.

corresponds to the 300 plane. The peak corresponding to the 300 plane is approximately three quarters of the height of the peak corresponding to the 002 plane which indicates that the 002 plane has more long range order and hence there is elongation along the c axis.

The axis parameters determined by Pawley and Rietveld refinement are very similar across all samples. In all case the fitting of the diffraction patterns to a known standard of FHA were poor as shown by the large R_{wp} and R_{wpd} values which denote goodness of fit. This is due to the elongation of the peak at 26 ° 2θ which corresponds to the 002 plane. As the peak had a greater intensity than pure FHA diffraction pattern it meant that the fitting was distorted to account for the increased intensity, and hence reduced the goodness of fit in all cases. It was not possible to determine crystallite sizes from these samples as the inclusion of polymer creates an unknown phase. While the polymer phase is amorphous and hence does not appear in the FHA diffraction patterns, the fact that it is shown to disrupt the crystal lattice by the elongation of the 002 plane means it has an effect on the crystal lattice and would need to be included as a separate phase in order to determine crystallite size. As such, the XRD analysis showed that FHA had been formed in all cases, but further analysis was needed to determine the effect of the polymer on the unit cell.

7.3.2.2 Fourier Transform Infrared Spectroscopy

FTIR was used to study the crystal chemistry of FHA and the chemical interactions between the ceramics and PEG-co-HEA. The spectra were normalised and overlaid and compared to determine if any difference was caused the intrinsic structure of the unit cell by the inclusion of PEG-co-HEA in the samples. All spectra are shown in figure 7.9.

Comparing the overlaid spectra of the FHA showed a change in the intensity and shape of the OH and PO_4 peaks as was also evident in the HA spectra described previously. The difference in the OH peaks between samples can be attributed to adsorbed water on the sample surface along with the fact that KBr is extremely hygroscopic. The small peak at 3570 cm^{-1} which could be seen in the HA spectra protruding from the broad OH peak corresponding to non hydrogen bonded OH is no longer present suggesting that the fluoride substitution of OH was successful. This is also evident by the loss of the peak at approximately 640 cm^{-1} corresponding to the OH bending vibration.

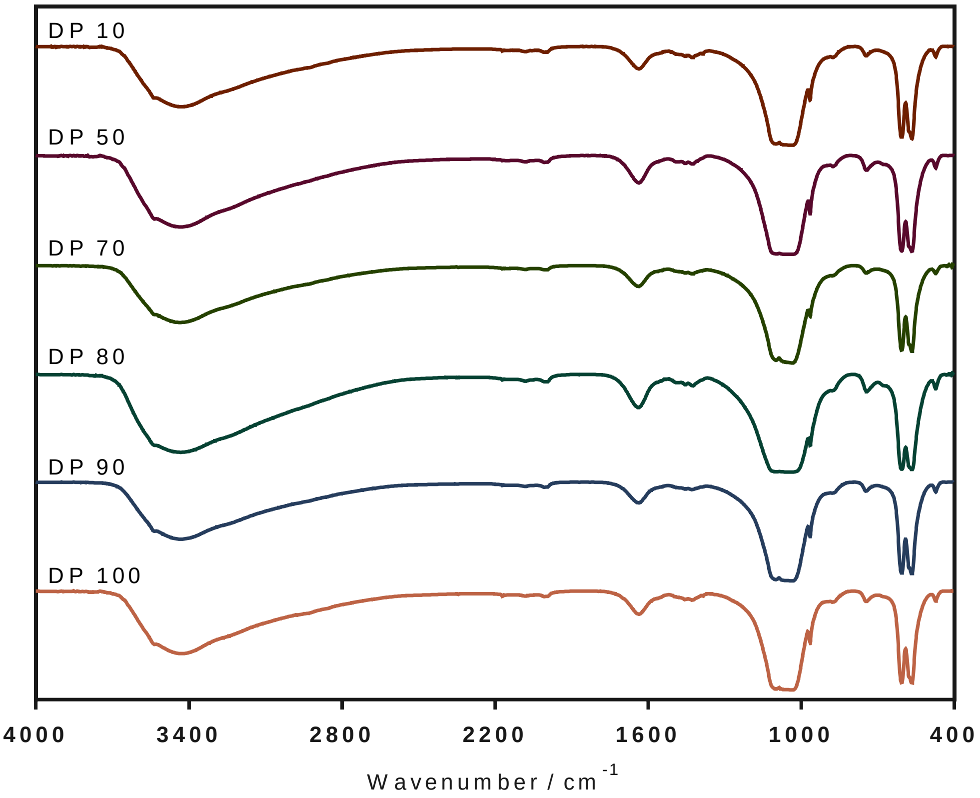

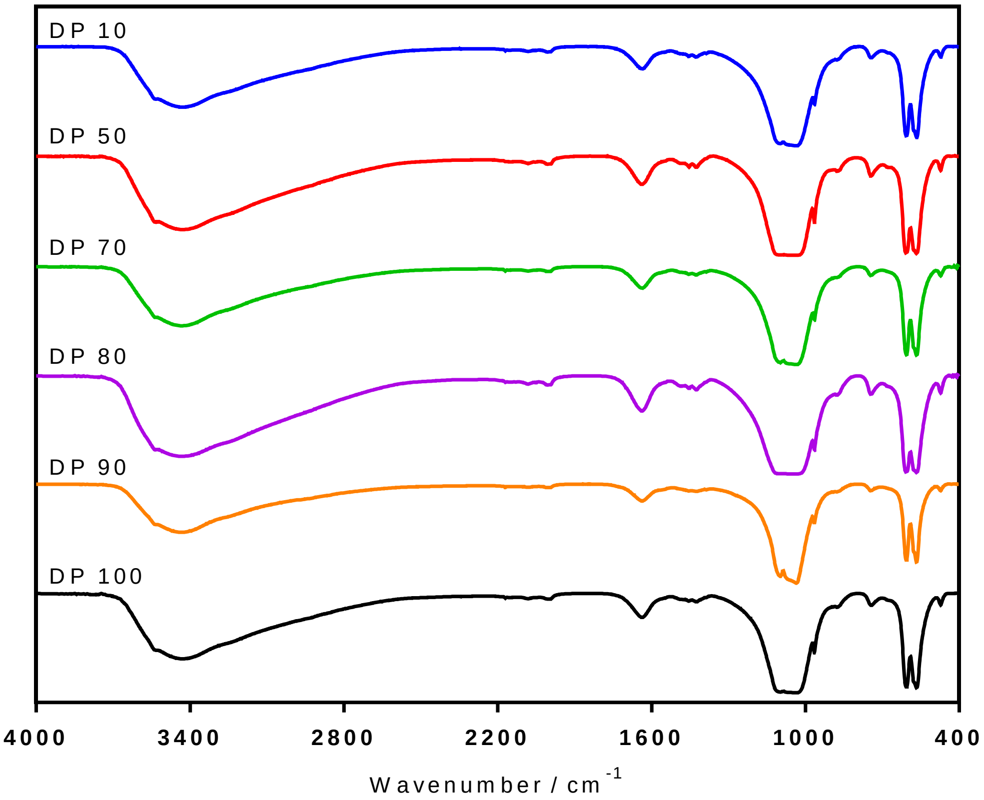

Figure 7.9. Overlaid normalised FTIR spectra of FHA samples prepared with a range of polymers with varying HEA DP$_{\text{targeted}}$ and PEG molecular weights. Samples synthesised with PEG 1900 macroinitiator are shown in the top figure while those produced using the PEG 5000 macroinitiator are shown in the bottom figure.

The peaks corresponding to the phosphate groups at approximately 1030 cm^{-1} and 600 cm^{-1} are strong and broad in all cases. This is likely due to disruption of the crystal lattice caused by the inclusion of polymer as seen in the XRD analysis which showed an elongation of the *c* axis of the unit cell. As the phosphate group lies perpendicular to the c axis in the unit cell, increased long range order along the *c* axis will mean loss of long range order along the *a* axis which will mean disruption to the phosphate group alignment within the crystals and hence will cause peak broadening. Comparison of the shape and position of the peaks shows the characteristics of fluorhydroxyapatite showing that the synthesis of FHA was successful in all cases. Extra peaks around 1640 cm^{-1} correspond to the polymer and adsorbed carbonate groups on the surface of the apatite particles showing that the PEG-co-HEA polymers have been incorporated into the crystal structures of FHA in all cases.

7.3.2.3 Thermogravimetric analysis

FTIR cannot give quantitative data in order to determine the amount of polymer ingrained in the samples; therefore, thermogravimetric analysis was used as a quantitative technique. Thermogravimetric analysis was conducted to determine the percentage weight of polymer ingrained in each sample of FHA. Figure 7.10 shows the TGA traces of all samples while table 7.8 describes the percentage weight lost during the thermogravimetric analysis.

Table 7.8: A summary of the results from the thermogravimetric analysis of FHA samples synthesised using PEG-co-HEA polymers of varying HEA degree of polymerisation and molecular weights of PEG. The percentage weight of polymer present in each HA sample is listed alongside the targeted and actual DP of the HEA block and molecular weight of the PEG macroinitiator used during the polymer synthesis.

Sample	HEA $DP_{targeted}$	HEA DP_{actual}	PEG initiator	$Wt\%_{Initial}$	$Wt\%_{Final}$	$Wt\%_{Polymer}$
FHA PEG-co-HEA 1	10	13	1900	99.97	95.87	4.10
FHA PEG-co-HEA 2	10	11	5000	99.98	96.07	3.90
FHA PEG-co-HEA 3	50	53	1900	100.17	95.23	4.94
FHA PEG-co-HEA 4	50	51	5000	99.96	95.39	4.57
FHA PEG-co-HEA 5	100	110	1900	100.04	96.08	3.96
FHA PEG-co-HEA 6	100	107	5000	99.98	95.46	4.52
FHA PEG-co-HEA 7	90	98	1900	99.99	95.98	4.01
FHA PEG-co-HEA 8	90	94	5000	99.92	95.05	4.86
FHA PEG-co-HEA 9	80	85	1900	99.96	94.70	5.26
FHA PEG-co-HEA 10	80	89	5000	99.89	95.36	4.53
FHA PEG-co-HEA 11	70	84	1900	99.87	95.23	4.64
FHA PEG-co-HEA 12	70	88	5000	99.90	95.27	4.63

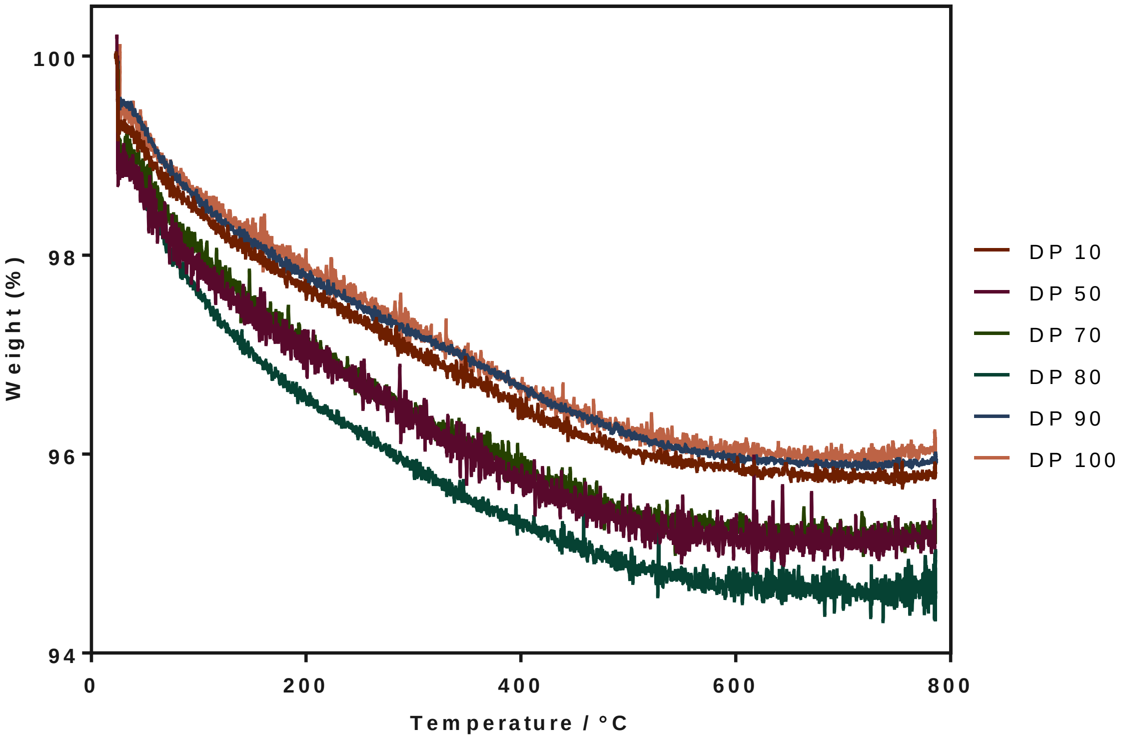

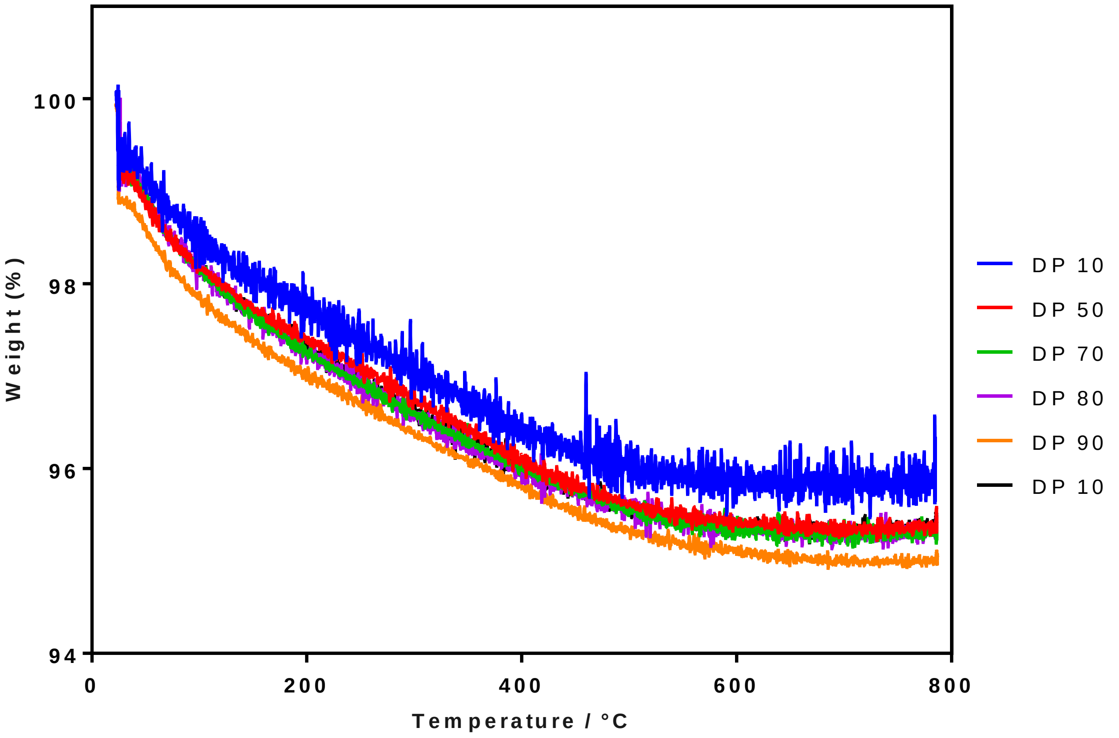

Figure 7.10. Overlaid thermogravimetric curves of FHA samples prepared with a range of polymers with varying DP $_{\text{targeted}}$ HEA blocks and PEG molecular weights. Samples synthesised with PEG 1900 macroinitiator are shown in the top figure while those produced using the PEG 5000 macroinitiator are shown in the bottom figure.

Weight was lost from all samples which, when viewed alongside the FTIR analysis, determined that polymer had successfully been incorporated into all samples. The amount of polymer incorporated into the FHA samples seemed to be relatively consistent across the samples unlike the HA samples described previously. However, it is also evident that the final weight percentage of polymer in the samples is still far less than the 10 wt% originally added to the synthesis as was seen previously.

In general, the total percentage weight loss during the TGA is fairly consistent across all samples with a difference of only 1.36 wt% between the highest and lowest weight lost, samples 9 ($DP_{targeted} = 80$, PEG 1900) and 2 ($DP_{targeted} = 10$, PEG 5000) respectively. Looking back at the FTIR spectra for both samples shows no real difference between the highest and lowest samples in terms of the polymer peak at 1690 cm^{-1}. As FTIR is not a quantitative technique, this cannot be said for certain; however, the combination of the data collected from the FTIR and TGA measurements appears to suggest that there is no discernible difference between any of the FHA samples in terms of polymer inclusion. Allowing for the error of the instrument the fact that such small amounts were lost from all samples increases the error associated with the measurement due to the prevalence of pan buoyancy which can have an adverse effect on the measurements. This is evident in all samples as can be seen by the levels of noise in the thermogravimetric curves shown in figure 7.10. Looking at the thermogravimetric curves shows that all samples from both the PEG 1900 (top figure) and PEG 5000 samples (bottom figure) were relatively consistent in shape in terms of the temperatures at which the greatest weight loss occurs. There appears to be no correlation between the percentage weight lost and the molecular weight of the PEG block or the $DP_{targeted}$ of the HEA block as was seen with the HA samples described previously. As such it is likely that the polymers interact differently with the apatite crystals compared to the polymers tested in previous chapters. In all cases, it appears that polymer has been included into all of the composite samples when compared with evidence from the XRD analysis.

7.3.2.4 Transmission Electron Microscopy

Transmission electron microscopy was used to image the particles to determine their size and morphology. Figure 7.11 shows TEM micrographs of the HA samples prepared with the PEG 1900 co-HEA polymers, while figure 7.12 shows the TEM micrographs of the composite

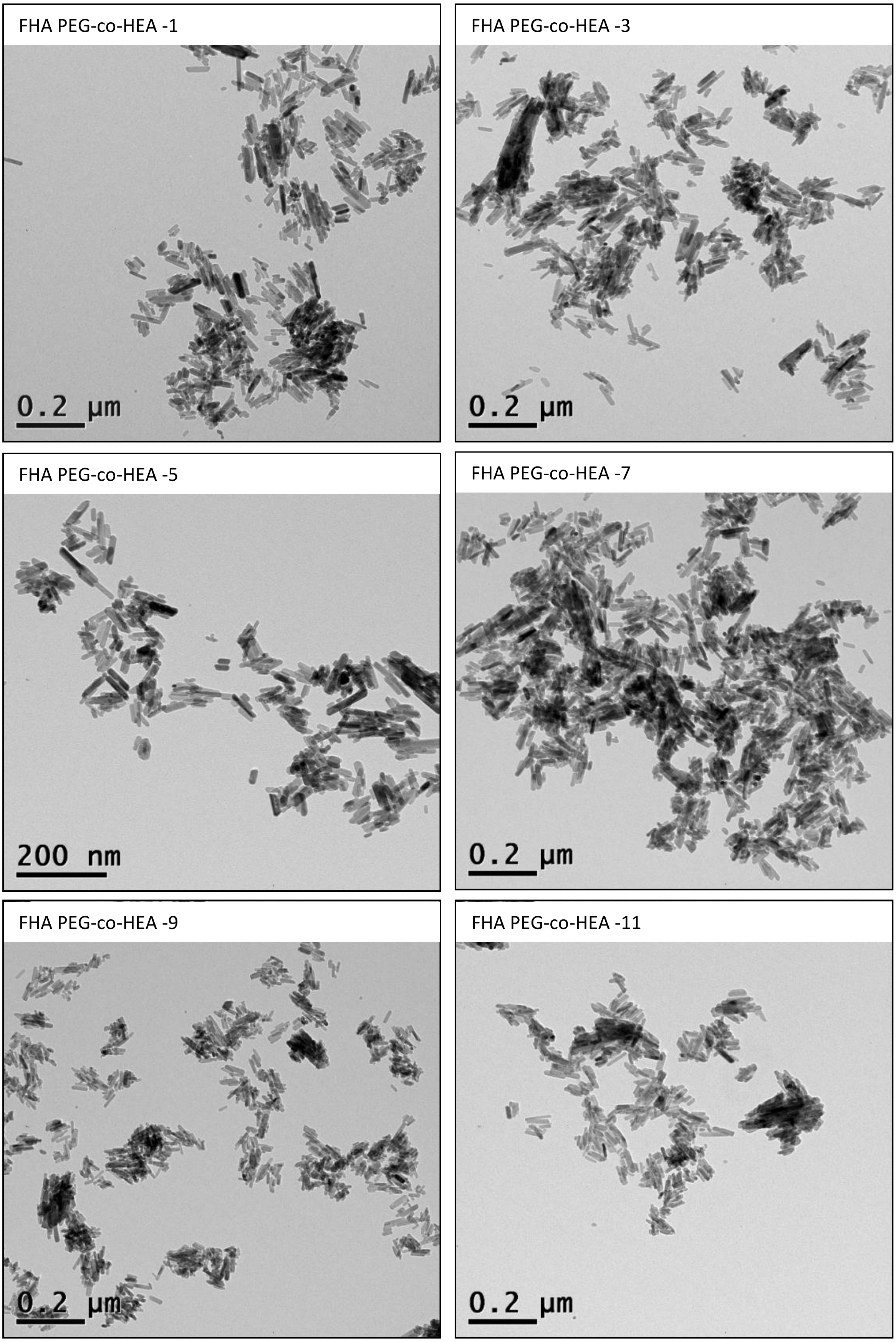

Figure 7.11. Transmission electron micrographs of FHA samples prepared with 10 wt% PEG-co-HEA polymers synthesised using the macroinitiator PEG 1900 isobutyryl bromide with varying DP $_{\text{targeted}}$ for the HEA blocks as follows: (x = DP $_{\text{Targeted}}$) 1 = 10, 3 = 50, 5 = 100, 7 = 90, 9 = 80 and 11 = 70.

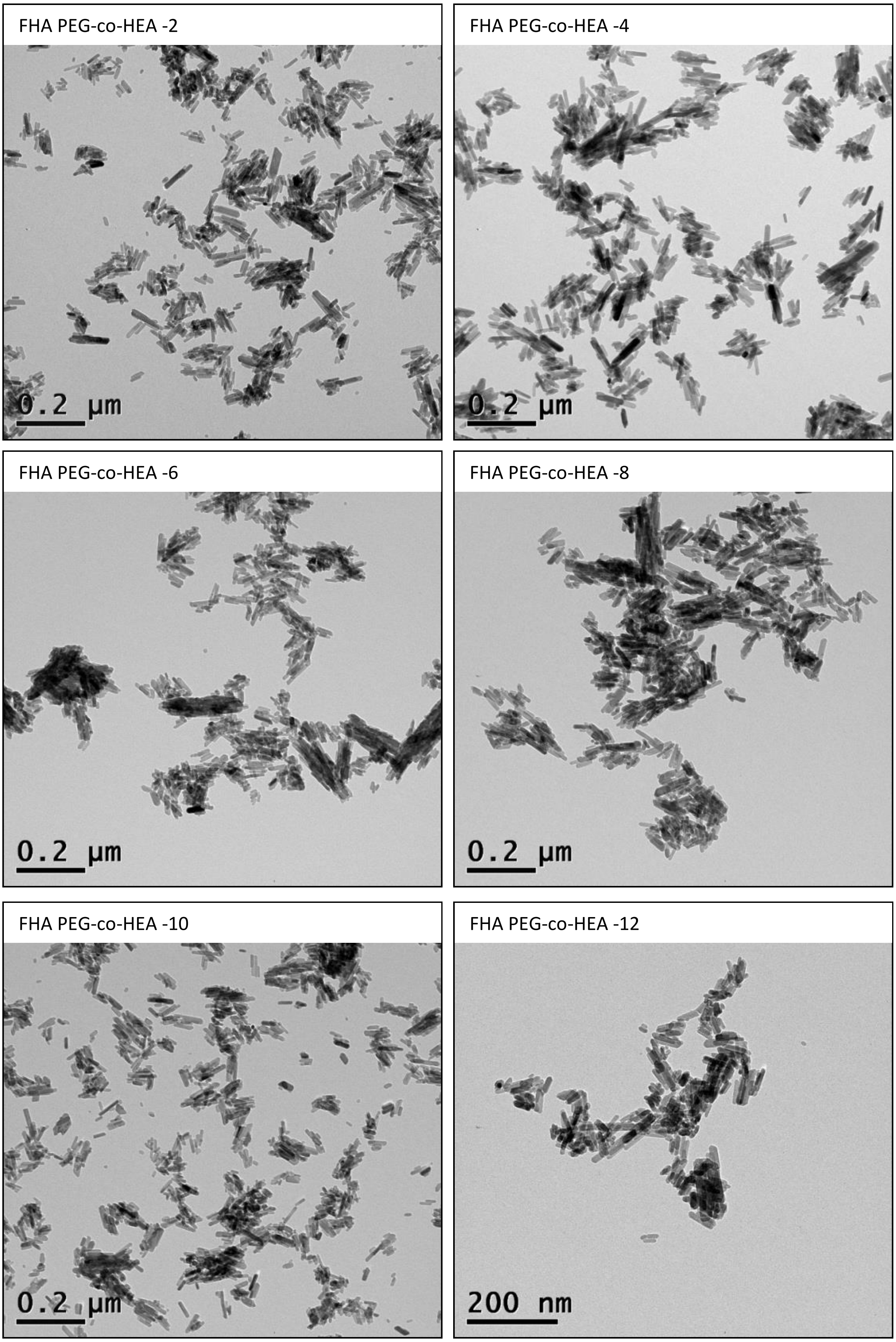

FHA PEG-co-HEA -2

FHA PEG-co-HEA -4

FHA PEG-co-HEA -6

FHA PEG-co-HEA -8

FHA PEG-co-HEA -10

FHA PEG-co-HEA -12

Figure 7.12. Transmission electron micrographs of FHA samples prepared with 10 wt% PEG-co-HEA polymers synthesised using the macroinitiator PEG 5000 isobutyryl bromide with varying DP $_{\text{targeted}}$ for the HEA blocks as follows: (x = DP $_{\text{Targeted}}$) 2 = 10, 4 = 50, 6 = 100, 8 = 90, 10 = 80 and 12 = 70.

sample prepared with PEG 5000 co-HEA polymers. Upon visual inspection of the TEM micrographs it is evident that the particles are all fairly consistent in terms of size and shape. There is a small range of particle sizes within all samples with all samples showing particle aggregation. This indicates that the PEG group of the copolymers incorporated into the samples has not acted as a steric stabiliser. ImageJ was used to determine the particle sizes and aspect ratios,[1] a summary of the results for the FHA PEG 1900 samples are shown in table 7.9.

Table 7.9. A summary of the particle sizes and aspect ratios of FHA particles synthesised in the presence of 10 wt% PEG 1900-co-HEA polymers with varying DP $_{\text{Targeted}}$ and DP $_{\text{Actual}}$. Values of DP $_{\text{Actual}}$ are given in the table alongside particle sizes, standard deviation, standard error of measurement and aspect ratios measured by ImageJ.[1]

Sample	**HEA DP$_{\text{Actual}}$**	**Lengths / nm**			**Widths / nm**			**Aspect ratios**
		Mean	SD	SE	Mean	SD	SE	
FHA PEG-co-HEA 1	13	84.75	15.30	0.76	12.32	2.18	0.22	6.88
FHA PEG-co-HEA 3	53	74.56	13.59	0.68	10.58	2.10	0.21	7.05
FHA PEG-co-HEA 11	84	70.22	13.94	0.69	7.46	1.49	0.15	9.41
FHA PEG-co-HEA 9	85	60.50	12.73	0.63	10.40	2.24	0.22	5.82
FHA PEG-co-HEA 7	98	45.03	10.42	0.52	12.93	2.85	0.28	3.48
FHA PEG-co-HEA 5	110	40.88	11.39	0.57	12.52	1.94	0.19	3.26

The standard deviation values for all samples are much smaller than the HA samples synthesised using the same polymers. This supports the observation from viewing the micrographs that the particle sizes appear to be fairly consistent. These values also show that the FHA particle sizes decrease with increasing HEA ratio in the polymers used to synthesise the composite materials. Plotting DP$_{\text{actual}}$ against mean particle length (figure 7.13) shows a definite trend towards the HEA block allowing control over the particle size formation. Sample 11 (PEG 1900, DP $_{\text{Targeted}}$ = 70:1, DP $_{\text{Actual}}$ = 84:1) shows a slightly anomalous result with a particle size that was closer to sample 3 (PEG 1900, DP $_{\text{Targeted}}$ = 50:1, DP $_{\text{Actual}}$ = 53:1) than sample 9 (PEG 1900, DP $_{\text{Targeted}}$ = 80:1, DP $_{\text{Actual}}$ = 85:1) as would have been expected due to the similarities in DP $_{\text{Targeted}}$. However, the standard deviation of both samples overlap, hence the trend of decreasing particle size with increasing HEA ratio is still valid.

The FHA samples prepared with the PEG 5000 polymers show a similar trend as the FHA PEG 1900 samples. ImageJ was used to determine particle sizes of the FHA PEG 5000 composite samples;[1] a summary of the particle sizes is shown in table 7.10.

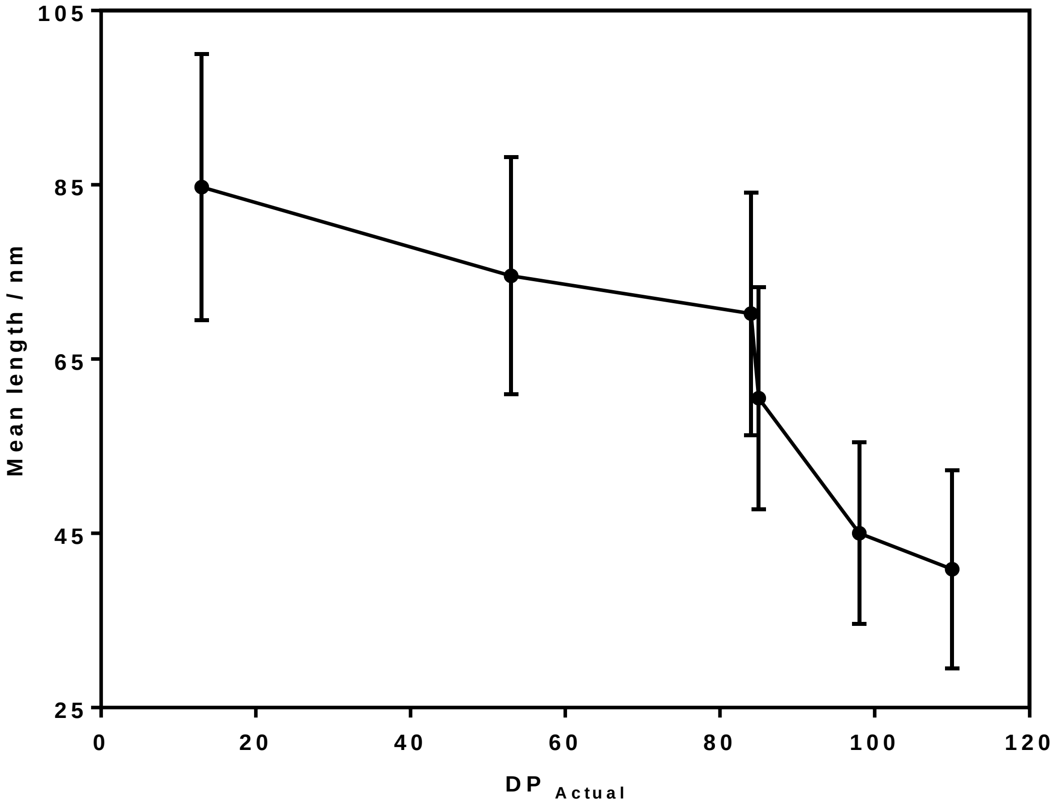

Figure 7.13. A plot showing the decrease in particle size of synthesised composite particles with increasing DP $_{Actual}$ of the HEA block in the PEG 1900-co-HEA polymers used to produce the composite particles. Error bars are the calculated standard deviation of the particle mean lengths measured using ImageJ.[1]

Table 7.10. A summary of the particle sizes and aspect ratios of FHA particles synthesised in the presence of 10 wt% PEG 5000-co-HEA polymers with varying DP $_{Targeted}$ and DP $_{Actual}$. Values of DP $_{Actual}$ are given in the table alongside particle sizes, standard deviation, standard error of measurement and aspect ratios measured by ImageJ.[1]

Sample	**HEA DP$_{Actual}$**	**Lengths / nm**			**Widths / nm**			**Aspect ratios**
		Mean	SD	SE	Mean	SD	SE	
FHA PEG-co-HEA 2	11	78.50	16.35	0.81	10.64	2.29	0.23	7.38
FHA PEG-co-HEA 4	51	76.11	15.52	0.77	14.26	3.11	0.31	5.34
FHA PEG-co-HEA 12	88	62.18	15.07	0.75	8.50	1.94	0.19	7.31
FHA PEG-co-HEA 10	89	59.98	7.77	0.39	8.73	1.52	0.15	6.87
FHA PEG-co-HEA 8	94	58.54	14.43	0.72	24.28	5.74	0.57	2.41
FHA PEG-co-HEA 6	107	45.18	9.57	0.48	11.05	2.88	0.29	4.09

Table 7.10 again shows that as the DP $_{Actual}$ of the HEA block increases the size of the composite particles synthesised decreases. The standard deviations of each sample show that the particle sizes are more consistent within the samples than the HA composites synthesised using the same polymers. Figure 7.14 shows a plot of actual ratio against mean particle length of the FHA composites. This plot suggests that even when the standard deviation of the mean particle size is taken into account, the particle length decreases with the increased ratio of

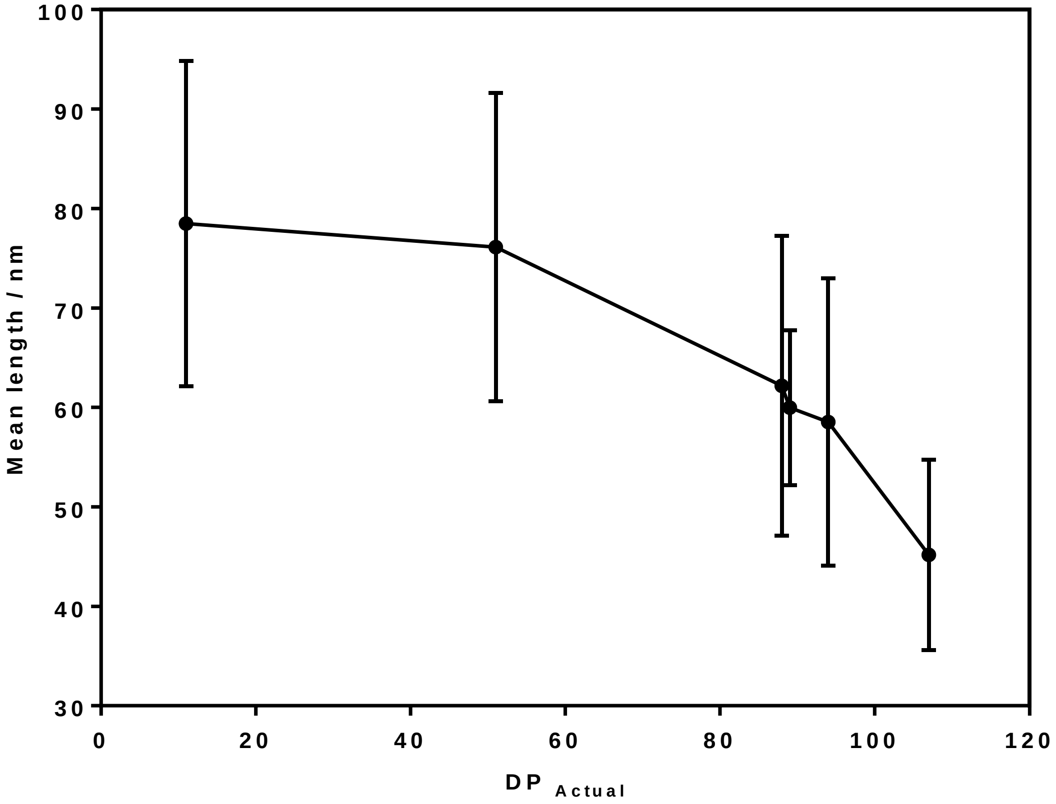

Figure 7.14 A plot showing the decrease in particle size of synthesised composite particles with increasing DP $_{\mathrm{Actual}}$ of the HEA block in the PEG 5000-co-HEA polymers used to produce the composite particles. Error bars are the calculated standard deviation of the particle mean lengths measured using ImageJ.[1]

HEA in the polymer used to form the composite particles. Again samples 12, 10 and 8 where the DP $_{\mathrm{Targeted}}$ = 70, 80 and 90 respectively while DP $_{\mathrm{actual}}$ = 88, 89 and 94 respectively show a similarity in particle sizes while still maintaining the trend of increasing HEA DP $_{\mathrm{Actual}}$ leading to decreasing particle size. This suggests that the amount of HEA in the polymers used to create the composite particle has a direct impact on particle formation and therefore it is likely that the HEA block of the copolymer acts as a nucleation point for the growth of the FHA particles. Comparing the results from the TEM analysis of the FHA samples with those of the HA samples suggests that human error may have caused the HA PEG 1900 not to show the same trend as all the other samples. This may have been due to high levels of particle aggregation making particle sizing difficult due to the particles overlapping. It is also possible that the HA PEG 1900 samples did not fit with the trend of the HA PEG 5000 and FHA data sets due to other intrinsic properties of the sample that were not evident in any of the analysis methods. This seems unlikely due to the similarity of all samples in the HA and FHA data sets across all the XRD and FTIR analysis as these characterisation methods are used to determine intrinsic properties of the unit cell and chemical interactions therein. As a result, human error in measuring the particle sizes seem a more likely explanation for the differences seen in the HA PEG 1900 -co-HEA TEM results.

Also evident by the TEM analysis is that the FHA samples are much smaller than the HA samples as was also seen in previous chapters. This along with the loss of OH peaks at 3570 and 640 cm^{-1} in the FTIR spectra of the FHA samples shows that fluoride was successfully incorporated into all the FHA samples.

7.4 Conclusion

Synthesis of hydroxyapatite and fluorhydroxyapatite samples containing PEG-co-HEA block copolymers with varying HEA DP$_{\text{Targeted}}$ and DP$_{\text{Actual}}$ and differing molecular weights of the PEG block were successful. Characterisation by x-ray diffraction, fourier transform infrared spectroscopy, thermogravimetric analysis and transmission electron microscopy showed that apatite had been formed in all cases.

TGA analysis showed that the 10 wt% of polymer included in the synthesis of the (F)HA particles was not all incorporated into the final composite particles. The HA samples showed far less polymer ingrained in the composite structure than the FHA samples when measured by TGA. However, all samples produced less than 5.3 wt% of polymer in the final composite material. It is likely that the polymer complexed with calcium ions during the apatite synthesis and were subsequently washed away during the material processing.

TEM analysis showed that in all but the HA PEG 1900 -co-HEA samples, the increase in the DP$_{\text{Actual}}$ of the HEA block lead to a decrease in the particle size of the (F)HA composite particles produced. This suggests that the HEA block acts as a nucleation point for the formation of apatite, proving the original hypothesis correct. The reason this was not seen in the HA PEG 1900 -co-HEA samples was put down to human error in measuring the particle sizes due to high levels of particle aggregation.

All of the (F)HA PEG-co-HEA samples showed that the PEG block had no effect on particle formation or aggregation. This showed that the hypothesis that the PEG block would act as a steric stabiliser and disperse the particles was false.

7.5 References

1. C. A. Schneider, W. S. Rasband and K. W. Eliceiri, *Nature Methods*, 2012, **9**, 671-675.
2. D. Gunes, O. B. Kurtarel and N. Bicak, *Journal of Applied Polymer Science*, 2013, **127**, 2684-2689.
3. C. Zhao, K. Patel, L. M. Aichinger, Z. Liu, R. Hu, H. Chen, X. Li, L. Li, G. Zhang, Y. Chang and J. Zheng, *Rsc Advances*, 2013, **3**, 19991-20000.
4. N. Bhattarai, F. A. Matsen and M. Zhang, *Macromolecular Bioscience*, 2004, **5**, 107-111.
5. R. B. Greenwald, *Journal of Controlled Release*, 2001, **74**, 159-171.
6. R. A. Scott and N. A. Peppas, *Biomaterials*, 1999, **20**, 1371-1380.
7. Bruker, *DIFFRACplus TOPAS 4.2 User ManualDIFFRACplus TOPAS 4.2 User Manual*, Bruker AXS GmbH, Karlsruhe, Germany., 2009.
8. V. K. Pecharsky and P. Y. Zavalij, *Fundamentals of Powder Diffraction and Structural Characterization of Materials, Second Edition*, Springer US, 2009.
9. L. Berzina-Cimdina and N. Borodajenko, *Research of Calcium Phosphates Using Fourier Transform Infrared Spectroscopy InTech*, 2012.
10. A. W. Coats and J. P. Redfern, *Analyst*, 1963, **88**, 906-&.

Chapter 8 – Conclusions

This work has investigated the interactions of nanoscale calcium phosphate apatites with polymer additives of various architectures and functionalities. The addition of polymers, or the modification of the nanoparticle synthesis using a polymer environment, allows both control over particle size and morphology and the prospect of developing novel functional materials for biomedical and wider applications. Very little work on the fabrication of nanoscale calcium phosphates in the presence of polymers has been reported to date despite the potential value of these approaches. Therefore, the main aim of this PhD was to synthesise nanoscale hydroxyapatite and fluorhydroxyapatite in the presence of functional polymers, and investigate the effects of this novel process on the properties of the products. Several methods of apatite synthesis were attempted before the most promising route was determined. The main objectives of this this work can be summarised into six areas:

8.1 Synthesis of hyperbranched homopolymers of acrylic acid (AA), methacrylic acid (MAA) and 2-acrylamido-2-methylpropane sulfonic acid (AMPS) via RAFT polymerisation

The RAFT agents 4-vinylbenzyl N-pyrrolecarbodithioate and 4-vinylbenzyl dithiobenzoate were used to synthesise highly branched polymers of acrylic acid, methacrylic acid and 2-acrylamido-2-methylpropane sulfonic acid. The polymerisations of acrylic acid were the most successful, while the AMPS polymers were extremely difficult to process. The methacrylic acid polymerisations varied with some reactions undergoing gelation. RAFT polymerisation using AMPS frequently lead to gelation and a loss of colour of the RAFT agent suggesting it was either degraded or reacted irreversibly with the AMPS monomer. The acrylic acid and methacrylic acid polymers were taken forward for the synthesis of composite materials while the AMPS polymers were abandoned.

8.2 Characterisation of these polymers through nuclear magnetic resonance (NMR) spectroscopy, gel permeation chromatography (GPC) and small angle x-ray scattering (SAXS)

Characterisation of the polymers by nuclear magnetic resonance spectroscopy showed that the RAFT polymerisation was successful due to the loss of peaks corresponding to the vinyl group of the monomer. Peaks corresponding to the pyrrole and/or benzyl groups of the RAFT agent showed the incorporation of the RAFT agent into the final polymer and were used to determine the degree of branching of the polymers. It was found that the AMPS polymers had the highest degree of branching from 12 - 21 % while the PAA and PMAA samples had degrees of branching ranging from 2 – 7 %. The degree of branching differed between the different monomers with AMPS showing the highest degree of branching at 21 % but the lowest yield of polymerisation. The (meth)acrylic acid polymers were less branched but had higher yields suggesting that the free radical polymerisation reaction at the vinyl end of the RAFT agents was inhibited to some degree by the (M)AA monomers but not by the AMPS and the RAFT polymerisation was more successful with the (M)AA monomers.

Gel permeation chromatography (GPC) was attempted on several occasions but failed in all cases. Initially samples were methylated to prevent the acid end groups from sticking to the GPC column. However, this caused the polymers to become completely insoluble in all solvents. As a result of this small angle X-ray scattering (SAXS) was used to determine the polymer molecular weights.

Using SAXS it was possible to determine the radius of gyration (Rg) of the polymers via the Guinier approximation. Using the radius of gyration, it was possible to determine values of molecular weight for the polymer. Comparing the values gained from SAXS with the theoretical molecular weights of the polymers determined through the relative ratios and molar masses of the monomers and RAFT agents used and the percentage conversion of the polymerisation showed good correlation which gave confidence in the values measured by SAXS.

8.3 Determination of the most effective method for combining the homopolymers and calcium phosphate particles

Several different methods of combining the acrylic acid polymers with the apatite nanoparticles were considered via small scale reactions using a carousel reactor. Adding (F)HA nanoparticles to the synthesis of the polymers was not viable as the acidic polymerisation environment degraded the (F)HA. Combining the polymers and (F)HA particles once both had been synthesised separately had some success but was extremely unreliable and proved to be inconsistent between batches. The addition of presynthesised polymers to the precipitation of the (F)HA nanoparticles proved to be the most successful method of combining the two materials. The addition of the polymer allowed control over the size and shape of the (F)HA nanoparticles by controlling the amount of polymer in the system and lead to the formation of polymer-apatite composite nanoparticles which were confirmed by FTIR, XRD, TGA and TEM.

8.4 Synthesis and characterisation of hydroxyapatite (HA) and fluorhydroxyapatite (FHA) composite nanoparticles via precipitation in the presence of hyperbranched and linear acid homopolymers

Having determined the best method to create the composite nanoparticles, commercially sourced linear poly(acrylic acid)s were compared to hyperbranched poly[(meth)acrylic acid]s synthesised during the project in terms of their effect on the synthesis of (F)HA. The acid sensitivity of the apatites meant that polymer coatings could not be formed around the (F)HA particles by placing them into the polymer synthesis, instead the opposite method was attempted and polymers were added to the synthesis of (F)HA particles. Analysis by TEM showed that the polymers caused the morphology of the particles to change from flat plates to needle-like crystals. XRD analysis of the particles showed an increase in long range order of the unit cell along the *c* axis of the apatite where the calcium ions lie, while FTIR analysis showed broadening of the signals belonging to the phosphate groups indicating a loss of long range order along the *a* axis due to the reorganisation of the unit cells. The TEM, XRD and FTIR results implied that the polymers acted as a nucleation point for apatite growth and caused the calcium ions to align along the polymer chains forming needle-like particles. The polymers were also found to affect the size of the particles, particularly when fluoride was included in the apatite synthesis. The (F)HA particles were all found to be significantly smaller than the HA particles due to the fluoride ion being smaller and fitting better into the apatite unit cell, hence causing it to shrink.

8.5 Synthesis and characterisation of hydroxyapatite (HA) and fluorhydroxyapatite (FHA) composite nanoparticles via precipitation in the presence of poly(ethylene glycol-co-hydroxyethyl acrylamide) (PEG-co-HEA) copolymers with differing length PEG blocks and HEA block with differing degrees of polymerisation

Block copolymers of poly(ethylene glycol-co-[2-N-hydroxyethyl acrylamide]) (PEG-co-HEA) were synthesised with varying lengths of the PEG and HEA blocks. Upon adding the polymers to the synthesis of (F)HA particles, it was found that the length of the PEG block had no effect on the particles, while increasing the length of the HEA block caused the (F)HA particles to become smaller. This suggests that the charged HEA block acts as a nucleation point for apatite growth. XRD analysis again showed an increase in long range order along the c axis which implies the calcium ions align to the charged HEA block of the copolymer during synthesis. The lack of effect shown by the PEG block on the particle size and morphology suggests another method should be sought in order to create discrete dispersed nanoparticles.

8.6 Determination of the in vitro biocompatibility of novel materials using cell viability testing based on cytotoxicity evaluation using PrestoBlue (resazurin), LDH and live/dead assays

The cytotoxic effect of the some (F)HA particles was assessed using metabolic assays to determine cell viability, cell membrane damage and the number of live and dead cells present after incubation. Cell viability assays showed that the FHA samples were marginally more cytotoxic than the HA samples and that by increasing the concentration of particles in the suspension added to the cells, the percentage cytotoxicity increased. LDH assays to determine the effect of the particles on the cell membrane supported the cell viability assay result which showed that increasing the particle concentration caused an increase in the perceived percentage cytotoxicity. However, for both concentrations (1 mg ml^{-1} and 10 mg ml^{-1}) the percentage cytotoxicity indicated by the LDH assay was very low, suggesting that the particles had very little effect on the cell membrane. Live/dead staining showed predominantly living cells in all samples with a much smaller number of dead cells in each sample. The staining was hindered slightly by the fact that the (F)HA particles absorbed and were stained by the EthD-1 (red) dye along with the dead cells. As such the number of living and dead cells could not be determined accurately due to the possibility that the observed dead cells were in fact particles.

Overall, this thesis has shown the successful production of composite polymer-apatite nanoparticles with low cytotoxic effects on living cells. The nanoparticles' size and morphology can be controlled by the type, size and concentration of polymer added to the precipitation of apatite. To this end there is scope for these nanoparticles to be tailored for use in specific applications in medicine and dentistry with minimal effect on the body.

Chapter 9 – Future Work

There is scope to extend the present work further through the use of other polymers to create new nanocomposite materials and by continuing the cell testing using other assays and or cell types. MG63 cells are bone cancer cells, therefore it could be useful to try cell testing with non-cancer cells in order to determine whether the particles could be preferentially cytotoxic towards cancer cells and hence become a potential cancer treatment.

It would also be interesting to take the current work further by investigating the effect of different amounts of polymer on the particles formed. In the present study, polymer loadings of 4, 10 and 16 wt% were used and only the 4 wt% samples were tested against cells. It would be interesting to investigate whether different amounts of polymer could have an effect on the cytotoxicity of the particles as well as their size and morphology. Furthermore, as natural bone has a critical concentration of collagen within it, it would be pertinent to determine whether this same critical concentration applies to polymers in synthetic hydroxyapatite and whether or not it would have further effects on the properties of the composite nanoparticles.

It would also be interesting to use different types of polymers. The block copolymers of PEG-co-HEA described in chapter 6 appeared to have an effect on the particles only when the charged HEA block was changed. Other copolymers containing blocks with different charge densities could be used to determine whether this would enable the formation of discrete dispersed nanoparticles. This could include different polyanions which would likely interact with calcium ions in the (F)HA particles as seen in the present work, or polycations which could potentially interact with the phosphate and or hydroxyl groups. Other polymers which could be investigated include those which are biologically inert as these could be used as a block of a copolymer in order to prevent cytotoxicity and create functionalised nanoparticles for applications in drug delivery systems. The use of alternate polymers may lead to new particle morphologies not seen in this study, which could have further biological effects.

In terms of cytotoxicity testing, the present work could be extended to determine whether there is an optimum concentration of particles which has therapeutic benefits on cells as opposed to being cytotoxic. The present work only used two concentrations at an order of magnitude apart. It is possible that within the region between concentrations of 1 and 10

$mgml^{-1}$ of particles in media, or potentially even less than this, there is a therapeutic level at which the particles cause the cell to become more virile. Moreover, if the particles could be functionalised, either by modifying the polymers or the surface of the particles, this could lead to new methods of drug delivery by attaching drugs to the modified particles.